3D modelling of Soft soil Improvement by Rigid Inclusions - Complex and Cyclic loading

van Hung Pham

Communauté
UNIVERSITÉ Grenoble Alpes

THÈSE

Pour obtenir le grade de

DOCTEUR DE LA COMMUNAUTE UNIVERSITE GRENOBLE ALPES

Spécialité : **Matériaux, Mécanique, Génie civil, Electrochimie**
Arrêté ministériel : 25 mai 2016

Présentée par

Van Hung PHAM

Thèse dirigée par **Daniel DIAS, professeur à Université Grenoble Alpes**

Préparée au sein du **Sols, Solides, Structures-Risques** dans **l'École Doctorale I-MEP2**

Modélisation tridimensionnelle de l'amélioration des sols par des inclusions rigides – Chargement complexe et cyclique

3D modeling of Soft soil Improvement by Rigid Inclusions – Complex and Cyclic loading

Thèse soutenue publiquement le **17 Septembre 2018,**
devant le jury composé de :

M. Pascal VILLARD
Professeur, Université Grenoble Alpes, Président du jury
M. Hussein MROUEH
Professeur, Université de Lille 1 Sciences et Technologies, Rapporteur
Mme Anne PANTET
Professeur, Université du Havre, Rapporteur
M. Laurent BRIANÇON
Maître de Conférences, INSA Lyon, Examinateur
Mme Orianne JENCK
Maître de Conférences, Université Grenoble Alpes, Examinateur
M. Daniel DIAS
Professeur, Université Grenoble Alpes, Directeur de thèse

Acknowledgments

First of all, I would like to express my sincere gratitude and appreciation to my supervisor, Professor Daniel DIAS for all his scientific ideas, his direct guidance and his encouragement throughout my study. We had interesting discussions about my research direction and the specific work we did together. I really appreciate his patience and his English corrections for my writing and speaking.

I also would like to say thanks to Mr. Briançon in INSA Lyon, France and Portuguese colleagues at the Department of Civil Engineering, University of Minho, Portugal for their collaborations.

I would like to thank the jury members for their suggestions, comments and remarks which made my dissertation more complete. And it also made my dissertation defense more attractive and interesting. Especially, I want to say sincere thanks to two reviewers, Prof. Pantet and Prof. Mroueh, for their opinions and advice for my further study.

Thanks should also be given to my friends at the 3SR laboratory. And deep thanks also go to my best friends for their support and friendship: Lopez Jimenez Guillermo Alfonso, Aleksandr Dudchenko, Quijing Pan and QiangQiang Sun.

Finally, I would like to express my thanks to my small family. I appreciate my wife, Thi Thu, for her support and encouragement throughout my PhD study. I also would like to acknowledge my two children, Bich Ngoc and Quang Minh, who took my time while filling it with joy. And my deep thanks go to my parents for the love and support.

This research project was funded by the 911 scholarship of the Vietnamese government. This support is highly appreciated.

Abstract

The technique of soft soil improvement by rigid inclusions (RI) under embankments or foundations has been increasingly gathered interest in the geotechnical research community. These kinds of structures can be affected by natural and artificial factors such as wind, waves, earthquakes, industrial cranes, traffic vehicles, eccentrically compressive stresses, or water level fluctuations. All these factors induce complex loadings on the soil. Previous researches often focused on the behavior of the rigid inclusion-improved soft soil subjected to uniform static loading (embankment weight and surcharges). A few attention was paid to the response of a rigid inclusion-reinforced soil under complex loading as well as under cyclic loading. The aim of the study is to investigate the soil improvement by rigid inclusions under complex and cyclic loadings, and to highlight the effect of some parameters related to complex and cyclic loading on the system behavior.

Concerning the static complex loading, footings over rigid inclusion-reinforced soil without mattress subjected to centered, eccentrically vertical and horizontal loads, and load cycles are first studied. Numerical and experimental approaches are presented. Monitored and numerical results permit to show the behavior of these reinforced systems in terms of stresses on the inclusion head and soft soil, vertical and lateral displacements of the footings and lateral displacement of the inclusions. The efficiency of the reinforced footing is also presented and compared to the unreinforced one.

A 3D modeling of the foundation solutions for wind turbines is presented. The combination of vertical loading and different moments applied to the foundation is taken into account. The inclusion-improved soft soil under footing is considered as a foundation option and, compared to classical ones (shallow foundation and piled raft). The obtained results are illustrated concerning the ground surface settlements, the foundation rotations, the axial forces and bending moments of the reinforcements. The numerical results indicate that the soil improvement technique by rigid inclusions can be an appropriate solution for the wind turbine foundations.

With regard to the cyclic aspects, three main concerns are studied. Firstly, the numerical modeling of laboratory tests on a soil improvement by rigid inclusions subjected to monotonic loading and a limited load cycles is carried out, in which the hypoplasticity (HYP) model is used to model the load transfer platform (LTP). The numerical results are validated against both the experimental data and numerical ones of Houda (2016). The influence of the boundary condition and soft soil state are figured out. The numerical results indicate that it is possible to address the cyclic

behavior of the rigid inclusion-reinforced soil by using the HYP model.

Secondly, a piled embankment under a high number of cyclic loadings is studied. Two different levels of complexity for the constitutive models are used (HYP and a simpler one the linear elastic perfectly plastic constitutive model with a shear criteria of Mohr-Coulomb). These models were considered to model the behavior of the LTP and analyze the cyclic behavior of the system. The HYP model is then suggested for the following studies since it can capture well the arching decrease and the cumulated settlements under the load cycles number. The effect of the parameters that are load cycles number, amplitude and frequency (induced by traffic speed), and embankment height is illustrated as well.

Finally, a study on the cyclic response of a GRPS embankment is conducted. By comparing the geosynthetic-reinforced pile-supported (GRPS) embankment with the piled embankment (PE), the role of the geosynthetic is verified under static and cyclic loading aspects. The influence of the load cycles number and the geosynthetic layers number on the arching effect and cumulative settlements is shown as well.

Résumé

La technique d'amélioration des sols compressibles par des inclusions rigides (RI) sous des remblais ou des fondations suscite de plus en plus d'intérêt de la part de la communauté géotechnique. Les structures peuvent être impactées par des facteurs naturels et artificiels tels que le vent, les vagues, les tremblements de terre, des grues industrielles, les cycles liés à la circulation de véhicules, des contraintes de compression excentrées ou des fluctuations du niveau d'eau. Les recherches effectuées précédemment portaient essentiellement sur le comportement de sol compressibles renforcés par des inclusions et soumis à des charges statiques uniformes (poids du remblai et surcharge). Moins d'attention a été portée à la réponse des sols renforcés par inclusions rigides sous chargements complexes et cycliques. Le but de cette étude est d'étudier le renforcement des sols par des inclusions rigides sous chargements complexes et cycliques. L'effet de certains paramètres liés à la définition d'un chargement complexe et cyclique sur le comportement du système est également mis en évidence.

Du point de vue des chargements statiques complexes, des semelles de fondation posées sur un sol compressible renforcé par inclusion rigide sans matelas soumis à des charges centrées, excentrées verticales et horizontales et à quelques cycles de charge ont été étudiées. Des approches numériques et expérimentales sont présentées. Les résultats des mesures expérimentales et numériques permettent de mettre en évidence le comportement de ces systèmes en termes de contrainte sur la tête d'inclusion et sur le sol compressible, de déplacements verticaux et latéraux de la semelle et du déplacement latéral de l'inclusion. L'efficacité de la semelle renforcée est comparée à celle d'une semelle non renforcée.

Une modélisation 3D de solutions de fondations pour les éoliennes est étudiée. La combinaison d'un chargement vertical et de différents moments appliqués à la fondation est prise en compte. Le sol compressible renforcé par inclusions rigides est considéré comme une option qui est comparée à d'autres solutions plus classiques (fondation superficielle et radier sur pieux). Les résultats obtenus permettent de présenter l'impact sur le tassement du sol, la rotation de la fondation, les efforts axiaux et les moments fléchissants dans les inclusions rigides. Les résultats numériques indiquent enfin que la technique d'amélioration du sol par inclusions rigides peut être une solution appropriée pour les fondations d'éoliennes.

En ce qui concerne les aspects cycliques, trois points principaux sont abordés. Dans un premier temps, la modélisation numérique d'essais en laboratoire d'un renforcement

de sol par inclusions rigides soumis à des chargements monotones et des cycles limités de chargement mise en œuvre. Le modèle hypoplastique (HYP) est utilisé pour modéliser le comportement de la plate-forme de transfert de charge. Les résultats numériques sont validés à la fois par rapport aux données expérimentales et numériques de Houda (2016). L'influence des conditions aux limites et de l'état du sol compressible est mise en évidence. Les résultats numériques indiquent qu'il est possible de considérer le comportement cyclique du sol renforcé par inclusions rigides en utilisant le modèle HYP.

Dans un second temps, un remblai renforcé par des inclusions rigides sous un nombre élevé de chargement cyclique est étudié. Deux niveaux de complexité différents pour le modèle constitutif (HYP et le modèle élastique linéaire parfaitement plastique avec un critère de rupture de type Mohr-Coulomb) ont été pris en compte pour étudier le comportement de la LTP et analyser le comportement cyclique du système. Le modèle HYP est proposé pour la suite des études car il permet de bien capturer la décroissance et l'accumulation des tassements avec le nombre de cycles de charge. L'effet des paramètres qui sont le nombre de cycles de charge, l'amplitude et la fréquence (induite par la vitesse du trafic) et la hauteur du remblai est également présentée.

Finalement, une étude sur la réponse cyclique d'un remblai de GRPS est menée. En comparant le remblai renforcé par des géosynthétiques (GRPS) avec le remblai renforcé par inclusions (PE), le rôle du géosynthétique est mis en évidence sous des chargements statiques et cycliques. L'influence du nombre de cycles de chargement et du nombre de géosynthétiques sur l'effet de voute et les tassements cumulés est également discutée.

Table of contents

Notations

The following symbols are used in the thesis:

Symbol	Unit	Explanation
1D		One dimensional
2D		Two-Dimensional
3D		Three-Dimensional
A	m^2	area of raft foundation
A	N/pile	Load part transferred directly to the pile ('arching A' in this thesis) expressed as kN/pile = kN/unit cell
a	m	Width of the square pile cap
B	N/pile	Load part that passes through the geosynthetic reinforcement (GR) to the pile expressed as kN/pile = kN/unit cell
B	m	Width of the embankment at the crest
BEM		Boundary Element Method
b	m	Width of the square pile cap
C	N/pile	Load part that is carried by the soft soil between the piles (this soft soil foundation is called 'subsoil' in this thesis) expressed as kN/pile = kN/unit cell
C_c	-	Arching coefficient adapted in BS8006
c	Pa	Cohesion
CPT		Cone Penetration Testing
D	-	Damping ratio
D	m	Diameter of raft foundation
DEM		Discrete Element Method
d	m	Diameter circular pile (cap)
E	%	Pile efficacy or pile efficiency
E	Pa	Young's modulus of the material
E_p	Pa	Young's modulus of piles
E_p	Pa	Pressuremeter modulus obtained in the Pressuremeter Testing
e	-	Void ratio at the given pressure
e_o *or* e_{ini}	-	Initial void ratio

e_{c0}	-	Critical void ratio at zero pressure in the hypoplasticity model
e_{do}	-	Minimum void ratio at zero pressure in the hypoplasticity model
e_{i0}	-	Maximum void ratio at zero pressure in the hypoplasticity model
FDM		Finite Difference Method
FEM		Finite Element Method
f	Hz	Frequency of cyclic loading
G	Pa	maximum elastic shear modulus in the Cam-clay model
G^e_{ref}	Pa	Reference elastic tangent shear modulus in the CYsoil model
GR		Geosynthetic reinforcement
GRPS		Geosynthetic-reinforced pile-supported
H	m	Height of the fill above the bottom layer of GR, or height of fill above a pile
H	N	Horizontal loading on the footing
HYP		Hypoplasticity
h_g	m	Thickness of mattress under foundation
h_s	Pa	Granulate hardness that controls the shape of void ratio curve in the hypoplasticity model
J	N/m	Isotropic stiffness of geosynthetic
K_p	-	Rankine passive earth pressure coefficient
K^{iso}_{ref}	Pa	Slope of the laboratory curve for p' versus e at reference effective pressure in the CYsoil model
k_s and k_n	N/m/m	Shear stiffness and normal stiffness of the interface
L	m	Length of pile or inclusion
M	-	Slope of the critical state line in p'-q space
MC		Mohr-Coulomb
MCC		Modified Cam-clay
MPM		Material Point Method
M_y	N.m	Overturning moment by the y-axis
m	-	Constant that controls the variation of elastic tangent shear modulus by the effective stress in the CYsoil model, m ≤ 1.0

m_R	-	Parameter controls the initial shear modulus upon 180^o strain path reversal and in the initial loading in the hypoplasticity model
m_T	-	Constant controls the initial shear modulus upon 90^o strain path reversal in the hypoplasticity model
N	-	Number of load cycles
n	-	Exponent controls the shape of void ratio curve in the hypoplasticity model
P	N	Total load carried by the piles
P	Pa	Static vehicle wheel load
PE		Piled embankment
P_L	Pa	Limit pressure obtained in the Pressuremeter Testing
P_t	Pa	Cyclic vehicle wheel load
p *or* q	Pa	Uniformly distributed surcharge on top of the fill/footing (top load)
p_1	Pa	Reference pressure in the CYsoil model
p'	Pa	Effective pressure
p_c *or* p'_{c0}	Pa	Pre-consolidation pressure in the Cam-clay model
p_{ref}	Pa	Reference effective pressure in the CYsoil model
q	Pa	Deviator stress
q_c	Pa	Static cone resistance obtained in the Cone Penetration Testing
q_{max}	Pa	Maximum vertical pressure on the raft
q_{min}	Pa	Minimum vertical pressure on the raft
R	-	Constant controls the initial shear modulus upon 90^o strain path reversal in the hypoplasticity model
R_f	-	Failure ratio in the CYsoil model
RI		Rigid inclusion
RC		Reinforced concrete
S_{max}	mm	Maximum settlement
SCR	-	Stress concentration ratio
SRR	%	Stress Reduction Ratio

s, s_x, s_y	m	Centre-to-centre distance between piles along x-, y-axis
s_d	m	Diagonal centre-to-centre distance between piles
T_{max}	N/m	Maximum tension in geosynthetic
t	second	Period of time during the passage
t	m	Thickness of geosynthetic
V	N	Vertical loading on the footing
v	km/h	Speed of traffic vehicle
v_0	-	Specific volume at reference pressure in the Cam-clay model
WT		Wind turbine
W_y	m^3	Bending resistance moment of section by the y-axis
x	m	Distance in the x-axis direction
Δs	mm	Differential settlement
Δz_{min}	m	smallest dimension of the neighboring zones in the normal direction at the interface
α	%	Improvement ratio or area replacement ratio
α	-	Exponent that controls a dependency of peak friction angle on relative density in the hypoplasticity model
α	-	Ménard rheological factor obtained in the Pressuremeter Testing
β	-	Exponent that controls the dependency of soil stiffness on relative density in the hypoplasticity model
β	-	Calibration factor in the CYsoil model
β_r	-	Constant manages shape of stiffness degradation curve
χ	-	Constant that controls the shape of stiffness degradation curve in the hypoplasticity model
ϕ_f	°	Ultimate friction angle in the CYsoil model
γ	N/m^3	Unit weight of material/soil
φ *or* ϕ	o	Friction angle
φ_c	o	Critical state friction angle
κ	-	Slope of a swelling (reloading-unloading) line in $v - lnp'$ space
λ	-	Slope of the normal compression (virgin consolidation) line and critical state line (CSL) in $v - lnp'$ space

μ		-	Interface friction coefficient
ν		-	Poisson's ratio
ρ		-	Soil arching ratio
σ_1		Pa	Vertical pressure applied in triaxial test
σ_3		Pa	Confining pressure in triaxial test
σ'		Pa	Vertical pressure applied in oedometer test
σ_p	*or*	Pa	Average stress on pile head
σ_{pile}			
σ_s		Pa	Average stress on soil
ω		rad	Angular velocity
ψ		^{o}	Ultimate dilation angle
ψ_f		^{o}	Mobilized dilatancy angle in the CYsoil model

Introduction

Background

Constructing embankments and buildings over weak soils is a significant challenge for civil engineers. A soft soil is usually characterized by the settlements, low bearing capacity, high void ratios, high saturation and consolidation settlement. As external loads are applied, excessive total settlements, differential displacements (foundation rotations), large lateral movements and instability of slopes can cause the damage of the structures. Many available techniques are applied for solving these issues such as preloading and vertical drains (PVD), sand columns, geosynthetic reinforcement, soil replacement, compaction and setup of light material.

The technique of soil reinforcement by rigid inclusions (RI), known as a piled embankment, has been increasingly gathered interest from the geotechnical research community. The technique has some clear benefits, like its versatility, cost-effectiveness and fast construction (Deb and Mohapatra, 2013); as well as its technical efficiency both in terms of bearing capacity and reduction of absolute and differential settlements (Jenck et al., 2006, 2007, 2009a, 2009b; Hassen et al., 2009 ; Nunez et al., 2013; Girout et al., 2014; Briançon et al., 2015). The rigid inclusion-supported raft over soft soil can overcome some of the disadvantages of the piled raft foundations. The significant concentration of the efforts on the top of piles in terms of axial forces and bending moments often requires a steel bar reinforcement of the concrete structures, which leads to increase the construction cost. Cracks can appear at the rigid connection between piles and the raft under cyclic loading, which leads to structural problems. In other words, many analytical and design methods for a piled embankment have also been promulgated to guide practical engineers (BS8006, 2010 in England; ASIRI, 2012 in France; EBGEO, 2010 in German and CUR226 in Dutch).

Thanks to the simplification in method statement and in design calculation and due to their given advantages, piled embankments were increasingly applied for projects of highways, railways, oil tanks, buildings, retaining walls and wind turbines, as pictured below in Fig. 1.

a)

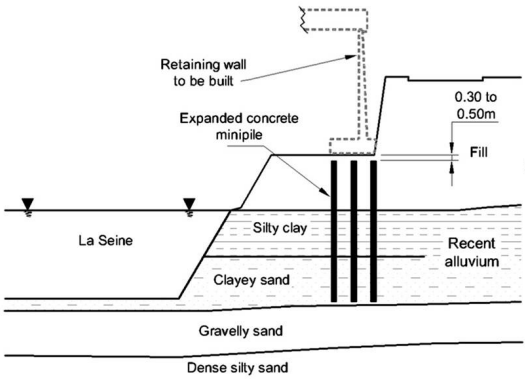

b)

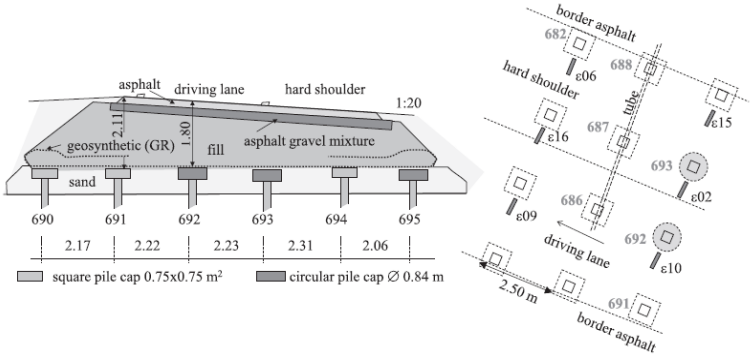

c)

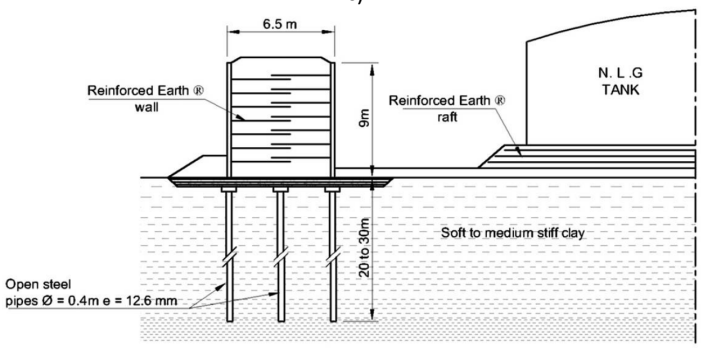

d)

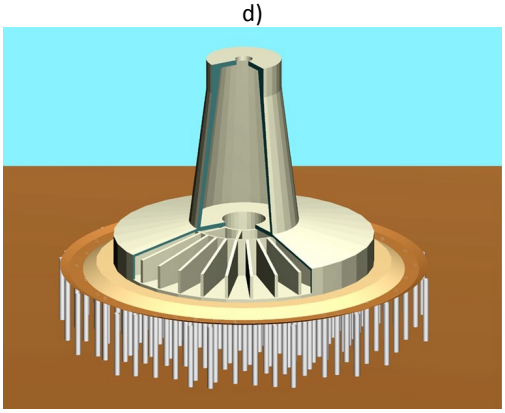

Fig. 1. Several applications of piled embankment method for infrastructure projects: a) Retaining wall foundation at Clichy; b) Reconstruction of the highway's exit near Woerden; c) Bontang earth reinforced protection dykes; d) Rion - Antirion bridge pier, Greece in Combault et al. (2000); Simon and Scholsser (2006); van Eekelen et al. (2015)

Statement of the problem

Many research and design instructions have considered the behavior of piled and GRPS embankments under static loading. Meanwhile, the studies of these systems subjected to complex and cyclic loadings are still limited and did not take into account the complexity of loading (the eccentrical vertical and horizontal loads, and the moment) or the high number of cyclic loading.

The French national project ASIRI (2012) "*Amélioration des Sols par Inclusions Rigides*" studied the technique of soil improvement by rigid inclusions. In the project, laboratory tests, full-scale tests and numerical studies were performed. However, the studies mainly focused on the behaviors of rigid inclusion improved soil technique under static and monotonic loading.

The numerical analyses have successfully and increasingly been applied for piled and GRPS embankments thanks to their reliability, efficiency, and credibility. However, the previous numerical studies had employed simple constitutive soil models to analyze the piled and GRPS embankments under complex and cyclic loading. It leads to an under or overestimation of the cumulated settlements and the load transfer mechanisms. Moreover, the influence of parameters on the cyclic response of the systems has not clearly studied.

To overcome the above disadvantages, 3D numerical studies on the rigid inclusion-reinforced soft soil under foundations and embankments are conducted. In this study, complex and cyclic actions on the reinforced systems are considered. Besides, advanced constitutive models for soils enable the behavior of structures to be accurately modeled. Furthermore, the influence of load cycles number, of vehicle speed, of embankment height and of geosynthetic on piled embankments is studied. The objectives of the study are as follows.

- Understanding well the response of footings over rigid inclusion-reinforced soft soil without load transfer platforms under complex loading including centered and eccentrically vertical loading, horizontal loading under a few load cycles.
- Analyzing the wind turbine foundation solutions under the combinations of vertical loading and moments. The rigid inclusions improved soft soil method is compared to classical ones (shallow foundation and piled raft) in terms of surface displacements, foundation rotations (differential settlements), axial forces and moments on the inclusions/piles.
- Validating the numerical analysis against former experimental works and other

numerical ones on the cyclic response of a rigid inclusion-improved soft soil. The boundary condition and the soft soil state are considered under the behavior of the system.

- Investigating the behavior of a piled under a high number of cyclic loading. The results are presented in terms of load transfer mechanism and cumulative settlements. The influence of the number of load cycles, amplitude and frequency (traffic velocity), and embankment height is considered.
- Studying the cyclic response of a GRPS embankment. It is then compared to the piled embankment one. In addition, the effect of the geosynthetic layers number is indicated.

Research outline

In Chapter 1, a literature review on piled embankments is presented. The main concerns of this technique include the load transfer phenomenon within the earth platform, settlements, soft soil resistance and geosynthetic reinforcement. The influence of the geometric configuration, geotechnical parameters and GR on the structure is discussed.

The numerical modeling of piled embankments is highlighted in Chapter 2. Concerning the software used for the simulations, FLAC3D and ABAQUS are known as suitable ones for geotechnical engineering problems. The steps for the numerical simulations are then summarized. The state of art related to soil constitutive models for static analyses is detailed in terms of constitutive laws, mathematical equations and required parameters.

Chapter 3 analyzes the response of the rigid inclusion-reinforced footing under complex loading. Two main studies are performed, which includes the footings over the rigid inclusion-reinforced soft soil and the reinforced soil option for wind turbine foundations.

- The first analysis is a footing directly lying upon a rigid inclusion-reinforced soft soil. Both experimental and numerical studies are presented. Single rigid inclusion tests and non-reinforced footings are monitored and numerically studied to show the multi-layered soil and to determine the soil parameters for the numerical analyses. After that, reinforced footings under complex loading cases are investigated. A comparison between numerical results and monitoring data is carried out in terms of stresses on inclusions, vertical and

lateral footing displacements, and lateral rigid inclusion displacements.

- The second analysis investigates wind turbine foundations over inclusion-reinforced soil subjected to the combinations of loadings. The constitutive models of the mattress and different improvement densities are taken into consideration. The rigid inclusion solution is compared to the classical foundation solutions (shallow and piled raft foundations). The efficiency of each foundation option is assessed related to the surface settlements of the foundation soil, the axial forces and bending moments of the vertical reinforcements. Recommendations concerning the rigid inclusion-improved soft soil for wind turbine foundations are finally presented.

In Chapter 4, the behavior of soils under cyclic loading is described. Two main parameters governing the cyclic behavior of soil known as the stiffness degradation and damping evolution are presented. The strain accumulation under load cycles is also given, and the effect of various factors on the cumulative strain is indicated. The advanced constitutive models for soils under cyclic loading in numerical analyses are produced as well.

In Chapter 5, the cyclic response of piled and GRPS embankments under a high number of cyclic loading is studied using three-dimensional numerical modeling. Different complexity levels for the constitutive model of the mattress (embankment) are proposed. The main issues addressed in this chapter include:

- A numerical modeling of experimental tests under monotonic and cyclic loadings is done. The advanced soil constitutive model (HYP) is applied for the mattress. The numerical results are validated their accuracy against both the monitoring data and numerical ones of Houda (2016).

- Secondly, a 3D simulation is conducted to study the piled embankment under a high number of load cycles. A comparison between the MC model and the HYP model for the embankment in both static and cyclic loading aspects is clearly indicated in terms of arching effects and cumulative settlements. The HYP constitutive model is suggested for modeling the embankment due to its capacities. The influence of the cyclic number of loads, traffic speed, and embankment height is also performed.

- For the last part, a geosynthetic-reinforced pile-supported (GRPS) embankment under cyclic loading is investigated. The following results are presented: load transfer mechanism, accumulative settlements, and geosynthetic tension. By comparing the unreinforced with reinforced piled embankments under static

and cyclic loadings, the important role of the geosynthetic is confirmed. The load cycles number and geosynthetic layers one are also taken into account.

Chapter 1

Literature review on piled and GPRS embankments

1.1. Introduction

In this chapter, some major concerns for piled embankments are reviewed, which include:

- The description of a piled and GRPS embankments;
- The load transfer mechanism in a piled embankment;
- The settlements;
- The soft soil support;
- The GRPS embankment;
- Parameter influence.

The given conclusions in the last part state the former obtained results and the faced restrictions.

1.2. Description of piled and GRPS embankments

The system involves the rigid inclusions/piles (with or without caps) embedded floatingly or totally in the compressible soil layers. The piles are typically arranged in the triangular or square patterns. Next, a granular earth platform (embankment or mattress) is embanked upper. This layer plays an important role in the load transfer mechanism, so it is called the load transfer platform (LTP). That complex system is termed a piled embankment (Fig. 1.1.a). The case that the earth platform is reinforced by one or several geosynthetic layers is known as a geosynthetic-reinforced pile-supported (GRPS) embankment, as illustrated in Fig. 1.1.b. The structures such as railway system, road pavement, or slab/footing are then placed on the top of LTP.

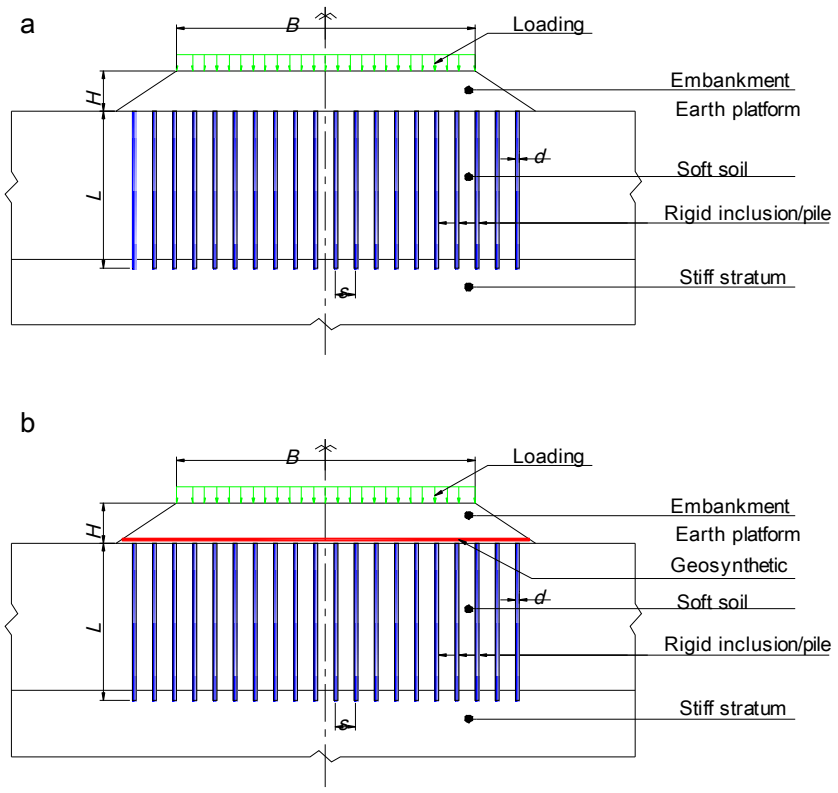

Fig. 1.1. Detail of the systems: a) Piled embankment; b) GRPS embankment

1.3. Load transfer mechanisms in piled embankments

1.3.1. Definition of soil arching

The phenomenon that the stress is transferred from the yielding part of the soil to the adjacent rigid zone is known as the soil arching. It means the soil arching takes place as there is a difference of stiffness between the structure and the surrounding soil. Since the structure is stiffer than the soil, the load arches onto the structure.

1.3.2. Load transfer mechanisms in piled embankments

The load transfer mechanism within the embankment of the system is based on the principle of soil arching. Due to the significant larger stiffness of the pile than the ground and shearing strength of soil, the shear stress results in an increase in the pressure acting on pile cap and a decrease in the pressure on foundation soil. Therefore, piles carry the large percentage of total loads (embankment weight, surcharge or external loadings) (load part *A*), and the soft soil takes the remaining amount of loading (residual loading), as drawn in Fig. 1.2.a. In the case of GRPS embankment, the residual load is divided into two parts: part *B* passes through the GR

to the piles and part *C* is applied to the subsoil (Fig. 1.2.b). Regarding the load part *C*, it will be transferred directly to the subsoil and indirectly the piles in terms of the negative skin friction along the shaft of piles. Due to less load applied to the soft soil, the soft soil and embankment settlements decrease. The load on pile cap and negative skin friction are transferred along the pile to deep bearing layers.

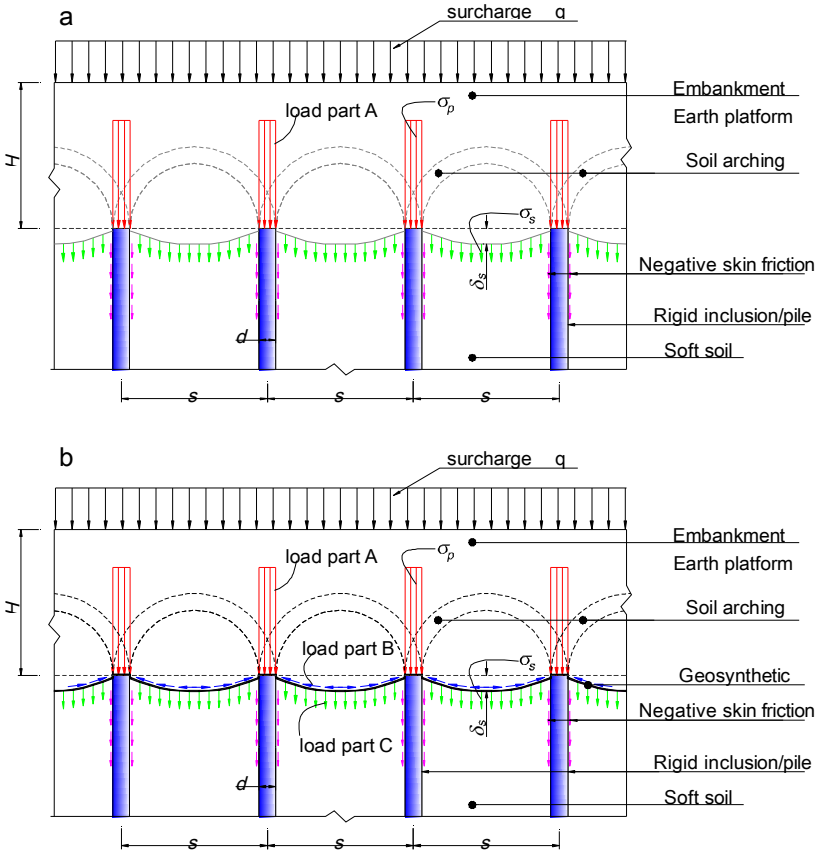

Fig. 1.2. Load transfer mechanism of the systems: a) Piled embankment; b) GRPS embankment

1.3.3. Analytical models for soil arching in piled embankments

In literature, the soil arching phenomenon was investigated early in Terzaghi (1943). Based on the theories for the shape of soil arching, several families of analytical models were developed. The representative analytical models of soil arching in piled embankments are briefly introduced herein.

1.3.3.1. The family of frictional models

The first frictional model was proposed by Terzaghi (1943), in which the arching effect is based on the sand shearing resistance. In this model, the lowering of the strip over the trapdoor is opposed to the frictional resistance along boundaries. As a result, the total stress on the yielding strip is reduced (Fig. 1.3).

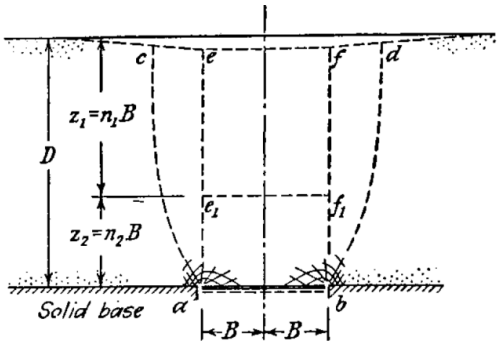

Fig. 1.3. Failure in cohesionless sand preceded by arching (Terzaghi, 1943)

McKelvey (1994) extended the Terzaghi's theory by assuming the presence of a 'plane of equal settlement' and combined this with a tensioned membrane theory. In addition, Russell and Pierpoint (1997) developed the Terzaghi's model based on adding a third dimension where the vertical friction planes are located along the edges of the square pile caps. However, frictional models are uncommon due to the fact that the results significantly depend on the value of K_0 (the ratio between horizontal and vertical pressure) while there is a difficulty to determine K_0 accurately.

1.3.3.2. The family of rigid arch models

The arch has a fixed shape in this class of models. The shape of the arch is usually triangular (2D or 3D), as presented in Fig. 1.4. It is assumed that the entire load above the arch is directly transferred to the piles, and the soil wedge weight under the arch is carried by the subsoil and geogrid. Nevertheless, there is a drawback that the mechanical properties of the fill, such as the friction angle, are not considered in these models. A group of rigid arch models is known as the Scandinavian models (Carlsson, 1987; Rogbeck et al., 1998) and the Enhanced Arching models (the Bush-Jenner's model or the Collin's model (Collin, 2004) and the present design method of the Public Work Research Centre in Japan (Eskişar et al., 2012).

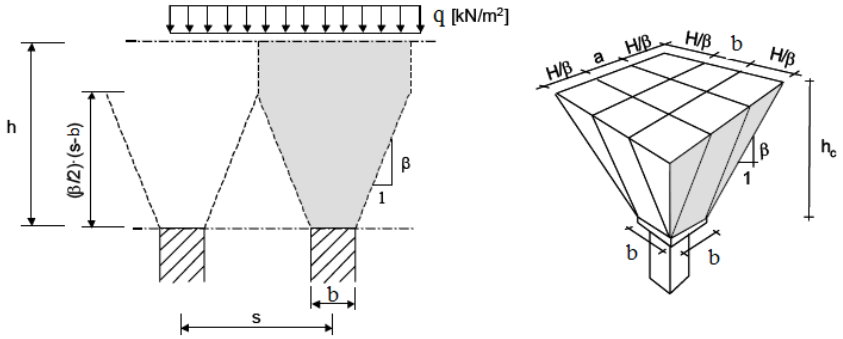

Fig. 1.4. 2D and 3D soil wedge theories (Carlsson, 1987)

1.3.3.3. The family of equilibrium models

In the class of equilibrium models, an imaginary limit-state stress-arch is assumed to be formed above the GR and the soft subsoil between the stiff elements. In the 3D situation, these stiff elements are piles; in the 2D situation, they are beams or walls. The pressure on the GR and subsoil (B + C) can be calculated by considering the equilibrium of the arch. In most models, the arch is considered to have a certain thickness.

Two limit-state equilibrium models are frequently used in the design standards for piled embankments. The main difference between all the limit equilibrium methods for soil arching is the assumed shape of soil arching. For the Hewlett and Randolph's model, the arches are semi-circular with a uniform thickness (Fig. 1.5). This analytical model was suggested in BS8006 (2010) and adopted in the French ASIRI guideline (2012). In the Zaeske's model (Kempfert et al., 2004), the arches are divided into different crown elements in Fig. 1.6. This model was adopted in the design guideline of EBGEO (2010) and CUR226. The Concentric Arches model was proposed by Van Eekelen et al. (2013) to account for the inclusion of soft soil and the load transfer on geosynthetic reinforcement, as given in Fig. 1.7.

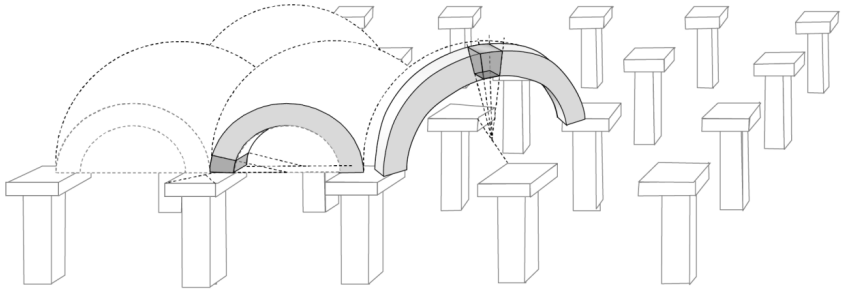

Fig. 1.5. Equilibrium of crown elements of the diagonal arches of Hewlett and Randolph model (van Eekelen et al., 2013)

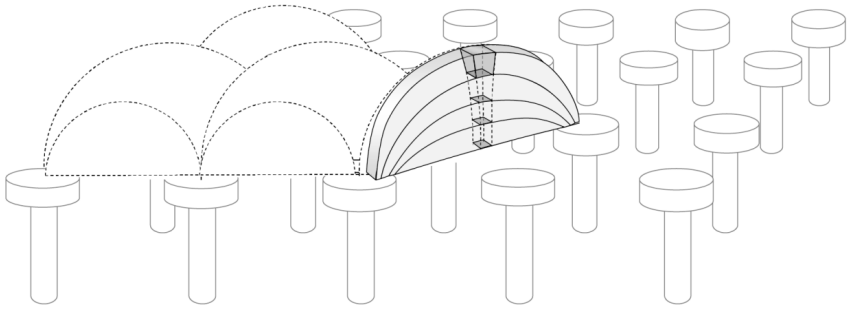

Fig. 1.6. Equilibrium of crown elements of the diagonal arches of Zaeske's model (van Eekelen et al., 2013)

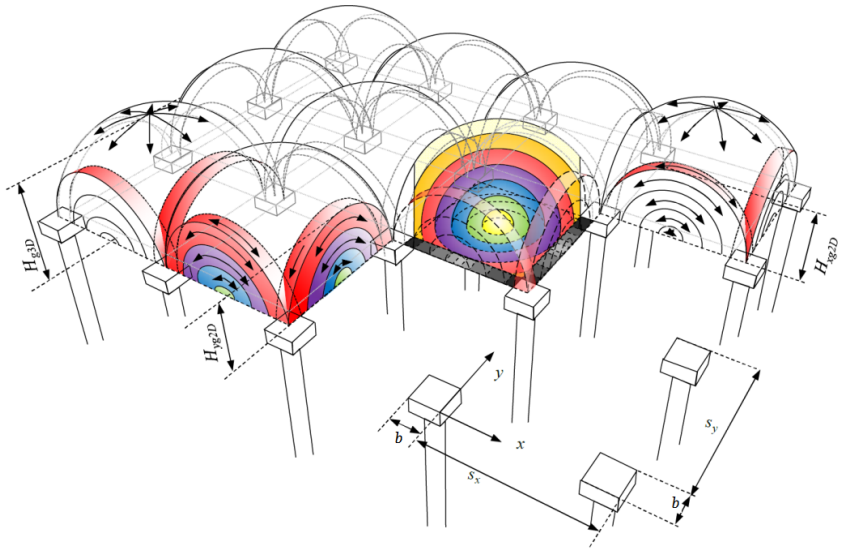

Fig. 1.7. Concentric Arches model (van Eekelen et al., 2013)

1.3.3.4. The family of empirical models

Based on experimental results, the shape of arches can be determined. Marston and Anderson (1913) first determined the arching above a pipe in the soil using a 2D equation. Jones et al. (1990) modified the Marston and Anderson's equation for 3D piled embankments. This model was used in the BS8006 standard. The arching coefficient C_c adapted in BS8006 for the 3D geometry of a piled embankment is determined as follows in Equations 1.1 and 1.2.

For end-bearing piles:

$$C_c = 1.95\frac{H}{b} - 0.18 \tag{1.1}$$

For friction and other piles:

$$C_c = 1.5\frac{H}{b} - 0.07 \tag{1.2}$$

Herein, H is the height of embankment (m); b is the size of pile cap (m).

The arching coefficient does not take into account the friction angle of embankment.

1.3.3.5. The family of mechanical elements

Another group of models considered in the literature is the mechanical elements, such as the one-dimensional model in Chen et al. (2008) (Fig. 1.8), the plane strain models in Deb (2010) and the load-displacement compatibility method in Filz et al. (2012). In this group, the fill, the GR, the piles and the subsoil are separate elements. The boundary condition for each element is matched with the neighboring elements. Due

to the complexity of the mathematical equations, the family of mechanical elements was only built for 1D or 2D models.

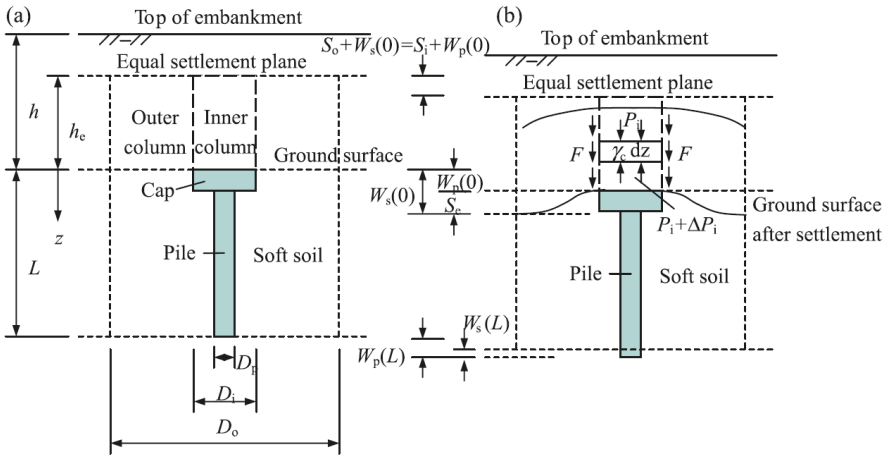

Fig. 1.8. Analytical model for the pile-supported embankment. a) Embankment before settlement; b) Embankment after settlement (Chen et al., 2008)

1.3.4. Definition of soil arching indicators

In the following work, the embankment height over pile-reinforced soft soil is noted *H*. It results in the overburden stress $\gamma.H$ (where γ is the unit weight of embankment fill), and the surcharge on the crest of the embankment is *q*. The arching effect is commonly evaluated by the following indexes.

1.3.4.1. Soil arching ratio (ρ) or Stress Reduction Ratio (SRR)

Soil arching is often assessed by the soil arching ratio (ρ) that is defined as the ratio of the average vertical stress on soil between the adjacent piles to the overburden stress plus the surcharge as given in Equation 1.3.

$$\rho = \frac{\sigma_s}{\gamma H + q} \tag{1.3}$$

Where σ_s - the average vertical stress over the soil foundation.

The soil arching ratio reflects the degree of the transferred load. When it is equal to 0, the stress on soil is zero. It means that all the loads are transferred onto the piles. As the soil arching ratio is equal to 1.0, (i.e. the stress applied to the subsoil is equal to γH + *q*). All the loads are carried by the soil foundation, no soil arching occurs. In general, the soil arching ratio ranges from 0 to 1.

1.3.4.2. Stress Concentration Ratio (SCR)

The stress concentration ratio is a parameter to evaluate the mechanism of load

transfer. It is defined as the ratio of the average stress on the pile head to the stress on soil between the adjacent piles, as shown in Equation 1.4. The stress concentration ratio is a global index which incorporates the mechanism of soil arching, tension membrane and apparent cohesion effect and pile-soil stiffness difference (Huang, 2003).

$$SCR = \frac{\sigma_p}{\sigma_s} \tag{1.4}$$

Where σ_p is the average vertical stress on the pile head.

1.3.4.3. Efficacy (*E*)

The efficacy of pile support is defined as the proportion of embankment weight and surcharge carried by the piles Hewlett and Randolph (1988), as seen in Equation 1.5.

$$E = \frac{P}{s^2(\gamma H + q)} \tag{1.5}$$

Where *P* is the total load carried by the piles and *s* is the pile center to center spacing.

1.4. Settlements

Owing to the embankment, the surcharge and the other loadings (building, traffic loading. etc.), the embankment and the compressible soils have a trend to settle. In the literature, many techniques have been applied to reduce these settlements including the techniques of reducing the embankment load (lightweight materials, change in geometry of embankment), the techniques of improving the soft soil (preloading, staged construction, excavation, and backfill, stone column), the techniques of accelerating the consolidation (vertical drainage, vacuum consolidation), methods of reinforcing the embankment (geosynthetic reinforcement) and techniques of providing an additional structure for embankment (piled embankments) (Magnan, 1994). The applicability of these methods is significantly dependent on the soil conditions, the equipment, and the construction cost.

To investigate the settlement of piled embankments, two types of settlement are considered, in which the total (maximum) settlement is defined as the vertical displacement at a certain point such as the soft soil settlement. The differential one is defined by the difference of two points. For example, the differential settlement of the soft soil can be calculated by the subtraction of the soft soil settlement at the mid-span of adjacent piles to the pile cap settlement.

Due to the complex nature of the reinforced system, there are not many analytical methods developed to determine the settlements. However, the experimental studies and site monitoring showed that the piled improved soft soil under embankments (piled embankments) can reduce the differential and total settlements compared to a non-reinforced case (Hewlett and Randolph, 1988). To study the settlements, the numerical modeling was carried out (Figs. 1.9 and 1.10). In the following parts, the load transfer mechanism and the settlements are considered as two the most important indicators for the efficient assessment of the piled embankment.

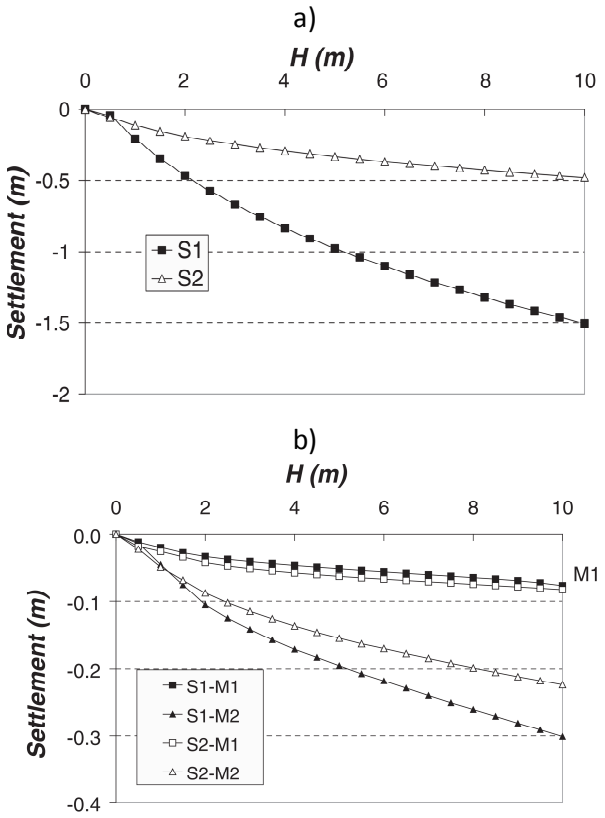

Fig. 1.9. Settlements without rigid inclusions improvement: a) Soft soil settlement; b) Embankment settlement (Jenck et al., 2006)

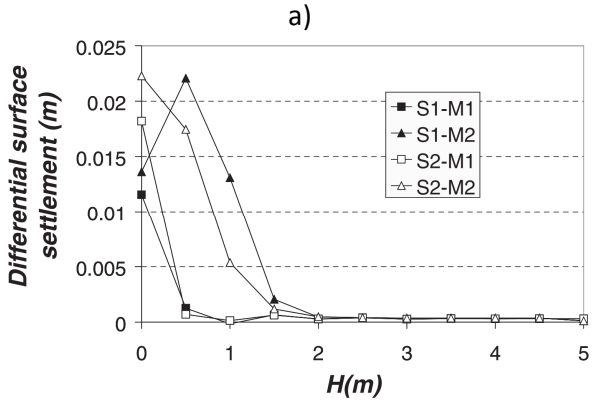

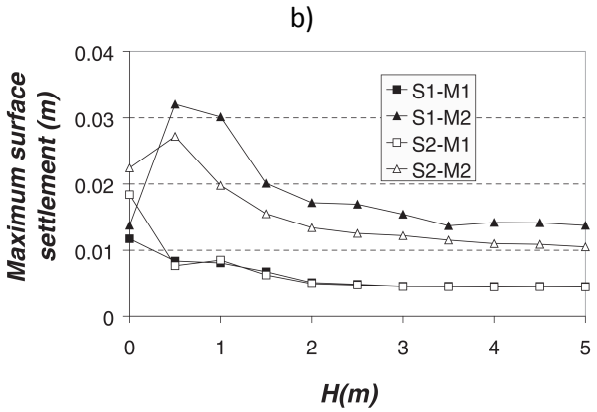

Fig. 1.10. Settlements due to next 0.5 m embankment layer with a rigid inclusions improvement: a) Differential settlement; b) Maximum settlement (Jenck et al., 2006)

1.5. Soil resistance

Different design methods of piled embankments showed that the load transfer mechanism within the embankment load is soil arching, in which different shapes of soil arch were given. These methods assume that the load above arching is transferred to piles (load part *A*) and the part under the arch is carried by the geosynthetic (load part *B*) and the soft soil (load part *C*). Concerning theoretical aspects, the former investigations have ignored the presence of the soft soil support (Terzaghi, 1943; Guido et al., 1987; Hewlett and Randolph, 1988). To improve the analytical models, the studies of Low et al. (1994); Kempfert et al. (2004); van Eekelen et al. (2013) had taken into account the soft soil to study the load transfer mechanism and the settlements. However, most of the studies only considered that the soft soil behaved in a linear elasticity.

To consider the complex behavior of soft soil, numerical analyses using nonlinear soil constitutive models have been performed to study the influence of soft soil on the piled embankments and the GRPS embankments (Han and Gabr, 2002; Huang et al., 2005; Huang and Han, 2010; Jenck et al., 2009a, 2009b, 2007, 2006). In these studies, the soil was considered as nonlinear elasticity and the time consolidation was studied.

1.6. GRPS embankments

Geosynthetics were efficiently incorporated into the earth platform combined with pile-improved soft soil, as an integrated system (called geosynthetic-reinforced pile-supported (GRPS) embankments), to reduce settlements, minimize yielding of the soil above the pile cap and enhance the load transfer mechanism (Hewlett and Randolph, 1988; Kempfert et al., 2000; Love and Milligan, 2000; Han and Gabr, 2002; Huang et al.,

2005). The integrated system combines vertical piles and horizontally placed geosynthetics to form a relatively stiff platform that could transfer the embankment load to a deep competent bearing layer. The load from the embankment is effectively transferred to the piles. The punching of the piles through the embankment fill can be prevented by the use of to the geosynthetic layer. The load in the piles will increase and less stress will be applied to the soft soil. This phenomenon results in the decrease of settlements.

1.7. Parametric influence

1.7.1. Embankment height

Based on small-scale model tests and an analytical model, Hewlett and Randolph (1988) stated that the pile spacing and the height of embankment are significantly influent on the efficacy. For a typical geometric design, where the reinforcement ratio is about 10%, the efficacy of pile support increases with the increase of the embankment height. It reaches 0.6 for a value of K_p of 3 (a friction angle of 30^o).

The influence of the embankment height has been clearly investigated thanks to numerical modeling tools. Performing a 2D numerical analysis, Han and Gabr (2002) figured out that the maximum and differential settlements (embankment and soft soil) increase with the embankment fill height. The maximum settlement at the pile head elevation is greater than the one at the embankment crest. Their results also showed that the stress concentration ratio (*SCR*) increases as the height increases. On the other hand, the 3D numerical results of Jenck et al. (2006) showed that as the height increases the total and differential settlements decreases, as given in Figs. 1.9 and 1.10. In addition, an increase in the height leads to an increase in the efficacy of the system, as given in Fig. 1.11. The experimental and numerical results of Okyay and Dias (2010) found the efficacy increases with increasing the height in the loaded mattress case, while it decreases in the loaded slab case. The reason might be the influence of the slab on the load transfer mechanisms.

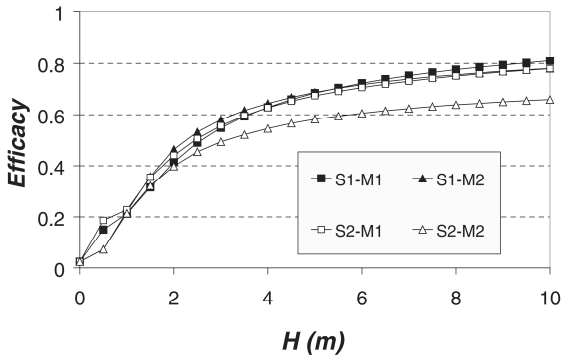

Fig. 1.11. Efficacy according to the equivalent platform height (Jenck et al., 2006)

1.7.2. Pile spacing

Setting up centrifuge models to study the change in the pile cap area ratio, Lee et al. (2005) indicated that the efficacy increases with increasing the pile cap area ratio. On the other hand, the tank settlement decreases with increasing the pile cap area ratio. It is recommended that the pile cap area ratio should be kept not far from 25% to achieve the optimal solution. Studying four small values of surface ratio corresponding to a pile spacing of 1.5×1.5 m, 2.0×2.0 m, 2.5×2.5 m, and 3×3 m, Okyay and Dias (2010) concluded that the pile spacing is an important factor, which controls the efficacy of the reinforcement. In their study, the surface ratio of the piles, α (improvement ratio or area replacement ratio) was used. It is defined as the ratio between the area of the pile and the total area of the grid zone (e.g. a larger spacing of piles leads to a smaller area replacement ratio). Fig. 1.12 showed that the efficacy increases as the improvement ratio. A significant role of the pile spacing has been found when the value of the surcharge load increases.

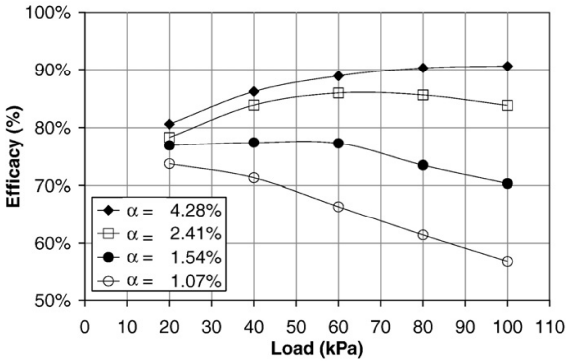

Fig. 1.12. Influence of pile spacing on efficacy (Okyay and Dias, 2010)

Figs. 1.13 and 1.14 show the significant influence of the pile spacing on the maximum and differential post-construction settlements (Huang and Han, 2010). An increase in the pile spacing resulted in a noticeable increase in the settlements. As it can be seen,

when the spacing of piles increased from 2.0 to 3.0 m, the maximum and differential settlements were doubled.

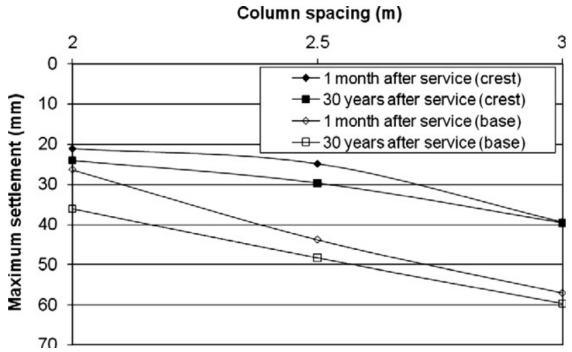

Fig. 1.13. Maximum settlement versus column spacing (Huang and Han, 2010)

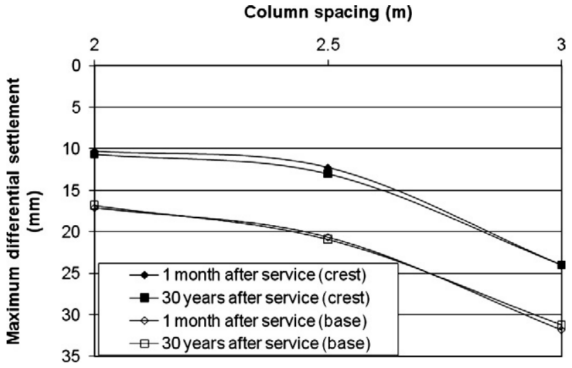

Fig. 1.14. Maximum differential settlement versus column spacing (Huang and Han, 2010)

1.7.3. Friction angle

Hewlett and Randolph (1988) established a relationship between the efficacy and the friction angle (φ), as in Equation 1.6.

$$E = 1 - \delta\left(1 - \frac{s}{2H}\right)(1-\delta)^{(K_p - 1)} \tag{1.6}$$

Where $\delta = b/s$, K_p is the Rankine passive earth pressure coefficient, it is related to φ by Equation 2.7.

$$K_p = \frac{1+\sin\varphi}{1-\sin\varphi} \tag{1.7}$$

Derived from the curves to estimate the efficacy, they found that the efficacy significantly increases with K_p corresponding to an increase of the friction angle.

In order to study the influence of the platform material friction angle, a 2D numerical analysis was performed by Jenck et al. (2007). The friction angle was varied from 10 to

40°. The numerical results pointed out that the efficacy increases noticeably with the friction angle (Fig. 1.15), whereas the settlements decrease. The explanation can be due to the fact that an increase in the friction angle enhances the shear mechanisms, which leads to more loads applied to the pile and fewer loads on the soft soil. Studying the influence of mechanical properties of earth platform, Okyay and Dias (2010) recommended that the cohesion and internal friction angle are influent on the efficacy. The experimental and analytical findings of van Eekelen et al. (2012) reported that the higher friction angle, the greater the increase of soil arching.

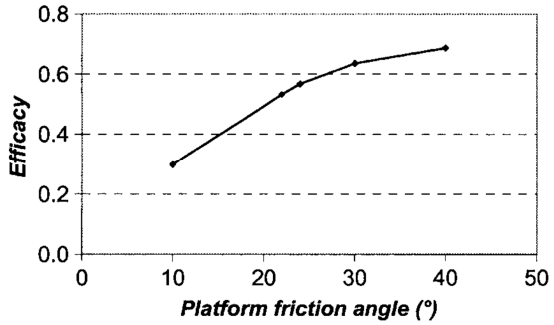

Fig. 1.15. Maximum efficacy according to platform friction angle (Jenck et al., 2007)

1.7.4. Pile stiffness

Owing to the current standard systems which do not consider the influence of pile modulus, Han and Gabr (2002) built a 2D numerical model to study the role of pile modulus on GRPS embankments. The results suggested that an increase in the pile modulus can decrease the maximum settlement and increase the differential settlements at the elevation of the pile head, as given in Figs. 1.16 and 1.17. In addition, in terms of load transfer aspects, the outcomes indicated that the higher the pile stiffness the higher the soil arching effect (Fig. 1.18).

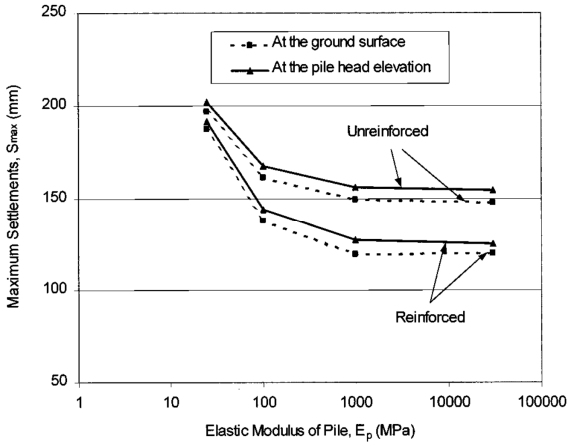

Fig. 1.16. Influence of the pile modulus on maximum settlements (Han and Gabr, 2002)

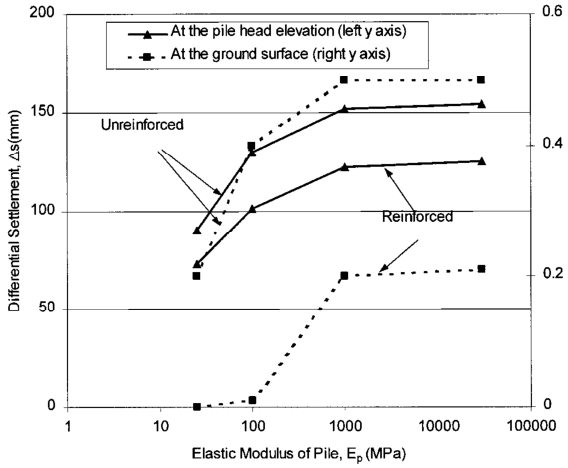

Fig. 1.17. Influence of pile modulus on differential settlements (Han and Gabr, 2002)

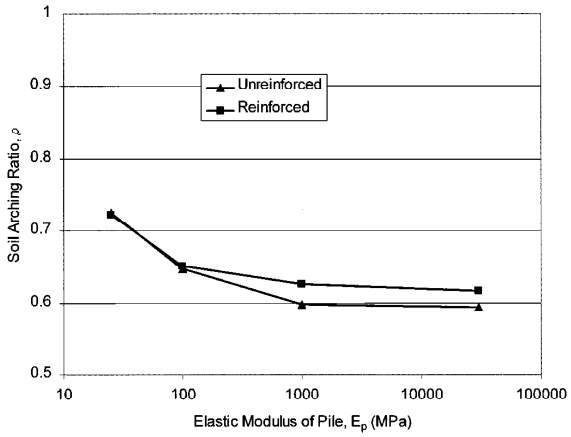

Fig. 1.18. Influence of pile modulus on the arching ratio (Han and Gabr, 2002)

Based on a 2D study of coupled hydraulic and mechanical modeling taking into account the time-dependent behavior of GRCS embankments, Huang and Han (2010) showed that the pile modulus has a significant influence on the maximum post-construction settlements of soft soil and embankment. The increase of the pile modulus results in decreasing the settlements. However, the maximum tension in the geosynthetic reinforcement and the excess pore water pressure were insignificantly affected by the pile modulus. To conclude, they recommended that the design of GRPS embankments should consider the influence of the material properties, the pile arrangement and geometry, and the construction rate.

1.7.5. Soft soil properties

In the existing design methods, the subsoil has not been taken into account yet, or it was simplified using assumptions (Jenck et al., 2009b). In fact, the soft soil is considered to carry a part of the applied loading, so the soft soil resistance should be

taken into account in the load capacity of system. Since the soft soil usually exhibits a high compressibility which can be quantified by the elastic modulus. The 3D numerical analysis of Jenck et al. (2006) showed that there is no noticeable influence of the soft soil compressibility neither on settlements nor on the load transfer mechanisms. Using a 2D physical and numerical models to investigate the influence of Young's modulus of soft soil, Jenck et al. (2007) indicated that a small value of the soft soil modulus is not influent on the efficacy while a high Young's modulus of the soil foundation can reduce by 13% the efficacy of the pile support. The settlement of the foam during this loading stage results in surface settlements as well (Table 1.1). Furthermore, a 2D modeling using the discrete element method (DEM) performed by Jenck et al. (2009b) found the same tendency with experimental results of Jenck et al. (2007). In terms of settlements, Huang and Han (2010) discovered that the increase of the soft soil modulus could reduce the embankment and soft soil settlements.

Table 1.1. Influence of the foam parameters on the efficacy and on the surface settlements (Jenck et al., 2007)

Parameter	Value	Maximum efficacy	Surface settlement (mm)
Reference case		0.57	1.5
Young's modulus (kPa)	12-27	0.57	5.1
	106-246	0.50	0.3
Poisson's ratio	0.2	0.57	1.1

1.7.6. Geosynthetic tensile stiffness

The presence of the geosynthetic reinforcement in a piled embankment can improve significantly the load transfer mechanism (soil arching), reinforce the earth platform, and reduce the settlements. In the analytical models, the geosynthetic stiffness was not usually considered. Based on the 3D numerical analysis, Han and Gabr (2002) concluded that an increase in the geosynthetic stiffness reduces the maximum and differential settlements, promotes the stress concentration and increases the maximum tension in geosynthetic, as followed in Figs. 1.19, 1.20 and 1.21. It was recommended that the geosynthetic tensile stiffness should be considered in the design guidelines. On the other hand, the numerical results of Liu et al. (2007) figured out that the settlement of a reinforced piled embankment was similar to the one of an unreinforced one. The findings of Huang and Han (2010) stated that an increase in the geosynthetic stiffness results in an insignificant decrease in the maximum and differential settlements, but it can increase significantly the tension in geosynthetic. The experimental results of van Eekelen et al. (2012) suggested that the stiffness of geosynthetic reinforcement does not affect the amount of arching.

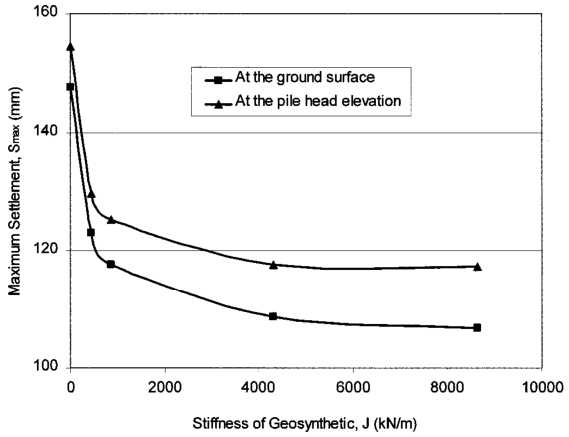

Fig. 1.19. Influence of the geosynthetic stiffness on maximum settlements (Han and Gabr, 2002)

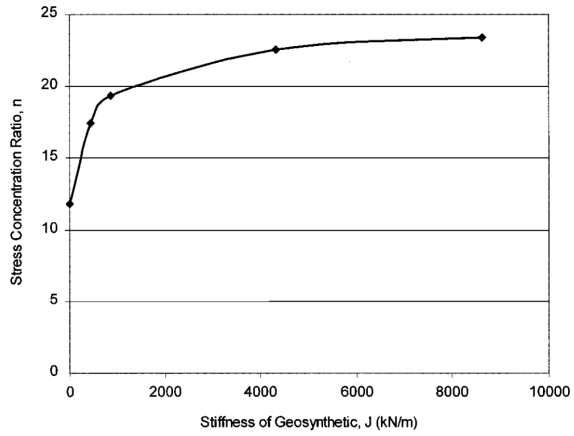

Fig. 1.20. Influence of the geosynthetic stiffness on SCR (Han and Gabr, 2002)

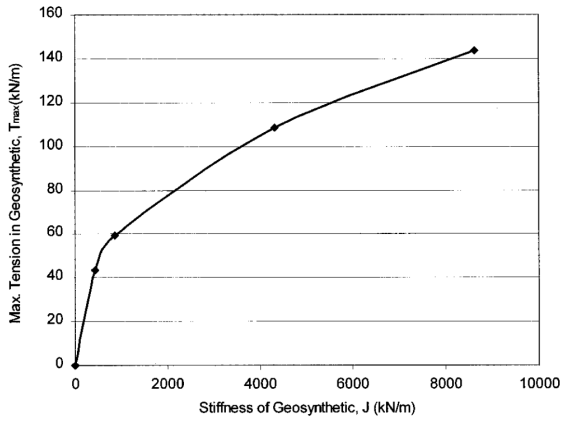

Fig. 1.21. Influence of the geosynthetic stiffness on the maximum tension in geosynthetic (Han and Gabr, 2002)

1.8. Conclusions

Based on the brief of literature review, some following conclusions are presented, as:

Firstly, based on different shapes assumed for soil arches in the LTP, several methods were proposed. The equilibrium group of models is frequently used in the design standards (BS 8006, 2010; EBGEO, 2010; ASIRI, 2012; CUR226, 2016) for piled and GRPS embankments thanks to the reality of arching shape and the simplification in the analysis.

Secondly, the complexity of the piled and GRPS embankment systems leads to the difficulty for the analytical models in the determination of total and differential settlements. Besides that, the influence of the soft soil resistance was absent in most analytical methods. The numerical methods can overcome these challenges.

Furthermore, the indicators that include the soil arching and the settlements are necessary to assess the efficiency of piled embankments.

Additionally, the presence of a geosynthetic in the piled embankment has a significant role to reduce settlements, minimize yielding of the soil above the pile cap, and increase the arching effect.

Furthermore, the parametric studies have been performed in former researches, which include geometric factors (embankment height and pile spacing), properties of the material (friction angle of the embankment fill, stiffness of pile and soft soil), and geosynthetic. The increase of the embankment height results in the increase of efficacy of pile support system and the settlements. Meanwhile, as the pile spacing increases, the efficacy, and the settlements decline.

With regard to the soil and structure parameters, the significant rise of the efficacy with an increase in the friction angle of LTP is shown. While the efficacy seems to be constant with an increase in the soft soil's modulus, the total and different settlements decrease. In addition, the stiffness of pile has not much effect on the settlements and the soil arching. As the stiffness of GR increases, the maximum and differential settlements decrease while the arching effect does not change much.

Chapter 2

Numerical modeling of piled and GRPS embankments

2.1. Introduction

Numerical simulations have been widely employed to solve problems related to geotechnical engineering.

There are some numerical methods used to solve geotechnical problems, such as Finite Element Method (FE, FEA or FEM), Finite Differential Method (FDM), Discrete Element Method (DEM), Boundary Element Method (BEM), and Material Point Method (MPM). Commercial programs have been built and developed, such as FLAC 2D and 3D (FDM), ABAQUS, ANSYS, PLAXIS (FEM); PFC 2D and 3D, 3DEC, and open-source code YADE (DEM), 3DynaFS-Bem (BEM), MPMsim™, Anura3D MPM (MPM).

The numerical simulations, nowadays, has been increasingly used due to some advantages compared to analytical methods and experimental works, such as cost-effectiveness aspects, reduced calculation time, complex problem-solving ability, and acceptable accuracy.

2.2. Usage software

In the study, the two software packages were suggested for the numerical analyses, which are FLAC3D (FDM) and ABAQUS (FEM). A general introduction of these softwares is briefly presented below.

2.2.1. FLAC3D

FLAC3D symbolizes *Fast Lagrangian Analysis of Continua in 3 Dimensions.* It is a numerical modeling software built on the Finite Different Method (FDM). Since no matrices are formed, heavy calculations can be performed without too much memory requirements. FLAC3D can analyze the behavior of three-dimensional structures built on soils or rocks. The presence of groundwater, construction phase, and discontinuity simulation are also considered in its analyses.

Materials are represented by polyhedral elements within a 3D mesh. A modeled object is built on the user-adjusted elements to fit its shape. The behavior of each element follows a prescribed linear or nonlinear stress-strain relationship responding to applied forces or boundary constraints. The material can yield and flow, and the grid can

deform (in large-strain mode) and move with the material that is represented.

The explicit finite different analysis used in FLAC3D, including the Lagrangian calculation scheme and the mixed-discretization zoning technique, ensure that the plastic flow and the collapse are simulated very accurately. The drawbacks of the explicit formulation (i.e. small timestep limitation and the question of required damping) are overcome by an automatic inertia scaling and automatic damping that does not influence the mode of failure.

2.2.2. ABAQUS

Abaqus is a simulation program built on the finite element method. It is possible to solve problems, from the simple linear simulations to the complicated nonlinear analyses. In addition, the various types of elements included in the library ensure that it can model virtually any geometry. Moreover, lots of material constitutive models are contained, which permits to easily model the behavior of most engineering materials (e.g. metals, polymers, rubber, concrete, and geotechnical ones like soils and rocks). As a result, Abaqus is not only useful for simulating structural problems, but it is also beneficial for solving problems concerning the heat transfer, the acoustics, the soil mechanics, the piezoelectric analysis, the electromagnetic analysis, the mass diffusion, and the fluid dynamics.

Abaqus can solve problems in 2D planar, axisymmetric and 3D simulations. Complex problems formed by multiple components can be modeled by associating single components with the appropriate material models and specifying component interactions. In a nonlinear analysis, appropriate load increments and convergence tolerances are automatically chosen, and they are continually updated throughout the implementation to make sure that an accurate result is acquired.

2.3. Numerical modeling for piled and GRPS embankments

In literature, many numerical simulations were performed to study the behavior of piled embankments by different software packages, such as PLAXIS (Jennings and Naughton, 2012; Zhang et al., 2013; Okyay et al., 2014), FLAC (Han and Gabr, 2002; Stewart and Filz, 2005; Jenck et al., 2006,2007; Okyay and Dias, 2010, Okyay et al., 2012; Nguyen et al., 2013; Dias and Simon, 2015), ABAQUS (Liu et al., 2007; Zhuang, 2009; Zhuang and Ellis, 2016; Zhuang and Wang, 2018) or ASTER (Messioud et al., 2016, 2017), and their validity has been regularly confirmed by the scale model results.

In overall, to model a piled and GRPS embankment, the several analyzing steps are

included: model idealization, discretized mesh, constitutive models and material parameters, soil/structure interaction, boundary conditions and loads, analysis procedure, and result visualization.

2.3.1. Model idealization

Many geometrical idealizations of PEs (or GRPS embankments) were employed for the numerical simulations.

In practice, piles are commonly arranged in the square or triangular grid. Using the geosynthetic reinforced embankment over the pile-square net, Han and Gabr (2002) assumed that the influence zone of a single pile was simply equivalent to a circle in a 2D plane (or cylindrical in a three-dimensional view). Based on the axis symmetry, the problem was finally solved using a 2D simulation, as shown in Fig. 2.1. Additionally, 2D models were recommended by Jenck et al. (2007).

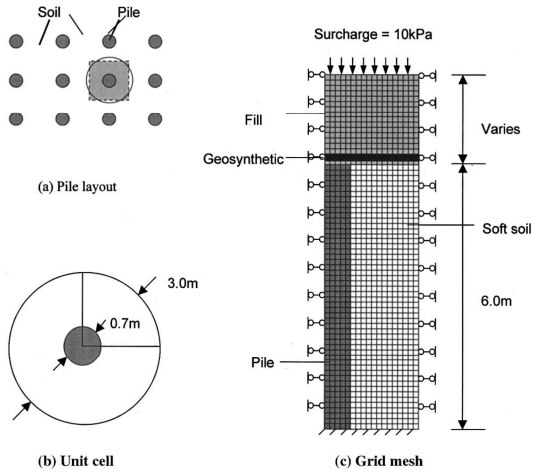

Fig. 2.1. Finite difference modeling of GRPS embankment (Han and Gabr, 2002)

Besides, the three-dimensional grid of piles can be solved into plane strain conditions (Satibi, 2009), where the equivalent thickness t_{eq} in the plane strain model was calculated based on keeping the improved area ratio (A_p/A) as a constant (Fig. 2.2).

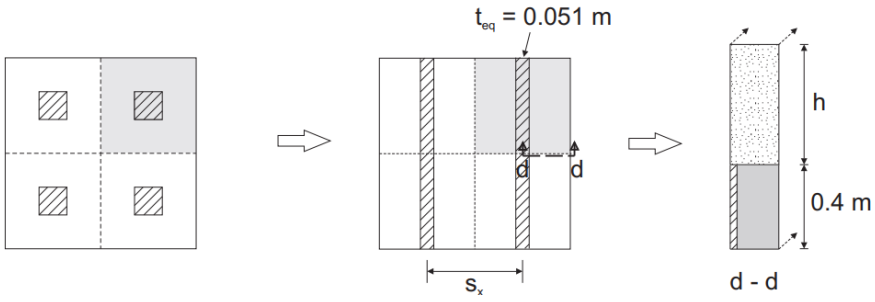

Fig. 2.2. Idealization of a plane strain model for a PE (Satibi, 2009)

Studying an embankment over a rigid inclusions-reinforced soft soil, Jenck et al. (2006) stated that the problem is truly three-dimensional. A unit cell was selected to represent for the full model, as given in Fig. 2.3. Similarly, a quarter of the elementary part of the embankment was modeled in the studies of Zhuang and Li (2015) and Moormann et al. (2016).

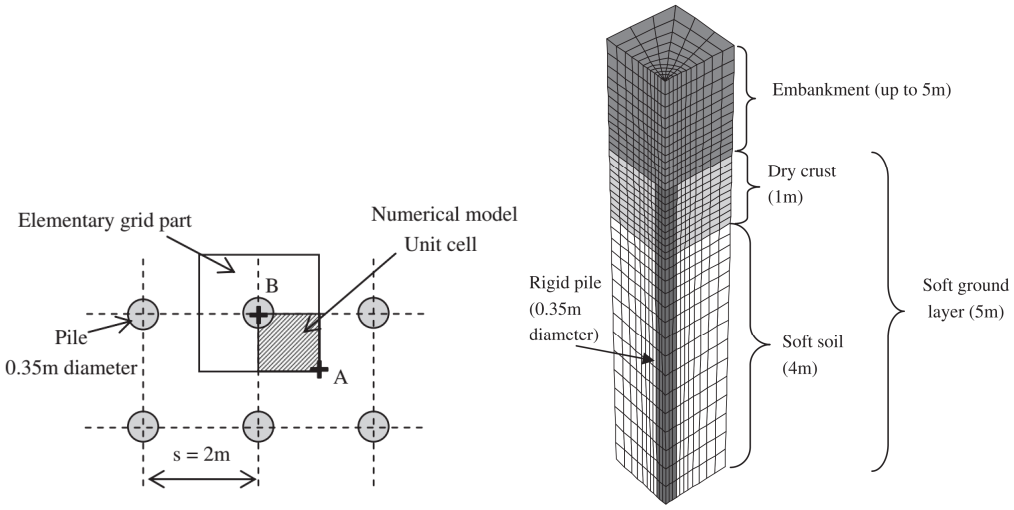

Fig. 2.3. Numerical model of a unit cell of Jenck et al. (2006)

Huang et al. (2005) and Liu et al. (2007) employed the 3D numerical simulations to investigated the GRPS embankments. In their studies, a strip of half the cross section was considered due to the symmetrical plane of the geometry (see in Fig. 2.4).

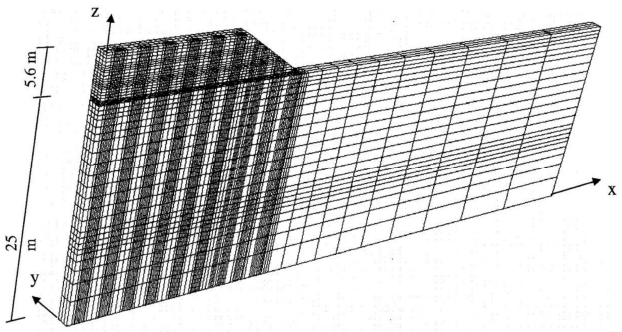

Fig. 2.4. Half the cross section in finite element discretization in Liu et al. (2007)

2.3.2. Discretized mesh

2.3.2.1. Mesh generation

The geometrical feature of the physical structures modeled in FEM or FDM is defined by elements of discretization and nodes. Each element, which stands for a discrete part, is interconnected with the other elements by shared nodes (continuum model). A collection of the elements and nodes is called *mesh*.

In general, the finer the mesh, the more accurate the results. However, the increase in mesh density results in an increase in the calculation time (HKS 2014).

In the case of PE, in order to reduce the computing time, an idealized geometry is taken into account where a full model can be represented by a part, a half, or a unit. Moreover, the variation of the mesh should be performed. It means that the mesh density of a structure is variably dependent on the deformation of the different parts. In particular, the fine mesh is generated at the high-stress and large-strain concentration areas.

2.3.2.2. Element type and shape

The element type and shape are also influent on the obtained results and the calculation time. For instance, the study of Ng et al. (2015) stated that the C3D8 finite elements replaced by the C3D20 ones resulted in declining the calculation time from 36 down to 2 hours (18 times), and produced a result difference of 6%. Finally, they recommended that the C3D8 elements were employed to simulate soil stratum. The number of nodes is then the important element which should be considered.

2.3.2.3. Element section features

In a piled embankment or a GRPS embankment analysis, volumetric elements in the FE analyses were usually considered to model the soft soil, the embankment fill, and the piles. Sometimes, the beam and pile structural elements were employed for piles to easily obtain the efforts (axial force, shear force and moment) inside them (Huang et al. 2005 and Kim 2017). The geosynthetic reinforcement was simulated by truss elements (Ariyarathne et al. 2013), shell elements (Zhou et al., 2016) or membrane elements (Liu et al. 2007, Zhuang and Wang 2018). In the case of structural elements, their section properties must be defined.

2.3.3. Constitutive models and material parameters

In numerical modeling, the materials behavior is represented by constitutive models. There are various types of constitutive models to simulate the behavior of materials, such as the elasticity, the plasticity (Mohr-Coulomb, Cam Clay, and Cap-Yield models), the hyperplasticity, the hypoplasticity and the damage models. Based on the behavior of materials, the appropriate model should be selected. It is a fact that the more complex the model, the more accurate the results. In order to simulate the piled embankment, plasticity models have usually been employed to represent the soft soil and the embankment fill (Han and Gabr 2002; Huang et al. 2005; Jenck et al. 2006, 2007, 2009a, 2009b; Liu et al. 2007; Briançon and Simon 2009; Le Hello and Villard

2009; Huang and Han 2009, 2010). The elasticity is a good suggestion for modeling the structural components like foundation and piles. The descriptions of the constitutive models are illustrated in the following section.

2.3.4. Interaction between soil and structures

When the difference in stiffness between the elements occurs, it is necessary to consider the interactions between elements. The interfaces between the pile-soil and soil-geosynthetic must be taken into account, and their parameters need to be provided. In general, the interface properties are dependent on the stiffness of the surround media, the cohesion, and the friction angle (Jenck et al., 2007, 2006; Liu et al., 2007). However, to simplify the interface effects, Han and Gabr (2002) and Jenck et al. (2009b) assumed that the interfaces of pile-soil and geosynthetic-soil were fully bonded as considering a relatively small deformation.

2.3.5. Boundary Conditions and Loads

Boundary conditions are utilized by blocking the displacements at the boundaries of the model. It permits considering the symmetry planes or axis used in the idealized geometries or infinite media. In a static analysis, boundary conditions have to be given to prevent the movement of the model in any direction; in other ways, the unrestrained rigid body motion leads to the stiffness matrix to be singular. Therefore, the proper domain of simulation should be selected, which does not only minimize the influence of boundary effect but also reduce the degrees of freedom. Analyzing a reinforced piled embankment, Liu et al. (2007) took into consideration that the length of the model was extended three times the width of half the embankment to disregard the boundary effect, and horizontal boundaries were fixed (displacements were set to zero) in the normal their directions. As assuming that the system was positioned on a non-deformable rigid stratum at the bottom plane of the mesh, the displacements were set to zero in the three directions x, y, and z.

In the case of pile embankments, the most common loads include the gravity, the hydrostatic loading (undrained analysis) and the pressure loads on the embankments (surcharge loading and traffic loading) (Zhuang and Li 2015).

2.3.6. Analysis procedure

Generally, in a geotechnical analysis, the first is the initial step where the initial conditions are assigned such as the initial stress, pore water, saturation, the void ratio, etc. Next is the geostatic phase that allows activating the body weight of soils and

initial conditions. The displacements are reset to zero after this step. The following step could be the static loading phase (the consideration of the embankment weight and surcharge loading). As a moving wheel load/cyclic loading is taken into consideration, it is applied to the embankment top (Zhuang and Li, 2015).

In other cases, the dynamic response of the structure to the loads may be of interest: for example, the effect of a sudden load on a component, such as the one occurring during a compaction, or the response of a building during an earthquake (HKS, 2014).

2.3.7. Result visualization

In this step, the stresses, strains, settlements and internal forces can be pictured out or output in the database.

Based on the analysis of each specific step to simulate the piled or GRPS embankments, the implementation steps are suggested and shown in Fig. 2.5.

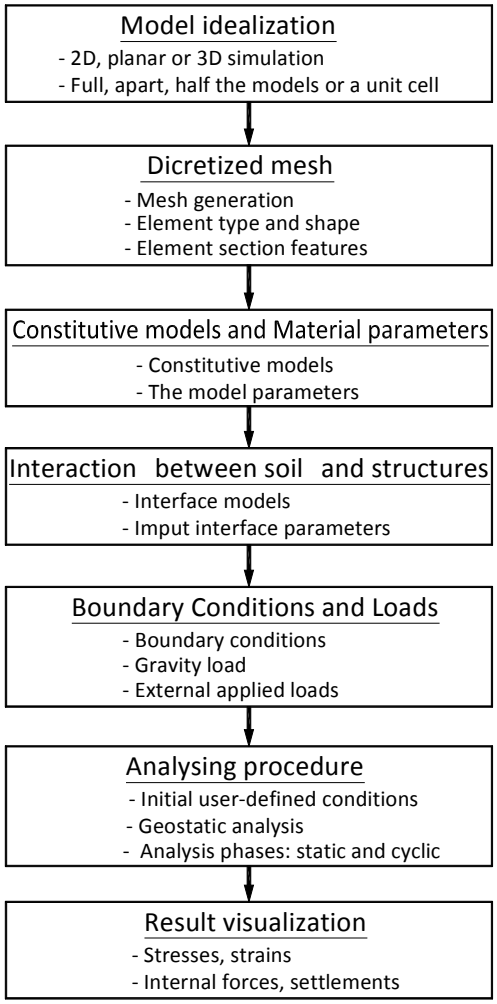

Fig. 2.5. Implementation steps for the PE and GRPS embankment analyses

2.4. Constitutive models

In the last forty years, the stress-strain relationship of soils has been representing by various constitutive models. They are widely used for the finite element and finite difference analyses to solve the problems related to soil structures and soil-structure interactions (Lade, 2005). Several useful constitutive models to model the soil behavior were used in this work and are presented in the following part. Each model is illustrated in terms of general introduction, mathematical equations, and parameter calibrations.

2.4.1. Elastic model

The elastic models are represented by resilient deformations upon unloading in which the stress-strain relationships are linear and path-independent. In addition, they do not produce yielding. Therefore, the linear elasticity is often used to model the behavior of metal, concrete, and rock.

In the elastic isotropic model, the constitutive equation is based on the Hooke's linear and reversible law, in which the stress increments are governed by the strain increments, as given:

$$\Delta\sigma_{ij} = 2G\Delta\varepsilon_{ij} + \alpha_2\Delta\varepsilon_{kk}\delta_{ij} \tag{2.1}$$

where δ_{ij} is the Kronecker delta symbol, and α_2 is the material constant correlated with the bulk modulus *K* and shear modulus *G*, as shown:

$$\alpha_2 = K - \frac{2}{3}G \tag{2.2}$$

New stresses are then updated from the expression

$$\sigma_{ij}^{N} = \sigma_{ij} + \Delta\sigma_{ij} \tag{2.3}$$

2.4.2. Mohr-Coulomb model (MC model)

The model is a linear elastic perfectly plastic model corresponding to the Mohr-Coulomb failure criterion, known as the Mohr-Coulomb model. The position of a stress point on the failure envelope is managed by a non-associated flow rule for the shear value (the plastic potential function is different from the yield function) (Itasca, 2009). The constitutive model is briefly presented below.

2.4.2.1. Elastic Law

Incremental stress-strain relationships are calculated based on Hooke's law as the

below equation 2.1:

$$\begin{aligned}\Delta\sigma_1 &= \alpha_1\Delta\varepsilon_1^e + \alpha_2\left(\Delta\varepsilon_2^e + \Delta\varepsilon_3^e\right)\\ \Delta\sigma_2 &= \alpha_1\Delta\varepsilon_2^e + \alpha_2\left(\Delta\varepsilon_1^e + \Delta\varepsilon_3^e\right)\\ \Delta\sigma_3 &= \alpha_1\Delta\varepsilon_3^e + \alpha_2\left(\Delta\varepsilon_1^e + \Delta\varepsilon_2^e\right)\end{aligned} \tag{2.4}$$

Herein, α_1 and α_2 are the material constants that are defined regarding the shear modulus *G*, and bulk modulus *K*, as given in Equation 2.2.

$$\alpha_1 = K + \frac{4}{3}G \text{ and } \alpha_2 = K - \frac{2}{3}G \tag{2.5}$$

2.4.2.2. Failure Criterion and Flow Rule

The three principal stresses are labeled

$$\sigma_1 \geq \sigma_2 \geq \sigma_3 \tag{2.6}$$

The criterion is represented in the (σ_1, σ_3) plane. The envelope of failure $f(\sigma_1, \sigma_3)= 0$ is defined by a Mohr-Coulomb failure criterion $f_s = 0$

$$f^s = \sigma_1 - \sigma_3 N_\phi + 2c\sqrt{N_\phi} \tag{2.7}$$

where φ is the friction angle, *c* is the cohesion.

$$N_\phi = \frac{1+\sin(\phi)}{1-\sin(\phi)} \tag{2.8}$$

The flow rule is represented by the potential function g^s, which defines the shear plastic flow. The potential function g^s concerns a non-associated law.

$$g^s = \sigma_1 - \sigma_3 N_\psi \tag{2.9}$$

Where

$$N_\phi = \frac{1+\sin(\psi)}{1-\sin(\psi)} \tag{2.10}$$

Where ψ is the dilatancy angle.

To represent the soil behavior of MC model, the stress-strain relationship behaves linearly in the elastic range with two parameters including the shear modulus *G* and the bulk modulus *K* (or Young's modulus *E* and Poisson's ratio ν). Two parameters manage the failure criterion, namely the friction angle φ and the cohesion *c*. The non-associated flow rule is represented by the parameter, known as the dilatancy angle ψ, and it is employed to consider a realistic irreversible volume change due to shearing. In

general, these parameters can be determined based on laboratory tests.

2.4.3. Cap-Yield model (CYsoil model)

The former model was the elastic linear perfectly plastic model with the shear failure criteria of Mohr Coulomb's type (MC). Due to its simplicity, this model is not capable of simulating the real behavior of granular soils, particularly their non-linearity, the variation of the modulus with the stress state and the overconsolidated response. To overcome these drawbacks, an advanced constitutive model was developed namely the Cap-Yield (CYsoil) model. It is a strain-hardening constitutive model, characterized by a frictional Mohr-Coulomb shear envelope (zero cohesion) and an elliptic volumetric cap in the (*p', q*) plane. Apart from the cap-hardening law and the compaction/dilatancy law, the model allows to capture the volumetric power law behavior observed in isotropic compaction tests as well as the irrecoverable volumetric strain that occurs as a result of ground shearing. In addition, the friction hardening law in the CYsoil model offers the alternative possibility of representing the hyperbolic behavior, in which the elastic modulus is expressed as a function of the plastic volumetric strain. The unloading-reloading excursion of soils is also characterized realistically (Itasca 2009).

2.4.3.1. Incremental elastic law

As similar to the MC model, the incremental elastic expression of CYsoil model is also represented by Hooke's law in the principle stress-strain planes. It has the form:

$$\begin{aligned}\Delta\sigma'_1 &= \alpha_1\Delta\varepsilon_1^e + \alpha_2\left(\Delta\varepsilon_2^e + \Delta\varepsilon_3^e\right)\\ \Delta\sigma'_2 &= \alpha_1\Delta\varepsilon_2^e + \alpha_2\left(\Delta\varepsilon_1^e + \Delta\varepsilon_3^e\right)\\ \Delta\sigma'_3 &= \alpha_1\Delta\varepsilon_3^e + \alpha_2\left(\Delta\varepsilon_1^e + \Delta\varepsilon_2^e\right)\end{aligned} \tag{2.11}$$

Therein α_1 and α_2 are material constants related to the current tangent shear modulus G^e, and current elastic bulk modulus K^e, as in Equation 2.9.

$$\alpha_1 = K^e + \frac{4}{3}G^e \text{ and } \alpha_2 = K^e - \frac{2}{3}G^e \tag{2.12}$$

In some cases, the values of the Young modulus E^e and Poisson's ratio ν are employed. They are in a relationship with G^e and K^e by the below expressions:

$$K^e = \frac{E^e}{3(1-2\nu)} \text{ and } G^e = \frac{E^e}{2(1+\nu)} \tag{2.13}$$

Just like to the double-yield model, the incremental elastic stiffness K^e is proportional

to the current incremental plastic stiffness in the CYsoil model. The factor of proportionality is a constant *R*. The current value of elastic shear stiffness G^e is derived from the below expression.

$$\frac{K^e}{G^e} = \frac{2(1+\nu)}{3(1-2\nu)} \tag{2.14}$$

2.4.3.2. Yield and potential functions

Shear yield criterion and flow rule - the Mohr-Coulomb criterion stands for the shear yielding. The envelope of shear yielding is consistent with the cap formulation in (*p', q*) plane:

$$f = Mp' - q \tag{2.15}$$

where *p'* is the mean effective stress, $p' = -(\sigma_1 + \sigma_2 + \sigma_3)/3$, and *q* is the deviatoric stress, it is defined as

$$q = -\left[\sigma_1' + (\delta - 1)\sigma_2' - \delta\sigma_3'\right] \tag{2.16}$$

The parameters are determined as $\delta = (3 + \sin\phi_m)/(3 - \sin\phi_m)$ and $M = 6\sin\phi_m /(3 - \sin\phi_m)$.

As can be seen in the above equations, the mobilized friction angle is influent on the parameter *M*. As the shear yielding criterion is satisfied, the evolution of mobilized friction angle results in the increase of *M*. A user-defined table is given to present the relationship between the mobilized friction angle ϕ_m and the plastic shear strain γ^p. In another way, the friction angle will be kept constant (equal to the input value) if no table is provided. The γ^p - ϕ_m correlation will be presented in the below part.

The potential function is expressed in the non-associated flow form, as given.

$$g = M^* p' - q^* \tag{2.17}$$

Where

$$q^* = \left[\sigma_1' + (\delta^* - 1)\sigma_2' - \delta^*\sigma_3'\right] \tag{2.18}$$

With $\delta^* = (3 + \sin\psi_m)/(3 - \sin\psi_m)$ and $M^* = 6\sin\psi_m /(3 - \sin\psi_m)$. Just like the above, the relationship of the mobilized dilatancy angle (ψ_m) and the plastic shear strain (γ^p) is given in the user-defined table. This relation can be clearly seen in Equations 2.22, 2.23 and 2.24. However, if no table is supplied, the dilatancy angle is constant and equals to the initial value.

Volumetric cap criterion and flow rule – the cap yield criterion is associated with the

function

$$f_c = \frac{q^2}{\alpha^2} + p'^2 - p_c^2 \tag{2.19}$$

Where α is the dimensionless parameter that controls the elliptical cap shape in the (p', q) plane, and p_c is the cap pressure. A user-defined table is produced to present a relationship between the cap pressure (p_c) and the plastic volumetric strain (e^p). This relationship is expressed in Equation 2.20. On the other hand, if no table is provided, p_c is assumed to be a constant (the initial value).

2.4.3.3. Hardening laws

Cap hardening – to model the volumetric power law behavior observed in isotropic compaction tests. A cap-hardening table is used to specify a power law behavior based on the correlation between the cap pressure and the volumetric plastic strain as in Equation 2.20. This law requires four parameters which include K_{ref}^{iso}, p_{ref}, m and R.

$$p_c = p_{ref}\left[(1-m)\frac{1+R}{R}\frac{K_{ref}^{iso}}{p_{ref}}e^p\right]^{\frac{1}{1-m}} \tag{2.20}$$

Friction hardening – For most soils, the deviatoric stress - axial strain curve for a drained triaxial test usually plots as a hyperbola. Due to the friction strain-hardening table, the model can reproduce this hyperbolic behavior. The user-defined table generating the relationship between the mobilized fiction angle and the plastic shear strain is given in Equation 2.21. The friction hardening law requests five parameters which include G_{ref}^e, p_{ref}, R_f, ϕ_f and β.

$$\gamma^p = \frac{p_{ref}}{G_{ref}^e}\frac{\sin\phi_f}{R_f}\left[\frac{1}{1-\frac{\sin\phi_m}{\sin\phi_f}R_f} - 1\right] \tag{2.21}$$

The friction, strain hardening, and cap hardening rules are clearly illustrated in Fig. 2.6.

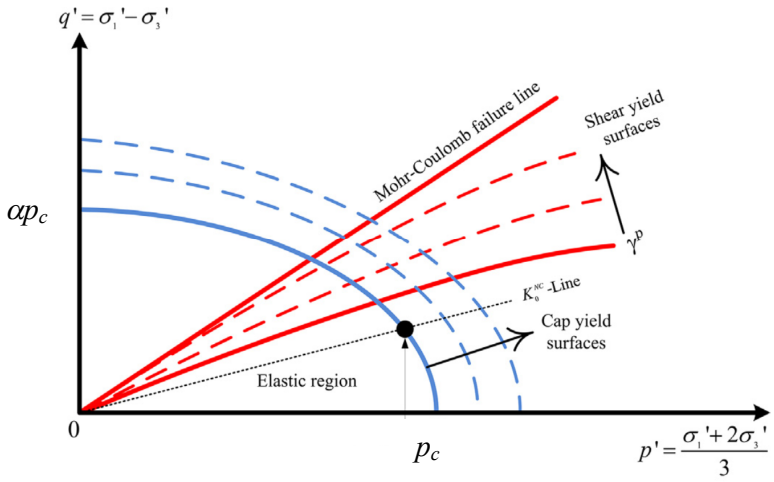

Fig. 2.6. Evolutions of shear and cap hardening laws (Pramthawee et al., 2017)

Dilatancy hardening - In the CYsoil model, a dilatancy strain-hardening table is used for the large shear strain to model the dilatancy of dense soils. Small shear strains (monotonic or cyclic) are disregarded. Dilatancy is expected as a result of a shearing hardening rule as the following expression. The volumetric plastic strain rate is in a relationship with the shear plastic train rate, which allows this rule to capture the irrecoverable volumetric strain taking place as a result of soil shearing.

$$\dot{e^p} = \dot{\gamma^p} sin\psi_m \tag{2.22}$$

Where ψ_m is the (mobilized) dilatancy angle. It is correlated with the mobilized friction angle based on Equation 2.23.

$$\sin\psi_m = \frac{\sin\phi_m - \sin\phi_{cv}}{1 - \sin\phi_m \sin\phi_{cv}} \tag{2.23}$$

Therein ϕ_{cv} is the constant-volume stress ratio. It can be defined by an equation based on Rowe stress-dilatancy theory (1962) as in Equation 2.24.

$$\sin\phi_{cv} = \frac{\sin\phi_f - \sin\psi_f}{1 - \sin\phi_f \sin\psi_f} \tag{2.24}$$

Where ϕ_f and ψ_f are ultimate values of the friction and dilatancy angles, respectively.

To represent the dilatancy hardening law, a table of the dilatancy versus the plastic shear strain is produced.

To produce a hyperbolic curve of the deviatoric stress versus the axial strain in a drained triaxial test, the friction strain-hardening law was implemented in the CYsoil model. This law needs six parameters including G^e_{ref}, ν, p_{ref}, R_f, ϕ_f and β. The the CYsoil

model parameters are described in Table 2.1. The five parameters (G^e_{ref}, ν, p_{ref}, R_f, ϕ_f) are determined based on the laboratory tests. The calibration factor of β is a constant. It manages the friction strain-hardening law. It is possible to obtain the value of β from triaxial tests based on fitting the stress-strain curves. To present the volumetric power law in the isotropic compaction tests, the four parameters that govern the cap-hardening table are provided in Table 2.1. They are calibrated derived from the data of isotropic compaction tests.

Table 2.1. Parameters for the CYsoil model

Constitutive laws	Parameters	Unit
Friction hardening	G^e_{ref} - reference elastic tangent shear modulus	Pa
	ν - Poisson's raio	-
	p_{ref} - reference effective pressure	Pa
	R_f - failure ratio	
	ϕ_f - ultimate friction angle	(^{o})
	β - calibration factor	
Cap hardening	K^{iso}_{ref} - slope in isotropic laboratory test *of p'* versus *e*	-
	p_{ref} - reference effective pressure	Pa
	m - exponential constant *(m < 1)*	-
	R - constant that is consistent with the choice for K^{iso}_{ref} and G^e_{ref}	-

2.4.4. Modified Cam-Clay model (MCC model)

The MCC model belongs to the family of the cap models. It can address the non-linear elasticity and the hardening/softening law. The nonlinear elasticity is based on the assumption that the bulk modulus is updated at each change of the specific volume. The hardening/softening rule represents the dependency of the size of the yield curves on the consolidation pressure that is a function of the plastic volume change and the specific volume. The MCC model is one of the useful models for representing the response of soft soils. In particular, it is appropriate for normally consolidated clays.

The mathematical equations of the MCC model are briefly presented below.

2.4.4.1. Incremental elastic law

The generalized stress components utilized in the model are the mean effective pressure *p'*, and deviatoric stress *q*, as shown in Equation 2.25.

$$p' = -\frac{1}{3}\sigma_{ij} \text{ and } q = \sqrt{3J_2} \tag{2.25}$$

Where the Einstein summation convention puts into the application, and J_2 is the second invariant of the effective deviatoric-stress tensor $\Delta[s]$:

$$J_2 = \frac{1}{2} s_{ij} s_{ij} \tag{2.26}$$

The incremental equation of the Hooke's rule corresponding to generalized stress and strain is written as the following equation:

$$\begin{aligned} \Delta p' &= K \Delta \varepsilon_p^e \\ \Delta q &= 3G \Delta \varepsilon_q^e \end{aligned} \tag{2.27}$$

Herein $\Delta q = \sqrt{3\Delta J_2}$, and the second invariant of the incremental deviatoric-stress tensor ΔJ_2 is defined, as shown in Equation 2.28.

$$\Delta J_2 = \frac{1}{2} \Delta s_{ij} \Delta s_{ij} \tag{2.28}$$

If it is assumed that both plastic and elastic principal strain increment vectors are coaxial with the current principal stress vector, the generalized strain increments are decomposed into elastic and plastic parts, as follows:

$$\begin{aligned} \Delta \varepsilon_p &= \Delta \varepsilon_p^e + \Delta \varepsilon_p^p \\ \Delta \varepsilon_q &= \Delta \varepsilon_q^e + \Delta \varepsilon_q^p \end{aligned} \tag{2.29}$$

The variables of incremental strain associated with generalized stress components (*q* and *p'*) are the volumetric strain increment $\Delta\varepsilon_p$ and shear strain increment $\Delta\varepsilon_q$, the relation is:

$$\begin{aligned} \Delta \varepsilon_p &= -\Delta \varepsilon_{ii} \\ \Delta \varepsilon_q &= \frac{2}{3} \sqrt{3\Delta J_2'} \end{aligned} \tag{2.30}$$

Where $\Delta J'_2$ represents the second invariant of the incremental deviatoric-strain tensor $\Delta[e]$:

$$\Delta J'_2 = \frac{1}{2} \Delta e_{ij} \Delta e_{ij} \tag{2.31}$$

In the modified Cam-clay model, the tangential bulk modulus *K*, which is controlled by the specific volume (Equation 2.10), is updated step by step to exhibit a nonlinear behavior acquired experimentally from isotropic compression tests in Equation 2.32. The result of the isotropic compression test is shown in the semi-logarithmic curve in Fig. 2.7.

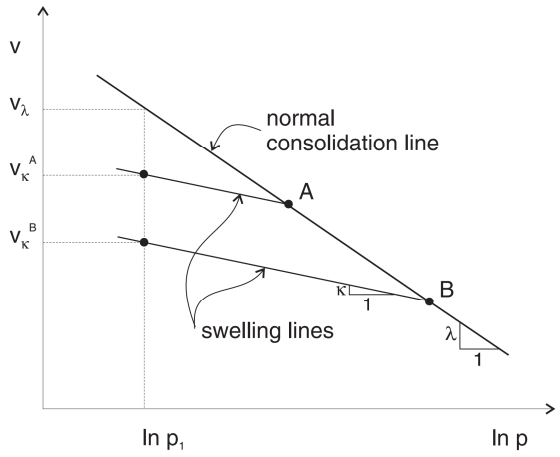

Fig. 2.7. Normal consolidation line and unloading-reloading (swelling) line for an isotropic compression test (Itasca, 2009)

$$K = \frac{vp'}{\kappa} \tag{2.32}$$

It can be clearly seen that an increase in the normal consolidation pressure *p'* results in a decrease in specific volume *v* of the material, it is determined by the expression:

$$v = v_\lambda - \lambda \ln\left(\frac{p'}{p_1}\right) \tag{2.33}$$

Where λ is the slope of the normal consolidation line, v_λ is the value of the specific volume at the reference pressure, and p_1 is the reference pressure. In the unloading-reloading excursions, the point A or B will travel along an elastic swelling line of slope κ, back to the normal consolidation line where the path will resume. The expression of swelling lines is written as below.

$$v = v_\kappa - \kappa \ln\left(\frac{p'}{p_1}\right) \tag{2.34}$$

2.4.4.2. Yield and potential functions

Corresponding to a given value of the consolidation pressure p_c, the yield function is illustrated, as seen:

$$f(q,p) = q^2 + M^2 p'(p' - p_c) \tag{2.35}$$

Wherein, *M* is a material constant. The yield function (f = 0) is exhibited by an ellipse with horizontal axis p_c and vertical axis Mp_c in the (p', q) plane. The failure envelop in the principal stress space is represented by an ellipsoid of rotation around the mean stress axis (Fig. 2.8).

The potential function g coincides with the yield function in an associated flow rule:

$$g = q^2 + M^2 p'\left(p' - p_c\right) \tag{2.36}$$

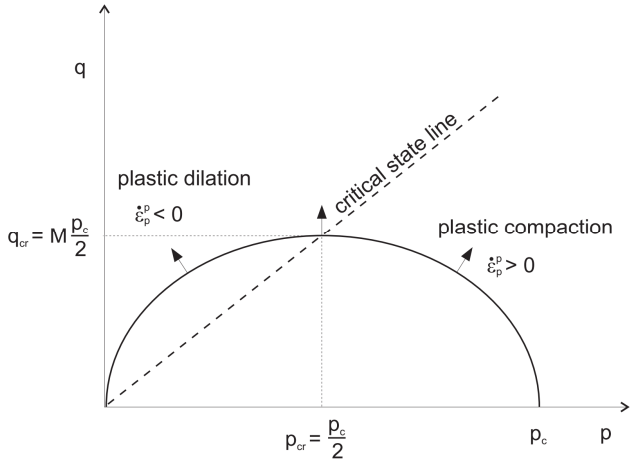

Fig. 2.8. Failure criterion of Cam-clay model (Itasca, 2009)

2.4.4.3. Hardening/softening rule

The size of yield curves depends on the consolidation pressure p_c, as seen in Equation 2.37. This pressure is a function of the plastic volume change and the specific volume. It is updated for the step using the mathematical relationship.

$$p_c^N = p_c\left(1 + \Delta\varepsilon_p^p \frac{\nu}{\lambda - \kappa}\right) \tag{2.37}$$

Where, $\Delta\varepsilon_p^p$ is the plastic volumetric strain increment for the step, ν is the current specific volume, λ and κ are material parameters which are above introduced.

Eight input parameters are required. They are listed in Table 2.2. For the calibrating procedure, the value of the maximum elastic shear modulus *G* is first set a large value, and the Poisson's ratio ν is kept as a constant. The parameters λ and κ can be determined based on the isotropic compression curve. Friction constant *M* is calculated derived from the friction angle, so it can be specified by the shearing tests. Pre-consolidation pressure p_{c0} determines the initial size of the yield surface. It is defined corresponding to the oedometer test. The initial specific volume v_0 and the reference pressure are given in a relationship according to the values of λ, κ, and p_{c0} given in Equation 2.38, which are calibrated from the ν - lnp' plot in the isotropic compression test.

$$v_0 = v_\lambda - \lambda \ln\left(\frac{p_{c0}}{p_1}\right) + \kappa \ln\left(\frac{p_{c0}}{p}\right) \tag{2.38}$$

Table 2.2. Parameters for the MCC model

Number	Parameters	Unit
1	G – maximum elastic shear modulus	Pa
2	ν – Poisson's ratio	-
3	λ - slope of normal consolation line	-
4	κ - slope of the elastic swelling line	-
5	M - the friction constant	-
6	p_{c0} - pre-consolidation pressure	Pa
7	p_1 - reference pressure	Pa
8	v_0 - specific volume at reference pressure	-

The summary of the basic constitutive models available in the FEM and FDM programs is presented in Table 2.3.

Table 2.3. Summary of the mathematical laws, the behavior representation, and the required parameters of soil constitutive models

Soil models	Failure criterions and laws	Representation of behaviors	Parameters required	Calibrating tests
Elasticity	Incremental elastic law	To reproduce a linear elasticity	K and G (or E and ν)	Isotropic compression tests
MC	Incremental elastic law	To manage the linear elasticity	K and G (or E and ν)	Triaxial tests and isotropic compression tests
	Failure criterion	To qualify the yield envelop	c and φ	
	Flow rule	To control the plastic behavior	ψ	
CYsoil	Incremental elastic law	To address a nonlinear elastic response	G and ν (or E and ν)	Triaxial tests and isotropic compression tests
	Yield and Potential Functions	To define the yield envelop	ϕ_f and ψ_f (the user-defined tables)	
	Frictional strain-hardening	To reproduce the hyperbolic stress-strain curve in a drained triaxial test;	G^e_{ref}, p_{ref}, R_f, ϕ_f and β	
	Cap hardening	To qualify the volumetric power law behavior in isotropic compaction tests	K^{iso}_{ref}, p_{ref}, m and R	
	Dilatancy hardening	To represent the irrecoverable volumetric strain	ϕ_f and ψ_f	
MCC	Incremental elastic law	Exhibit a nonlinear behavior acquired in isotropic compression tests	G, ν and κ	Isotropic compression tests and Shear tests (or triaxial tests)
	Failure criterion	To define the shear yielding envelop	M	
	Yield and Potential Functions	Represent the plastic volume changes as the consolidation pressure changes	p_{c0}, v_0, and p_1	

2.5. Conclusions

Numerical simulations have proved their abilities in the economic effectiveness, the calculation time, the complex problem solving, and the reliable results. Therefore, they are being increasingly used for studying, designing and auditing.

FLAC3D and ABAQUS are the favorite software packages for 3D simulations due to their friendly interface, their flexible mesh generation, their wide application possibilities, and their analyzing capacity. They have been broadly applied for solving the piled and GRPS embankments as well as the geotechnical problems.

The each numerical modeling step presented in the analysis shows that the tasks and the procedures need to be considered. The flow chart of the implementation steps for numerical simulations of piled or GRPS embankments is also suggested. It is useful for the users to conduct geotechnical problem simulations.

A short review of several available constitutive models is introduced in terms of the constitutive laws, the mathematical equations, the required parameters, and the calibration procedure. It would be beneficial for users to select the appropriate constitutive models in their analyses.

Chapter 3

Soft soil improvement by rigid inclusions under complex loading

3.1. Introduction

The structures are often subjected to the combination of different loads (vertical, horizontal and moment loads) acting on the foundations, such as the eccentricity of loading, the horizontal loading, the moment, and load cycles. Therefore, taking into account the complexity of loading on the foundation is really necessary for the geotechnical engineers. In this chapter, a footing over rigid inclusion-reinforced soft soil under complex loading will be studied in two cases.

The first case is a footing directly lying upon a pile-reinforced soft soil under complex loadings. Both experimental and numerical approaches are conducted. The examined cases include a single rigid inclusion test, a footing over non-reinforced and reinforced soft soil cases. The general soil behavior could be expressed based on the single rigid inclusion and non-reinforced footing tests that allowed determining the soil parameters for the numerical analyses. The rigid inclusion-reinforced footing was, furthermore, tested with different loading cases (centered and eccentric vertical loads and horizontal loads). In every test, unloading-reloading cycles were also considered. The responses of the structure are presented in terms of the pressure on the inclusion head, the vertical and lateral footing displacements, and the lateral inclusion displacement.

In the second case, 3D numerical simulations are performed to investigate a rigid inclusion-reinforced soil under the wind turbine foundation subjected to the combinations of loads. Then, the reinforced soil method is compared to the other foundation solutions (shallow and piled raft foundations). A parametric study is developed based on a real soil profile, and all the foundation solutions are analyzed for realistic static wind turbine loads. The assessment of the efficiency of each foundation system was performed in terms of surface settlements on the soil foundation, axial forces and bending moments on the vertical reinforcements.

3.2. Footing over the rigid inclusion-reinforced soft soil

3.2.1. Introduction

In the proposed study, an experimental on-site model and the corresponding numerical modeling are presented. The experimental tests were divided into three parts, including isolated rigid inclusion tests, footings over unreinforced and reinforced soils. In the case of reinforcement, different loading cases including centered and eccentric vertical loads, horizontal loads and a few load cycles were considered. A numerical modeling is performed permits to show with more details the behavior of the system.

3.2.2. Related works

Many studies of a footing over a rigid inclusion-reinforced soil with a granular mattress have been performed in the literature. The mattress plays an important role as the load transfer platform where the soil arches are formed (Han and Gabr, 2002; Hewlett and Randolph, 1988; Jenck et al., 2006, 2007; Kempfert et al., 2004). Andromeda and Briançon (2008) carried out experimental tests to investigate the behavior of a slab over a non-reinforced and reinforced soil and of an embankment on a reinforced soil. The results indicated larger differential settlements in the slab-mattress-reinforced soil case than in the case of piled embankment one. In addition, the efficacy increased with the embankment height increase for the concrete slab case. The numerical results of Chevalier et al. (2011) indicated that if the thickness of the fill layer reduced by half, the efficacy decreased more than a half (from 70% to under 30%). Studying spread foundations on rigid inclusion-improved soils subjected to complex loadings, Dias and Simon (2015) have presented a simplified design for such foundations based on a comparison of 3D numerical modeling and a simplified analytical method. A case study on a slab over rigid inclusion-reinforced soft soil with a mattress of 2 m was presented in Briançon et al. (2015). Their results mentioned that the measured pressure on the pile cap was nearly 7 times higher than the one on the soil. The reduction of the settlements was shown as well. Based on numerical modeling, Boussetta et al. (2016) showed that the maximum settlement and the efficacy increased linearly with the mattress layer thickness. As similar to the findings in an embankment, an increase of the improvement ratio leads to an increase of the maximum efficiency and a decrease of the settlements.

Concerning the case of a footing over a reinforced soil without mattress, there have not been many studies performed. Embankments over reinforced concrete slab on top

of the inclusions for a high-speed railway were studied by Raithel et al. (2008). The concrete slab plays a load transfer role. A comparison between a slab and a geosynthetic reinforced earth platform figured out that the settlements of the slab case were only two-thirds of the ones of the geosynthetic case. Seniwongse (2010) presented the concept of a transition slab (i.e. a slab placed on flexible lengths of rigid piles). The slab enables a smooth transition between slab-on-pile and slab-on-grade pavement. Zhan et al. (2013) introduced a design method for a pile-slab structure with no ballast on a soil subgrade. The soil properties were not considered in the analytical equations. The numerical analysis of Jiang et al. (2014) was also conducted to study a pile-slab-supported railway embankment. The results pointed out that rigid piles combined with a reinforced concrete slab permit to decrease significantly the vertical stress applied on the soils. Considering a thin cushion mattress of 0.3 m between the pile heads and the slab, the authors found that the maximum shear force and bending moment in the slab is respectively reduced by 28 and 17%. A slab over an inclusion-reinforced soil was considered as a foundation solution for the refinery and petrochemical tank farm due to its settlement reduction (Leclaire et al., 2017).

Based on reviewing the related works, it can be seen that a footing over a reinforced soil has been employed for infrastructural and industrial projects while a few studies were conducted. In addition, the research on this system subjected to complex loadings is still limited. Therefore, a study on footings over rigid inclusion-reinforced soft soil without a mattress was conducted.

3.2.3. Site experiment

3.2.3.1. Site investigations

The *in-situ* sites were located in the Venette city, France. Cone Penetration Tests (CPT) and Pressuremeter Tests (PMT) were performed to investigate the geometric and geotechnical properties of soils. The soil profile was obtained based on the CPT data, as described in Fig. 3.1. There is a 1-m-thick existing embankment layer at surface level, followed by a silt layer of 4 m (soft soil) below. Next is a 4.5 m sand and gravel layer, the bottom layers are soft limestone to altered rocks underneath (reaching 25 m in depth). The groundwater level was monitored at a depth of 3.7 m. PMTs allowed determining the pressuremeter modulus (E_p) and the limit pressure (P_L). Laboratory tests were also conducted to define the soil parameters. Finally, all the parameters obtained by the geotechnical investigation are presented in Table 3.1.

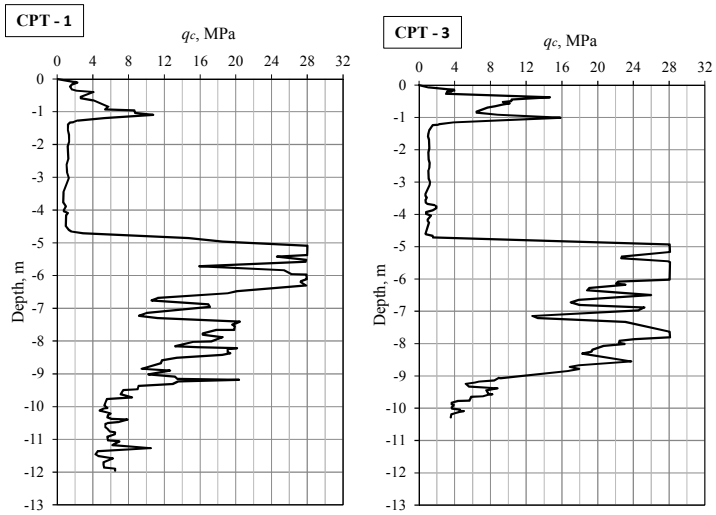

Fig. 3.1. Investigation of the soil profile based on CPT-1 and CPT-3

Table 3.1. Geometrical and geotechnical properties of soils based on *in-situ* and laboratory tests

Soil type	Depth (m)	γ (kN/m^3)	c (kPa)	φ (°)	E_p (MPa)	P_L (MPa)	α (-)	q_c (MPa)
In place embankment	0÷1	20	11	25	15	0.96	1/2	5
Silt clay	1÷5	20	6	31	5.5	0.43	1/2	1
Gravel and sand	5÷9.5	16.5	0	43	35	2.50	1/3	20
Soft limestone	9.5÷12	18	10	25	5.5	0.50	2/3	-
Altered limestone	12÷19	19	20	30	13	1.40	2/3	-
Compacted limestone	19÷25	20	30	35	164	5.00	1/2	-

3.2.3.2. Experimental test details

Rigid inclusion

Rigid inclusions are installed using a special auger that allows the *in situ* soils to displace laterally without vibrating or spoiling, and minimizes the risk of contamination. The auger is screwed into the soil to reach the designed depth of 5.5 m. The geometrical and mechanical characteristics of rigid inclusion include a diameter of 0.32 m, a length of 5.5 m (anchored of 0.5 m in the gravel and sand layer), Young's modulus of 5 GPa, and a compressive strength of concrete at 28 days of 10 MPa.

Test arrangement and loading system

Three testing areas were organized on the site, as seen in Fig. 3.2. The first area was carried out for testing two isolated rigid inclusions (CMC-A and CMC-B) at a distance of 2 m. The vertical load applied to the rigid inclusions permits to show the bearing capacity of the single rigid inclusion and the resistance of the existing ground. The second area was the footing over the existing ground (unreinforced soil) (test A). In

this area, a 2×2 m square reinforcement concrete footing with a thickness of 0.5 m was directly placed on the soil. Then, a vertical loading was applied to the center of the footing. The third area was to investigate the footing over the CMC-reinforced soil. Four 5.5-m-long rigid inclusions arranged in a square pattern by 1.2 m were installed and anchored of 0.5 m within the gravel and sand layer. The RC footing was then setup on the ground improvement without a granular platform. Complex loads were applied on the footing in the tests B and C.

In the single rigid inclusion tests, the hydraulic jack was directly located between the inclusion head and the drilling machine to set up the vertical loading system. In the tests for the footings, a loading frame was erected, in which a steel beam was fixed using a group through steel anchored bars on adjacent piles. Therefore, this system could produce an important vertical loading, and the hydraulic jack was inserted between the footing and the beam. The flexibility of the vertical loading system enables the tests to be carried out with different eccentricities by moving the hydraulic jack along the steel beam. To provide the horizontal loading on the footing, another hydraulic jack was placed between the footing and the reaction pile-raft. The arrangement of the loading systems is presented in Fig. 3.2.

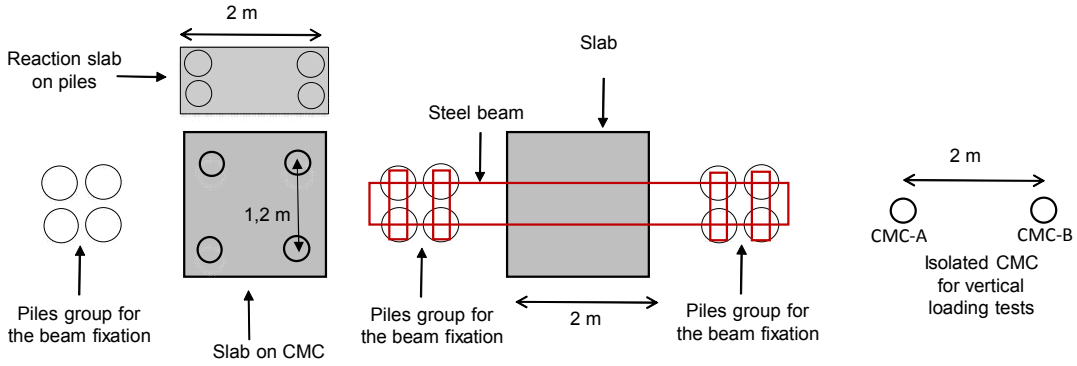

Fig. 3.2. The detail arrangement of the testing site

3.2.3.3. Installation of the measuring instruments

During the tests, the pressure on the rigid inclusions and on the soil, the footing displacements, and the subsoil settlement were measured. To monitor the pressure transferred to the inclusions and the subsoil, two thin pressure cells WPC-1 and WPC-2 were placed on the top of CMC3 and CMC4, and one earth pressure cell (EPC-1) was set at the middle of two adjacent inclusions on the subsoil. Four displacement transducers (D1 - D4) were located at the footing corners and one (D0) was positioned at the center, which allows monitoring the footing displacements during the tests. Besides that, a settlement gauge, Rod Extensometer System (RES), was placed at a

depth of 8 m near the centreline of the footing to record the subsoil settlements. Four points were measured at the depths of 1, 2, 4 and 8 m. In order to evaluate the concrete continuity, six wire extensometers (WE3 - WE8) were situated inside two inclusions at the depths of 0.5, 1, 1.5, 2.5 and 3.5 m, and the other extensometers (WE1 and WE2) were located inside the footing. The measurement instruments are presented in Fig. 3.3. In regard to the horizontal displacements, two sensors (d1 and d3) were placed on inclusions CMC1 and CMC2, a tiltmeter was attached on the shaft of CMC2, and sensors d4 and d2 were respectively installed on the footing and the reaction slab. An inclinometer located between the piles CMC1 and CMC2 to record the lateral soil settlement (Fig. 3.4) was also setup. During the horizontal loading tests, the displacement of the rigid inclusion caps, the footing, and the soil could be measured by the displacement sensors.

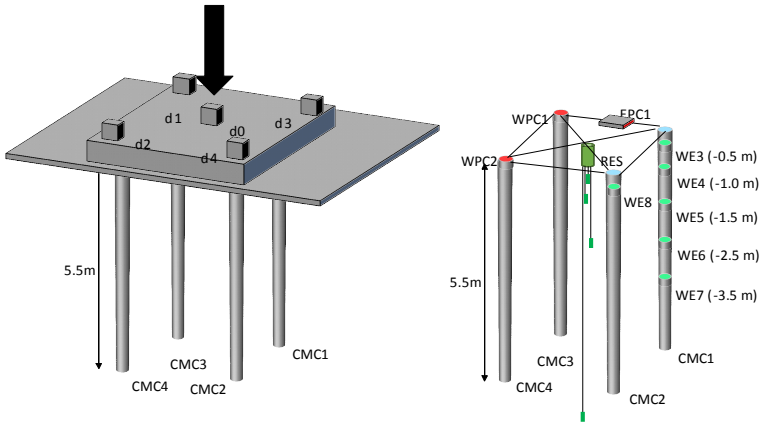

Fig. 3.3. Instrumental installation for measuring the pressures, the vertical displacements, and the soil settlement

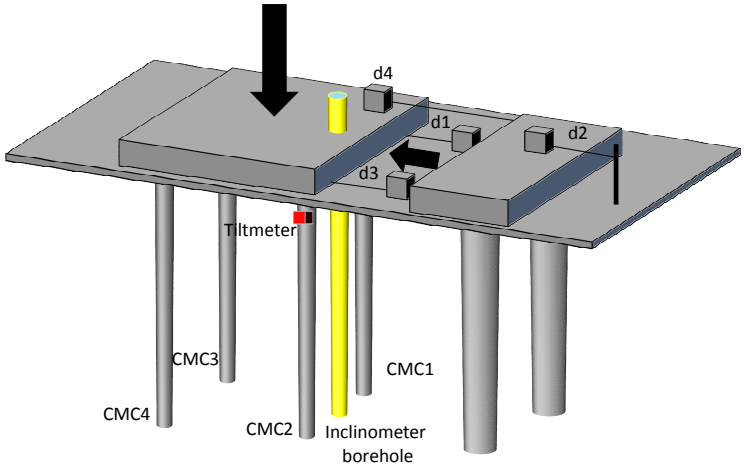

Fig. 3.4. Instrument arrangement for measuring the horizontal footing displacement and the lateral inclusion displacement

3.2.3.4. Loading procedure

The vertical static loading tests were performed on two different rigid inclusions (tests CMC-A and CMC-B) to determine the ultimate bearing capacity of the soil foundation. The loading sequence of these tests was carried out by a loading-unloading cycle of 300 kN, then followed by a loading-unloading cycle of 480 kN. In the case of a non-reinforced footing, the two different cycles of loading were vertically applied in the tests A1 and A2 corresponding to the loadings of 400 kN and 1800 kN (Table 3.2). The five tests were conducted to investigate the behavior of the footing over the rigid inclusion-improved soft soil without a granular platform. The tests 1B, 4B and 6B described the response of the system under centered vertical loads. Meanwhile, the structure was subjected to eccentric vertical loads in the tests 2B and 3B (Table 3.3). The eccentricities of loading were created by moving the hydraulic jack along the symmetric axis through the footing center and parallel with the line CMC3-CMC4. Two tests 1C and 2C were carried out to investigate the influence of the horizontal loading on the system as well. In these tests, the vertical loads were applied first. Increments of horizontal load were then applied to reach 20% of the vertical load (Table 3.4).

Concerning the tests order for the rigid inclusion-reinforced footing case, the test 1B was first carried out. The followings were the tests 2B and 3B with the eccentric loading. Thirdly, a loading-unloading operation of the test 4B was conducted. After that, the horizontal loading tests 1C and 2C were done. The centered vertical loading test 6B was finally performed. After each test, the displacement sensors were reset to zero.

Table 3.2. Vertical load tests for the unreinforced footing case

Tests	Eccentricity	Vertical loading, kN
1A	0	$0 \rightarrow 400 \rightarrow 0$
2A	0	$0 \rightarrow 1800 \rightarrow 0$

Table 3.3. Vertical load tests for the reinforced footing case

Tests	Eccentricity	Vertical loading, kN
1B	0	$0 \rightarrow 1000 \rightarrow 0 \rightarrow 1000 \rightarrow 0$
2B	0.30 m	$0 \rightarrow 690 \rightarrow 0 \rightarrow 690 \rightarrow 0$
3B	0.45 m	$0 \rightarrow 600 \rightarrow 0 \rightarrow 960 \rightarrow 0$
4B	0	$0 \rightarrow 1000 \rightarrow 0$
6B	0	$0 \rightarrow 1000 \rightarrow 0$

Table 3.4. Horizontal load tests for the reinforced footing case

Tests	Eccentricity		Loading, kN	
	V	H	V	H
1C	0	0	600	$0 \rightarrow 120 \rightarrow 0 \rightarrow 120 \rightarrow 0$
2C	0	0	1000	$0 \rightarrow 200 \rightarrow 0$

3.2.4. Numerical simulation

3.2.4.1. Numerical modeling

The finite difference software FLAC3D was used for the numerical analyses. The soil profile was simplified by three layers. This assumption was done considering the results of the CPTs (Fig. 3.1) which permit to clearly differentiate three soil layers. The first one was a fill layer of 1 m, followed by a 4-m-thick soft clay situated under a 7-m-thick gravel and a substratum beneath. The water table leveled out at -3.7 m. The three scenarios in the numerical analysis were similar to those of the experimental tests, including the single rigid inclusion tests, the footing without inclusions and the inclusion-reinforced footing (Fig. 3.5). Due to the symmetry of the geometry and the loading condition, a quarter of the model was selected for the single rigid inclusion case, and a half of the model was simulated for the non-reinforced and reinforced footing cases. Volumetric elements were used for soils, inclusions, and footing, and beam components embedded inside the volumetric elements of inclusions allowed to easily obtain the efforts (axial forces and bending moments). The mesh of the single inclusion model is composed of 23,450 elements, while for the unreinforced and reinforced footing models 81,968 elements, were used as illustrated in Fig. 3.6. In the analyses, the fill and stratum were modeled by the elastic perfect-plasticity model (MC), the soft soil was considered using the modified Cam-clay model (MCC), the footing and the inclusions were simulated by the linear elastic constitutive model. The MCC constitutive model cannot take into account of the soil behavior under cyclic loading (the yield surface coinciding with the plastic potential, is enlarged in the first loading and then will not be modified more, so that all changes in further stress loadings are elastic (O'Reilly and Brown, 1991), but insufficient laboratory data were available to calibrate the input parameters for a more complex constitutive model. Inclusion-soil and footing-soil interfaces were considered. Due to the soil layers situated on the hard substratum, the boundary at the bottom (z = -12 m plane) was fixed in the three directions, x, y, and z. The length of the model in the horizontal directions (10 m) was ten times the width of half the footing. This dimension permits to avoid boundary effects. The vertical boundaries were blocked in their normal

directions. Because of the thin layer of silty clay and the slow loading process, the analyses were performed in drained conditions.

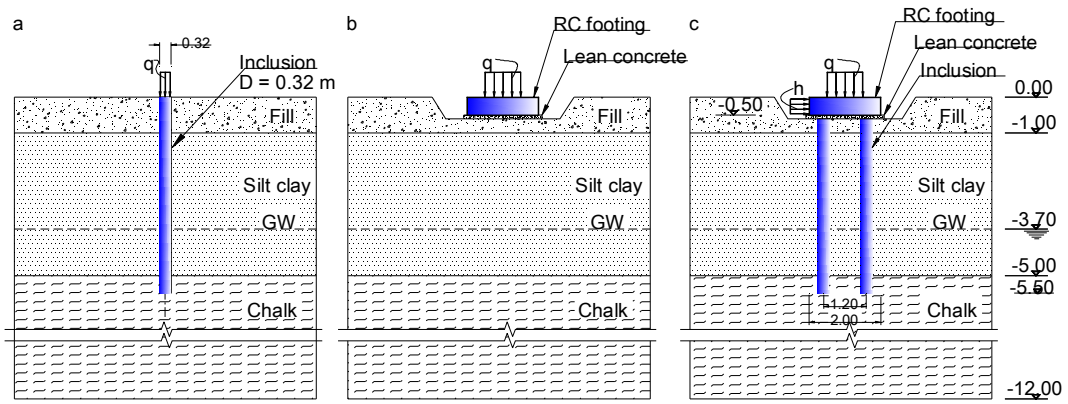

Fig. 3.5. Elevation view of the three testing cases in the study: a) the single pile; b) the non inclusion-reinforced footing; c) the inclusion-reinforced footing

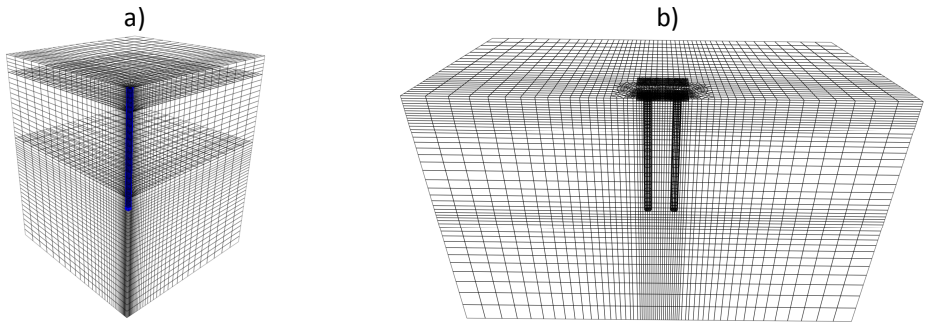

Fig. 3.6. 3D meshes for the numerical analyses: a) single pile; b) unreinforced and reinforced footings

3.2.4.2. Constitutive models and parameters

The vertical rigid inclusions and footing are made of concrete. They were modeled by the linear elastic constitutive model in the analyses. Two parameters are required and derived from the design data. The fill and stratum almost behave as granular materials, which were modeled using the linear elastic perfectly-plastic (with a shear criteria of Mohr-Coulomb's type) constitutive model. The parameters of the fill were taken from laboratory tests while the parameters of chalk were adjusted using the single rigid inclusion tests.

The modified Cam-clay permits to model the soft clays behavior due to its hyperbolic stress-strain relationship, critical state line and a softening-hardening rule (Itasca, 2009). It was considered for the silty clay. The parameters of this model could be defined based on the good fitting between experimental data and numerical results

using oedometer tests, as given in Fig. 3.7. The pre-consolidation pressure (p_c) obtained by the oedometer test was approximately equal to 67 kPa. It corresponds to a relatively small value. In fact, a small value of p_c leads to an early occurrence of plasticity, which can result in large settlements. In the case of the footing over unreinforced soil, the maximum pressure on the soil is about 450 kPa (1800 kN per 4 square meters), which cause a significant footing displacement if the pre-consolidation pressure is not well calibrated. In this study, a calibration of p_c has been performed using the vertical loading tests on the footing over unreinforced soil. Fig. 3.8 shows the footing displacement as a function of p_c. In overall, the footing displacement decreases significantly when the value of p_c increases. Derived from the figure, corresponding to a p_c equal to 315 kPa, the result obtained by numerical modelling coincides with the one obtained by the field test (corresponding to a footing displacement of 55 mm). This value of p_c is then used for all the following numerical analyses.

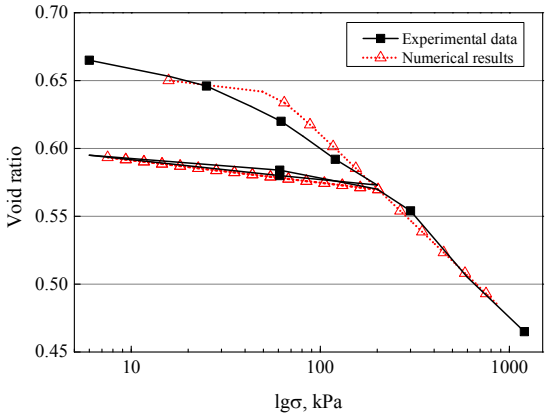

Fig. 3.7. Oedometric tests on the silty clay sample

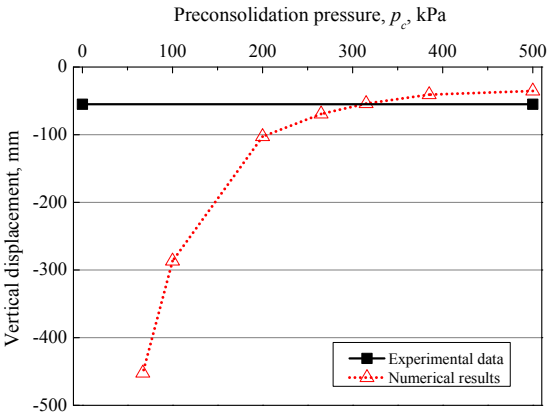

Fig. 3.8. Influence of p_c on the vertical footing displacement for the unreinforced footing

To take into account the interaction between the soil and structure, interface elements

were assigned at the contact faces. The shear and normal stiffnesses (k_s and k_n) were chosen based on a rule-of-thumb that k_s and k_n were set to equal the stiffest neighboring zone (Itasca 2009), so they were taken equal to 10^8 kN/m for the analyses. The sliding effect of the interface is also considered if the bond is broken. The sliding Coulomb criterion is applied to the interface segments and is represented by the friction angle and cohesion. In this study, the interface friction angle was taken equal to two-thirds of the one of the surrounding soil as in Jenck et al. (2007). The cohesion along the interface was taken directly from the cone resistance of CPT tests. It was equal to 30 kPa for the silt and 170 kPa for the chalk. The adopted parameters for the materials and the interface elements are summarized in Table 3.5.

Table 3.5. The geotechnical parameters of materials employed for numerical studies

Material	Model	Geotechnical parameters
Fill layer	MC	E = 30 MPa, ν = 0.3, φ = 20°, c = 11 kPa, γ = 19 kN/m^3
Silt clay	MCC	λ = 0.06, κ = 0.0072, M =1.244, v =1.892, p_c = 315 kPa, γ = 18 kN/m^3
Stratum	MC	E = 350 MPa, ν = 0.3, γ =19 kN/m^3, φ = 37°, c = 0 kPa
Inclusion	Elasticity	E = 5 GPa, ν = 0.2, γ = 25 kN/m^3
Footing	Elasticity	E = 24 GPa, ν = 0.2, γ = 25 kN/m^3
	Fill-Pile	$k_s = k_n = 1\times10^8$ kPa/m, φ = 13°, c = 7 kPa
Interface	Clay- Pile	$k_s = k_n = 1\times10^8$ kPa/m, φ = 15°, c = 30 kPa
	Chalk- Pile	$k_s = k_n = 1\times10^8$ kPa/m, φ = 22°, c = 170 kPa

3.2.5. Comparison of measured and computed results

3.2.5.1. Vertical load tests on single rigid inclusions

To estimate the ultimate bearing capacity of the chalk, *in situ* tests on two different single rigid inclusions (CMC-A and CMC-B) were carried out. The applied force and displacement of inclusion head were measured. Fig. 3.9 shows the plots of the inclusion head displacement versus the vertical loading. Both measured data and numerical analysis results are presented in this figure. The experimental data highlighted that the stress-strain relationship of the inclusion CMC-B mostly showed a linearly elastic behavior for the two cycles in Fig. 3.9.a. While for inclusion CMC-A, the behavior was different: an elastic response till 180 kN, then followed by a non-linear elastic one to 400 kN, ended by a plastic phase in Fig. 3.9.b. The difference could be explained by the soil heterogeneity.

As regards the numerical analysis, when the set of parameters given in Table 3.5 is used, the numerical single inclusion test behaves like the inclusion CMC-A (Fig. 3.9.b). The load-displacement relationship shows a linear response until the load reaches 180 kN, then followed by a nonlinear behavior. The final settlement is about 10.2 mm, which shows a difference of 7% compared to the site test on the inclusion CMC-A. The

cumulative footing displacements of two different unloading-reloading cycles in the numerical analysis are illustrated in Fig. 3.9 as well. The slopes of the unloading/reloading line of the numerical analysis are almost parallel to those of the experiment.

a)

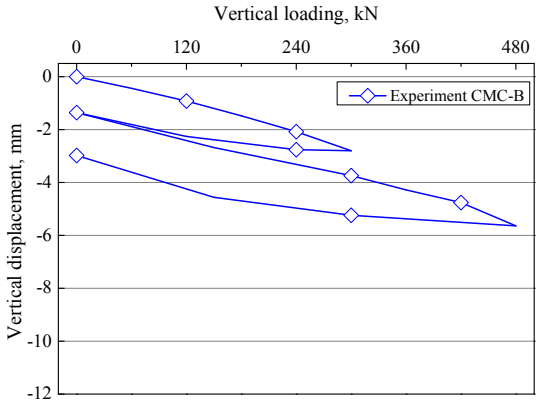

b)

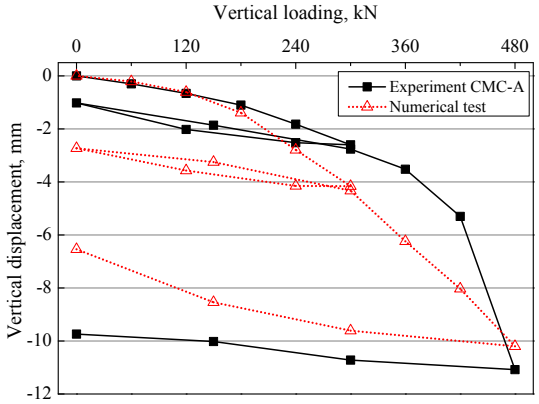

Fig. 3.9. Measured and numerical pile head displacement in the single pile tests: a) pile CMC-B; b) pile CMC-A

3.2.5.2. Vertical load tests on the unreinforced footing

To better understand the behavior of two shallow soil layers (fill and silty clay), the footing without inclusions (unreinforced footing) was tested. A relationship between the footing displacements and vertical loading is illustrated in Fig. 3.10. The displacement is linear until a vertical loading lower than 400 kN (Fig. 3.10.a), then it becomes non-linearly after, with a hyperbolic shape (Fig. 3.10.b). It finally reaches 55 mm. Concerning the unloading step, the stress-strain relations were not purely linear in the two load cycles. The unloading phase also does not return to coincide with the previous loading one, which results in a residual settlement. As can be seen from Fig.

3.10, the residual displacement obtained after the first load cycle was of only 1 mm (test 1A) while after the second loading cycle (test 2A) it reaches about 40 mm.

In comparison, the numerical curves indicate a linear behavior as the vertical loading is lower than 1200 kN. Then the load-displacement curve is over-predicted as a smaller load is applied to the footing, as in Fig. 3.10.a. However, an acceptable fitting between the numerical and the experimental data is figured out in Fig. 3.10.b. Additionally, the final raft displacement and the shape of the curve obtained from the numerical analysis are quite similar to those from the experimental test. The explanation can be that for small vertical forces on the raft, the pressure is carried by the fill layer. The MC model with a linear elastic manner cannot capture this behavior, which results in an over-estimation. Meanwhile, when the applied load is large enough, the soft soil modeled by the MCC constitutive model with a non-linear elasticity is mobilized, which leads to a good agreement with the experimental results in terms of final displacement and shape of the curve.

a)

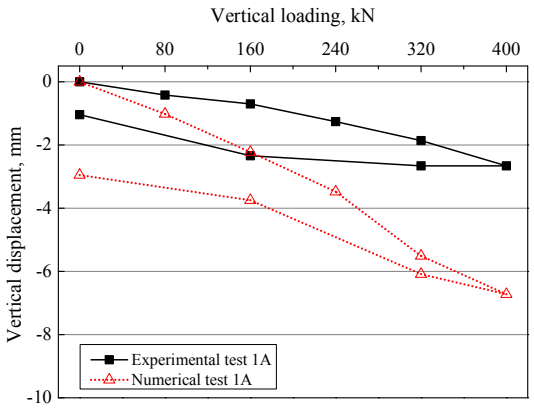

b)

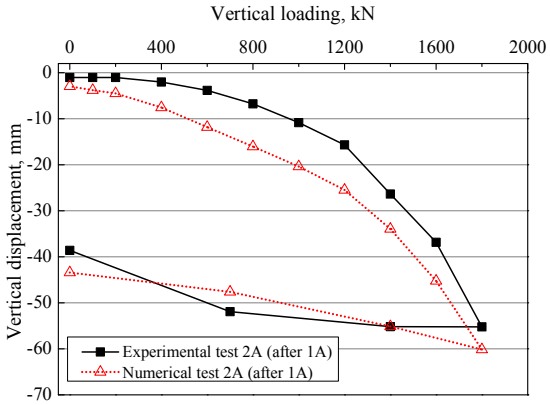

Fig. 3.10. Measured and numerical footing displacement – the case of the unreinforced footing: a) test 1A; b) test 2A

3.2.5.3. Centrally vertical loading test

In this part, the centered vertical load tests are presented for the footing directly over the rigid inclusion-reinforced soil (the reinforced footing). The results are shown in terms of pressure on inclusions and vertical footing displacements.

Three tests (1B, 4B, and 6B) were conducted on the same footing at different times. The vertical loading was subjected to the footing center. In each test, loading-unloading processes (the load cycles) were applied. The central footing displacement (D0) and the pressure cell WPC-1 on the inclusion CMC3 were monitored during the testing progress.

Pressure on the rigid inclusions

Fig. 3.11 shows the dependency of the pressure on the inclusion head on the vertical load applied to the footing. The pressure carried by inclusions increases linearly with the vertical force. In regard to the experimental curve in the test 1B, the pressure exerted on the inclusion CMC3 was about 800 kPa with a loading of 600 kN, it then increased to nearly 1400 kPa for a loading of 1000 kN. The pressure for a loading of 600 kN for the unloading process is equal to 1058 kPa. Its value is about 30% larger than the one obtained for the loading phase. This phenomenon could be justified by the soil shearing mechanisms which result in the dissipation of stress in the soils.

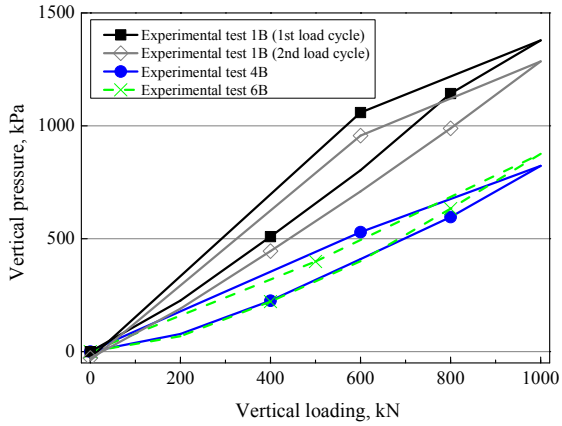

Fig. 3.11. Measured pressure on the top of the inclusion CMC3 during a few centrally vertical load cycles

After a few load cycles, the stress on the inclusion decreases significantly. It could be seen in the second load cycle of test 1B, the test 4B and the test 6B (Fig. 3.11). A pressure decrease onto CMC3 under several numbers of cyclic loadings at two loading levels was shown in Fig. 3.12. The pressure carried by CMC3 was reduced by half when comparing the tests 1B and 4B. The difference in the stress measured on the CMC3

between the first test and the fourth can be explained by the performance of the eccentric test 2B and 3B. Actually, the load of tests 2B and 3B has been applied to the CMC3 side. It produces an excessive settlement of CMC3 and CMC1. For the tests 4B and 6B, it seems that the slab transfers an upper load on CMC2 and CMC4. This new load transfer is perhaps due to the different level of the inclusion heads after the eccentric tests. CMC2 and CMC4 being less pushed in the soil.

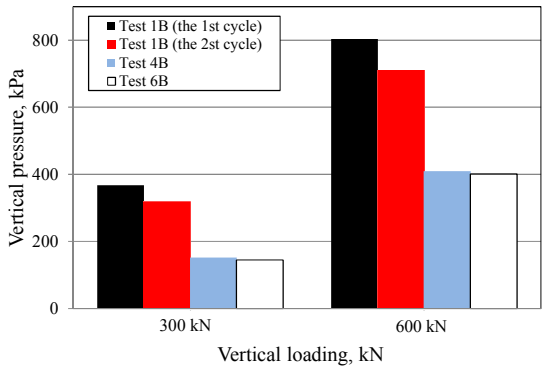

Fig. 3.12. Measured pressures on the top of the inclusion CMC3 at the load levels of 300 and 600 kN after several load cycles

Assuming that the full loading (weight of slab and vertical loading) is carried by four rigid inclusions, the pressure on the top of each one can be calculated. Fig. 3.13 compares the pressure exerted on the inclusion head by different methods. It can be seen that the numerical and measured data are in a fairly good agreement, and they are only a half of the theoretical results. The reason is that a part of the loading is carried by the subsoil. Fig. 3.14 shows the distribution of the vertical stress with the distance at the inclusion head plane at the vertical loading level of 600 kN. Due to the higher inclusion stiffness, the stress on the inclusion is 16 times as high as that on the soil (the inclusion head stress is about 990 kPa while the maximum soil stress is nearly 60 kPa). Due to the flexibility of the footing, the stress applied to the inclusion head is non-uniform. It can be seen more stress at the reinforcement edge than at the center. The stress at the inclusion head center equals 1000 kPa (like the pressure cell measures for the test 1B) while that at the edge of inclusion head is nearly twice as large (Fig. 3.14).

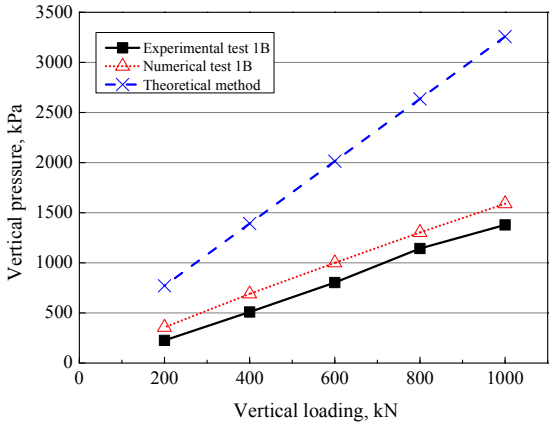

Fig. 3.13. A comparison of vertical stress on the top of inclusion by different methods

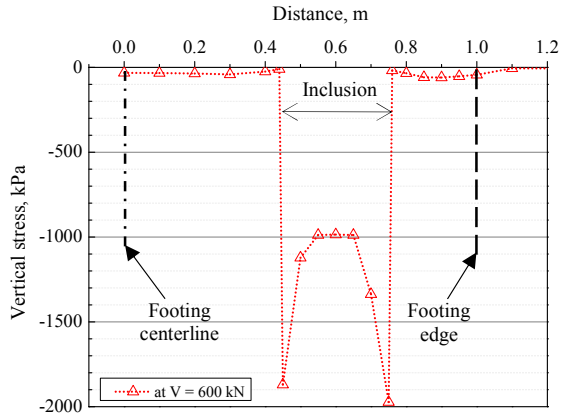

Fig. 3.14. Distribution of vertical stresses at the pile head plane at the vertical loading level of 600 kN

Similarly, the numerical results show a linear elastic behavior for the vertical loading-inclusion pressure relationship, as presented in Fig. 3.15. The difference between the simulating outputs and the experimental data in the loading phase is approximately equal to 10%. Using the MC model for the fill layer in the numerical analysis, the damping ratio evolution and the stiffness degradation are not considered, as the soil behaves elastically (Prisco and Wood 2012), which leads to an almost complete recovery during the unloading process.

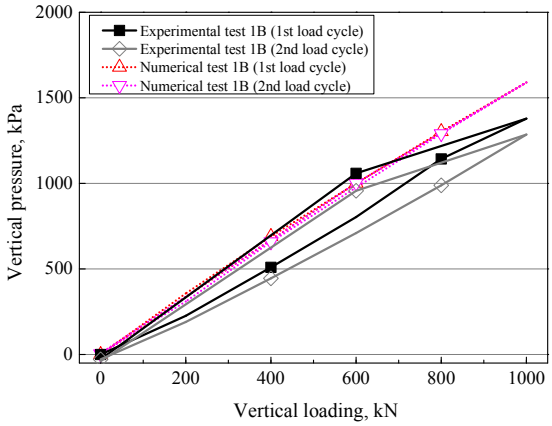

Fig. 3.15. Measured and numerical pressure on the top of the inclusion CMC3 in the test 1B

Footing displacement

The vertical displacement at the foundation center during the site tests was obtained based on the measurement of sensor D0. As can be seen in Figs. 16, the displacement for the reinforced case was about 5 mm for a load of 1000 kN, which is moreless a half of the one obtained for the unreinforced soil (Fig. 3.10). The footing settlement also shows a linear tendency with the vertical loading. Moreover, the cyclic loading results in an increase of the total settlements and a cumulative displacement. In the first cycle, the total settlement is about 5 mm for a loading of 1000 kN, and the cumulative one is equal to 2 mm. In the second cycle, the total settlement reaches 5.5 mm (an increase of 5%), and the settlement accumulation reaches 2.5 mm (a growth of 25%). Concerning the simulation results, they are in good concordance with the measured data for the loading phase (first cycle). However, since the constitutive model which is used for soils is too simple, the cumulative displacement could not be addressed under the numbers of cyclic loading, as illustrated in Fig. 3.16.

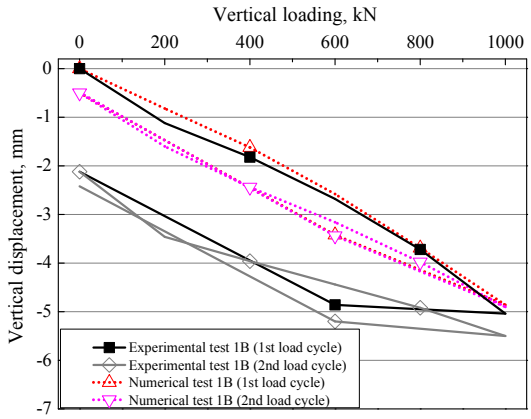

Fig. 3.16. Measured and numerical vertical displacement at the footing center during the test 1B

After each test, the displacement sensor was reset to zero. The results of test 4B and 6B are presented in Fig. 3.17. It is recognized that the cumulative displacement takes place during the cyclic loading, and the amount of the residual settlement decreases at each following cycle. The values for the residual settlement are respectively 2, 0.8 and 0.8 mm corresponding to test 1B, 4B and 6B. The residual settlement could cause an increase in the total settlement under the number of cyclic loadings.

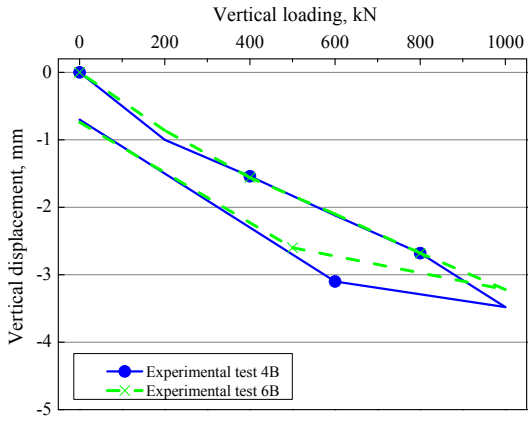

Fig. 3.17. Measured vertical displacement at the footing center during the tests 4B and 6B

3.2.5.4. Eccentric vertical loading test

In the literature, a few studies are focused on a footing over a rigid inclusion-reinforced soft soil subjected to an eccentric loading. Tests 2B and 3B were conducted and correspond to respectively eccentricities of 0.3 and 0.45 m.

Pressure on the rigid inclusions

The measured and computed pressures on the inclusion heads are compared in Figs. 3.18 and 3.19. The pressures on CMC3 obtained by the numerical analysis are in fairly good agreement with the experimental ones. The pressure on the inclusions seems to behave linearly with the loading on the footing. The eccentricity of the vertical loading also results in different vertical pressures on the inclusions, in which the inclusion in the weighted side (CMC3) suffers more pressure than on the lifted one (CMC4). The numerical outcomes figure out that the stress ratio on CMC3 to the stress on CMC4 is about 1.5 times in the test 2B while it was about 2.5 times in the test 3B. In addition, the larger the eccentricity, the higher the pressure on CMC3 and the lower the stress on CMC4. Evidently, as the eccentricity becomes larger the pressure on the inclusion CMC3 shows an increase, as presented in Fig. 3.20. The pressure in the case of an eccentricity equal to 0.4 m is nearly twice the one of the centered loading case.

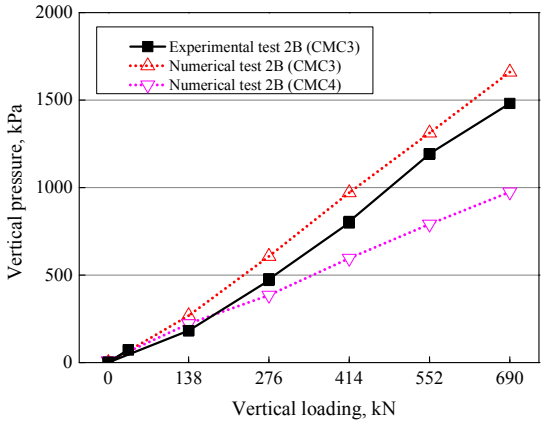

Fig. 3.18. Measured and numerical pressure on the top of the inclusions during the test 2B (with an eccentricity of 0.3 m)

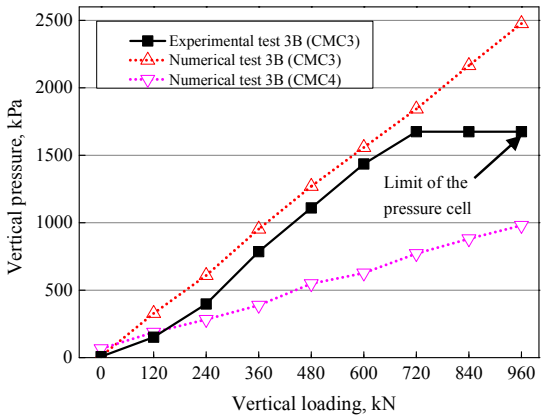

Fig. 3.19. Measured and numerical pressure on the top of the inclusions during the test 3B (with an eccentricity of 0.45 m)

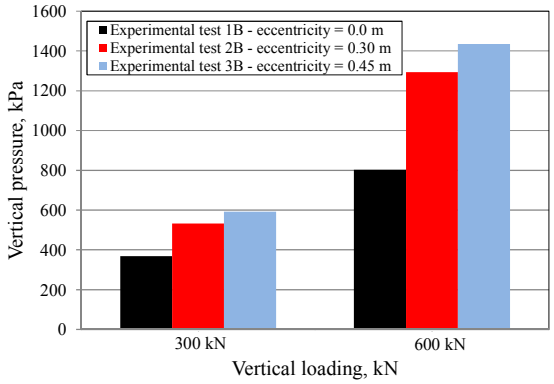

Fig. 3.20. Measured pressure on the top of the inclusion CMC3 at the load levels of 300 and 600 kN with different eccentricities

Footing displacement

Fig. 3.21 shows the measured and numerical results of the displacement at the footing

center for two different loading-unloading cycles (test 2B). Experimental and modeling results are generally consistent with each other. The obtained settlements were small, they were below 2 mm at the end of each loading phase. The relation between the load and the displacement is nearly linear during the loading processes while it is non-linear in the unloading phase. Nevertheless, the residual settlement seems to be insignificant in both the numerical analysis and the real-scale test. It might be due to the vertical load exerted on the slab top. It was insufficient to cause the plasticity of soils. A fairly good agreement between the numerical and experimental results in terms of settlement values and shape of the curves is presented in Fig. 3.22. Similarly to test 2B, the load-displacement relationship shows a linear behavior (1.5 mm displacement) as the load is lower than 600 kN. It is then followed by a non-linear one. The residual settlement after each load cycle is very small after the first cycle while it is equal to 1 mm after the following cycle.

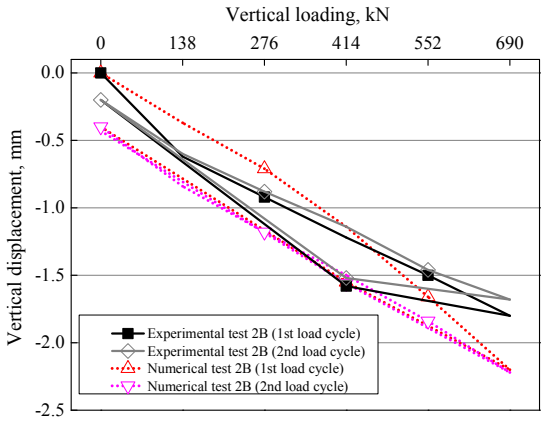

Fig. 3.21. Measured and numerical vertical displacement at the footing center during the test 2B (with an eccentricity of 0.3 m)

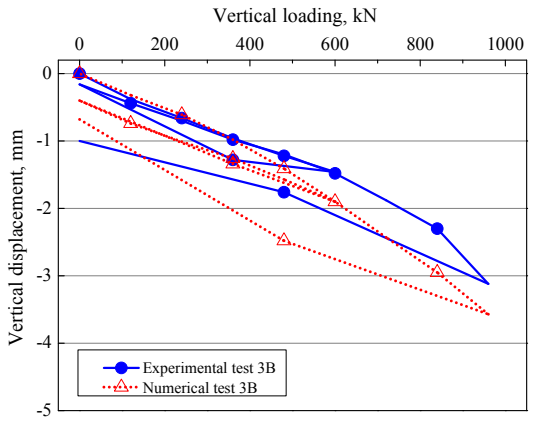

Fig. 3.22. Measured and numerical vertical displacement at the footing center during the test 3B (with an eccentricity of 0.45 m)

3.2.5.5. Horizontal loading on the reinforced footing

After finishing the test 4B, two horizontal loading tests 1C and 2C were performed on the reinforced footing. As presented in Table 3.4, for the test 1C, a vertical load of 600 kN was first applied. After that, it was kept constant. The horizontal load was then subjected to two cycles (0 $\rightarrow$ 120 kN $\rightarrow$ 0). For the test 2C, a vertical force of 1000 kN and a cycle of horizontal loading of 200 kN were exerted on the raft.

Pressure on the rigid inclusions

The pressure measured on the top of the inclusion CMC3 is shown in Fig. 3.23. An increase in the horizontal load induces an increase of the vertical stress on the rigid inclusion. With regard to the test 1C, the measured pressure was 386, 437 and 514 kPa corresponding respectively to horizontal loads of 0, 60 and 120 kN. Concerning the test 2C, the obtained pressure on CMC3 was about 923, 1034 and 1410 kPa as the horizontal loading was respectively equal to 0, 100 and 200 kN. For the calculation of the inclusion vertical stress, the horizontal loading cannot be neglected.

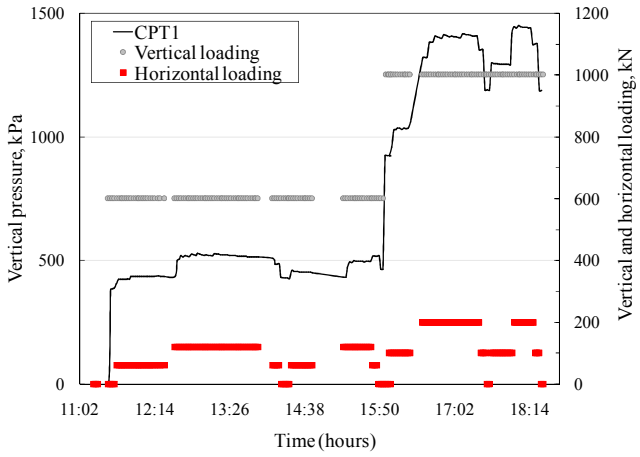

Fig. 3.23. Measured pressure on the top of the inclusion CMC3 during the tests 1C and 2C

Lateral displacement of footing

The measured and calculated data of the lateral displacement of the footing for the tests 1C and 2C is presented in Fig. 3.24. The obtained numerical outcomes are in good accordance with the experimental ones. It is obviously seen that when the horizontal loading is relatively small, the lateral displacement is also small, e.g. the measured displacement was only 0.3 mm with a loading of 60 kN. The shear stress could not overcome the friction resistance between the footing and the soil. As a significant horizontal loading was applied, the horizontal movement increased significantly. The lateral displacement obtained was respectively equal to 5.5 and 14 mm for horizontal forces of 120 and 200 kN. For the unloading progress, the high vertical stress on soil

results in a large friction resistance, which prevents the footing from coming back to its initial position. The residual lateral settlement was respectively measured to be equal to 3 and 7 mm after the tests 1C and 2C.

a)

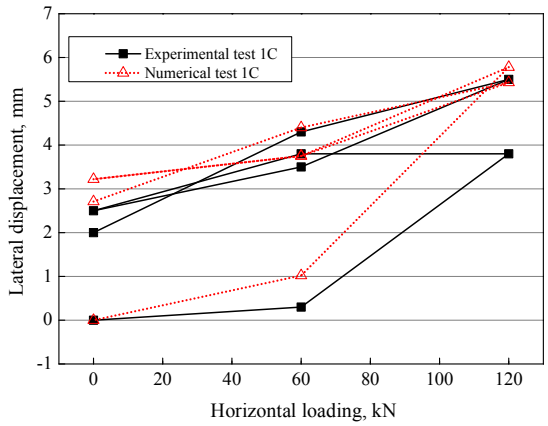

b)

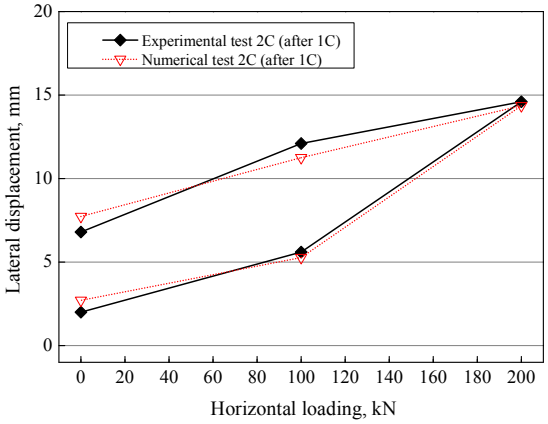

Fig. 3.24. Measured and numerical lateral displacement at the footing center during the horizontal loading tests: a) test 1C; b) test 2C

Lateral displacement of rigid inclusions

The lateral displacement of the inclusions is calculated based on the clinometer measurements using the equation, $h = L.\sin\alpha$ (herein L is the inclusion length, α is the angle of inclination). The angle of inclination during the tests is presented in Fig. 3.25. The lateral displacements of respectively the inclusions CMC1 and CMC2 were also obtained from the measurements of d1 and d3, as illustrated in Fig. 3.26. As the horizontal load was equal to 200 kN, the measured horizontal displacement by both clinometer and d1 and d3 sensors is equal to 5 mm. It is smaller than the footing displacement, which is different from the piled raft foundation (the pile cap displacement is similar to the footing one). It is due to the non-rigid connection

between the inclusions and the footing.

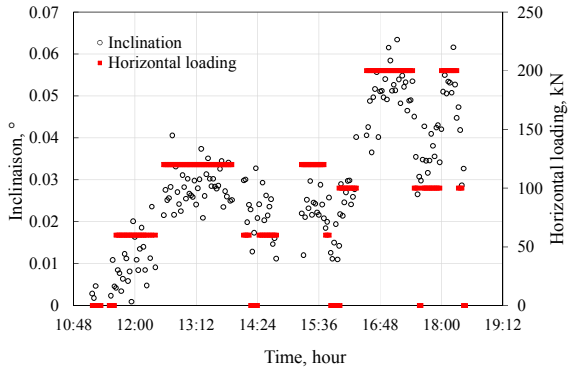

Fig. 3.25. Measured inclination of the borehole during the test 1C and 2C

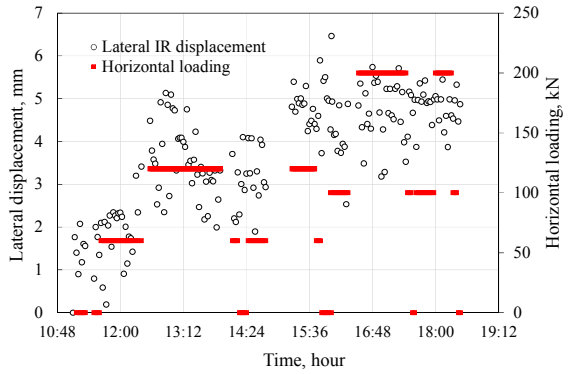

Fig. 3.26. Measured lateral displacement of the inclusions CMC1 and CMC2 during the test 1C and 2C

3.2.6. Conclusions

An investigation on the single rigid inclusions and the footing over unreinforced soils subjected to vertical loadings and the footing on reinforced soft soil under complex loading cases under real scale is presented. In this part, both experimental and numerical approaches were performed. The results permit to highlight the following points.

Two single rigid inclusion tests and footings over unreinforced ground allow to better understand the behavior of a multi-layered soil. Meanwhile, the tests on single rigid inclusions illustrate the response of the chalk layer. The on-site tests on the unreinforced footing show the behavior of the shallow soil layers. They have been employed for the calibration of the parameters for the numerical approach.

The efficiency of the rigid inclusion-improved soft soil technique shows that the stress on the inclusion is significantly higher than the one on the soft soil. The pressure on the inclusion increases linearly with the vertical loading. The eccentricity of the vertical

loading also originates a difference in the vertical pressure on the inclusions. Moreover, the larger the eccentricity, the higher the pressure on the weighted side (CMC3) and the lower the stress on the lifted side (CMC4). In addition, when comparing the measured results of the tests 1B, 4B and 6B for two load levels, a decrease in the stress acting on inclusions under a number of cyclic loading is found. An increase of the horizontal loading leads to an increase of the vertical stress on the inclusions.

In terms of displacements, the presence of inclusions inside a soft soil halves the vertical displacement as compared to the unreinforced footing case. When the loading on the footing is relatively small (test 2B), the behavior of the system seems to behave in a linearly elastic way, which results in small footing displacements and in an insignificant cumulative settlement after the load cycles. In contrast, as the vertical loading is large enough (over 700 kN), a significant footing displacement is monitored and the accumulation of settlements under the cyclic loading can be seen. The difference in lateral displacements between the footing and inclusions is due to a non-rigid connection between the footing and inclusions.

The used numerical approach permits to design single rigid inclusions, unreinforced and reinforced footings under vertical and complex loadings efficiently and economically. The numerical results are in fairly good agreement with the experimental data during the loading progress. However, the numerical outcomes are sometimes under-estimated for the unloading-reloading process. It might be due to the fact that the constitutive models which were adopted for soils were too simple and cannot account for the soil behavior under cycles.

3.3. 3D Numerical modeling of foundation solutions for wind turbines

3.3.1. Introduction

A 3D numerical modeling of wind tower foundations subjected to realistic static loadings is studied. The case of a shallow foundation and a piled case are investigated. The rigid inclusions case, for which not many former investigations were performed, is also considered. Additionally, a parametric study is done to evaluate the influence of the mattress constitutive model, of the loading cases (from purely vertical to vertical loading combined with overturning moments) and of the vertical reinforcement density. Three foundations types (shallow foundation, piled raft, and rigid inclusions) are then compared in terms of ground settlement, axial force and moment on piles. Based on the results obtained, some basic recommendations are given regarding the design optimization of wind turbines foundations.

3.3.2. Related works

Wind turbines (WT) constitute a very specific type of structure which strongly depends on the efficiency of the foundation system. Such dependency is a consequence of the extremely high levels of eccentricity generated at the base of the turbine shaft, which in turn results from the uncommon combination of high flexural moments and relatively low vertical forces. However, due to the increasing popularity of this type of alternative energy production, it is becoming increasingly common to meet poor geotechnical conditions at the sites where wind turbines are planned to be installed, and thus the use of spread foundations on unreinforced soil is either uneconomical (excessively large diameter) or just technically impossible (when design standards do not acknowledge the installation of direct foundations on the particular type of soil present at the base of the raft).

The foundation of the wind turbine allows the whole system to operate safely and stably under the vertical body load and the overturning moment due to winds, waves, and earthquakes. The types of foundation used for offshore turbines include large-diameter single pile, pile group, tripod, jacket, gravity base, bucket, floating, etc (Byrne and Houlsby, 2006). Piled raft has been widely used in wind turbine projects because it can effectively decrease the size of the foundation as well as the construction cost (Lang et al., 2015). Furthermore, it has been useful for developing theoretical and numerical methods to study pile group foundations subjected to complex loading (Byrne and Houlsby, 2003; Soldo et al., 2005; Matutano et al., 2014). Based on a simply piled raft modeled using the finite element method, Ciopec et al. (2013) developed a

more detailed understanding of the behavior of WT foundation. They concluded that it was necessary to continue their research to take into account the number, distribution, length and diameter of the piles. Catană et al., (2013) studied the soil-structure interaction of the piled raft by estimating three types of soil-structure interactions. The comparison between the three cases in terms of displacements, forces and reinforcement proved that the soil-structure model had an important effect on the final reinforcement, considering that the difference between methods reached almost 18%. The experimental studies and numerical simulations were established by Lang et al., (2015) to investigate the mechanism of four different types of pile group foundation. It was concluded that the combination of vertical piles and batter piles could increase the bearing capacity and decrease the construction cost. Nevertheless, there is less investigation on large-scale models, which is especially important to establish the real working conditions of WT.

Although the technique of soft soil improvement by rigid inclusions has a wide range of application in geotechnical engineering, its application in the foundation of wind towers, a type of structure which transmits a heavily eccentric load to the foundation layers, has not been tested yet, at least to the best of our knowledge.

3.3.3. Case study

A wind turbine is a structure with an extremely high slenderness ratio, where a complex cyclic loading is applied. Brendan et al., (2009) showed that the average tower height has gradually increased in recent decades, from 60 m to more than 90 m, and it is now capable to generate more than 3MW of electricity. Additionally, the tendency for increasing the height of the towers continues, and a maximum value of 125 m is expected soon, which will help to increase the electricity production up to 6MW.

3.3.3.1. Studied case

The wind turbine considered in this study is 100 m high and generates 3MW of energy (Fig. 3.27.a). The considered area is located on the relatively flat area of the Sieradz city, Lodz Province, in central Poland. A core drilling permitted to define the geological layers of the site. The soil profile from the boring logs included a soft soil layer with a thickness of 10 m overlying a bedrock stratum. Based on laboratory results, the physical properties of the soft clay layer were determined such as the water content (w) equals 12.3%, the saturation ratio (S) equals 0.82, and the soil particle density of 2.60. The initial void ratio (e_o) is equal to 0.39 and the soft clay was heavily over-consolidated. The groundwater level is assumed to be located at the top of the

compressible soil layer (worst-case scenario). The wind turbine foundation is a concrete slab of circular shape, with a varying thickness between 2.9 m (at the center) and 1.0 m (at the perimeter) and 18.2 m in diameter (Fig. 3.27.b).

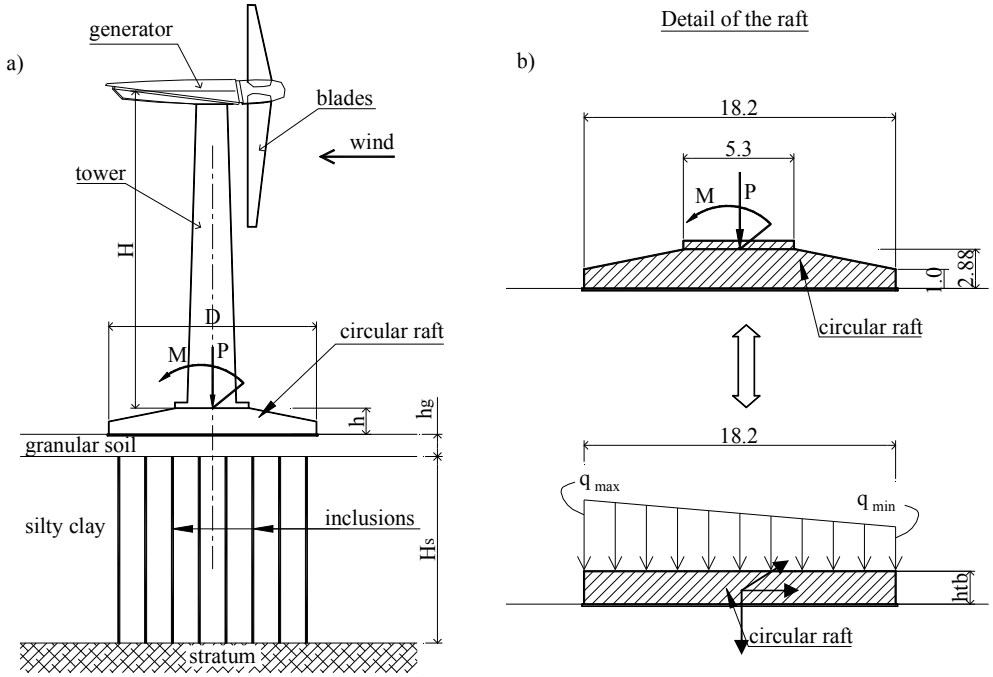

Fig. 3.27. Overview of the wind turbine: a) Elevation of the wind turbine; b) Detail of the raft

3.3.3.2. Vertical soil reinforcement

Four options for the foundation are investigated, all of them including a shallow foundation, with and without improvement of the soil underneath. In the first option (Fig. 3.28.a), the raft foundation is directly installed at the surface of the original soft soil. The second option consists of the raft foundation installed on a mattress, but without reinforcement (Fig. 3.28.b). In the third option (Fig. 3.28.c), the original soft soil is improved by rigid inclusions (RI), with 0.4 m in diameter, and an overlying 0.5 m thick sand mattress was installed on top of the RI, thus acting as the raft foundation. Finally, a piled raft was modeled (Fig. 3.28.d), with the piles having the same structural properties of the rigid inclusions. The difference between the two reinforcing systems is basically the type of connection between the reinforcements and the raft, which is non-existent in the first case and absolutely rigid in the second case.

The vertical columns (cases 3 and 4) are assumed to be installed through the whole soft clay layer, ranging from -0.5 m down to the stratum (the RI option) and zero to stratum (the piled raft case). Due to the fact that these columns are often bored piles, the excavation process was not simulated. Three different densities of vertical

reinforcement were studied (50, 100 and 150 reinforcements), resulting in area improvement ratios (reinforcement/soil area) of 2.4%, 4.8% and 7.2%, respectively. For each case, the vertical columns were uniformly distributed (Fig. 3.29).

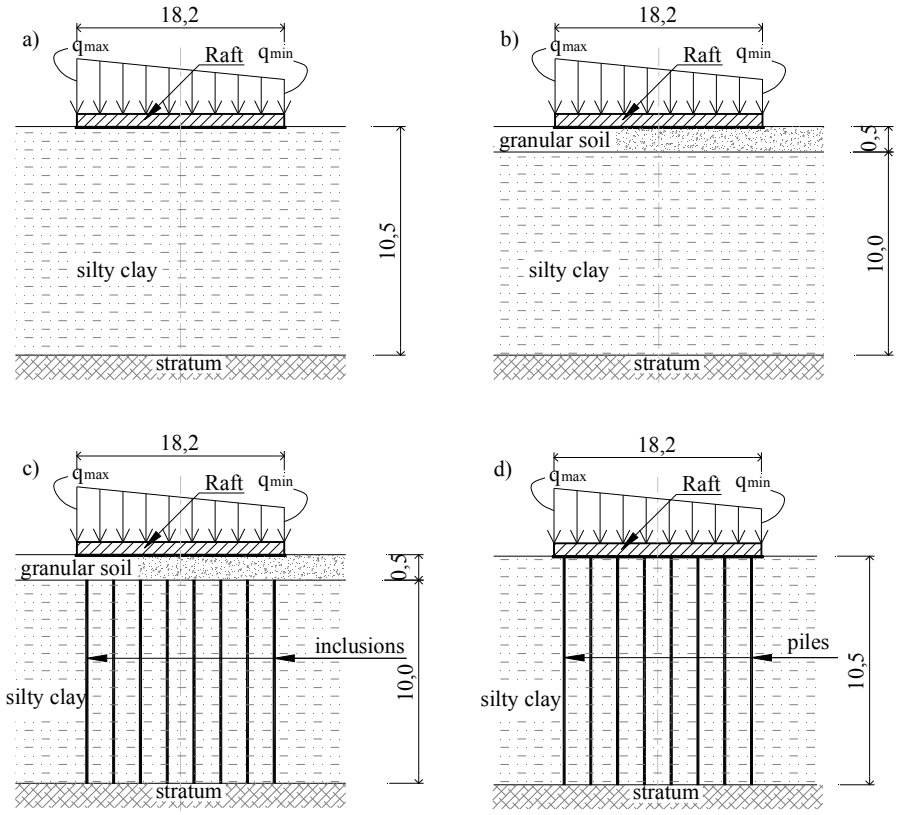

Fig. 3.28. Case studies: a) only raft foundation - reference case; b) raft foundation with mattress; c) RI-raft foundation; d) piled raft foundation (no scale)

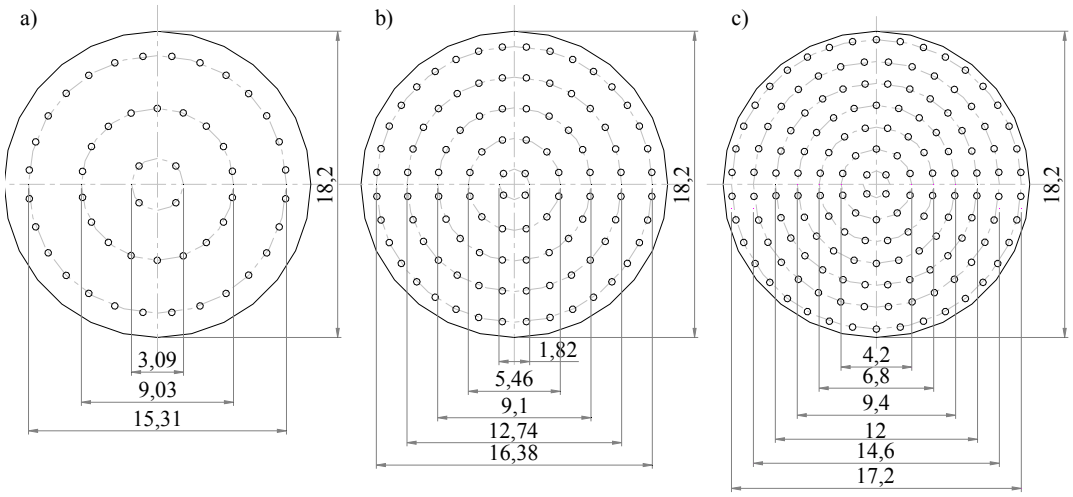

Fig. 3.29. Distribution of the vertical reinforcements under the raft: a) 50; b) 100; c) 150

3.3.3.3. Loading applied

In the study, the dynamic action associated with both the wind and the rotating blades was not considered. Instead, it was substituted by an equivalent static load (DLC1.0 Lift-off). The considered static loading is defined as a severe loading condition, which covers more than 99% of the production time of the wind turbine (C.F.M.S, 2011).

Such load is responsible for an overturning moment of 46 MN·m applied on the gravity center of the raft. In addition, the loading conditions include a vertical static load of around 29.4 MN, also acting on the gravity center of the raft, which is due to the self-weight of the turbine. These loads were given by the wind turbine producer and used in the geotechnical design. Several loading combinations were considered in order to simulate different real-case situations. In all of these cases, the vertical loading is taken into account. The difference between these different loading cases is the overturning moment, which ranges between 0% and 100%. A routine was defined to convert these loads (vertical and moment) to linear vertical pressure values acting on the raft (see Fig. 3.27). The calculation equation was presented by Mirza and Brant (2009), as in Equation 3.1:

$$q_{\max/\min} = \frac{P}{A} \pm \frac{M_y}{W_y} x \tag{3.1}$$

Where: P is the Vertical loading (N), A is the area of the raft foundation (m^2), M_y is the y-axis overturning moment (N·m), W_y is the y-axis bending resistance moment (m^3), D is the diameter of the raft foundation (m), x is the distance in the x-axis direction (m).

The different loading cases are shown in Table 3.6.

Table 3.6. Studied loading cases

Loading case	case 0 (purely vertical)	case 1 (vertical + 20% moment)	case 2 (vertical + 40% moment)	case 3 (vertical + 60% moment)	case 4 vertical + 80% moment)	case 5 (vertical + 100% moment)
Vertical loading, P (MN)	29.379	29.379	29.379	29.379	29.379	29.379
Overturning moment, M (MN·m)	0	9.192	18.384	27.576	36.768	45.96
Minimum vertical pressure, q_{min} (MPa)	0.1129	0.0977	0.0824	0.0672	0.0519	0.0367
Maximum vertical pressure, q_{max} (MPa)	0.1129	0.1282	0.1434	0.1587	0.1739	0.1892

Remarks: the plus sign convention (+) is adopted for vertical compressive pressures

3.3.4. Numerical model

3.3.4.1. Mesh and Boundary Conditions

Three-dimensional numerical calculations, using the explicit finite-difference program FLAC^{3D}, were conducted to analyze the behavior of the systems presented before. Owing to the complexity of the problem, FISH language embedded into FLAC^{3D} was used to generate the mesh of soil mass, the vertical columns, and the raft. Due to axisymmetric conditions, only half of the global model was considered. Fig. 3.30 presents the mesh used in the analysis of 25 rigid inclusions (approximately 140.000 zones for the soil mass, inclusions, and the raft; 300 beam elements for 25 inclusions).

The vertical reinforcements (piles or rigid inclusions) were considered using volumetric zones. 12 beam structural elements were inserted at the axis of the vertical reinforcements to easily obtain the efforts inside them. The global inertia and stiffness are presented hereafter.

The compressible soil was founded on a perfectly rigid layer - which justified the option to block the lower horizontal boundary nodes in all directions. A 0.5 m layer simulated the granular soil (mattress) overlying the soft ground.

The horizontal length of the mesh was 100 m, which was more than ten times the radius of the raft. The boundaries were fixed far from the raft foundation (more less 100 m around) to avoid boundary effects. Only half of the model was discretized in the Y direction and the displacements were blocked in the normal directions of the vertical planes to model the symmetry of the problem. The bottom boundary (at the z = -10.5 m plane) was set to zero in the x, y, and z directions to model the bedrock. All calculations were carried out considering drained conditions.

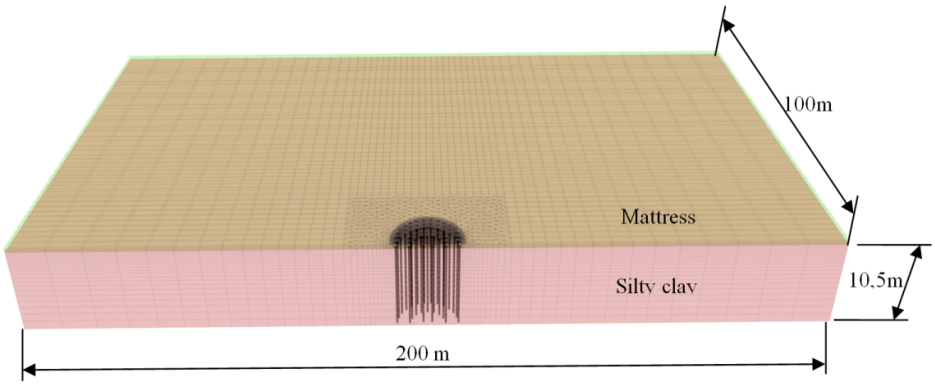

Fig. 3.30. Mesh adopted for the study (25 rigid inclusions)

3.3.4.2. Constitutive models and parameters

Mattress

The mattress layer is usually built using a type of granular soil. To simulate the behavior of this mattress, the two constitutive models with different levels of

complexity were used. The first one was the elastic linear perfectly plastic model with the shear failure criteria of Mohr Coulomb's type (MC). The second constitutive model used, necessarily more sophisticated, was the Cap-Yield (CYsoil) model. In this study, the values of the geotechnical parameters of the mattress were adopted based on the research of Croce (2011) and Do et al. (2013). The results are presented in Table 3.7.

Compressible soil

The silty soil employed in these analyses was sampled in the project. The oedometric tests were performed to determine the geomechanical parameters of the soft clay. The MCC parameters used for the following study are shown in Table 3.8.

Table 3.7. Geotechnical parameters of the mattress layer

MC model*	Value	CYsoil model**	Value
E (Young's modulus) (MPa)	150	G^e_{ref} (reference elastic tangent shear modulus) (MPa)	58
ν (Poisson's ratio)	0.3	G^e (elastic tangent shear modulus) (MPa)	98
ϕ (friction angle) (°)	37	K^e (elastic tangent bulk modulus) (MPa)	213
γ (dilatancy angle) (°)	0	p^{ref} (reference effective pressure) (kPa)	100
c (cohesion) (kPa)	0	R_f (failure ratio)	0.9
K_0 (earth pressure coefficient at-rest)	0.5	ϕ_f (ultimate friction angle) (°)	37
		β (calibration factor)	2.35

* Obtained from Croce (2011) ** Obtained from Do et al (2013)

Table 3.8. Modified Cam Clay model parameters for the silty clay soil

Slope of the normal consolidation line, λ	Slope of the elastic swelling line, κ	Friction constant M	Specific volume at a reference pressure, v_λ (kPa)	Pre-consolidation pressure, p_{c0} (kPa)
0.106	0.030	0.888	1.497	1750

Rigid inclusion/pile and raft properties

The vertical reinforcements (inclusions/piles) and the raft are made of concrete. The isotropic linear elastic constitutive model was used to simulate this material, which requires the definition of Young's modulus (E = 24 GPa), the Poisson's ratio (ν = 0.20) and the unit weight (γ = 25 kN/m^3).

Interfaces

Based on the FLAC3D manual (Itasca, 2009), to avoid penetration of the interfaces, a normal and shear stiffness of 10^8 kN/m/m were taken. The Mohr-Coulomb shear failure criterion for the sliding effect was managed by the cohesion of zero, and the friction angle of 22.3°. The last value corresponds to the two-thirds value of the soft clay friction angle as used in Jenck et al. (2007). Physically, it permits to consider a

degradation of the contact soil/pile due to the pile setup.

3.3.4.3. Parametric study

To assess the effect of every variable related to the foundations studied, the following parametric studies were given:

- Constitutive models of the mattress;
- Foundation solutions: raft, raft with mattress; raft improved by inclusions and piled raft;
- Loading cases: only vertical loading; and vertical loading combined with the different values of the overturning moment;
- The density of the vertical reinforcement.

In order to establish a threshold, the reference case to be studied was the raft directly over the compressible soil and was subjected to several loading cases. The efficiency of the soil improvement is then evaluated, by direct comparison of the total and differential settlements of the soil foundation; the axial force and bending moment on the reinforcements. Finally, the effect of the number of inclusions/piles was also studied, also based on the surface settlements and on the axial force and bending moment of the vertical reinforcements.

3.3.5. Numerical analysis results

3.3.5.1. Reference case

The reference case consists of the raft installed directly on the unreinforced compressible soil. The system is initially loaded by the vertical loading, and moment increments of 20% are then sequentially applied to the raft.

Fig. 3.31 provides the settlement of the soil mass below the raft. The central settlement seems to remain constant while the differential settlement of the raft increases with each moment increment. In addition, the settlement significantly decreases away from the edge of the foundation, up to a point where it can be considered negligible (at a distance of 20 m from the center).

For the vertical loading, due to the flexibility of the concrete raft, the settlement at the center of the foundation was slightly higher than that at the perimeter, 283 mm compared to 270 mm. For the complex loadings, the settlement at the center practically remained constant, while the maximum settlement at the perimeter increased to 309 and 367 mm with 40% and 100% of the total moment applied,

respectively. Furthermore, the differential settlement increased to approximately 200 mm when the total moment was applied (Fig. 3.32).

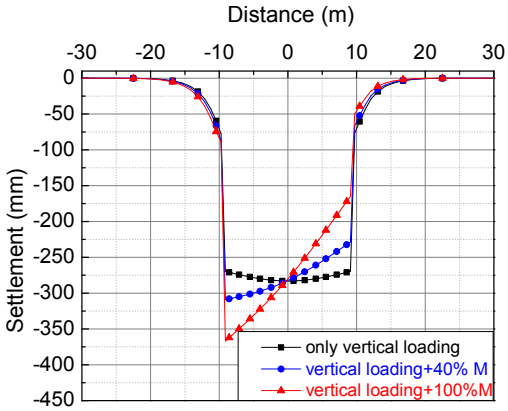

Fig. 3.31. Surface settlements (reference case)

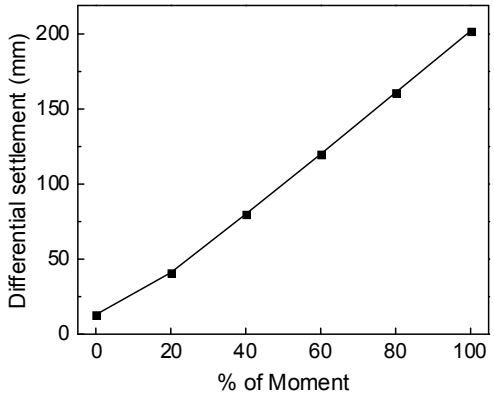

Fig. 3.32. Differential settlements (reference case)

3.3.5.2. Influence of the mattress

The next model to be studied consists of a 0.5-m-thick mattress on the non-improved soil (Fig. 3.28.b). Firstly, the mattress was simulated using the CYsoil model. Based on the results of two oedometric tests, the initial cap pressure parameter value (p_c) was determined to be equal to 500 kPa.

As it is not common to have the results of oedometric tests for granular materials, a study on the influence of the initial cap pressure parameter (p_c) on the maximum settlement (Fig. 3.33) was done. The increase in the settlement is very significant when the value of the initial cap pressure is less than 200kPa. For higher p_c values, the settlement remained approximately constant. It is due to the fact that the parameter p_c defines the cap softening/hardening behavior of the soil. The soil response is nonlinear elasticity until the stress state of the soil reaches the yield surface, then soil

behaves in a plastic manner.

In all the following calculations with the CY constitutive model, a value of 500 kPa for the initial cap pressure parameter value (p_c) is considered.

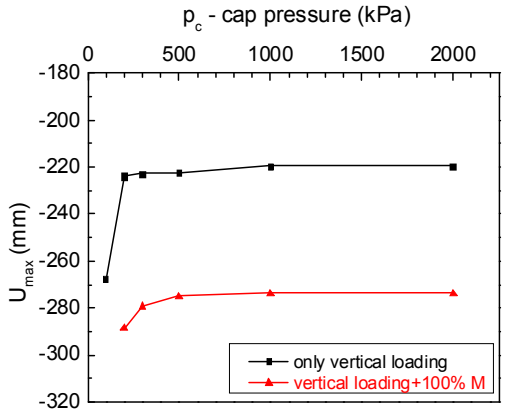

Fig. 3.33. Influence of cap pressure of CYsoil model on the maximum settlement (mattress case)

The MC constitutive model was then used to simulate the behavior of the mattress. The mattress behavior was very similar for each of the models considered (MC and CY), which can be concluded from the similarity between the respective settlements (Fig. 3.34). The maximum surface displacement was approximately 220 mm for the vertical loading and reached 274 mm when the full moment load was applied. The stress paths of some points inside the mattress were also investigated (Fig. 3.35.a), again showing a rather similar tendency between the MC and CY constitutive models. Fig. 3.35 (b, c, d) shows that the full stress paths considered were under the failure envelope and the initial yielding surface in the (p',q) plane, which could be related to the nonlinear elastic behavior of the mattress under the current stress state levels.

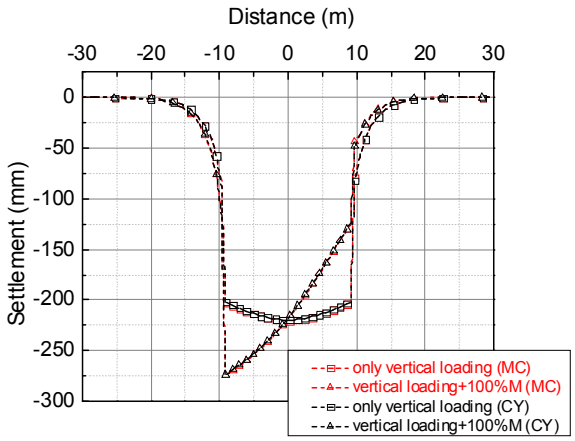

Fig. 3.34. Surface settlements of the mattress case (MC and CYsoil model)

a)

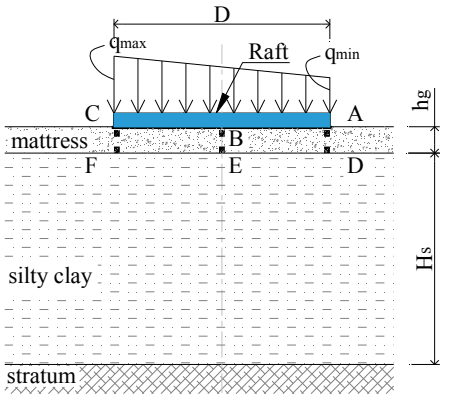
D
qmax
Raft
qmin
C
A
hg
mattress
B
F
E
D
silty clay
Hs
stratum

b)

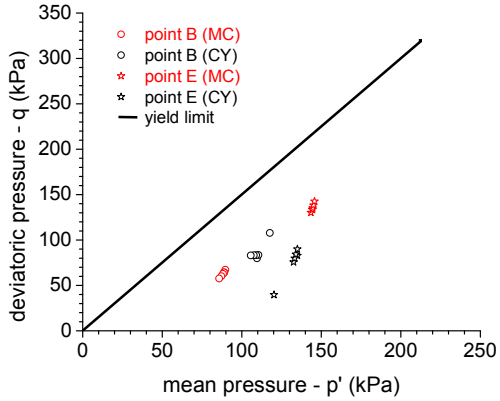
point B (MC)
point B (CY)
point E (MC)
point E (CY)
yield limit
deviatoric pressure - q (kPa)
mean pressure - p' (kPa)
0
50
100
150
200
250
300
350

c)

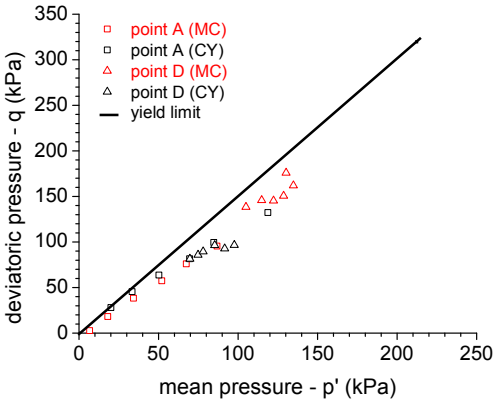
point A (MC)
point A (CY)
point D (MC)
point D (CY)
yield limit
deviatoric pressure - q (kPa)
mean pressure - p' (kPa)
0
50
100
150
200
250
300
350

d)

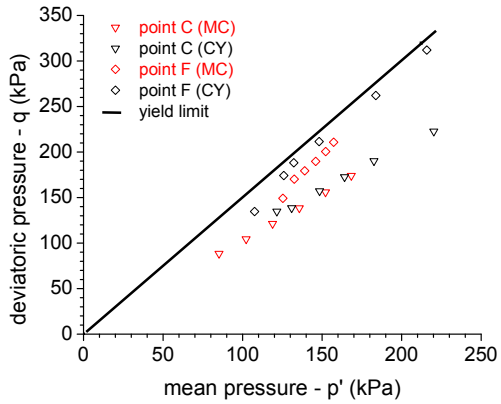

Fig. 3.35. Stress path of the points inside the mattress: a) Visualised points inside the mattress b) Stress path of points B, E; c) Stress path of points A, D; d) Stress path of points C, F

The surface settlements shown in Table 3.9, corresponding to each loading case for the two constitutive models, reveal that the constitutive model of the mattress had no significant influence on the overall performance of the structure. The comparison between the reference case and the mattress cases was also presented. The presence of the mattress resulted in a significant settlement reduction (between 22 to 25%), which was assumed to be due to the higher stiffness of the mattress when compared to the compressible soil.

The raft rotation is also presented and is equal to the ratio of the raft differential settlement to the foundation width. Under combined loadings, the raft rotation increases as the moment increases, as shown in Table 3.9. The use of a mattress induces a decrease of 25% of the raft rotation when compared to the reference case. Therefore, the role of the mattress can be thus considered as an important component, and must not be neglected.

Table 3.9. The surface settlement and raft rotation of reference case and mattress cases for the defined loading combinations

Foundation solutions	Loading cases					
	V+0%*M*	*V*+20%*M*	*V*+40%*M*	*V*+60%*M*	*V*+80%*M*	*V*+100%*M*
Raft on existing ground						
Surface settlement (mm)	283	290	309	328	348	367
Raft Rotation (^{o})	0.000	0.128	0.253	0.379	0.506	0.635
Raft on mattress (MC model)						
Surface settlement (mm)	220	220	231	245	260	274
Raft Rotation (^{o})	0.000	0.088	0.181	0.276	0.372	0.469
Raft on mattress (CYsoil model)						2
Surface settlement (mm)	220	220	230	245	259	74
Raft Rotation (^{o})	0.000	0.088	0.182	0.277	0.374	0.471

Studying the constitutive model's influence, Do et al. (2013) concluded that the CYsoil model is able to consider the real soil behavior under static loading. Therefore, the mattress is simulated using the CYsoil model in the following steps of numerical analysis in this study.

3.3.5.3. Improvement of the foundation soil with 50 rigid inclusions

The improvement of the soil foundation beneath the raft with 50 inclusions was analyzed in this section in terms of ground settlement, axial force and bending moment acting on the inclusions.

Settlements

Figs. 3.31 and 36 illustrate the total surface settlements of the unreinforced and rigid inclusion-reinforced soft soil cases. For the uniform load case, the maximum settlement with improvement was only one-quarter of the one without improvement, being 65 mm compared to 280 mm. When 100% of the overturning moment is added, the total settlement with rigid-improved case increases to 90 mm, but it was only one-fourth of the unreinforced value. This result is in good agreement with the results of Jenck et al. (2007), in which the reduction in the total settlement was about 5 times.

Fig. 3.37 compares the differential settlements between the improved and the unreinforced cases. The different settlement of the improved case decreases by 7 times compared to the one of the unreinforced one when the overturning moment is considered at 40%. The soft soil improvement by rigid inclusions is significant induces a reduction of the total and the differential settlements as confirmed by Hewlett and Randolph (1988) and Han and Gabr, (2002).

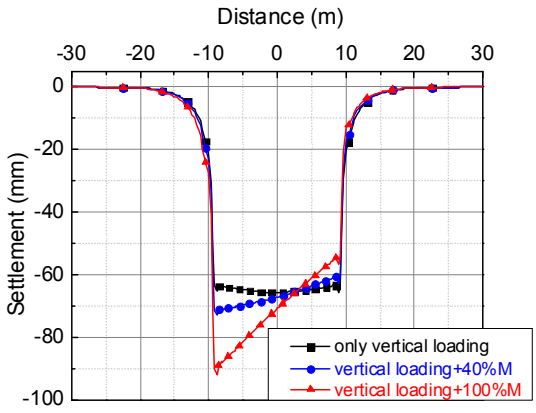

Fig. 3.36. Surface settlements (50 inclusions)

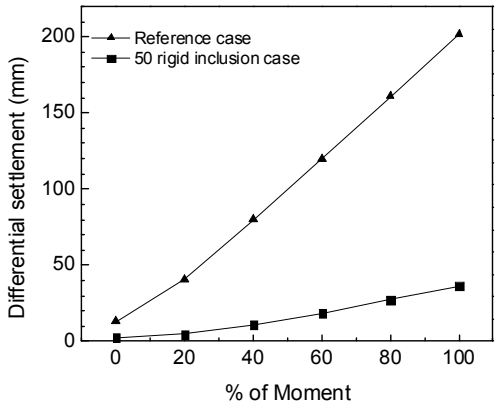

Fig. 3.37. Differential settlements in comparison (reference and 50 rigid inclusion cases)

Axial forces

Due to the presence of a load transfer platform where arching mechanisms can occur, a large part of the loading is transferred to the rigid inclusions. In this study, the stress efficacy value was found equal to 54%, which is good agreement with the results obtained by Hewlett and Randolph (1988), in which the efficacy of pile support was estimated to be equal to 0.50.

The influence of the distance (along the x-axis) on the axial force at the inclusion top is illustrated in Fig. 3.38. For purely vertical loading, the distribution of the vertical force on the inclusions was relatively uniform. The forces fluctuated around 350 kN. As the raft was subjected to a combined load (vertical and overturning moment), the axial force at the top of inclusion increases to 600 kN on the loaded zone. In addition, a significant difference of the axial forces between nearby inclusions was visualized due to the fact that inclusions were located at different Y positions in the three different rings (Fig. 3.29).

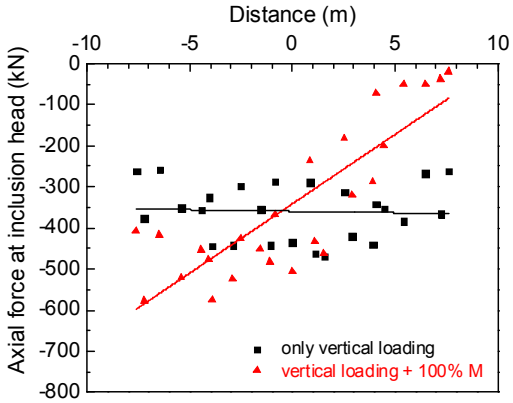

Fig. 3.38. Distribution of the axial force on inclusion heads (50 inclusions)

Bending moments

Due to the fact that there is no connection between the inclusions and the raft, no bending moment is formed at the head and tip of the inclusions. Fig. 3.39 shows the correlation between the maximum bending moment on each inclusion and its geometrical position. The values obtained as only the vertical loading was applied are relatively small (between 2 and 6 KN·m) compared with the values obtained for the complex loading. Due to the unequal pressure at the soil surface introduced by the moment loading, an additional lateral pressure was applied on the inclusions. The inclusions at the loaded side where the raft pressure on the soil was higher suffer a significantly smaller bending moment than those at the lifted side where the raft pressure on the soil was lower. It is due to the fact that the more compressive soil zone caused the horizontal displacement to surroundings, it resulted in the normal pressure exerting on the reinforcements. With regard to the given results in Fig. 3.39, the maximum moment of inclusions at the further left side was about 5 kN·m while that value at the further right side was over 20 kN·m.

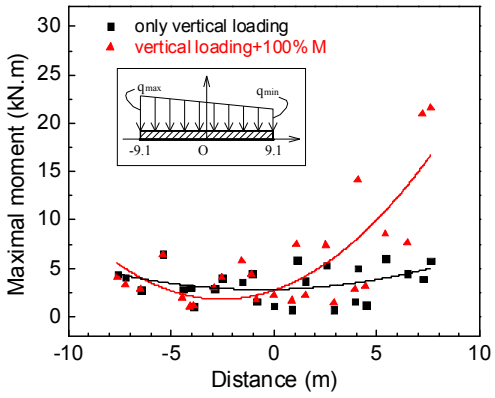

Fig. 3.39. Distribution of the maximum bending moment on each inclusion (50 inclusions)

Effect of the number of inclusions

The effect of the number of inclusions is assessed in terms of surface settlement, axial force and bending moment on the inclusions. A comparison of three sets of inclusion, including 50, 100 and 150, corresponding to area improvement ratios of 2.4%, 4.8% and 7.2%, respectively, was performed. The results are presented in Fig. 3.40, regarding both vertical and combination loading cases. Overall, an increase in the area improvement ratio leads to a significant reduction of the surface settlement, as well as the axial force and bending moment on the inclusions.

From Fig. 3.40.a, a total settlement of 283 mm was obtained for the reference case,

non-improved soil foundation, when only the vertical load was applied. This value significantly decreased to 66 mm when the area improvement ratio of 2.4% was considered, and a further reduction to just 22 mm was registered when 150 inclusions were used. The results were in good agreement with the ones of Huang and Han (2010), in which a maximum settlement decrease was more than doubled as the column spacing increase from 2.0 to 3.0 m. As the entire overburden moment was applied on the raft, the maximum ground settlement was approximately 367 mm for the reference case, it then declined to 90 mm, 51 mm and 35 mm with the improvement ratios of 2.4%, 4.8% and 7.2%, respectively. Fig. 3.40.b describes the significant reduction in the maximum axial force at the top of inclusions due to the increase of the area improvement ratio. As compared to the case of 2.4% reinforcement, the maximum force on the inclusions is reduced by a third and a half corresponding to an area ratio of 4.8% and 7.2%. Similar to the trend observed with the axial force, the maximum bending moment acting on the inclusions decreases with the area improvement ratio (Fig. 3.40.c).

a)

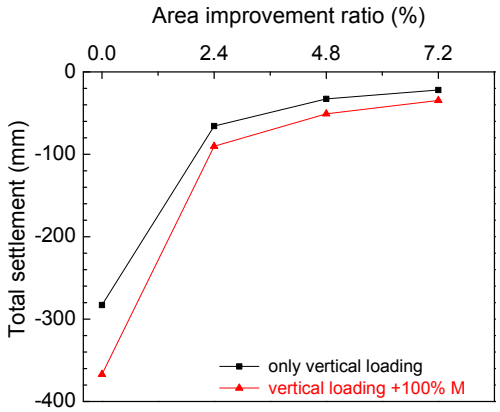

b)

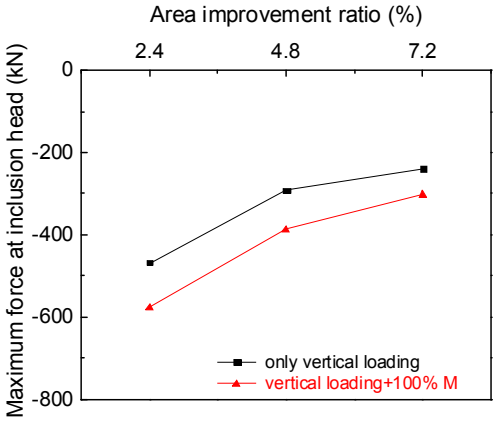

c)

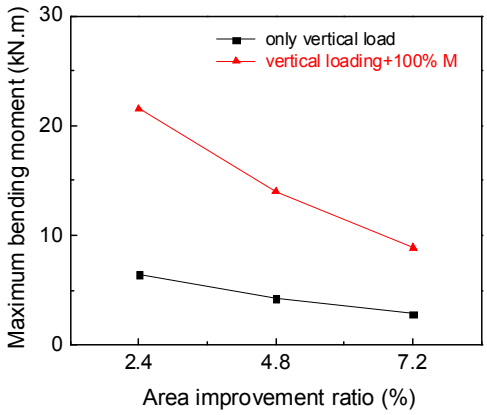

Fig. 3.40. Influence of the area improvement ratio on: a) total settlements; b) axial force; and c) bending moment

3.3.5.4. Piled raft

The cases of the piled raft with 50, 100 and 150 piles were performed and were compared with the above solutions concerning settlements, axial force and moment.

Settlements

Fig. 3.41 shows that the surface settlement of the piled raft case depends on the loading. The settlement for the purely vertical loading case was just below 2.6 mm. The maximum value increases slightly to 3.3 mm with 40% of the total moment applied and reaches 4.4 mm for 100%.

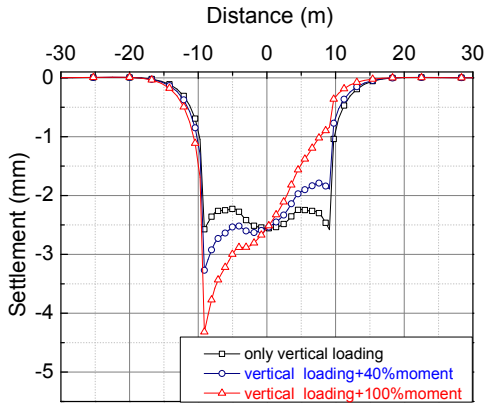

Fig. 3.41. Surface settlements (50 piles)

Table 3.10 compares the efficiency of each foundation solution in terms of its maximum surface settlement and of the raft rotation. It is clear that the piled raft is the most effective solution. In addition, the RI-raft system can be considered as an

acceptable solution. It induces a significant decrease of the surface settlement and of the foundation rotation. The influence of the inclusion/pile density on settlements is also clear. As the area improvement ratio was doubled and tripled, the settlement reduced to a half and a third, respectively.

Table 3.10. The surface settlement and raft rotation depend on foundation solutions corresponding to the loading cases

Loading cases	Foundation solutions							
	Existing ground	Mattress case	Inclusions			Piles		
			2.4%	4.8%	7.2%	2.4%	4.8%	7.2%
Only vertical loading								
Surface settlement (mm)	283	220	66	33	22	2.6	1.2	1.1
Vertical loading with 100%*M*								
- Surface settlement (mm)	367	274	90	51	35	4.4	2.1	1.3
- Raft Rotation (^{o})	0.635	0.471	0.115	0.073	0.050	0.010	0.005	0.003

Axial forces

Fig. 3.42 shows the axial force on the piles head as a function of the distance between the pile and the raft center. It can be seen that, for the purely vertical loading, the axial forces acting on the piles are relatively uniform and be equal to 600 kN. When the entire overturning moment was applied, the axial forces linearly vary between 250 and 950 kN.

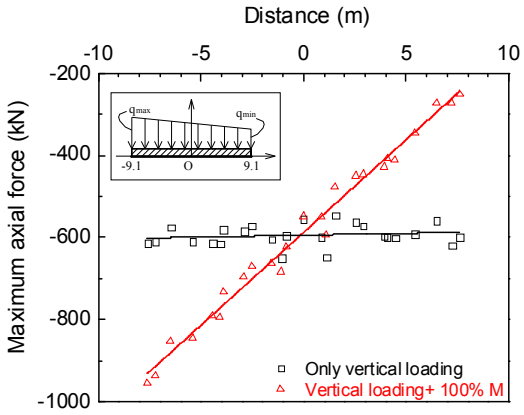

Fig. 3.42. Distribution of the axial force at the top of piles (50 piles case)

Fig. 3.43 compares the influence of improvement area ratio on the maximum axial force registered for the RI-raft and pile-raft systems. The maximum force acting on the inclusions was only 60% of the one on the piles for an improvement ratio of 2.4%. This is deemed to be related to the presence of the mattress which helps to share the load from the raft to soil mass. However, an increase in the number of piles proved to be more effective than the increase in the number of inclusions, since the maximum axial

force acting on the former decreased to a value lower than the maximum force acting on the latter. In these cases, the presence of the mattress was not sufficient to counteract the higher efficiency of the pile-based system.

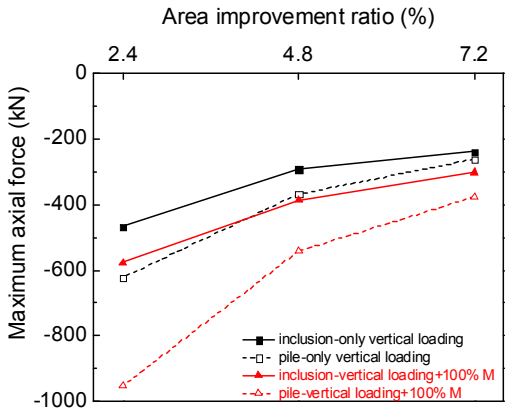

Fig. 3.43. Influence of the improvement area ratio on the maximum axial force at the top of inclusions/piles

Bending moments

The correlation between the maximum bending moment on each pile and the respective distance to the center of the raft is shown in Fig. 3.44. It can be seen that as only the vertical load was applied, the moment on the piles near the center of the raft (5 kN·m) was significantly smaller than the moments on the piles at the perimeter (30 kN·m). When the complex loading was applied, there was a redistribution of the moments on the piles. The moments on the heavily loaded piles reached a value above 70 KN·m, while the moments on the lightly loaded piles decreased to a value below 15 kN·m. This could be due to the large diameter of the raft that imposes a high rotation angle, which, in turn, led to a higher rotation movement to the top of the peripheral piles than to the top of the central piles.

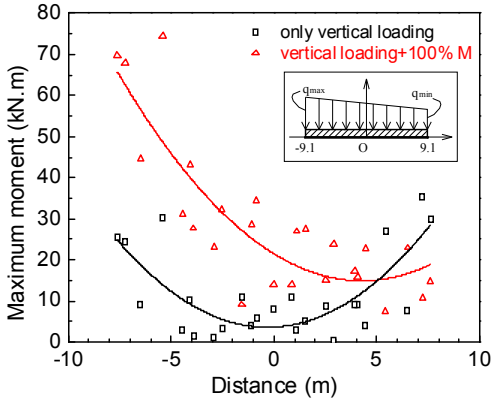

Fig. 3.44. Distribution of the maximum bending moment on each pile (50 piles case)

Fig. 3.45 depicts the maximal bending moment on the two types of reinforcement when the system is subjected to the two loading cases. Overall, the maximum moment on the inclusions was significantly smaller than that acting on piles in both loading cases. For the improvement ratio of 2.4%, the maximum moment on the inclusions and piles were 22 kN·m and 70 kN·m, respectively, representing an approximate difference of more than 300%. This scenario repeated itself when the area improvement ratio increased to 4.8% and 7.2%, i.e. the inclusion-based system proved to be the better solution in terms of the maximum bending moment.

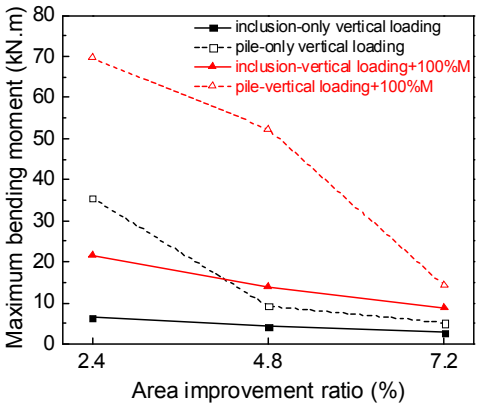

Fig. 3.45. Influence of improvement ratio on the maximum bending moment of inclusions/piles

Due to the noticeable performance of the RI-raft system in terms of axial force and bending moment, this solution can be regarded as more efficient than the pile-raft system. This is further highlighted as considering its versatility, cost-effectiveness and fast construction (Deb and Mohapatra, 2013), and all contribute to the acceptation of this solution as the future primer option for soil improvement under WT foundations.

3.3.6. Conclusions

The study presents a 3D numerical modeling of four foundation solutions for wind turbines subjected to realistic static loadings. The results obtained have permitted to verify that the soil improvement technique by rigid inclusions can overcome the drawbacks of traditional foundation options, as stated in the detail conclusions.

Firstly, concerning the constitutive models for a mattress, a good agreement between the CYsoil and the MC constitutive models is found when the cap pressure (p_c) for the CYsoil model is set higher than 500 kPa;

In addition, there is a significant decrease in the total and differential surface settlements for the piled raft and for the rigid inclusion cases compared to the shallow

raft case;

Thirdly, it is observed that the soil settlements, the foundation rotation, the axial forces and bending moments exerted on the reinforcements decrease with the area improvement ratio increase;

Furthermore, the presence of the overturning moment on the raft does not only increase the total and differential soil settlements, but it also leads to a redistribution of the axial force and moment on inclusions/piles.

In addition, as regards with the axial force and bending moment of the reinforcements, the rigid inclusion reinforced soft soil method regarded as more efficient than the pile-raft system.

Last but not least, the ground improvement using rigid inclusions can bring an appropriate and reliable choice for wind turbines foundation owing to its efficiency and applicability.

3.4. Conclusions

In this chapter, the behavior of soft soil improvement by rigid inclusions under complex loading has been investigated. Two main studies are presented: footings over a reinforced soft soil and wind turbine foundation solutions.

In regard to the reinforced footing under complex loading, the achieved results figure out in some points.

The vertical loading tests on the single rigid inclusions and the unreinforced footing permit to verify the multi-layered soil behavior. These tests are also useful for calibrating the soil parameters for the numerical analyses.

The centrally vertical loading tests indicate that the stress on the inclusion increases linearly with increasing the vertical loading on the footing. Moreover, the efficacy of a reinforced soil method is proved by the fact that the significant higher stress on the inclusion than on the soft soil is shown. Moreover, the eccentricity of vertical loading causes differences in the stresses on the inclusion. A larger eccentricity produces a lower inclusion pressure on the lifted side and the higher inclusion stress on the weighted one. In regard to a few load cycles, the decline of the vertical stress in inclusions is found for the later repetitions. An increase in the horizontal loading results in a rise in the pressure on the inclusion as well.

Concerning the displacements, the footing displacement of the reinforced footing is half of that of the unreinforced one. When the vertical load is relatively small (test 2B), small footing displacements are obtained, and the accumulated settlements are insignificant under a number of load cycles. On the contrary, as the applied loading is large enough, significant footing displacements are observed, and cumulative settlements are monitored.

In the case of horizontal loading tests, a significant dependency of the lateral footing displacement on the horizontal loading is found. The lateral footing displacement is really small as the horizontal loading is small. Meanwhile, it is significant when the horizontal loading is large enough. Due to the non-rigid connection between the footing and the inclusions, the lateral displacement of the inclusions differs from the footing one.

Concerning the foundation solution for WTs subjected to real loading cases, the achieved results indicate several valuable conclusions.

Regarding the constitutive models for the mattress, the results obtained by the

CYsoil model are in a good agreement with the MC ones as the cap pressure of the CYsoil model is high enough;

Secondly, the total and differential surface settlements of the piled raft and the RI-reinforced foundation solutions significantly decrease as compared to the shallow foundation case;

Moreover, as regards with the RI-improved raft, as the area improvement ratio increases the soil settlements, the foundation rotation, the axial forces and bending moments exerted on the reinforcements decrease;

In addition, the overturning moment applied to the raft results in an increase in the total and differential soil settlements and causes a redistribution of the axial forces and bending moments on inclusions/piles.

Finally, the solution of the foundation over reinforced rigid inclusion is more efficient than the pile-raft system as regards of the axial forces and bending moments on the reinforcements. The reliability, economic aspect, and flexibility of the rigid inclusion-reinforced soil method can be a good a good solution for wind turbine foundations.

Chapter 4

Soil behavior under cyclic loading

4.1. Introduction

Structures are subjected to cyclic loading effects due to the change in applied loading intensity with time. In the cases, the variation of the load by time is large enough, the impact of cyclic loading on the structure and the soils needs to be taken into account. The theoretical studies concerning the soil behavior under cyclic loading are presented in this chapter, which aims to bring an insightful overview of the cyclic response of soils. The main contents are presented as follows:

Firstly, the cyclic loading is defined. The difference between static and cyclic loadings is then figured out in terms of the frequency, the load amplitude and the number of load cycles. The sources of cyclic loading are introduced as well.

Secondly, the stress-strain relationships are analyzed. As similar to the static condition, the established theoretical models to represent the soil response during cyclic loading are mainly based on the fitting of the stress-strain curve between the numerical results and experimental data.

In addition, the two key parameters namely the damping ratio and stiffness are defined. It is well recognized that they have a significant influence on the soil behavior under load cycles. The geotechnical and physical parameters that control the stiffness degradation and the damping ratio are shown.

Furthermore, the strain accumulation of soils under the number of cyclic loadings is introduced. In this part, various factors influencing the cumulative strains are presented including the cyclic loading conditions, the mechanical indicators and the current stress state.

The advanced constitutive models able to consider the cyclic loading of soils are then introduced. Some parameters and their calibrating procedure are also brought here.

4.2. Cyclic loading definition and sources of cyclic loading

4.2.1. Cyclic loading definition

The term '*cyclic loading*' suggests a system of loading which exhibits a degree of regularity both in its magnitude and in its frequency. In another way, cyclic loading can be defined as a periodic action, that when it is applied to a material body, tends to

change its reverse stress or strain state over time.

The difference between static and cyclic loading conditions may be derived from impulse phenomena, vibrations and waves that are described in terms of speed of loading (a frequency) and effect of repetition loading (a number of cycles and an amplitude). The effect of the load repetition is a feature of cyclic loading, in which the load is repeatedly applied many times with a given frequency. The rapidity of applied load (e.g., a short period of time or high frequency) is considered as a dynamic phenomenon, such as an earthquake event, pile driving compaction, and traffic loading. During earthquakes, the load repetitions are generally subjected to 10 to 20 times with different magnitudes. They can be repeated from 100 to 1000 times with the frequency ranging from 10 to 60 Hz in pile driving and in vibro-compaction (Ishihara, 1996).

In reality, most structures are subjected to cyclic loading effects due to the change in applied loading intensity in time, such as wind loading, traffic loading or loading induced by the operation. The phenomenon is that the small loading fluctuation applied upon structures can be ignored. However, in some cases, the presence of cyclic loading cannot be neglected, in particular, wave loading on offshore structures, wind loading on largely slenderness constructions, traffic loadings on roads, and the vibrations on heavy machine foundations. A cyclic loading effect on structural components could result in a cyclic loading on soils.

To solve the above problems, engineers have to give the best solution in a safe, efficient and economical manner. Static analyses might be appropriate for the cases with very low applied loading rates. When the change in stress or strain magnitude and loading frequency are not ignorable, static analyses will possibly give underestimated predictions, which lead to unsafe and inefficient designations due to their inaccurate results. Therefore, in geotechnical designs, the consideration of cycle loading impacts and its influences play an extremely important role, in which the soil behavior under cyclic loading should be noticed as the root of the problem.

4.2.2. Sources of cyclic loading

Cyclic loadings are caused by non-endogenous or endogenous natures. The non-endogenous sources impose the cyclic loadings from the exterior into the soil, including traffic loadings (trains or vehicles), industrial loadings (crane bridge or machine operation), wind loading (high and slenderness structures) or wave loading (offshore structures), filling and emptying processes (silos and tanks), mechanical

compactions and construction process. Earthquake event is known as an endogenous source caused by a cyclic shear of soil that is generated by the slip between tectonic plates (it creates a propagation of shear waves) (Wichtmann and Triantafyllidis, 2012). Structural elements are analyzed in cyclic loading conditions, and their foundations that are located on soils cannot also be ignored the influence of load cycles. Therefore, several main sources of cyclic loading are analyzed here.

4.2.2.1. Wind loading

Wind loading acting on high slenderness structures induces a cyclic loading on the foundations. It is particularly important for tall flexible structures such as towers, chimneys and long bridges (Cook, 1990). As wind load applied to structures causes horizontal loadings and moments on their foundations, the velocity and direction of wind loading changes over the time. It results in the cyclic loadings of soils. In the case of high-rise structures, wind load may cause an increase in the movements amplitude of about 25% compared with conventional static loads (O'Reilly and Brown, 1991). In construction, most structures are advisedly built to minimize the wind effect. With the exception of wind turbine towers, they are constructed to attract wind. The loading caused by wind is not only considered, but the high-frequency rotating turbine also needs taking into account. The cyclic actions on foundation must be carefully analyzed (Clare and May, 1990).

4.2.2.2. Wave loading

The propagation of waves on the sea is considered as an infinite number of wave strains with a constant amplitude and wavelength. Passage of such an array of waves creates a harmonic pressure change on the sea floor, which increases the pressure at the crests and decreases the pressure at the trough. Thus, the induced stresses in the seabed are modeled by applying a sinusoidal shape of loading that varies in the horizontal surface from minus to plus infinity. A significant challenge for geotechnical engineers is to model accurately both physical and theoretical aspects of the wave cyclic loading. The cyclic effect applied to offshore structures results in a cyclic or dynamic impact on foundations and soils. It is particularly important for the offshore engineers to consider the periodic wave loading on the structures and foundations, and the dynamic response of soils.

4.2.2.3. Earthquake event

An earthquake event is an endogenous source induced by a cyclic shear mechanism. A slip between tectonic plates that creates a propagation of shear waves induces a cyclic

shear of soils. For a given value of stress or strain amplitude, permanent loss of strength and stiffness, and residual strain accumulation are observed in soils because of the build-up of excess pore water pressure and particle structure breakdown, as the number of load cycles increases.

4.2.2.4. Traffic loading

Traffic loading induced by high-speed train and trucks as encountered in road pavements or railways may be simply described by an elastic half-space subjected to a uniform load over the surface unit. The cyclic loading induced by the repeated passage of traffic vehicles over time could result in a reduction of the shear modulus of materials, which leads to a cumulative deformation in the ballast, embankment, and ground.

4.2.2.5. Structures supporting traveling machinery

The structures such as bridge cranes, radar antennas, and telescopes are considered like non-endogenous cyclic loading sources due to the movement of machinery or equipment on them. The viaduct piers are also classified to belong to this category, in which the cyclic effect occurs when the relative position of the vehicle along the viaducts or the presence of traffic passages in the horizontal direction. The moving machinery and equipment during their operation can cause repeated load cycles and variable loading on soils. In these cases, the cyclic aspects should be taken into consideration.

4.2.2.6. Groundwater level change

The change of groundwater level results in a difference in effective stresses in soils even the externally applied loadings remain static. The groundwater table often varies seasonally and cyclically, or in the locations adjacent to water where tidal changes or fluctuation of rivers occur. The effective cyclic loading of the ground is caused by a cyclic variation of the water level, which leads to cumulate long-term settlements in soils.

4.2.2.7. Storage facility

The finished and semi-finished storage such as grain silos or liquid storage tanks are frequently used in the industrial facilities. The generic characteristic of these structures is that the largest pressure exerted on foundations reaches as the tank is fully filled, and smallest pressure occurs when it is empty. The cyclic filling-empty process in storage transmits the cyclic loading to the soils.

4.3. Stress-strain relationship

As for the static loading condition, theoretical models proposed for the cyclic response of soils are also based on the fitting of the stress-strain curve between numerical results and experimental data. In the experimental curve, two different facets of the soil's stress-strain relationship are illustrated in Fig. 4.1. The first aspect is called *path of first loading* where the strain state has a higher magnitude than the previous maximum. This path is described through the backbone curve (or skeleton curve). Besides that, as the strain state that has a lower magnitude than its previous maximum, it is called *unloading path* or *reloading path*, in which the unloading and reloading are corresponding to a decrease and an increase of strain over time. In the case of cyclic loading, the close cycle of unloading and reloading paths is typically called the *hysteresis loop*. The hysteresis loops are set up in stress-strain space.

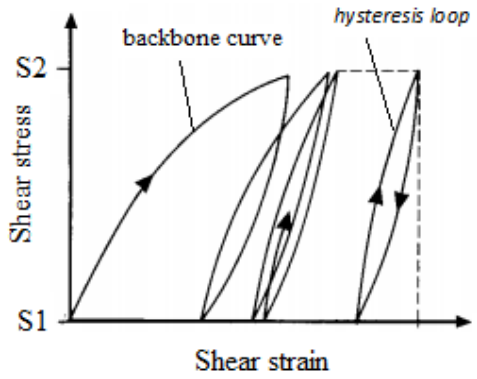

Fig. 4.1. Stress-strain relationship under cyclic loading of a soil

The range of shear strain is important for the soil response under cyclic loading, as illustrated below.

- As the shear strain applied on soil is small (less than 10^{-4}), the soil deformation is purely elastic and recoverable. The shear modulus is a major parameter.
- As the shear strain has a medium value (from 10^{-4} to 10^{-2}), the soil behavior becomes elasto-plastic and produces irrecoverable permanent deformations. The shear modulus tends to decrease as the shear strain increases, and the energy dissipation happens during the application of cyclic loading. The absorbing energy can be explained due to the presence of damping characteristics. The damping ratio and shear modulus are functions of the shear strain and are independent of the cycles of loading.
- As the shear strain is superior to 10^{-2}, the shear stiffness and damping ratio are dependent on both the shear strain and the number of load cycles. To specify

the stress-strain relationship in this strain range, current methods have employed the numerical procedure involving step-by-step integration techniques. The backbone curve is coupled with a series of constitutive laws, which allows each step of loading, unloading and reloading to be shown in a stress-strain relationship (Ishihara, 1996). Additionally, many researchers have worked on the dependency of the loading conditions, soil physical properties (e.g. initial relative density, grain-size distribution, plasticity index) and stress history on stress-strain relationship under cyclic loading (Habib et al., 2010).

To conclude, the two most important parameters are the shear stiffness (or shear modulus) and the damping ratio. The shear stiffness represents the effective stiffness of soil while the damping ratio exhibits the dissipation of energy within the soil. They are considered as key parameters to build a stress-strain curve (backbone curve and hysteresis loops) under cyclic loading (Habib et al., 2010).

4.4. Stiffness degradation and damping ratio evolution of soils under cyclic loadings

4.4.1. Definition of the soil stiffness and damping ratio

4.4.1.1. Soil stiffness

Shear modulus (*G*), expressed in units of pressure, is the ratio of shear stress (τ) to the shear strain (γ), as in Equation 4.1.

$$G = \frac{\tau}{\gamma} \tag{4.1}$$

In the case of low and medium shear strains cyclic loading, the stiffness of the soil is well presented by the secant shear modulus G_{sec}. To be convenient, a secant shear modulus is generally referred to as simply shear modulus.

4.4.1.2. Damping ratio

During each cycle of loading, the loss of energy is represented by the damping feature. Its value is determined to be equal to the area enclosed by the hysteresis loop, ΔW. Since the energy loss that is a function of shear strain amplitude is not a material property, it is not easy to measure damping characteristics. In this way, the damping ratio *D* is suggested, which is the ratio of energy loss per cycle to the maximum elastic energy stored in a unit volume of a viscoelastic body, *W* (Ishihara, 1996).

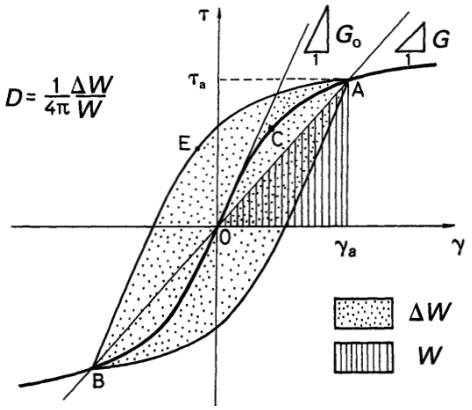

Fig. 4.2. Definition of the elastic stored energy and dissipation of energy

By Ishihara (1996), the damping ratio is expressed in Equation 4.2.

$$D = \frac{1}{4\pi}\frac{\Delta W}{W} \tag{4.2}$$

As seen in Fig. 4.2, the loss of energy per one cycle and maximum elastic energy are quantified, as follows.

$$\Delta W = \int \tau d\gamma \tag{4.3}$$

and

$$W = \frac{1}{2}\tau_a \gamma_a = \frac{1}{2} f(\gamma_a)\gamma_a \tag{4.4}$$

4.4.2. Stiffness degradation

The maximum shear modulus G_{max} manages the elastic behavior for the very small strain range ($\gamma \leq 1\times10^{-4}$). In this case, the dynamic shear modulus G_{sec} is nearly constant and is taken by the initial value G_{max}. Whereas, for medium and large values of strains, the cyclic response of soils is represented by the stiffness and damping ratio that are not constants with the shear strain amplitude. It is obviously seen in Fig. 4.3, the stiffness decreases and the damping ratio increases as the shear strain amplitude increases. The decrease of stiffness and the increase of damping ratio with increasing the shear strain amplitude are called the stiffness degradation and the damping evolution, respectively.

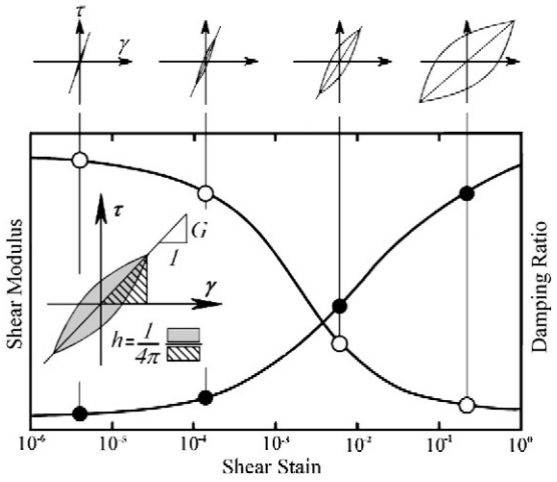

Fig. 4.3. Dependency of the damping ratio, shear modulus, and stress relationship to the shear strain amplitude (Habib et al., 2010)

Former researches related to medium and large cyclic shear strains, Okur and Ansal (2007) indicated that as the number of cyclic loading on soil sample (with a specific value of stress or strain amplitude) increases, the permanent loss in strength (stiffness) of soils occurs due to the accumulation of excess pore water pressure and the breakdown of particle structure.

Derived from the experimental results, Kramer (1996) and Ishihara (1996) indicated that the soil stiffness depends on some parameters that include cyclic strain amplitude, void ratio, effective confining pressure, plasticity index, over-consolidation ratio and number of load cycles. As performing some multi-stage loading program, Okur and Ansal (2007) presented that the change in cyclic shear strain amplitude and plasticity index have a significant effect on the shear modulus reduction while the impact of the void ratio is much less significant than plasticity, as seen in Figs. 4.4 and 4.5.

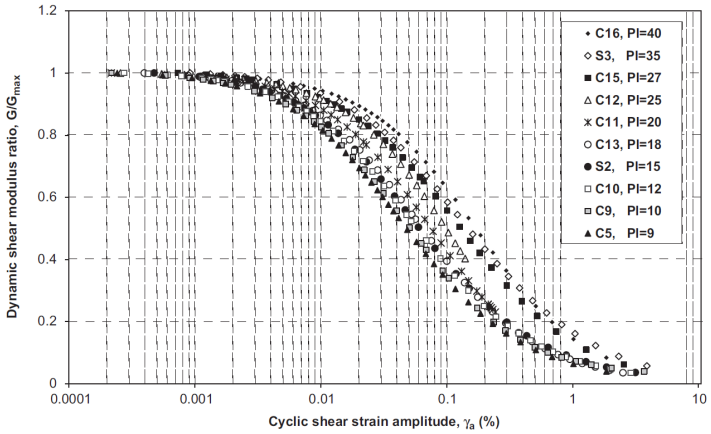

Fig. 4.4. Dependency of dynamic shear modulus on shear strain amplitude and different

plasticity indices (Okur and Ansal, 2007)

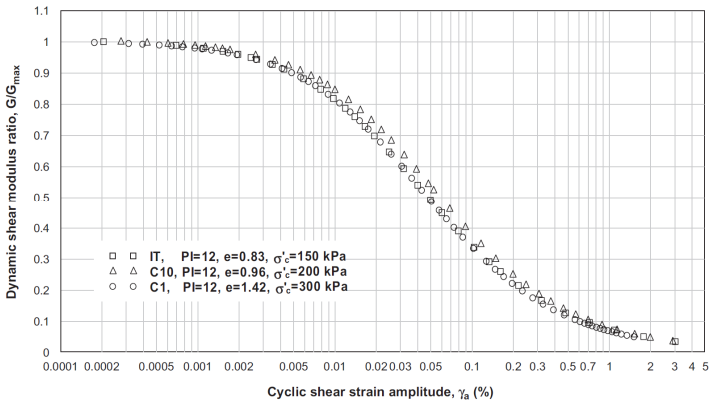

Fig. 4.5. Variation of the dynamic shear modulus with the shear strain amplitude for different void ratios (Okur and Ansal, 2007)

A correlation between the shear modulus and shear strain amplitude was adapted using the hyperbolic function by Kondner (1963).

$$\frac{G}{G_{\max}} = \frac{1}{1+\gamma_a/\gamma_r} \tag{4.5}$$

Wherein γ_a is the cyclic shear strain amplitude, γ_r is the reference strain known as a function of the plasticity index *PI*, as given

$$\gamma_r = \frac{1}{21\left[1-\exp\left(-106.PI^{-1.585}\right)\right]} \tag{4.6}$$

4.4.3. Damping ratio evolution under cyclic loadings

In the duration of the deformation process induced by the cyclic loading, the dissipated energy is expressed by the hysteretic damping. As can be seen from Equations 4.2, 4.3 and 4.4, the damping ratio *D* is not only dependent on the shear strain amplitude, but it is also affected by the material properties. Therefore, different soils will have different values of damping ratios. Similarly to the cyclic shear stiffness, the damping ratio is also influenced by the cyclic shear strains, soil plasticity, effective confining pressure and void ratio. The damping ratio increases significantly as the shear strain amplitude increases, the plasticity index decreases, and the confining pressure increases, as presented in Figs. 4.6 and 4.7. By contrast, the damping ratio is slightly influenced by the void ratio, as seen in Fig. 4.8.

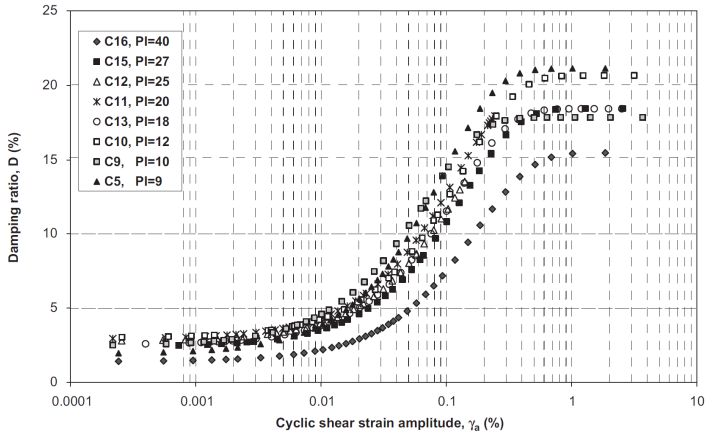

Fig. 4.6. Effect of the plasticity index and shear strain amplitude on the damping ratio (Okur and Ansal, 2007)

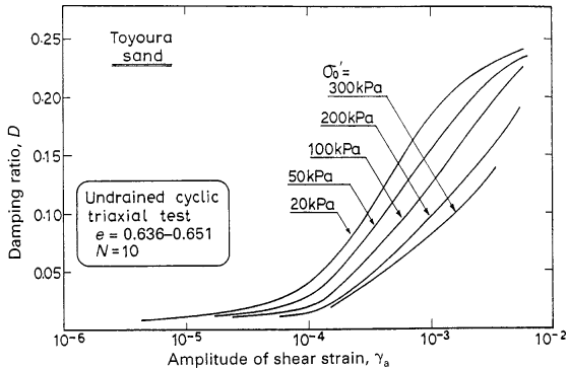

Fig. 4.7. Effect of the confining stress and shear strain amplitude on the damping ratio (Kokusho, 1980)

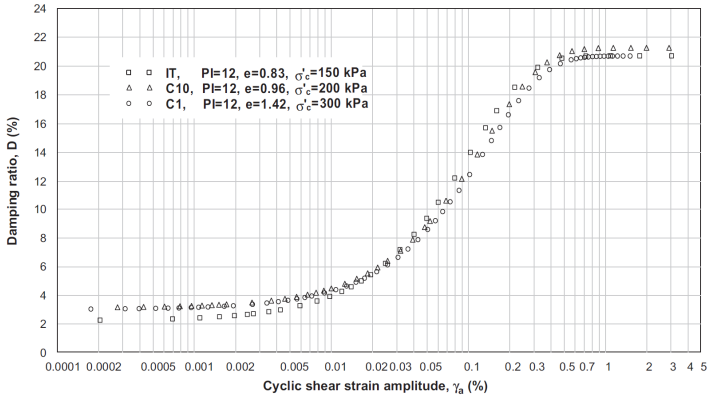

Fig. 4.8. Effect of the void ratio and the shear strain amplitude on the damping ratio (Okur and Ansal, 2007)

Based on the fitting with given experimental curves, Okur and Ansal (2007) proposed a mathematical correlation between the damping ratio, the cyclic strain amplitude, and the plasticity index, as given in Equation 4.7.

$$D = C_0 + C_1.C_2^{PI}\left[C_3 - \exp\left(-C_4.\gamma_a.C_5^{PI}\right)\right] \quad (4.7)$$

Herein, C_0 to C_5 are the empirical constants that are determined by fitting a nonlinear curve using the cyclic triaxial test.

By another approach, Hardin and Drnevich (1972) suggested the damping ratio as a function of the soil stiffness in Equation 4.8.

$$D = -18.114\left(\frac{G}{G_{\max}}\right) + 20.033 \quad (4.8)$$

4.5. Strain accumulation due to cyclic loadings

4.5.1. Definition of the strain accumulation

In the case of a small range of shear strain, as a soil is subjected to the repetition of load cycles, the strain of the soil is purely elastic and recoverable. For medium or large shear strain amplitudes, the deformation of the soil is irrecoverable during the number of load repetitions. This phenomenon that the irrecoverable strain increases under the number of load cycles is known as the strain accumulation. Based on the laboratory tests, the accumulated strains during cyclic loading could be explained by the rearrangement of grains, the drainage effects and the abrasion of soil particles.

In terms of civil engineering aspect, the accumulated strain of soils induced by the load cycles leads to excessive settlements and significant differential settlements (large rotation angle) that causes the instability and the unsafe for the structures. In the case of saturated soils subjected to the undrained cyclic loading (a high loading increase in a short time), the excess pore pressure is developed under a number of cyclic loading. In particular, as the pore pressure reaches the total stress (it means that the effective shear stress becomes nil), the ground works like a suspension. This phenomenon is called *soil liquefaction*. It can increase the risks of damage and reduce the serviceability.

In the following part, the parameters that are influent on the cumulated strain for granular soils under cyclic loading are considered.

4.5.2. Strain accumulation of granular soils under cyclic loading

The strain of granular soils is accumulated under cyclic loading due to the formation of non-perfectly closed strain loops. In general, the strain accumulation of soils is dependent on the cyclic loading conditions, the physical indicators, and the soil's

current stress state. The cyclic loading conditions include the number of load cycles, the cyclic stress amplitude, the frequency, and the strain amplitude. The group of the physical parameters consists of the initial relative density (or void ratio), the particle shape, the grain-size distribution, and the soil fabric. The current stress state, considers the effect of the average mean pressure.

4.5.2.1. Influence of the strain/stress amplitude

Several experimental works were carried out to investigate the effect of the strain and stress amplitude on the accumulated rate of strain. While the cyclic simple shear tests were conducted for changing the shear strain amplitude, the cyclic triaxial ones were performed for varying the shear stress magnitude. Youd (1972) found the remarkable growth of accumulation rate accompanied by the increase of the shear strain amplitude. In other words, no strain is accumulated as the shear strain amplitudes are less than 10^{-4}. Silver and Seed (1971a) claimed that instead of changing the shear stress amplitude, it is easy to vary the shear strain amplitude to process a cyclic loading. Their obtained results were in a good agreement with the findings of Youd (1972). Performing the shear strain amplitude tests on the sand samples at the given initial density, Sawicki and Swidzinski (1987, 1989) plotted a relationship of the accumulation strain (ε^{acc}) with the weighted number of cycles, $\widetilde{N} = N\left(\gamma^{ampl}/2\right)^2$. From the drained cyclic triaxial tests of Wichtmann et al. (2005), the experimental results figured out that the accumulation of residual strain tends to increase proportionally to the square of the shear strain amplitude (Fig. 4.9). Besides, derived from the curve of the accumulated strain versus the logarithm of *N*, it can be seen that the strain accumulation increases linearly with the logarithm of the cyclic numbers up to *N* = 10,000, and then over-proportionally (Fig. 4.10). Based on the above review, it is obviously recognized that the higher the stress amplitude, the larger the accumulated strain rate.

4.5.2.2. Number of load cycles (*N*)

In the previous studies of Lentz and Baladi (1980); Marr and Christian (1981); Suiker (1999); Gotschol (2002); Gotschol (2002); Wichtmann et al. (2005) and Helm et al. (2010), the significant effect of the number of load cycles on the strain accumulation has been figured out. An increase in the number of load cycles results in an increase in the residual strain. Lentz and Baladi (1980) showed that the residual axial strain increase is proportional to the logarithm of the number of load cycles. Suiker (1999) found that the decrease of the accumulation rate is proportional to 1/*N* through two coefficients, c_1 for $N < 1000$ and c_2 for $N > 1000$ with $c_1 > c_2$. Similarly, using cyclic

triaxial tests on gravel, Gotschol (2002) recognized a general consent with previous studies. Marr and Christian (1981) expressed the correlation $\varepsilon^{acc} = a\zeta^{b}$, in which b ranges from 1.91 to 2.32 with N from 10 to 1,000, ζ is the amplitude ratio. Wichtmann et al. (2005) also indicated that there was a proportional increase of the accumulated strain in correlation with the logarithm of the number of load cycles (up to 10.000), followed by the over-proportional trend, as given in Fig. 4.10.

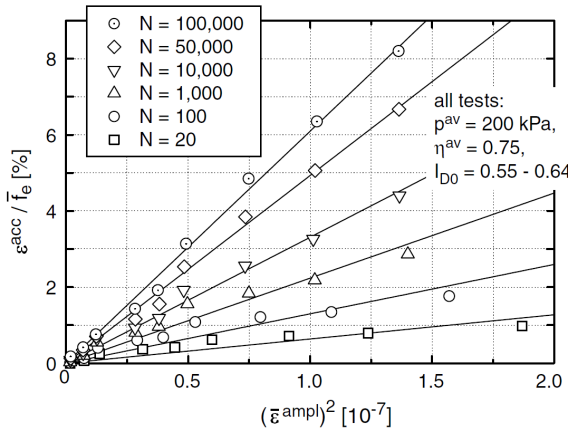

Fig. 4.9. Accumulated strain as a function of the square of the strain amplitude (Wichtmann et al., 2005)

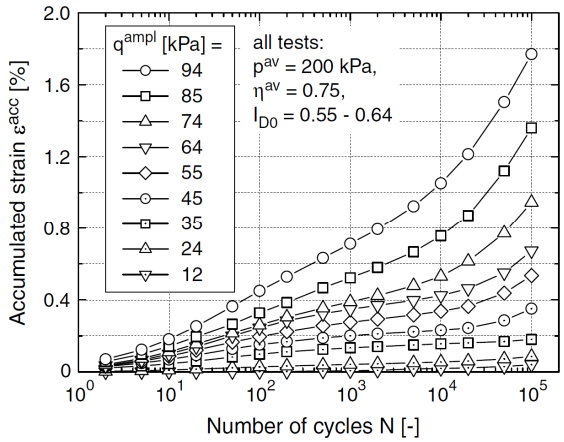

Fig. 4.10. Accumulation curves in tests with different stress amplitudes (Wichtmann et al., 2005)

4.5.2.3. Influence of the average mean pressure

Some experimental studies using cyclic shear and triaxial tests discovered the influence of the average mean pressure on the cumulative strains. The obtained results by cyclic shear tests in Silver and Seed (1971b) and Youd (1972) indicated that there is no effect of the average mean pressure on the strain accumulation. In the cyclic triaxial tests of Marr and Christian (1981), the average stress ratio $\eta^{av} = q^{av}/p^{av} = 0.43$, the amplitude

ratio ζ = 0.19 and initial density D_r = 28% were kept constant, and the average mean pressures (p^{av}) ranged from 140 kPa to 420 kPa. They found that as p^{av} increases, the strains accumulated slightly. However, different shear strain amplitudes were not considered in the tests due to the stress-dependence of stiffness. In the drained triaxial cyclic tests of Wichtmann et al. (2005), the obtained results showed an opposite tendency with the findings obtained by Silver and Seed (1971a,b) and Youd (1972), in which the strain amplitudes rise slightly as the average mean pressure increases. The reason might be the influence of the shear stiffness G on the mean pressure p^n (herein n = 0.75), as presented in Fig. 4.11.

Fig. 4.11 describes the dependency of accumulated strains on the average stress p^{av} with different load cycles as well. The residual strains are divided into the amplitude function f_{ampl} and the void ratio function f_e to avoid side effects. It can be seen that the accumulated strains increase significantly as the average stress reduces, and vice versa (Wichtmann et al., 2005). Derived from the experimental tests with different average stress ratios ($\overline{Y}^{av}$), they also found that an increase in the average stress ratio resulted in a significant strain accumulation.

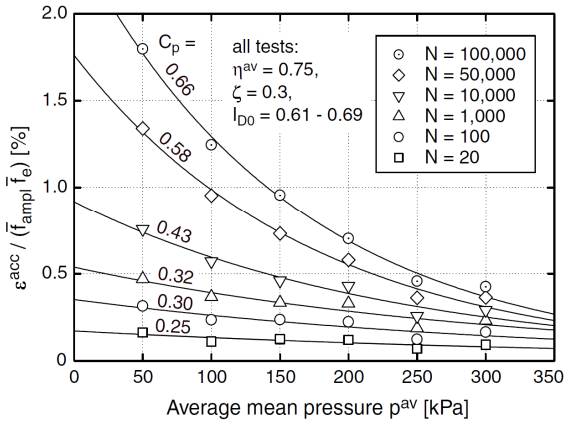

Fig. 4.11. Influence of the average mean pressure on the normalized accumulated strain (Wichtmann et al., 2005)

4.5.2.4. Influence of the loading frequency

The influence of the frequency of cyclic loading on the strain rate was reported in some researches. The strain accumulation was not observed in the cyclic simple shear tests with different values of frequency (0.1 to 1.9 Hz) by Youd (1972), in the cyclic triaxial tests with ranging of frequency (0.1 and 30 Hz) by Shenton (1985). In addition, Wichtmann et al. (2005) argued that there is no effect on the strain amplitudes caused by different loading frequencies in Fig. 4.12. However, derived from the cyclic triaxial tests on the gravel samples, Kempfert et al. (2000) recognized that an increase in

frequency during the first cycle of loading can accelerate the permanent strains, whereas a reduction of the strain rate was found during the following load cycles. Carrying out tests using a change of the loading frequency $0.05 \leq f \leq 2.0$, the results obtained were in good accordance with the findings of Youd (1972) and Shenton (1985).

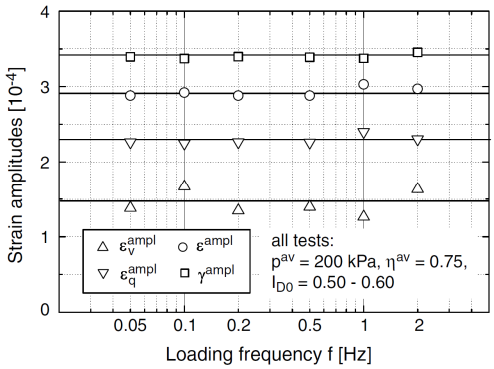

Fig. 4.12. Dependency of the strain amplitudes on the loading frequency (Wichtmann et al., 2005)

4.5.2.5. Influence of the initial relative density

The studies of Silver and Seed (1971b); Youd (1972) and Marr and Christian (1981) found that the initial soil density has a significant impact on the strain accumulation. As the cyclic loading tests were conducted on the loose sand samples, a high accumulation rate was found. Based on the results of the triaxial tests on a series of saturated soil samples with different initial void ratios ($0.58 \leq e_0 \leq 0.80$), Wichtmann et al. (2005) presented that the lower the value of the initial void ratio, the slightly higher the strain amplitude, as illustrated in Fig. 4.13**,** and the strains of loose sand accumulates larger than those of dense sand (Fig. 4.14).

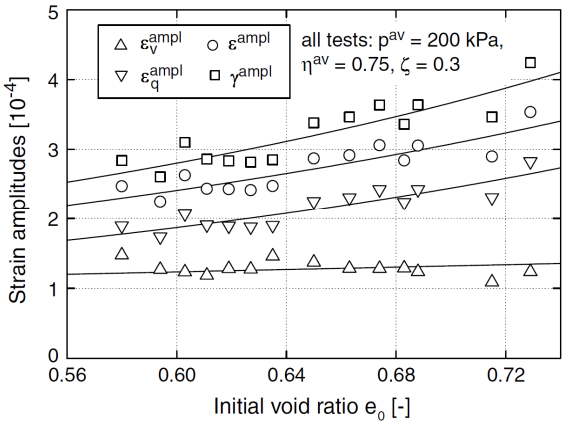

Fig. 4.13. Strain amplitudes in tests of the dependency of the strain amplitude with different initial void ratios e_0 (mean values during 10^5 cycles) (Wichtmann et al., 2005)

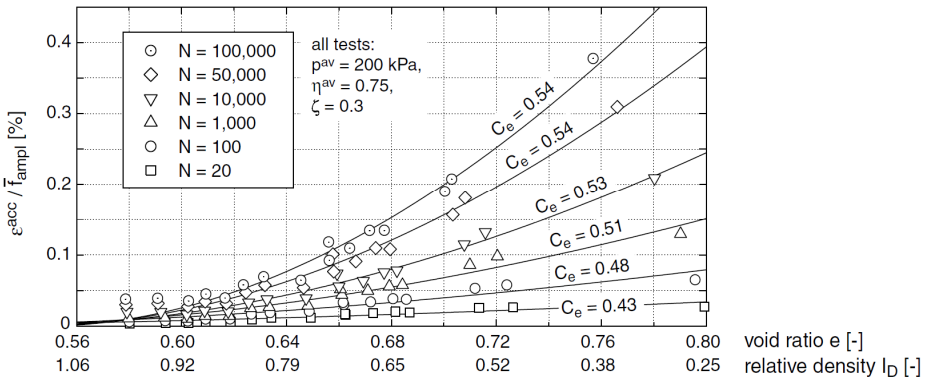

Fig. 4.14. Influence of the void ratio (or the relative density index I_D) on accumulated strain (Wichtmann et al., 2005)

4.5.2.6. Influence of the grain-size distribution

Studying the different gradations of a sand subjected to cyclic loading, Wichtmann et al. (2005) explored that the strain accumulation rate was significantly dependent on the distribution of the grain size (Fig. 4.15). The increase of the uniformity coefficient leads to the increase of the cumulative strains. It means that strains of well-graded sands are cumulated faster than those on poorly-graded ones, which explains why a well aggregate gradation easily reaches a required vibration compaction. The decrease of the mean diameter (d_{50}) at constant uniformity (U = const) led to the increase of the accumulated strains as well. A recommendation was given that it is necessary for further studies to take into account the influence of grain gradation that are the grain size distribution, the grain shape and the content of fines.

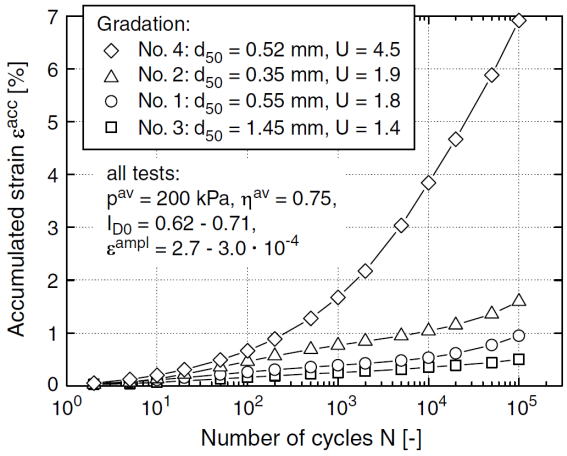

Fig. 4.15. Strain accumulation for different gradations under cyclic loading (Wichtmann et al., 2005)

4.6. Constitutive models of soils under cyclic loading

The previous constitutive models addressed the soil response during a change of the total stresses. However, the solution has been met the many limitations in applicability, particular in drained and undrained problems. The effective stress is well-controlled for the behavior of a soil, even under monotonic loading and cyclic loading. Therefore, most constitutive models recently are based on the stress history and the changes in effective stresses. Given a tensor of total stress is σ_{ij} (compression positive) and the pore pressure is u, the tensor of effective stress is σ'_{ij}. The effective stress tensor is defined as given

$$\sigma'_{ij} = \sigma_{ij} - u\delta_{ij} \tag{4.9}$$

Herein, the tensor, δ_{ij}, is called the Kronecker delta, $\delta_{ij} = 1$ for $i = j$; and $\delta_{ij} = 0$ for $i \neq j$

4.6.1. Elastic-perfectly plastic model

With a linear elasticity behavior of the model, it is impossible to address the hysteresis loops of the soil behavior under monotonic or cyclic loading due to their non-incremental stiffness. The experimental results and theoretical aspects figured out that the stiffness degradation and the damping evolution occur as the cyclic shear strain level increases in both monotonic and cyclic loading cases. An elastic-perfectly plastic model can exhibit a decrease of the average secant stiffness with an increase of the strain amplitude (Prisco and Wood, 2012), as described in Fig. 4.16. The response of the secant tangent stiffness is considered as the combination of a constant pre-failure stiffness at an imposed strain and a stiffness at failure that is zero (Fig. 4.17). If the shear strain at the failure of an elastic-perfectly plastic soil with shear modulus G is γ_f, then γ_m corresponds to the shear stress of $G\gamma_f$, the secant stiffness G_s is defined as the below equation.

$$G_s = G\frac{\gamma_f}{\gamma_m} \tag{4.10}$$

The dissipated energy and the maximum stored elastic energy in each cycle are shown in Equation 4.11 and 4.12, respectively. After that, the damping ratio D is calculated in Equation 4.13.

$$W = 4G\gamma_f^2\left(\frac{\gamma_m}{\gamma_f} - 1\right) \tag{4.11}$$

$$\Delta W = \frac{1}{2} G \gamma_f^2 \frac{\gamma_m}{\gamma_f} \tag{4.12}$$

so that

$$D = \frac{2}{\pi}\left(1 - \frac{\gamma_f}{\gamma_m}\right) \tag{4.13}$$

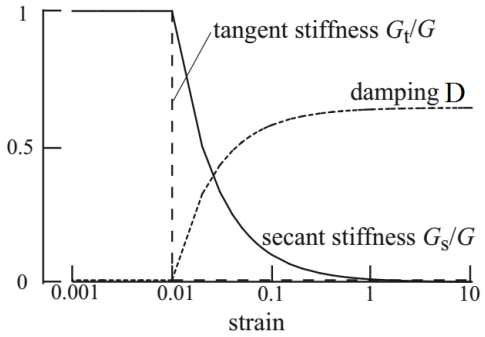

Fig. 4.16. Variation of stiffness and damping ratio with a shear strain of the elastic-perfectly plastic Mohr-Coulomb model (at yield strain = 0.01) (Prisco and Wood, 2012)

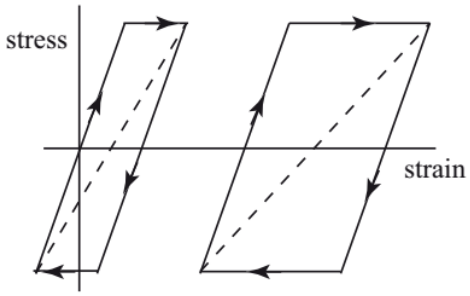

Fig. 4.17. Dependency of the strain amplitude on the secant stiffness under load cycles of the elastic-perfectly plastic model (Prisco and Wood, 2012)

4.6.2. Cam Clay model

The modified Cam-clay (MCC) is an incremental hardening/softening elastoplastic model, in which the nonlinear elasticity and the hardening/softening behavior are governed by volumetric plastic strains. This model was successfully used to reproduce the behavior of soft soils (Roscoe and Burland, 1968; Wood, 1990). However, the MCC model is also not often used for soil under load cycles. Some soil response modelings under cyclic undrained loading have employed the MCC model. O'Reilly and Brown (1991) indicated that under the cycles of constant amplitude of deviatoric stress, the yield locus (coinciding with the plastic potential) was developed on the first loading and then remained at constant size, so that all changes in further stress could be

elastically supported. Under the cycles of the constant amplitude of the distortion strain ε_q, the yielding occurs in each reversal path in order to generate sufficient plastic strain (Prisco and Wood, 2012) as depicted in Fig. 4.18. From the theoretical point of view, the formulations of the model were based on elasticity, plasticity and critical state theories which were suitable to characterize realistically the volume changes by different loading types, the nonlinearity behavior, the softening and hardening, and the critical state.

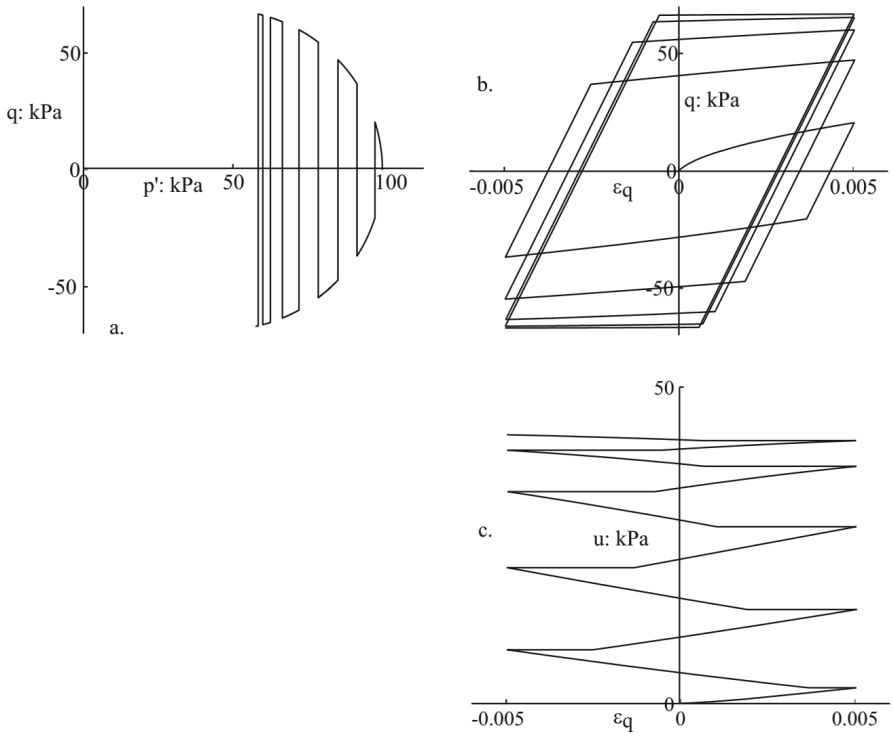

Fig. 4.18. Undrained cyclic triaxial tests using the Cam-clay model: (a) effective stress paths; (b) stress-strain relationship; (c) Pore pressure accumulation (Prisco and Wood, 2012)

4.6.3. Kinematic hardening plasticity

When the stress state reaches the yield surface, this surface will be expanded outwards, and the increase of the yield surface increases the elastic region that remains. The consideration of a kinematic rule allows the elastic region to change both in its size and its position. The Cam-clay model cannot model the development of plasticity for the unloading paths. Therefore, the extension of a kinematic rule for plasticity models can address such response. As a suggestion in Prisco and Wood (2012), the kinematic hardening extension should be so far advisable for isotropic hardening models: the yield locus of Cam-clay model keeps its shape and orientation, and it will pass through the original stress space as the stress path interacts with it; the

Mohr-Coulomb model's yield locus opens gradually its size.

4.6.3.1. Kinematic Hardening Mohr-Coulomb Model

To overcome the shortcomings caused by purely elastic for all stress ratios lower than the previous maximum stress ratio, adding kinematic hardening extension in this model allows the elastic region for high stiffnesses to be modified with different stress histories (Fig. 4.19). Obviously, the boundary of this elastic region is the yield surface. However, to specify and retain a hierarchical link with previous models, the elastic range is called a yield surface and the previous yield surface called a bounding surface plasticity (Dafalias and Popov, 1975). Therefore, the plastic-hardening stiffness can be separately dependent on the yield surface and bounding surface. Based on the careful choice of the interpolation function of stiffness, the continuous and smooth variation of stiffness is translated from the elastic to the fully plastic value as the stress state moves from the inner yield surface towards the outer surface. The effects of initial density and stress level are taken into account by a single set of soil parameters. The softening developed within a localized shear band can also be described. The effects of localization in sand samples are also brought in more detailed by (Gajo et al., 2004) based on an equivalent model to the Severn-Trent sand. The results of Gajo and Muir Wood (1999) indicated that the model can be successfully validated using triaxial tests data for the Hostun sand, as shown in Fig. 4.20.

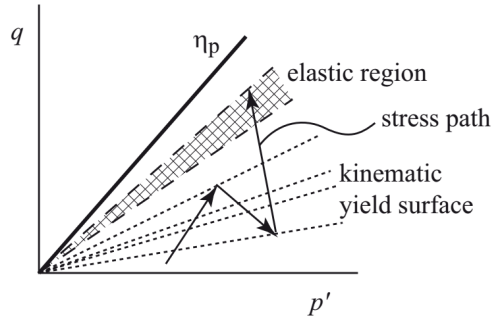

Fig. 4.19. Kinematic hardening Mohr-Coulomb model

A trial of this model to validate undrained cyclic triaxial tests of Hostun sand was carried out by Gajo and Muir Wood (1999). The numerical results showed that the soil sample was reached liquefaction after 25 cycles compared to 89 cycles in the experimental data, as illustrated in Fig. 4.21. However, the important conclusion here is that it is possible for this model to introduce the cyclic soil response concerning the volume change of soil characteristics.

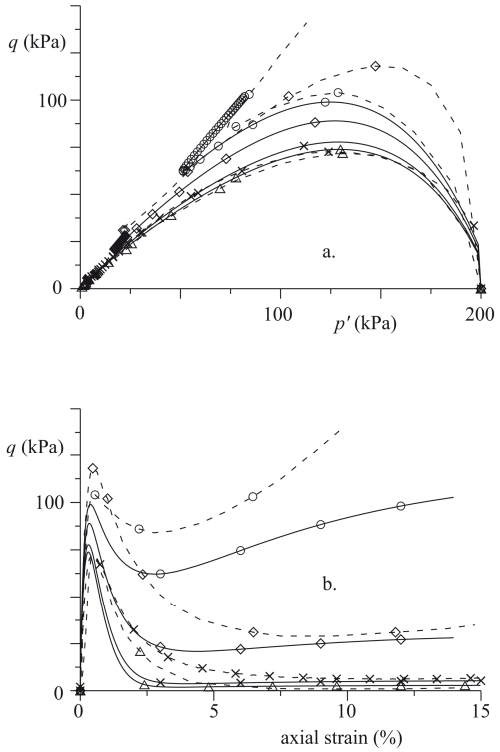

Fig. 4.20. Comparison of simulations and experiments: effect of initial density on triaxial undrained compression tests on Hostun sand with an initial mean effective stress *p'*= 200 kPa (Gajo and Muir Wood, 1999)

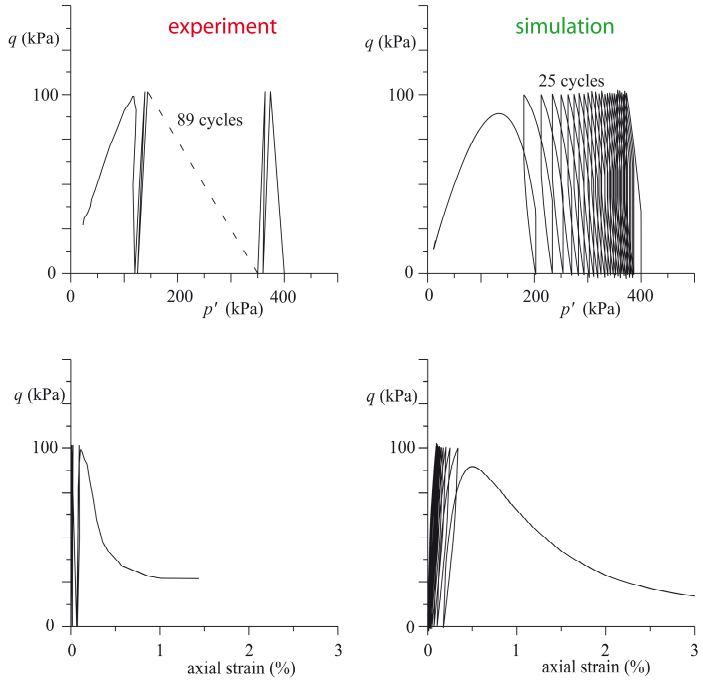

Fig. 4.21**.** Comparison between simulations and experiments for undrained cyclic loading on loose Hostun sand (Gajo and Muir Wood, 1999)

4.6.3.2. Kinematic Hardening 'Bubble' Cam-clay Model

A kinematic hardening extension for the Cam-clay model was proposed by Al-Tabbaa and Muir Wood (1989). The elastic region is confined by a yield surface named 'bubble', it can float around the bounding surface (representative for the current stress state). The movements of the 'bubble' result in plastic strains. The 'bubble' surface can be in contact with the bounding surface, but it never crosses the bounding surface. The plastic stiffness varies flexibly with the distance between the 'bubble' and the outer bounding surface, *b*. It reduces as the 'bubble' approaches the bounding surface, as presented in Fig. 4.22.

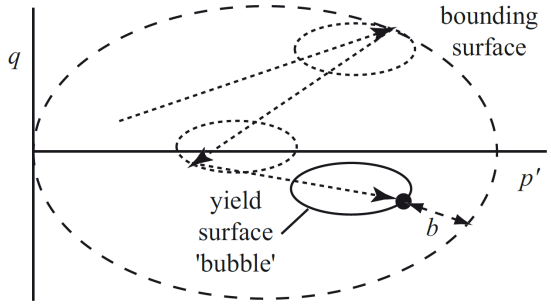

Fig. 4.22. Kinematic hardening extension of Cam-clay (Al-Tabbaa and Muir Wood, 1989)

Related to the cyclic response of this model, the adopted non-associated flow rule enables the change in shear and volume behavior to be suitably described, especially for the shear dilatancy. The Cam-clay model's flow rule is determined, as below.

$$\frac{d\varepsilon_v^p}{d\varepsilon_s^p} = \frac{\left(M_g^2 - \eta^2\right)}{2\eta} \tag{4.14}$$

Where η is the stress ratio q/p_0; M_g is the critical state slope related to the stress ratio as there is no further volumetric strain. In the loading phase, a plastic compression occurs if $\eta < M_g$, and a plastic dilatancy occurs if $\eta > M_g$. An associated plastic flow rule is then adopted, as follows.

$$\frac{d\varepsilon_v^p}{d\varepsilon_s^p} = \frac{\left(p' - \alpha_p\right)M_f^2}{q - \alpha_q} \text{ for } p' \le \alpha_p$$

$$\frac{d\varepsilon_v^p}{d\varepsilon_s^p} = \frac{\left(p' - \alpha_p\right)b^2 M_f^2}{(1-b)^2\left(q - \alpha_q\right)} \text{ for } p' > \alpha_p \tag{4.15}$$

With $M_f = M_g$

Obviously, the functional plastic phase, the critical state, and the dilative phase expressed in Equation. 4.15 are dependent on the relative position between the

current effective stress path and the center of bubble yield surface instead of the value of M_g-η (as in the MCC model). Therefore, a non-associated flow rule is defined by modifying the associated flow rule expressed by Equation. 4.15.

$$\frac{d\varepsilon_v^p}{d\varepsilon_s^p} = \frac{\left(M_g - \eta\right)\left(2p' - 2\alpha_p + Rp'_c\right)}{k_g\left[2\left(q - \alpha_q\right) + Rp'_c\right]} \text{ for loading/reloading}$$
$$\frac{d\varepsilon_v^p}{d\varepsilon_s^p} = \frac{\left(M_g + \eta\right)\left(2p' - 2\alpha_p - Rp'_c\right)}{k_g\left[2\left(q - \alpha_q\right) - Rp'_c\right]} \text{ for unloading} \quad (4.16)$$

Therein, k_g is the material constant that manages the magnitude of the ratio of the plastic volumetric strain increment to the plastic shear strain increment. Additionally, thanks to introducing the three model parameters that stand for the hardening rate during the first unloading-reloading cycle, the elastoplastic model combining isotropic-kinematic hardening is able to model the cyclic loading response for natural stiff clays (Hong et al., 2014).

4.6.3. Hypoplasticity model

The model was proposed by Kolymbas (1977). The generalized hypoplastic constitutive law was represented by Kolymbas (1985) and (Kolymbas and Karlsruhe, 1991) in which the inelastic behavior of materials had formulated using a single nonlinear tensorial equation of rate-type. Due to neither yield surface nor the decomposition of the deformation into elastic and plastic components, the hypoplastic constitutive equations are substantially different from the previous elastoplastic constitutive ones. These model's constitutive equations do not only address the nonlinearity of the soil, the influence of density and dilatancy (*pyknotropy*), and pressure level (*barotropy*) (Gudehus, 1996), but also take into account the effect of the recent history of deformation on the soil response at small to very small strains (Niemunis and Herle, 1997).

In terms of cyclic loading aspects, thanks to introducing the concept of *intergranular* strain, the model allows the stiffness to increase with the stress rotation. Several former studies considering complex loadings were successfully carried out: a building affected by an earthquake (Gudehus et al., 2008), the prediction for a long-term behavior of a building under a low number of cyclic loading (Von Wolffersdorff and Schwab 2009), and a GRPS earth platform under static and variable loads (Moormann et al. 2016). Due to its advanced laws, the HYP model will be for studying the piled embankment under cyclic loading in the following works. A brief presentation about constitutive equations, parameters, and calibration procedure is given just below.

4.7. Hypoplasticity constitutive model (HYP)

4.7.1. Constitutive equations

4.7.1.1. General hypoplastic model

The proposed constitutive equation can be written as (Gudehus, 1996)

$$\overset{o}{T}_s = f_b f_e \left[L\left(\hat{T}_s, D_s\right) + f_d N\left(\hat{T}_s\right) \left\| D_s \right\| \right] \tag{4.17}$$

Where $T_s := T_s / trT_s$ is the sign of the granulate stress ratio tensor. The tensor-valued function is linear with respect to D_s. The term with $\left\| D_s \right\|$ is nonlinear is the Euclidean norm of D_s. The factor f_b stands for *barotropy,* and f_e and f_d represent for *pyknotropy*. L and N were determined by (Bauer, 1996), as

$$L := a_1^2 D_s + \hat{T}_s tr\left(\hat{T}_s D_s\right) \tag{4.18}$$

$$N := a_1 \left(\hat{T}_s + \hat{T}_s^*\right) \tag{4.19}$$

Wherein $\hat{T}_s^* := \hat{T}_s - 1/3I$ denotes the deviator stress tensor of $\hat{T}_s$. The component depends on T_s^*, given as

$$\frac{1}{a_1} := c_1 + c_2 \left\| T_s^* \right\| \left[1 + \cos(3\theta) \right] \tag{4.20}$$

With the modulus $\left\| T_s^* \right\|$ and $\cos(3\theta)$ are derived $\left\| T_s^* \right\| := \sqrt{tr \cdot T_s^{*2}}$ and the Lode parameter $\cos(3\theta) = -\sqrt{6} tr\left(T_s^{*3}\right) / \left[tr\left(T_s^{*2}\right) \right]^{3/2}$. The constants c_1 and c_2 are defined using the critical friction angle φ_c.

4.7.1.2. The comprehensive hypoplastic constitutive model

Based on the extension of the hypoplastic constitutive model developed by Gudehus and Bauer, the modified constitutive model of von Wolffersdorff (1996) is presented in Equation 4.21.

$$\overset{o}{T}_s = f_b f_e \frac{1}{tr\left(\hat{T}^2\right)} \left[F^2 D + a^2 tr(TD) \hat{T} + f_d a F \left(\hat{T} + \hat{T}^*\right) \left\| D \right\| \right] \tag{4.21}$$

With

$$a = \frac{\sqrt{3}\left(3 - \sin\varphi_c\right)}{2\sqrt{2}\sin\varphi_c} \tag{4.22}$$

F is a function of $\hat{T}^*$, it is can be shown by the equation, as

$$F = \sqrt{\frac{1}{8}\tan^2\psi + \frac{2-\tan^2\psi}{2+\sqrt{2}\tan\psi\cos(3\vartheta)}} - \frac{1}{2\sqrt{2}}\tan\psi \tag{4.23}$$

Herein

$$\tan\psi = \sqrt{3}\left\|\hat{T}^*\right\|, \cos\vartheta = -\sqrt{6}\frac{tr\left(\hat{T}^{*3}\right)}{\left[tr\left(\hat{T}^{*2}\right)\right]^{3/2}} \tag{4.24}$$

And the characteristic void ratios are

$$\frac{e_i}{e_{i0}} = \frac{e_c}{e_{c0}} = \frac{e_d}{e_{d0}} = \exp\left(-\left(\frac{trT}{h_s}\right)^n\right) \tag{4.25}$$

The dependencies of *pyknotropy* are

$$f_e = \left(\frac{e_c}{e}\right)^\beta \tag{4.26}$$

and

$$f_d = \left(\frac{e-e_d}{e_c-e_d}\right)^\alpha \tag{4.27}$$

Barotropy function influences, as shown

$$f_b = \frac{h_s}{n}\left(\frac{1+e_i}{e_i}\right)\left(\frac{e_{i0}}{e_{c0}}\right)^\beta\left(-\frac{trT}{h_s}\right)^{1-n}\left[3+a^2-\sqrt{3}a\left(\frac{e_{i0}-e_{d0}}{e_{c0}-e_{d0}}\right)^\alpha\right]^{-1} \tag{4.28}$$

4.7.1.3. Combination of the hypoplasticity model with the elastic strain range

By introducing an *intergranular strain* δ (interface deformation), Niemunis and Herle, (1997) considered the small strain stiffness and the recent stress history effects as a new state variable, so the strain can be defined based on both the intergranular-interface-layer deformation and the skeleton rearrangement. By this way, the general stress-strain relation can be written as:

$$\overset{o}{T} = M : D \tag{4.29}$$

The fourth-order tensor (*M*) represents the stiffness. It is determined from the hypoplastic tensor *L(T,e)* and *N(T,e),* which may be adjusted by scalar multipliers m_T and m_R depending on $\left(\hat{\delta} : D\right)$ as in the below equation.

$$M = \left[\rho^{\chi} m_T + \left(1-\rho^{\chi}\right) m_R\right] L + \begin{cases} \rho^{\chi}\left(1-m_T\right) L : \hat{\delta}\hat{\delta} + \rho^{\chi} N\hat{\delta} & \text{for } \hat{\delta} : D > 0 \\ \rho^{\chi}\left(m_R - m_T\right) L : \hat{\delta}\hat{\delta} & \text{for } \hat{\delta} : D \le 0 \end{cases} \tag{4.30}$$

To consider the limit state of the intergranular strain concept, a constant, namely *R,* is used to control the maximum value of the intergranular strain region, it is not dependent on the stress level. Moreover, the development of the strains inside the elastic range can be described by the following equation.

$$\overset{o}{\delta} = \begin{cases} \left(I - \hat{\delta}\hat{\delta}\rho^{\beta_r}\right) & \text{for } \hat{\delta} : D > 0 \\ D & \text{for } \hat{\delta} : D \le 0 \end{cases} \tag{4.31}$$

To describe the general model, eight material constants are required (parameters 1 to 8). The small strain range concept was modeled by five additional constants (parameters 9 to 13). The thirteen parameters of the model are presented in Table 4.1. To be unified in the following parts, the term 'hypoplastic model' (HYP) is used for the hypoplastic model with the intergranular strain concept.

Table 4.1. Parameters of the HYP model

No.	Parameters	Unit	Symbol
1	Critical state friction angle	°	φ_c
2	Granulate hardness controls the shape of the void ratio curve	Pa	h_s
3	Exponent controls the shape of the void ratio curve	-	n
4	Minimum void ratio at zero pressure	-	e_{d0}
5	Critical void ratio at zero pressure	-	e_{c0}
6	Maximum void ratio at zero pressure	-	e_{i0}
7	Exponent controls a dependency of peak friction angle on relative density	-	α
8	Exponent controls the dependency of soil stiffness on relative density	-	β
9	The parameter controls the initial shear modulus upon 180° strain path reversal and in the initial loading	-	m_R
10	The constant controls the initial shear modulus upon 90° strain path reversal	-	m_T
11	The size of the elastic strain range in the strain space	-	R
12	The constant manages shape of stiffness degradation curve	-	β_r
13	The constant controls the shape of stiffness degradation curve	-	χ

4.7.2. Calibration procedure

This model requires the thirteen parameters in Table 4.1. The calibrating procedure for eight constants of the model was clearly presented by Herle and Gudehus (1999). Large strain shearing tests were first used to define φ_c. Oedometer tests were then used to identify h_s and n based on the relationship of the void ratio and of the

logarithm curve with the mean pressure (*e-lnp'*). The values of e_{d0} and e_{i0} were indirectly determined using the curves proposed by Youd (1973) and Equation 4.32, while e_{c0} is obtained from the laboratory tests based on its similarity with e_{max}. The constants α and β were determined using triaxial tests based on dense sand samples. The different values of α led to the change in the peak of the stress-strain curve while β influences the size of the response envelope (bulk and shear stiffness).

The void ratios at a null pressure are extrapolated by Equation 4.32, below:

$$e_{d0} = e_d \exp\left(\left(\frac{3p_s}{h_s}\right)^n\right) \tag{4.32}$$

In addition, the five parameters that manage the cyclic response of the soil are defined based on the data from bender element tests and from cyclic loading tests. As recommended by Masin (2015):

- m_R is specified based on the bender element test
- m_T is difficult to determine. It is taken = $0.7m_R$
- χ, β_R and R are calibrated using the degradation curve or cyclic loading data

m_R is a proportionality constant. It is calibrated by fitting the initial shear stiffness derived from bender element tests, as presented in Fig. 4.23.

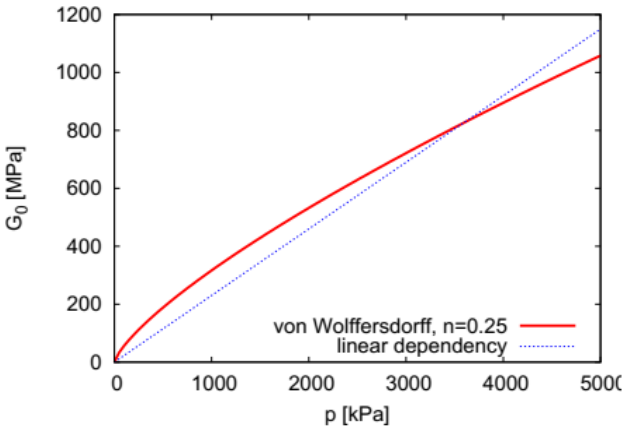

Fig.4.23. The generation of the G_0-p curve

The values of χ, β_r and R are determined based on degradation curve, as in Fig. 4.24.

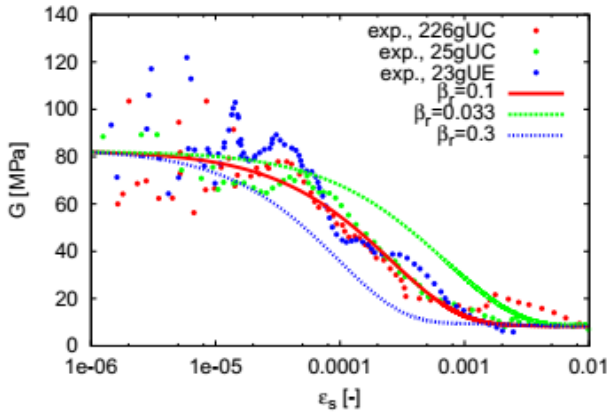

Fig. 4.24. The degradation curve of stiffness versus strain

Additionally, the cyclic loading data is used for defining the set of parameters of intergranular strain concept of the HYP model. However, it is difficult to distingush the influence of individual parameters. The parameters χ and β_r have the same influence as the parameter m_T. The cyclic loading test has been suggested for determining β_r in Fig. 4.25.

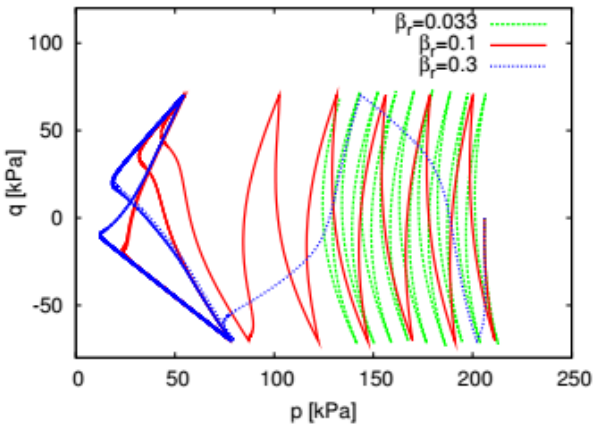

Fig. 4.25. The influence of β_r on the cyclic response of HYP model

Due to the complexity of calibration procedure and the experimental tests required, not many sets of the *intergranular* strain parameters for sands were obtained in the literature.

4.7.3. Sensitivity of parameters

In the study, the Karlsruhe sand is selected for the embankment since it was well documented in the literature relating to physical and mechanical properties (Kolymbas and Wu 1990; Bauer 1996). A set of general model parameters for the Karlsruhe sand was proposed by Herle and Gudehus (1999) as given in Table 4.2. The sources of the

HYP model were used and implemented in the Abaqus software. Firstly, the set of parameters is tested in the Abaqus software with three different confining pressures. The initial value of void ratio was taken equal to 0.6 in the analyses. The initial results are presented in Fig. 4.26.

Table 4.2. A set of HYP model's parameters for the Karlsruhe sand proposed by Herle and Gudehus (1999)

φ_c [°]	h_s [MPa]	n	e_{d0}	e_{c0}	e_{i0}	α	β	e_{ini}
30	5,800	0.28	0.53	0.84	1.00	0.13	1.0	0.6

As can be seen from Fig. 4.23, the fitting between the numerical results and experimental ones is not good enough. It was necessary to calibrate it again. Derived from basic parameters, sensitivity analyses on the parameters were done. Based on Table 4.1, the three parameters which control the stress-strain relationship in the triaxial tests are φ_c, α and β. The results of the sensitivity analyses are shown in Figs. 4.27, 4.28 and 4.29. Several minor adjustments for these parameters were given to obtain a better fitting between the numerical results with the experimental data in the triaxial tests in Table 4.3.

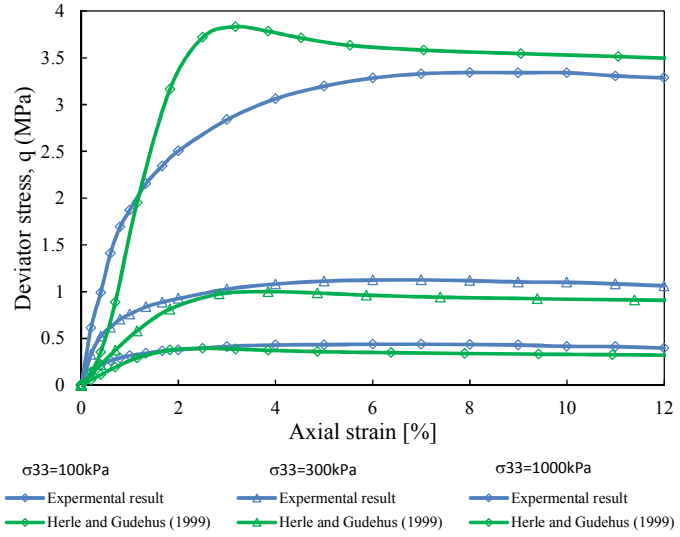

Fig. 4.26. A comparison of numerical triaxial tests of parameters of Herle and Gudehus and experimental data

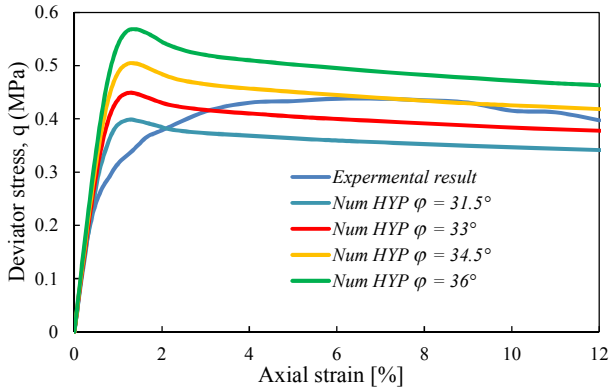

Fig. 4.27. Dependency of φ_c on the peak of the stress-strain curve

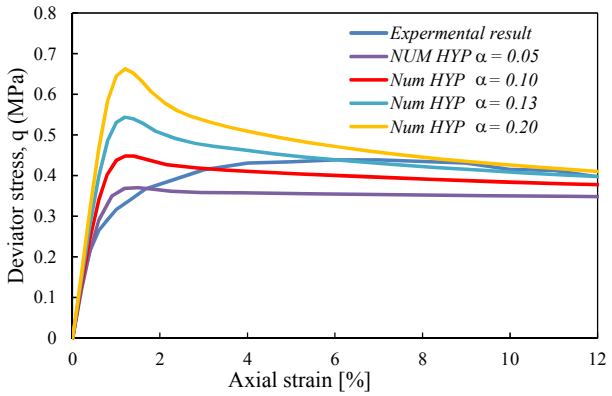

Fig. 4.28. Dependency of α on the peak of the stress-strain curve

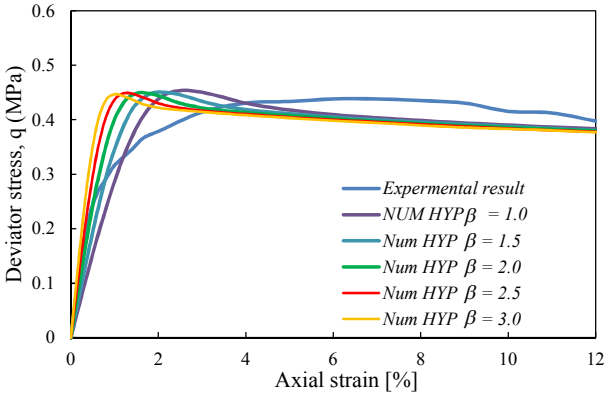

Fig. 4.29. Dependency of β on the shear stiffness (slope) of the stress-strain curve

Due to the insufficient data for calibrating these parameters, the set of parameters estimated by Niemunis and Herle (1997) for the Hochstetten sand is suggested to use. They have been formerly demonstrated that they were appropriate for several types of sand under cyclic loading (von Wolffersdorff and Schwab, 2009; Salciarini and Tamagnini, 2009; Ochmański et al. 2015; Li et al. 2016; Poblete et al. 2016). In this

study, these HYP intergranular strain parameters were employed, as shown in Table 3. The numerical triaxial tests with the new set of parameters are described in Fig. 4.27.

Table 4.3. Parameters of the HYP model for the Karlsruhe sand

φ_c [°]	h_s [MPa]	n	e_{d0}	e_{c0}	e_{i0}	α	β	R	m_R	m_T	β_r	χ	e_{ini}
33	5,800	0.28	0.53	0.84	1.00	0.10	2.5	$1x10^{-4}$	5	2	0.5	6	0.6

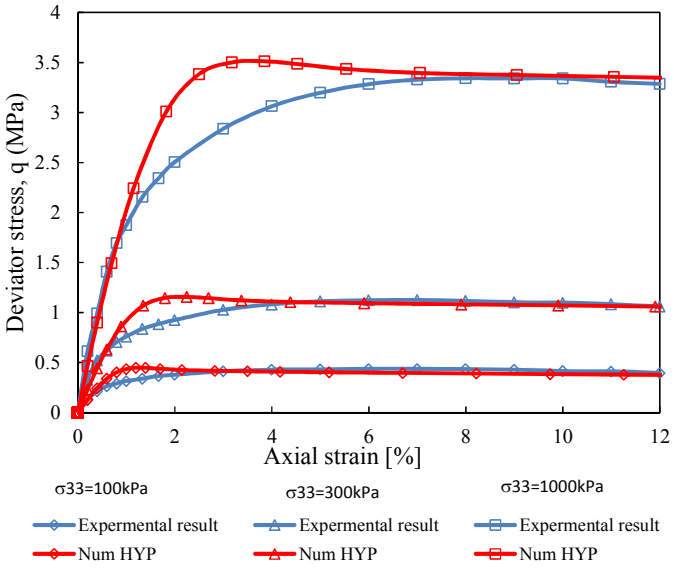

Fig. 4.30. Drained triaxial test results for the Karlsruhe sand sample at different confining pressures (e_{ini} = 0.6)

4.8. Conclusions

The theoretical studies for the cyclic behavior of soils provide to the valuable conclusions, which are.

Firstly, the variation of the loading intensity with time often encounters for real structures. The cycle loading influence should be considered as the applied loading rate is large enough.

Secondly, the analyses of the stress-strain relationship indicate that the shear strain level is really important for the soil response under cyclic loading. For the medium and large values of the shear strains, irrecoverable permanent deformation occurs. The shear modulus and damping ratio are considered as two important parameters for the soil response under cyclic loading. The influence of the loading conditions, soil physical properties and stress history on the stress-strain relationships are figured out.

Thirdly, the accumulated strains of a soil induced by the load cycles leads to significant additional settlements and differential settlements, so the structures may become unstable and unsafe. Strain accumulation under cyclic loading may be derived from the rearrangement of particles, the breakdown of texture and the abrasion of particles.

In addition, considering the influence of the factors on the cumulative strain, the strain accumulation is significantly affected by a number of load cycles, stress/strain amplitude, initial relative density and grain-size distribution. Meanwhile, it is less influenced by the frequency of the cyclic loading and the average mean stress.

In addition, based on the literature review, several constitutive models of soils under cyclic loading were presented, the conventional soil models (MC and MCC models) under-predict the soil response under load cycles, particularly the stiffness degradation and strain accumulation. The advanced soil constitutive models, like the kinematic hardening and the hypoplasticity, can reproduce in a better way the cyclic behavior of soils.

Furthermore, the hypoplastic model will be used in the following parts of this work because of its advantages. Firstly, by introducing the concept of *intergranular* strain, the model allows the stiffness to increase with the stress rotation. The consideration of density, dilatancy and stress level in the model permits to model the soil behavior in a realistic manner. The degradation of stiffness is also taken into account by three additional constants.

Finally, the calibration procedure and sensitivity analysis of parameters are introduced. The Karlsruhe sand parameters are presented with some minor adjustments.

Chapter 5

Soft soil improvement by rigid inclusions under cyclic loading

5.1. Introduction

While the embankment over a rigid inclusion-reinforced soil (a piled embankment) subjected to static loading has been well understood, a limited attention was paid to the study of the structural behavior under cyclic loading. The aim of this chapter is to investigate the cyclic response of a piled embankment using 3D numerical simulations. As mentioned in Chapter 4, the HYP model has been successful in simulating the cyclic behavior of granular soil and will be used in the following analyses. In this chapter, the main contents are presented as follows:

After reviewing the cyclic behavior of piled and GRPS embankments, the numerical modeling of laboratory tests on a soil improvement by rigid inclusions under monotonic and cyclic loadings is performed, in which the HYP model is used for the load transfer platform (LTP). The numerical results are compared against both the experimental data and numerical ones of Houda.

In the following part, a study on the behavior of a piled embankment subjected to different traffic cyclic loadings is carried out. The HYP is used for granular soil and compared to the conventional one (a linear elastic, perfectly plastic model with the Mohr-Coulomb's failure criterion, MC) for static and cyclic loading aspects. The influence of the number of traffic load cycles, the vehicle speed, and the embankment height are taken into account. The results are represented in terms of load transfer mechanisms, arching effects, and settlements. The comparisons with former investigations are performed.

In the last section, the cyclic response of a geosynthetic-reinforced pile-supported (GRPS) embankment is studied in terms of soil arching, geosynthetic tension, and cumulation of soft soil and embankment settlement. The role of geosynthetic in the piled embankment is first considered by comparing between the unreinforced and reinforced piled embankments under static and cyclic loading aspects. Parametric studies related to the cyclic loading number as well as the number of geosynthetic layers are studied as well.

The conclusions and perspectives are given in each part of the chapter.

5.2. Literature review on piled and GRPS embankments under cyclic loading

The studies of piled embankment subjected to static loading (embankment and surcharges) are often studied. In fact, the cyclic loading impact cannot be ignored in some cases, particularly for foundation vibrations, traffic, wave and wind loadings. To better understand the stress transfer within a piled embankment induced by a cyclic loading, Heitz et al. (2001) employed a small scale (1:3) model test. They stated that the parameters that influence on the arching effect are the number of cycles, the frequency, the amplitude, the *H/s* ratio and the geosynthetic layers. However, how they influence the on load transfer and on the settlements are not mentioned. Additionally, Han et al. (2011a,b) investigated the mechanical features of soil arching subjected to dynamic loads using experimental tests and the Discrete Element Method (DEM). They showed that the embankment height and the load amplitude were significantly influent on the failure arching: the required time for the collapse of the arching significantly increases with the embankment thickness while the soil arching failure increases with the loading amplitude. Similarly, Yu et al. (2009) also conducted experimental tests subjected to the embankment weight and to the traffic loading. They found that the vertical stress applied onto soil increases with the repeated number of load cycles. When the number of cycles is over 300, the vertical stress did not change more with the depth, which showed no soil arching effect. They also suggested the wedge theory proposed by Carlsson (1987), in which it is suitable to calculate the stress state in piled embankment under traffic loads. The dependence of the soil arching collapse with the embankment height was investigated by model tests without a geogrid and subsoil (Han et al., 2015). They indicated that the soil arching collapsed after the dynamic load was applied when *H/D*, the ratio of the height of the embankment to the diameter of the hole, was less than 3. The small-scale model tests of Houda et al. (2016) were performed to analyze a pile-supported earth platform subjected to low-frequency cyclic loadings (f = 0.33×10^{-3} to 0.83×10^{-3} Hz). They specified that the efficacy increased with the number of cycles up to 30 cycles, and then, remained stable. The settlements significantly increase during the first ten cycles.

Numerical analysis was also often used to deal with this problem. Okyay et al. (2008) studied the dynamic characteristics of the piled embankment by 3D modeling using FDM, in which the influence of the mechanical properties, the geometry, the dynamic boundary, the element size and the damping were shown. A study of Han and Bhandari (2009) based on DEM showed a cumulation of plastic strain within the embankment fill with the number of loading cycles. In addition, the setup of a geogrid

led to a decrease of the permanent deformation and to the increase of the stress concentration ratio in comparison to the unreinforced case. Nonetheless, only 25 load cycles were performed in the study. The influence of the fill height and of the loading amplitude on the soil arching under dynamic load were presented by Han et al. (2011a). A 3D numerical modeling using FEM was carried out to study the soil arching under traffic loading (considering sinusoidal curves) (Zhuang and Li, 2015). The influences of the cyclic loading amplitude and of the number of cycles on the arching effect were figured out, especially for the embankment settlements. The soft soil was simulated by a uniform vertical stress *(σ_s)* applied upward the fill layer. A constitutive model as the elastoplastic model with the Mohr-Coulomb failure criterion was considered to be insufficient to characterize the embankment fill response under a cyclic loading. Han et al. (2015) performed 2D modeling using FEM to study the influence of embankment height on the soil arching under dynamic load. The numerical results showed that due to the existence of the geogrid and the subsoil, the soil arching was stable even the value of *H/D* was equal to 1.4. Moormann et al. (2016) built a 3D numerical model to study the influence of GRPS embankments under a few load cycles. The numerical simulations showed that there was no significant influence of the multiple layers of reinforcement on the soil arching. Lehn et al. (2016) investigated the stress distribution inside the embankment and over the geogrid under cyclic loading numerically. The results indicated that the stress distribution inside the geogrid is well described using the Concentric Arches theory (van Eekelen et al. 2013). The shape of the arch in the sand layer changed under non-static actions.

The behavior of piled and GRPS embankments in terms of load transfers and settlements under cyclic loading has not been clearly presented in the literature. In addition to that, the research on the influence of a high number of loading cycles has not been conducted. Some of the former studies considered simple constitutive models for the granular embankment, which cannot address the cumulative settlements to the number of loading cycles.

5.3. Numerical modeling of rigid inclusions experimental tests - Monotonic and cyclic loading

5.3.1. Introduction

The aim of the numerical study is to investigate the load transfer mechanism and cumulative settlements of the soil improvement system under monotonic and cyclic loading. The advanced soil constitutive model (HYP) is applied for the LTP. The numerical results are compared with both the experimental data and the numerical results of Houda (2016).

5.3.2. Experimental tests

5.3.2.1. Objective

The experimental work was performed by Houda et al. (2016). The aim of its study was to investigate the monotonic and cyclic response of a rigid inclusion-reinforced soil. Parametric studies concerning the load transfer platform (LTP) thickness, the loading sequence, and the different boundary conditions were done. The influence of a cyclic loading on the system was also considered.

5.3.2.2. Description of the physical model

A 1:10 scale physical model under normal gravity was set up, in which all the dimensions were reduced 10 times. The detail of the model was presented in Houda (2016). 16 aluminum cylinder piles were installed in a square box of 1 $\times$ 1 m. The piles have a diameter of 35 mm and a length of 600 mm. They were arranged in a square grid of 0.2 $\times$ 0.2 m, with an improvement area ratio α = 2.4%. In addition, four half piles were added next to the window, which allowed visualizing the mechanisms within the LTP, as shown in Fig. 5.1. A 0.4-m-thick layer of soft material was setup followed by a layer of gravel (LTP or mattress). Different testing cases were done by changing the thickness of LTP (50 and 100 mm). A rigid slab on the gravel layer top was considered as the pavement. The monotonic and cyclic loadings were applied onto the surface of the mattress or slab by a pressured control system via a membrane.

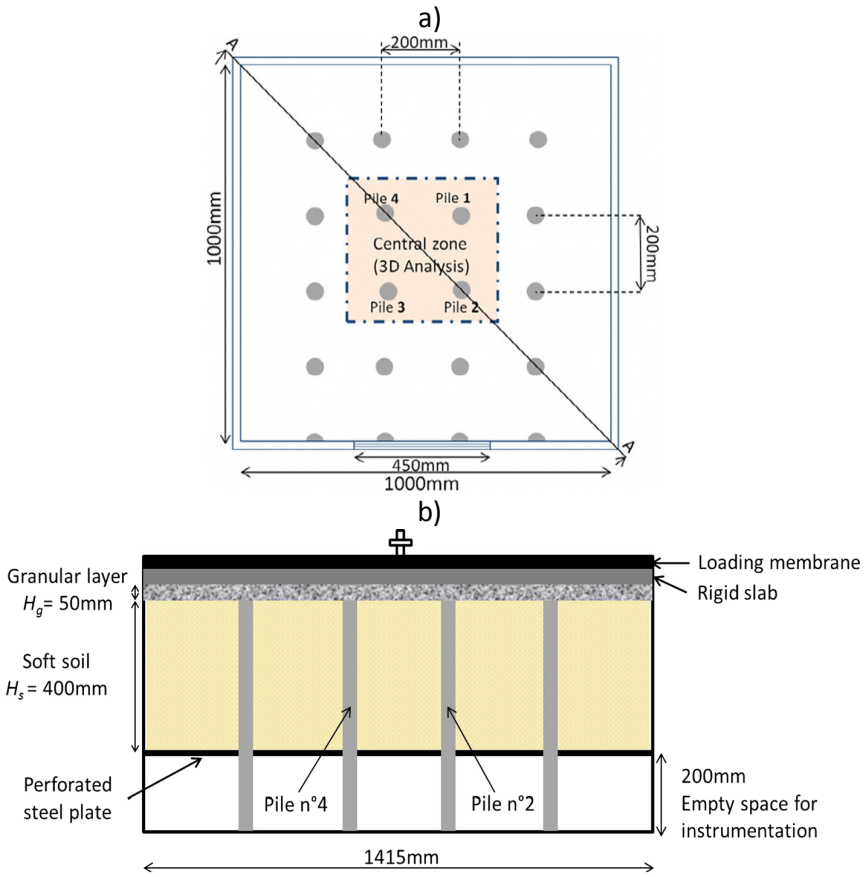

Fig. 5.1. Arrangement of the physic model: (a) Plan view; (b) View A-A (Houda et al., 2016)

5.3.2.3. Installation of the sensors for the instrumentation

The sensors for instrumentation were placed in the central zone, as seen in Fig. 5.2. Four 1-kN force sensors (Ft1, Ft2, Ft3 and Ft4) were integrated into the pile heads to measure the pile head forces. The displacement sensors (Disp1, Disp2 and Disp3) were positioned diagonally between pile 2 and 4. They permit to measure the LTP base settlement. Each one was fixed under the steel plate and extended up to the LTP-soft soil interface by a 3-mm-diameter steel rod. While the settlement at the mid-span of two adjacent piles was monitored by D3, the one next to the pile was visualized by D1. The volume and pressure of the water inside the membrane were also measured.

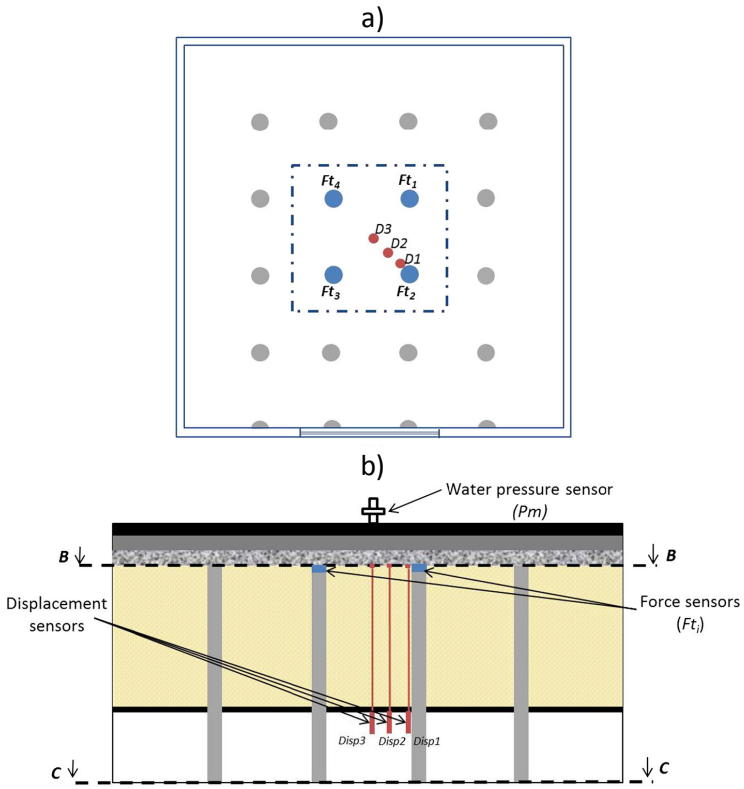

Fig. 5.2. Installation of the instrumentation sensors: a) view B-B; b) view B-B (Houda et al., 2016)

5.3.2.4. Testing and loading procedures

In the experimental campaign, three geometric configurations were set up to investigate the effect of the mattress thickness and boundary conditions, which include:

- A mattress of 100 mm with a rigid slab at the surface D100;
- A mattress of 50 mm with a rigid slab at the surface D50;
- A mattress of 100 mm without rigid slab at the surface R100.

The testing program was performed to evaluate the behavior of the system in terms of load transfer mechanism and cumulative settlements under monotonic and cyclic loadings.

The monotonic loading (M) was applied sequentially by three pressure loading stages of 10, 20 and 30kPa, followed by a discharge. Four types of cyclic loading (C) were subjected to the model, as illustrated in.

- Cyclic 1 (C1) was started with a loading of 20kPa followed by 50 cycles between 10 and 20 kPa. It was then continued by a loading until 30 kPa before an unloading to 0 kPa.

- Cyclic 2 (C2) began with a loading progress of 30 kPa. Then 50 cycles between 10 and 20 kPa were achieved and finally an unloading.

- Cyclic 3 (C3) was the same as Cyclic 1, but the cycle number was equal to 250.

- Cyclic 4 (C4) started with a monotonic loading of 10 kPa, then 50 cycles between 10 and 0 kPa followed by a loading of 30 kPa. Finally, a discharge was operated.

For every 50 load cycles, two stages were considered: the first 6 cycles duration was of 50 min and the following 44 cycles of 50 min. The detail of the applied cyclic loadings is shown in Figs. 5.3 and 5.4. All the testing cases on the physical model are summarized in Table 5.1.

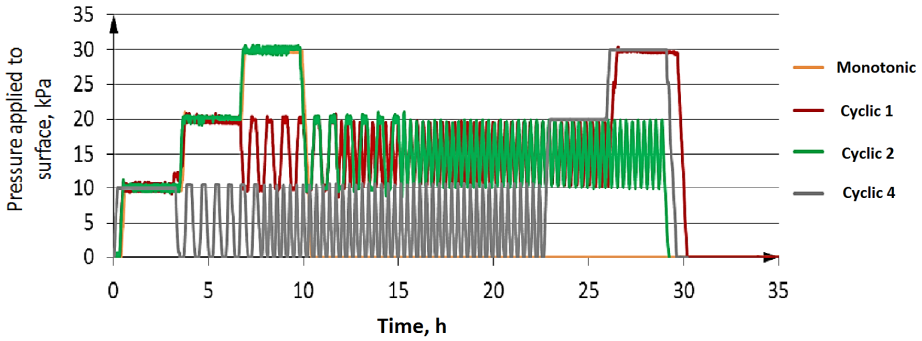

Fig. 5.3. Types of cyclic loading for the experimental studies (Houda, 2016)

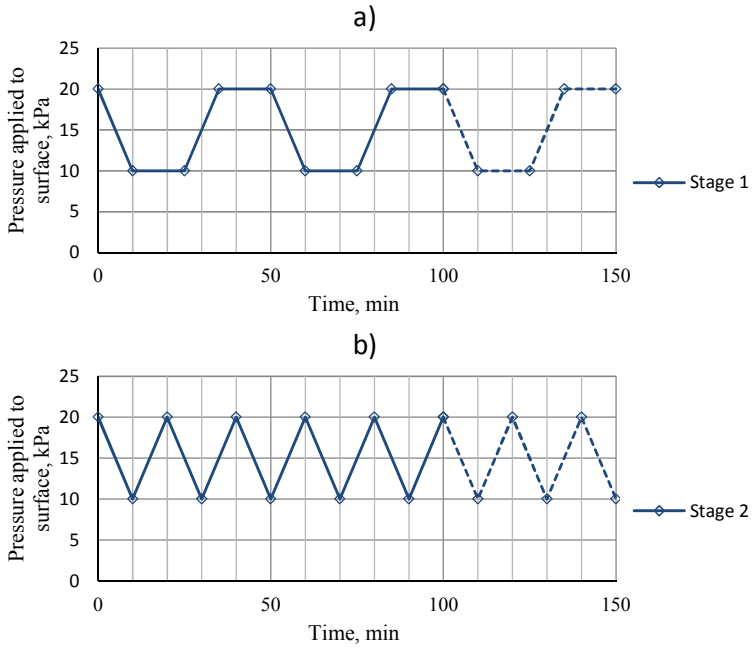

Fig. 5.4. Details of the cyclic loading: (a) for the first six load cycles; (b) for the following 44 cycles

Table 5.1. Testing cases used in the tests of Houda

Testing type	Testing name	Repeatability	Earth platform thickness	Testing conditions	Number of load cycles
Monotonic	M_D100	M_D100_a	100 mm	With a slab	–
		M_D100_b			
		M_D100_c			
Cyclic 1	C1_D100	C1_D100_a			50
		C1_D100_b			
Cyclic 2	C2_D100	C2_D100_a			50
		C2_D100_b			
Cyclic 3	C3_D100	C3_D100_a			250
Monotonic	M_D50	M_D50_a	50 mm		–
		M_D50_b			
		M_D50_c			
Cyclic 1	C1_D50	C1_D50_a			50
		C1_D50_b			
Cyclic 4	C4_D50	C4_D50_a			50
		C4_D50_b			
Monotonic	M_R100	M_R100_a	100 mm	Without a slab	50
		M_R100_b			
Cyclic 1	C1_R100	C1_R100_a			50
		C1_R100_b			
Cyclic 2	C2_R100	C2_R100_a			–
		C2_R100_b			

5.3.2.5. Numerical work by Houda

Numerical simulations were also done by Houda (2016). The gravel and soft foam were respectively modeled by the CYsoil and Cam-clay constitutive models. Numerical simulations were done using the finite difference method with the FLAC3D software. The numerical results of Houda were compared with the experimental outcomes of the tests.

The work which was done did consider a simple constitutive model for the mattress (CYsoil) which is not able to consider in a rigorous way the cyclic loading. A complementary study is then presented hereafter using a constitutive model which is more suitable to consider the effect of cyclic loading.

5.3.3. 3D Numerical modeling

5.3.3.1. Geometry and mesh

Due to the geometric and loading symmetry, a unit model has been used for analyzing the behavior of piled embankment under static and cyclic loading. This permits to

obtain reliable results and a time-consuming (Han and Gabr, 2002; Jenck et al., 2006,2009a, 2009b; Zhuang et al., 2014; Zhuang and Li, 2015; Zhuang and Wang, 2018). Two geometrical configurations were considered: a slab-mattress-reinforced soil and a mattress-reinforced soil system. The model consisted of a 0.4-m-thick soil layer reinforced by 35-mm-diameter piles followed by a mattress of 0.1 m and a rigid slab (slab case), as presented in Fig. 5.5. The numerical simulations were performed using the finite element method with ABAQUS V6.14. A UMAT subroutine developed by (Gudehus et al., 2008) for the HYP model was integrated. The piles, soils and slab were represented by 5,742 3C8D volumetric elements (8-node linear brick) in the 3D mesh (Fig. 5.6).

The bottom of the model (z = -0.4 m) was blocked in the *z*-direction. Due to the symmetry, the vertical boundaries were fixed in their perpendicular directions (Fig. 5.5).

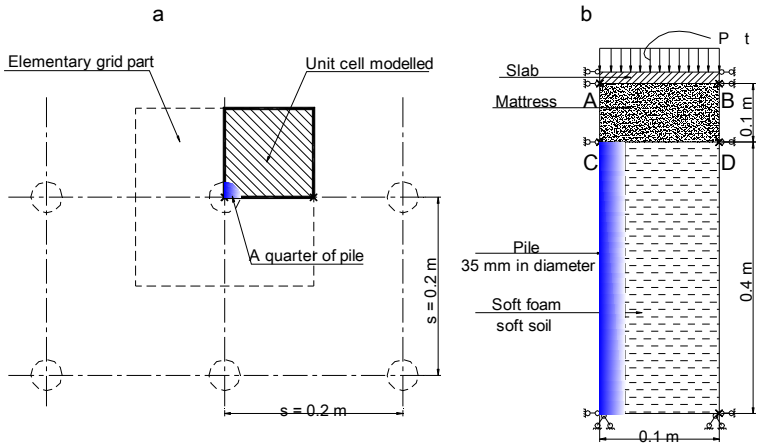

Fig. 5.5. Unit model used for the 3D numerical analyses

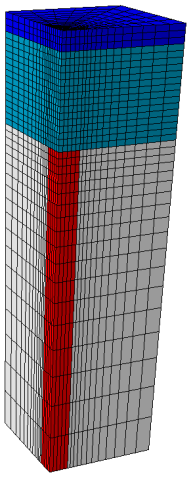

Fig. 5.6. 3D mesh for the numerical studies

5.3.3.2. Soil constitutive models and used parameters

The HYP model was suggested for the gravel layer because it could capture the cyclic response of soils under cyclic loading, as described in Chapter 4. Concerning the calibration procedure, the basic parameters were determined based on a fitting with the experimental results of triaxial tests (Fig. 5.7), in which the initial void ratio of the gravel was set at 0.7. A set of parameters for the intergranular strain concept proposed by Niemunis and Herle (1997) had been successfully applied to study the cyclic response of some sands (von Wolffersdorff and Schwab, 2009; Salciarini and Tamagnini, 2009; Ochmański et al. 2015; Li et al. 2016; Poblete et al. 2016). This set of parameters was used in the analyses since the experimental data was insufficient to improve the parameters calibration. The HYP model parameters for gravel are presented in Table 5.2. In addition, the Cam-clay model was chosen for the foam material. The fitting between experimental and numerical results in the oedometer test allows determining the parameters (Fig. 5.8). The parameters of the Cam-clay model were listed in Table 5.3.

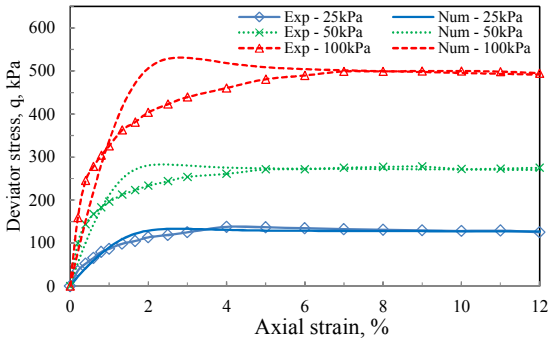

Fig. 5.7. Experiment and numerical results in triaxial tests on the gravel sample

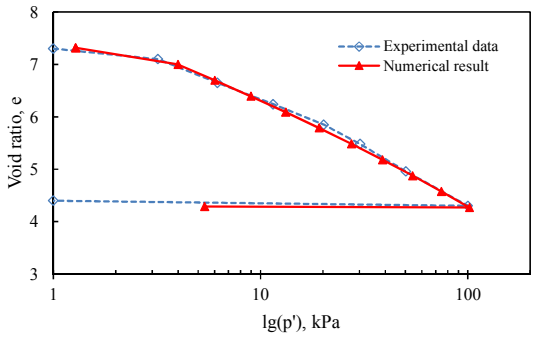

Fig. 5.8. Experiment and numerical results in oedometric test for the foam

Table 5.2. The HYP model parameters considered for the gravel in the analyses

φ_c [°]	h_s [MPa]	N	e_{d0}	e_{c0}	e_{i0}	α	β	R	m_R	m_T	β_r	χ	e_{ini}
39	5,800	0.28	0.53	0.84	1.00	0.10	0.35	$1x10^{-4}$	5	2	0.6	6	0.70

Table 5.3. The MCC model parameters considered for the foam material

Material	κ	ν	λ	M	a_0 (kPa)	e_o
Soft foam	0.02	0.3	0.9	1.30	3000	7.4

The vertical piles behavior is assumed to be linear elastic. A Young's modulus of E = 72.5 GPa, a Poisson's ratio of ν = 0.20 and an unit weight of γ = 27 kN/m^3 were considered.

An interface between pile and soil was considered. Interface elements were modeled by the Coulomb friction model. The coefficient of friction was assumed to be equal to 0.67 in the analyses.

5.3.3.3. Analysing procedure

The cases of slab-mattress-reinforced soil and mattress-reinforced soils were analyzed. In each simulation, the loading procedure was conducted by the following steps:

Firstly, an initial analysis step was performed, in which the geometry, the material properties, the interfaces and the boundary conditions were assigned;

Then a geostatic phase where the initial stresses, the initial void ratio and the body weight of materials was done;

Thirdly, the monotonic loading was applied to the top of the model;

After that, the number of cyclic loading was subjected to the model in two stages: 6 cycles (50 min/cycle) and then 44 cycles (20 min/cycle);

Finally, the process was closed by an unloading progress.

5.3.4. Experimental and numerical results

The measured data and both the numerical results are presented in terms of load transfer mechanisms within the LTP and cumulative settlements at the LTP base.

5.3.4.1. Case of the slab-mattress-reinforced soil (D100)

Under monotonic test (M)

Fig. 5.9 shows the variation of the system efficacy as a function of the pressure (P_m) on the top of the slab in the monotonic test M_D100. A comparison between the numerical results and experimental data is presented as well. The efficacy increases as the vertical surcharge increases. With regard to the experimental curve, after activating the weight of LTP, the efficacy value is equal to 30%. It then increases

significantly till 60% to reach a peak with a pressure of 6 kPa followed by a plateau still a pressure of 18 kPa. After that, it gradually reduces from 90 to 70% as the loading increases from 18 to 30 kPa. Both the numerical results underestimate the efficacy and show a difference of about 10 to 15%. The efficacy is about 40% as the vertical pressure of 6 kPa. It then rises 80% at a pressure of 12 kPa then followed by a slight increase. The relationship between the LTP base settlement and the pressure on the slab during the monotonic test is shown in Fig. 5.10. A good agreement between the numerical results and the experimental data is obtained (loading and unloading phase, and final settlements). It can be seen that the settlement for a loading of 30 kN is about 33 mm. Due to the small value of swelling line slope (Fig. 5.8), the settlement is irrecoverable in the unloading phase.

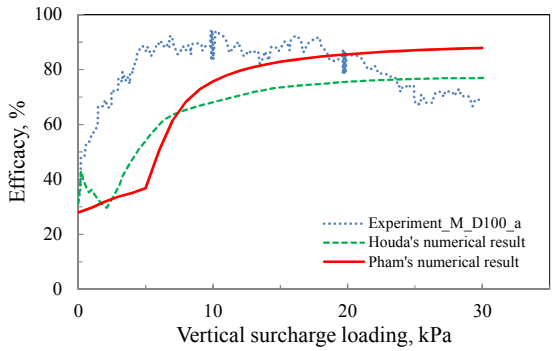

Fig. 5.9. Measured and numerical efficacy in the monotonic test M_D100

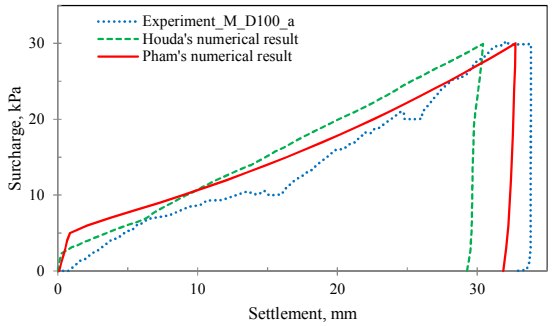

Fig. 5.10. Measured and numerical settlements of LTP base in the monotonic test M_D100

Under cyclic tests (C1, C2)

Fig. 5.11 depicts the variation of the average efficiency in the cyclic test C1_D100. The experimental data figures out that the efficacy slightly increases during 30 load cycles, it is then followed by a decrease. The contact forces between grains are accumulated, and the rearrangement of grains in the LTP gradually arise once the local friction limit is reached (Houda et al., 2016). In comparison, the efficacy of both the numerical studies decreases significantly till a specific number of load cycles, it then remains

constant. The efficacy falls to 15% after 20 cycles in the Houda's simulations while it decreases by 30% using the HYP model. A soil stiffness decrease (stiffness degradation) caused by the shear strain increase due to the load cycles leads to a reduction of the system efficacy.

Fig. 5.12 presents the dependency of the efficacy with the load cycles number for test C2_D100. As similar to the test C1_100, there is an inconsiderable increase in the measured efficacy in the first 30 cycle numbers. Furthermore, although there is a drop in efficacy during the first ten cycles, the numerical results using the HYP model and the experimental data are in good agreement, a difference of 10% still remains. Meanwhile, the efficacy of Houda's modeling is only 60% of the experimental one.

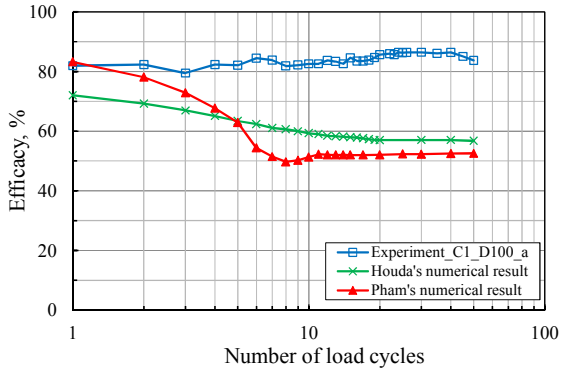

Fig. 5.11. Measured and numerical efficacy in the cyclic test C1_D100

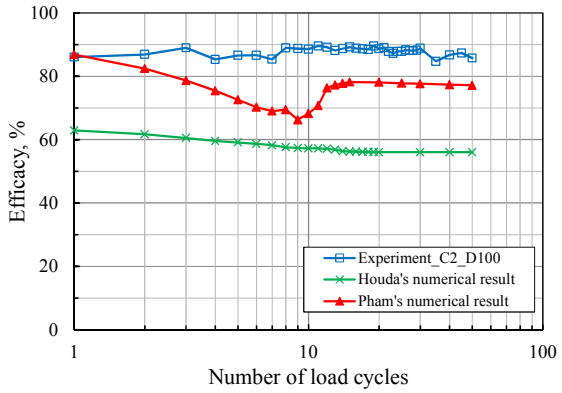

Fig. 5.12. Measured and numerical efficacy in the cyclic test C2_D100

In terms of the settlement, Fig. 5.13 compares the measured and numerical cumulative settlements at the mattress base during the cyclic test C1_D100. It is obvious that the cumulation of settlements takes place with a certain number of cycles. It increases when the number of repetition increases. In addition, the cumulation per one cycle slowly reduces with the following cycles. The settlements are cumulated until 50 cycles. The measured cumulative settlement has a value of about 6 mm after 10 cycles

followed by an increase of 4 mm after the following 40 cycles. By comparison, the cumulative settlements after 10 cycles are respectively equal to 11 and 16 mm for the proposed numerical study and the Houda's simulations.

Fig. 5.14 shows the influence of the cumulative settlements on the load cycles for the test C2_D100. As can be seen in Fig. 5.3, the loading started by an increase of 30 kPa, it then continued by an unloading of 20 kPa, i.e. the test considered the influence of the over-consolidated state of the compressible soil before applying a cyclic loading. The experimental plots indicate that the cumulative settlements after 50 cycles in the test C2 are only a third of the C1 test ones. The cyclic loading (10 to 20 kPa) in the test C2 was performed within the elastic region, which is not able to reproduce the cumulative settlement than in the test C1. In comparison, the numerical result obtained by Houda shows a significant cumulative settlement after the first load cycle then followed by a gradual one. In overall, it is four times greater than the experimental one. The pre-consolidation pressure is not updated in the CYsoil model, its cap still enlarged gradually under the cyclic loading number. By contrast, the result acquired by the proposed numerical work coincides well with the experimental result.

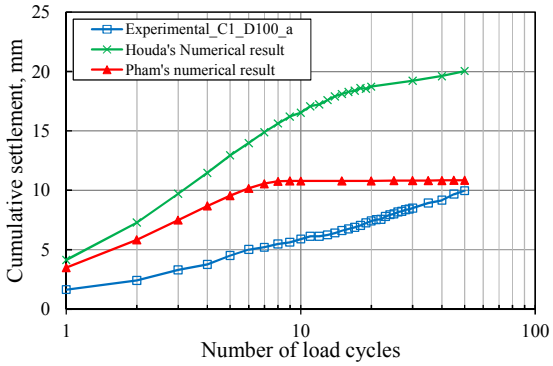

Fig. 5.13. Measured and numerical cumulative settlements for the cyclic test C1_D100

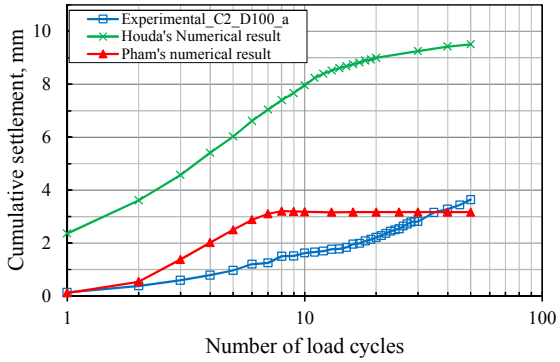

Fig. 5.14. Measured and numerical cumulative settlements for the cyclic test C2_D100

5.3.4.2. Case of the mattress-reinforced soil (R100)

In order to consider the boundaries condition influence, the case of a mattress over a reinforced soil (without slab) was also studied. The response of the system under monotonic and cyclic loading was analyzed.

Under monotonic test (M)

Fig. 5.15 shows a comparison between the numerical results and experimental data for the settlement of the LTP base. The numerical results predict well the settlements. Furthermore, a good fitting in the transition from elastic to plastic zones (where P_m ranges 0 to 8 kPa) between the numerical results and the measured data of test M_R100_a is shown with the given pre-consolidation pressure ($p_c = 2*a_0 = 6$ kPa).

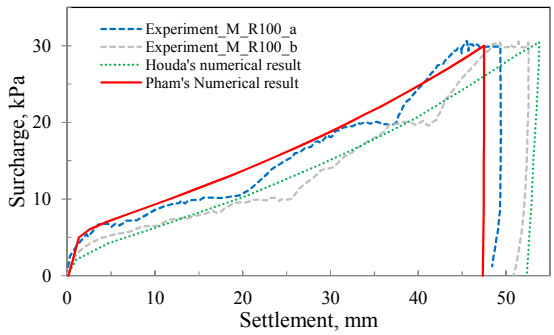

Fig. 5.15. Measured and numerical settlements of the LTP base

Under cyclic loading (C1, C2)

Figs 5.16 and 5.17 present the measured and numerical cumulative settlements of the LTP base under different cyclic tests. Lower cumulative settlements in the mattress-reinforced soil system (R100) than in the slab-mattress-reinforced soil (D100) are found (about two-thirds). The measured cumulation after 50 cycles is respectively equal to 6.5 and 1.3 mm for the experimental tests C1 and C2. Additionally, the higher the number of load cycles, the larger the cumulative settlements.

As regards of the numerical settlements, the numerical modeling with the advanced constitutive model HYP is able to address the cumulation of the residual strains after each load cycle. Moreover, the HYP model for the gravel can better simulate the cumulative settlements than the CYsoil model. While the Houda's simulation always gives a very high cumulation with a number of load cycles, the proposed numerical modeling can simulate well the first 10 cycles. The characteristic stiffnesses and the transition between the intergranular strain and grain rearrangement deformations allows the HYP model to eliminate ratcheting (an excessive cumulation of deformation for small stress cycles) (Niemunis and Herle, 1997). Nevertheless, no cumulation after

the 10th cycle is found in the numerical study. It might be due to the fact that the Cam-clay soil model is inefficient to capture the foam behavior under cyclic loading.

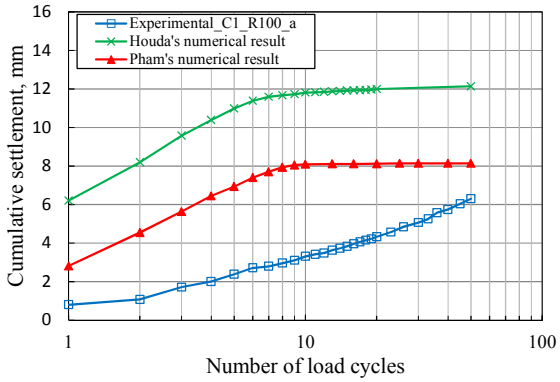

Fig. 5.16. Measured and numerical accumulative settlement for the cyclic test C1_R100

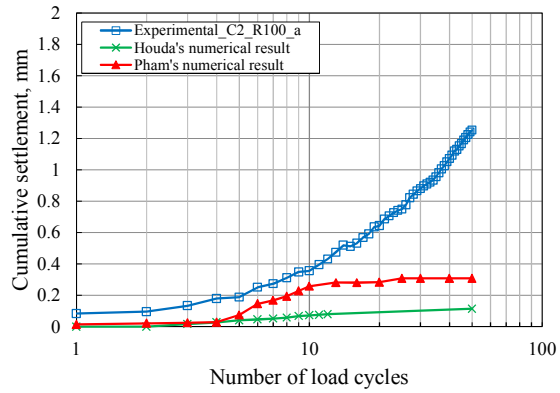

Fig. 5.17. Measured and numerical accumulative settlement for the cyclic test C2_R100

5.3.5. Conclusions

A comparison between laboratory experimental tests and two levels of constitutive models complexity is presented for a rigid inclusion-improved soil under monotonic and cyclic loadings.

For the monotonic loading configuration, the obtained settlements from both numerical simulations are in good accordance with the experimental ones. Meanwhile, the numerical efficacy is 10 to 15% smaller than the measured one.

With regard to the cyclic loading, both the numerical results underestimate the measured data considering the efficacy. Numerical results show an efficacy decrease under the cyclic loading while the efficacy is constant for the experimental tests. The experimental and numerical results indicate that as the number of cyclic loading increases, the settlements cumulation increase. The cumulation per cycle decreases gradually with the following cycles. The over-consolidated soft soil cumulated less than

the normally consolidated one under cyclic loading. The cumulative settlements in the slab case are one-third larger than in the case without a slab.

The application of the hypoplastic constitutive model for granular soils can address the response of the rigid inclusion-improved soil under monotonic and cyclic loading. In addition, its results are more accurate in terms of efficacy and the cumulative settlement than the ones obtained with the CYsoil model.

To be able to improve the numerical results, an additional characterization of the materials introduced in the tests (foam and granular materials) should be done. It will permit to improve the knowledge of the materials behavior under cyclic loading. The parameters to be introduced in the numerical analysis will be more accurate and will permit to better simulate the experimental tests.

5.4. 3D numerical modeling of a piled embankment under cyclic loading

5.4.1. Introduction

The behavior of a piled embankment under cyclic loading has not clearly been shown in the literature in terms of load transfer/arching effect and of cumulation of settlements. Moreover, the development of soil arching with the loading cycles number was not investigated. Additionally, some of the former investigations only took into account simple constitutive models for the granular embankment behavior. To overcome the limitation of the former studies, a 3D numerical model is set up to better understand piled embankments under cyclic loadings. Suitable constitutive models for the embankment fill and the soft soil to represent the complex behavior during cyclic loading are considered. The arching effect and the cumulative settlements with a number of load cycles are presented. The influence of the vehicle speed (considering several cyclic amplitudes and frequencies) and embankment heights are given as well.

5.4.2. Geotechnical profile and geometry

A simplified geotechnical profile consisting of a 10-m soft silt clay layer lying over a non-deformable substratum is considered. The water table is located at the soft silt clay layer surface. Piles with a diameter of 0.4 m are installed through the soft soil. The pile toes are founded on the non-deformable strata. A square grid arrangement with a distance between piles of s = 2.28 m is considered (Fig. 5.18.a). An embankment made of granular soil lies upon the pile-improved soft soil foundation with a height of H. A concrete slab is located on the crest of the embankment for loading application purpose. Due to the geometry symmetry, only a quarter of the model is simulated. From Fig. 5.18.b, it can be seen that the points A, B are placed at the crest of the embankment, and C, D are positioned at the pile head level. The point E is located at the level of the pile toe on the soft soil.

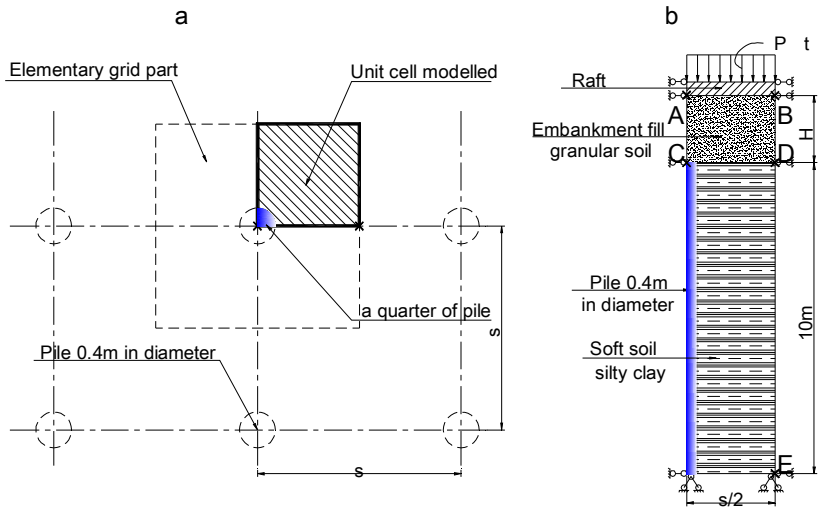

Fig.5.18. Layout of the simulated unit cell (a) plan (b) elevation view

5.4.3. Finite element modeling

In order to solve the above-mentioned problem, a three-dimensional (3D) numerical analysis using the finite element method (FEM) was performed using the software ABAQUS/CEA version 6.14-5 (HKS, 2014).

Studying both a full model and a column model (a quarter of a pile) with dynamic loadings, Zhuang and Wang (2018) observed that there was only a slight difference (less than 5%) in terms of settlements, excess pore pressures and maximum earth pressure coefficient between them. Due to symmetry conditions, the column model was then considered to carry out the following studies. To investigate the behavior of a reinforced piled embankment under static and variable loads, a quarter single pile model was also used by Moormann et al. (2016). Additionally, due to the lower number of finite elements, the column model allows users to reduce the calculation time. Therefore, the quarter pile model was proposed in the study. The pile, the soft soil, the embankment and the concrete slab were discretized using solid elements. Since the calculation time was significantly affected by the type of the discretization elements, (e.g., the computational time could increase by 18 times if C3D20 elements were used, compared to using C3D8 elements (Ng et al., 2015)), the C3D8 type elements, which are 8-node linear bricks, were used in the analysis. The finite element mesh of the piled embankment is presented in Fig. 5.19.

The modified Cam-clay (MCC) constitutive model was selected to simulate the soft soil layer. For the embankment, two constitutive models were considered, including the MC model known as a simplified model and the HYP one. The user-defined hypoplastic soil model was implemented by (Gudehus et al., 2008), as an open-source one. A linear

elastic behavior was defined for the piles and the slab. Interactions between the soil and the pile, the pile and the embankment, and the slab and the embankment were considered.

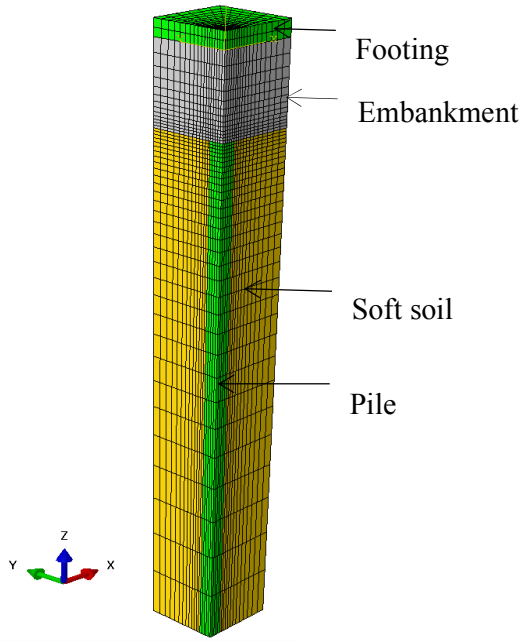

Fig.5.19. Finite element mesh of the piled embankment

In dynamic analyses, the fixed boundary conditions do not represent adequately the outward radiation of energy. The outward propagating waves reflected back into the model must be taken into account through boundary conditions. The solution of a larger model to minimize the material damping leads to increase the computational time (Patil et al. 2013). In the study, to consider the response of substratum layers under dynamic loading, an artificial boundary using infinite elements is assigned at the bottom, which allows the supporting infinite soil media to consider the near-field finite domain and the far-field infinite domain. The four vertical surrounding boundaries were blocked in their perpendicular directions. Only the case where piles are placed on the bedrock was considered. In most cases, in real works, the pile toe is placed on the bedrock, to avoid excessive deformations.

As the height of the embankment is sufficiently large, the development of excess pore pressure in the soft soil under cyclic loading is minimized. Therefore, only drained calculations were considered in this study. In case of low thickness embankments, this approach is no more valid as the generation of excess pore water pressure can affect the overall results.

5.4.4. Soil constitutive models and their parameters

5.4.4.1. Granular soil (embankment)

Two constitutive models for the granular soil were employed to evaluate the behavior of the embankment, which included the linear elastic perfectly-plastic model with the Mohr-Coulomb failure criterion (MC) and the hypoplastic model (named HYP model).

Mohr-Column model (MC model)

In the literature, embankments were successfully simulated by the MC model (Huang et al. 2005, Jenck et al. 2006, Zhuang et al. 2008, Huang and Han 2009). However, this constitutive model has some drawbacks. Firstly, it cannot capture the non-linearity in the elastic part. Secondly, the unloading-reloading modulus is equal to the primary loading modulus. In addition, since the isotropic or kinematic hardening rules are not considered, the model is not able to reproduce the soil behavior during cyclic loadings. In the study, the MC model was considered as a reference case to be compared with the more sophisticated one (HYP model).

The five parameters required of MC model consists of Young's modulus (E), Poisson's ratio (ν), cohesion (c), friction angle (φ) and dilatancy (ψ). A variation of Young's modulus with the minor principal stress σ_3 was considered. The relationship is followed by Equation 5.1, that is given by the authors (Janbu, 1963; Jenck et al., 2006).

$$\frac{E}{p_a} = k\left(\frac{\sigma_3}{p_a}\right)^m \tag{5.1}$$

Where p_a is the atmospheric pressure (Pa), k and m are two constants controlling the shape of the curve. Based on the 3D numerical triaxial tests with different confining pressure (Fig. 5.20), three pairs of E-σ_3 were obtained, a set of k = 910, m = 0.87 was qualified then. For a value of σ_3 equal to 30 kPa, Young's modulus is equal to E = 15 MPa. The parameters φ = 30^o and c = 0 were taken from the literature, and ψ = 0 was assumed. These parameters are listed in Table 5.4.

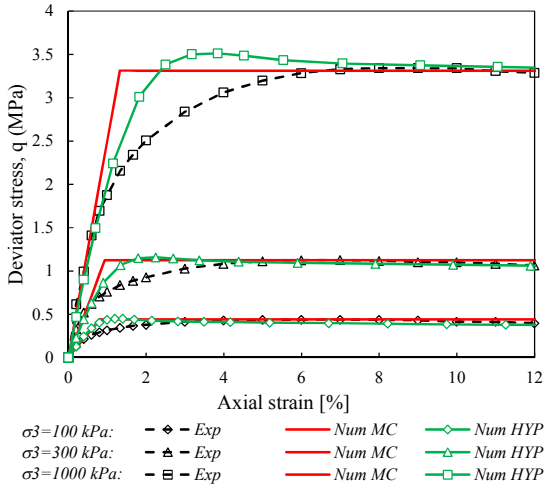

Fig. 5.20. Drained triaxial tests with different confining pressures for the Karlsruhe sand sample

Table 5.4. The parameters of the MC constitutive model of the Karlsruhe sand (σ_3 = 30 kPa)

E (MPa)	ν	φ (°)	c (kPa)	ψ	ρ
15	0.3	30	0.0	0.0	1800

Hypoplastic model (HYP model)

In the study, the Karlsruhe sand was considered to be the constituent of the embankment fill. This soil is well documented in the literature concerning its physical and mechanical properties deriving from geotechnical tests (Kolymbas and Wu, 1990; Bauer, 1996). As mentioned in Chapter 4, these parameters of the HYP are summarized in Table 5.5.

Table 5.5. HYP model parameters considered for the Karlsruhe sand

φ_c [°]	h_s [MPa]	n	e_{d0}	e_{c0}	e_{i0}	α	β	R	m_R	m_T	β_r	χ	e_{ini}
33	5,800	0.28	0.53	0.84	1.00	0.10	2.5	$1x10^{-4}$	5	2	0.5	6	0.6

5.4.4.2. Soft Soil

The soft clay considered in this study comes from the Sieradz County located in the Lodz Province in central Poland. The MCC model parameters were described in Chapter 3. They are listed in Table 5.6.

Table 5.6. The parameters of the MCC constitutive model of soft soil employed in the analysis

Material	κ	ν	λ	M	a_0 (kPa)	e
Poland clay	0.028	0.3	0.106	1.42	850	0.328

5.4.4.3. Piles and footing

The vertical piles and the footing are made of concrete. The isotropic linear elastic

constitutive model was used to simulate the concrete, which requires the definition of Young's modulus (E = 20 GPa), the Poisson's ratio (ν = 0.20) and the unit weight (γ = 24 kN/m^3).

5.4.4.4. Interface

The basic Coulomb friction model was used. It permits to consider that two contacting surfaces could carry shear stresses up to a certain magnitude across their interface before they start sliding. The critical shear stress was defined by the normal effective stress, σ', between the two contact surfaces multiplied by an interface friction coefficient, μ (HKS, 2014). The coefficient of friction was assumed to be equal to 0.67 as in Jenck et al. (2007).

5.4.5. Loading and analysis steps

The traffic loading applied on the footing top is considered to be a sinusoidal shape (Equation 5.2). This way to consider a traffic cyclic loading was proposed by (Zhang and Liang, 2001; Zhuang and Li, 2015). The function enables it takes into account a dependency of traffic loading on the static wheel load, the traffic speed and the road condition (roughness).

$$P_t = P_0 + P\sin(\omega t) \tag{5.2}$$

Where $P = M_0 \mu_{w/r}(y)\omega^2$ and $\omega = \dfrac{2\pi V}{L}$

P_0 is the static vehicle wheel load, whose value is taken equal to 50 kN/m^2; M_0 is the unsprung weight, M_0= 250 Ns^2/m, $\mu_{w/r}(y)$is the road roughness function, with a value of 2 mm; V is the speed of the vehicles, and a vehicle of 60 km/h is taken as the reference case, L is the geometric curve wavelength of the pavement, whose value is considered to be equal to 6 m, and t is the duration time of the loading passage. Table 5.7 illustrates that the different traffic speeds lead to changes of the amplitude and of the frequency of the cyclic loading. The time-history curve of the different traffic loadings within a cycle is shown in Fig. 5.21.

Table 5.7. The parameters of sinusoidal traffic loading

Traffic speed, V (km/h)	P_0 (kPa)	Angular frequency - ω (rad/s)	P (kPa)
60	50	17.45	0.152
80	50	23.27	0.271
100	50	29.09	0.423
130	50	37.82	0.715

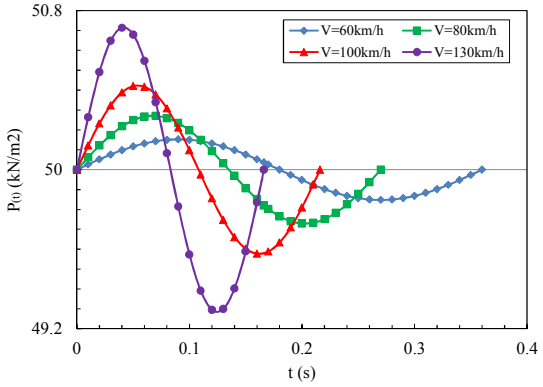

Fig. 5.21. The sinusoidal time–history curve of the different traffic loadings

For the calculations, a specific procedure *was* defined. Firstly, the initial step was established to obtain the initial stress state and predefined the variables (void ratio), in which the passive earth pressure coefficients at rest, $K_0 = 1 - \sin\varphi$, were taken equal to respectively 0.5 and 1.0 for the granular soil and the soft soil. The following step was the geostatic one in which the gravity loading was assigned to the soil mass (soft soil and embankment fill). Subsequently, the static vehicle wheel loading (P_0 = 50 kPa) was applied. Finally, a number of traffic load cycles were applied at the top of the footing.

5.4.6. Numerical results

5.4.6.1. Case studies

To investigate the piled embankment under load cycles, the reference case was first set up. It consists of an embankment height of 1.5 m over a 10-m soft silty clay. The cyclic loading induced by a vehicle speed of 60 km/h was then applied at the top of the footing. The following factors are considered to check their influence:

- Constitutive models of the embankment;
- Influence of the number of load cycles;
- Vehicle speeds: 60, 80, 100 and 130 km/h;
- Embankment heights: 1.5, 2.5, 4.0 and 6.0 m.

The influence of these parameters is presented in terms of load transfer and settlements with the loading cycles.

5.4.6.2. Influence of the constitutive model of the embankment

Two different constitutive models were used for the granular soil of the embankment. Under static loading, the stress acting on the pile using the MC model is the double of the HYP one, which leads to less stress transferred on soft soil for the MC case, as

shown in Fig. 5.22 and 5.23. Therefore, the vertical displacements at the embankment and soft soil with the MC model are only a half of those with the HYP model, as illustrated in Fig. 5.24. The differences may be due to the fact that the density evolution with the stress level was taken into account with the HYP model.

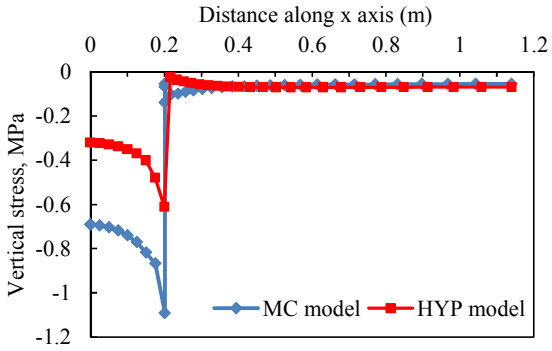

Fig. 5.22. Stress distribution along the line CD for different constitutive models (under static loading)

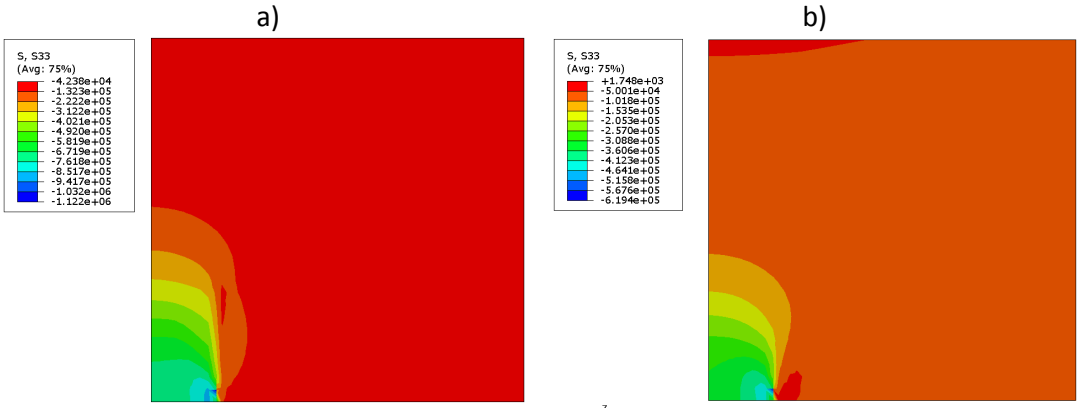

Fig. 5.23. Vertical stresses within the embankment fill for different constitutive models (under static loading): a) vertical stress for the MC model; b) vertical stress for the HYP model

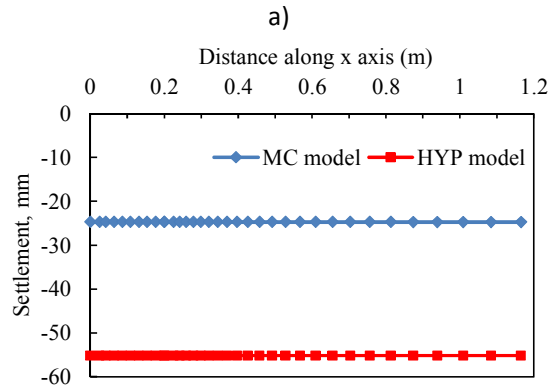

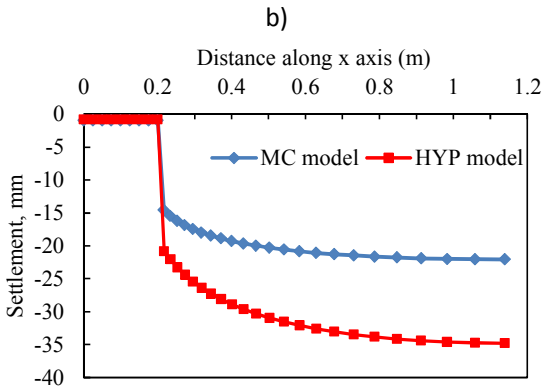

Fig. 5.24. Settlements for different constitutive models (embankment under static loading): a) settlement along AB line (at crest); b) settlement along CD line (at soft soil)

Just before the static step, the displacements are set equal to zero in all the models.

For the traffic cyclic loading of 60 km/h, the settlements are not cumulated when using the MC model while cumulative incremental settlements are obtained with the HYP model due to the cycles (Fig. 5.25). This is due to the linear elasticity of the MC constitutive model.

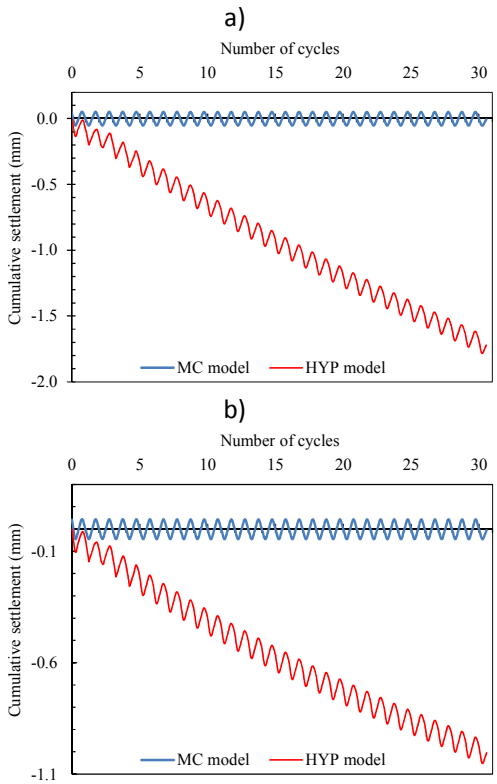

Fig. 5.25. Cumulative settlements for different embankment constitutive models: a) Settlement at point B (embankment); b) Settlement at point D (soft soil)

A decrease of the pressure acting on the pile and a minor increase of the subsoil stress during the load cycles are also found with the HYP model in Table 5.8. It can be due to

the soil arching decrease under repeated cycles, which was also illustrated by previous studies (Heitz et al., 2001; Han et al., 2011b, 2015). Thanks to its advantages and the former recommendations, the HYP model, proves that it better numerically simulates the soil behavior under cyclic loading. In the following analysis, the embankment is simulated using only the HYP constitutive model.

Table 5.8. Stress on the pile and on the soft soil for different embankment constitutive models

Vertical stresses (MPa)	MC model		HYP model	
	Static step	After 30 cycles	Static step	After 30 cycles
Average stress on the pile head (point C)	-0.873	-0.872	-0.481	-0.437
Stress on the soft soil (point D)	-0.054	-0.054	-0.069	-0.072

5.4.6.3. Influence of the load cycles

To consider the influence of the number of load cycles on the piled embankment, a case with a vehicle speed of 60 km/h was first analyzed as the reference case.

Due to the heavy computation time, only 2000 cycles of loading were conducted. For the reference calculation, the computation time is equal to 7 days using the computer PC i7 with the processor Intel 3.5GHz (8CPUs) and 32GB RAM.

Load transfer mechanism

Fig. 5.26 illustrates the change of the maximum principal stress distribution inside the embankment fill with the load cycles. In general, an increase in the number of load cycles applied on the embankment induces a decrease of the stress on the pile and an increase of the soft soil pressure. It can be seen that the arching mechanisms with 30 and 180 cycles induce the higher value of stress above the pile head. Then no more arching is visualized when the number of load cycles reaches a value of 1000 cycles. It means that the arching effect decreases with the number of the load cycles, probably due to grains reorganization. The obtained results are in good accordance with the experimental results of Heitz et al., (2001) which shows that the soil arching can only be seen for a limited number of cycles.

Additionally, the stresses applied to the pile and to the soft soil under a number of load cycles are presented in Table 5.9 and Fig. 5.27. It can be clearly seen that the stress acting on the pile decreases significantly while that on the soft soil slightly increases as the number of cycles increases. The average stress on the pile is equal to 481 kPa for the static loading case. After 30 cycles, there is a minor decrease in stress value of 10%. This stress significantly decreases under more loading cycles: stress decreases of 25% and 50% correspond to 330 and 630 load cycles, respectively. When the number of

cycles overpasses 1000, the average value on pile remains stable at approximately 59 kPa, which represents a decrease of the vertical stress of nearly 90%.

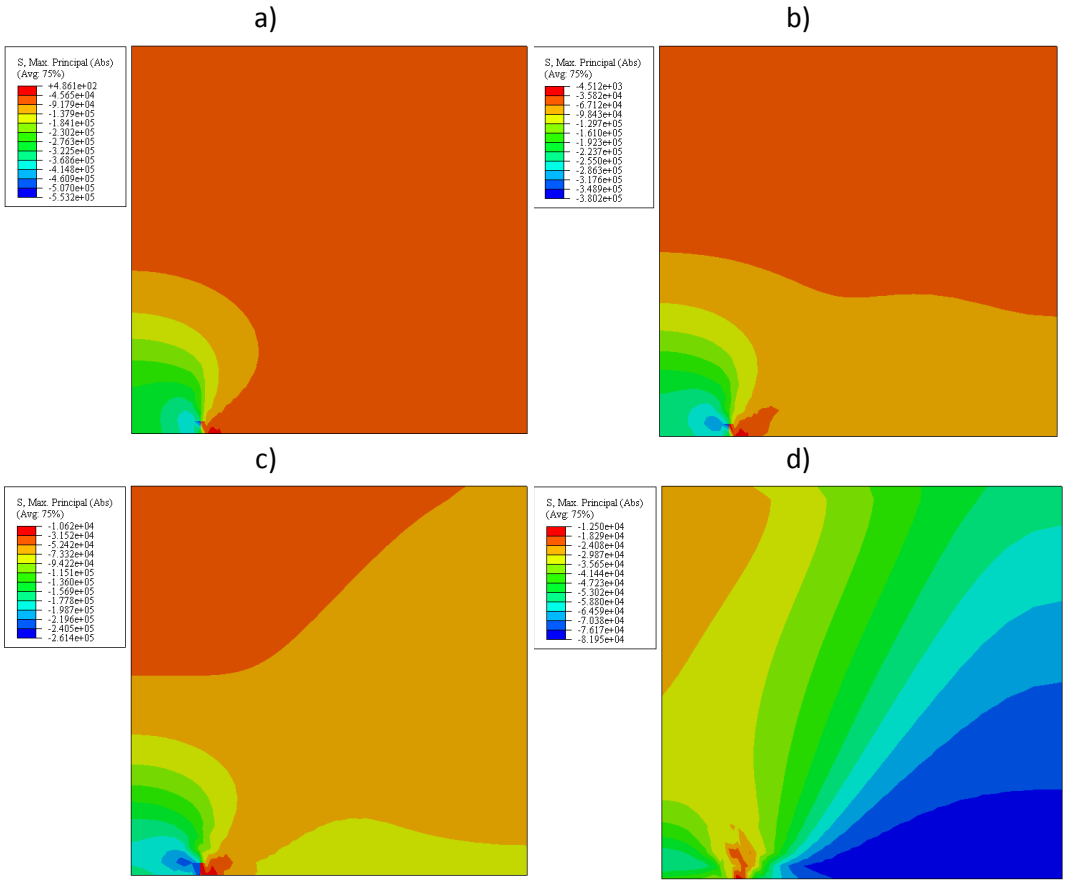

Fig. 5.26. Stress distribution within the embankment fill under load cycles: a) after 30 cycles; b) after 180 cycles; c) after 330 cycles; d) after 1000 cycles

The load transfer from the soil to the pile is governed by the soil arching within the embankment fill. The load transfer mechanism in the LTP is often assessed by the stress concentration ratio (*SCR*). For the static loading, the *SCR* equals 6.23 which is in good agreement with the literature (range from 1 to 8) (Liu et al., 2007). Under a number of repeated loads, the *SCR* decreases from 5.66 to 1.54 as the number of cycles increases from 30 to 630. It then decreases by half for 1000 cycles, before remaining constant. A cyclic loading with a small amplitude causes the compaction and the rearrangement of the soil particles, as well as the plastic strain inside granular materials. The phenomenon results in the degradation of the arching effect (Han et al., 2015). This process occurs till a number of cycles of around 1000 cycles.

On the other hand, Fig. 5.27 shows a moderate increase of the soft soil stress with the repeated number of load cycles. The stress on the soft soil is equal to 69 kPa for the static loading, it then increases to 70 kPa for 30 cycles. After that, it slightly increases

to 75 kPa for 1000 cycles, and later insignificantly grows until 2000 cycles.

Table 5.9. Stress Concentration Ratio (*SCR*) evolution with the number of load cycles

Model	Parameters	Static	Cyclic loading (number of cycles)						
		0	30	130	330	630	1000	1400	2000
HYP	Average vertical stress on pile head (σ_p) (MPa)	-0.481	-0.437	-0.362	-0.238	-0.119	-0.058	-0.058	-0.059
	$SCR=\sigma_p/\sigma_s$	6.23	5.66	4.70	3.09	1.54	0.75	0.75	0.76

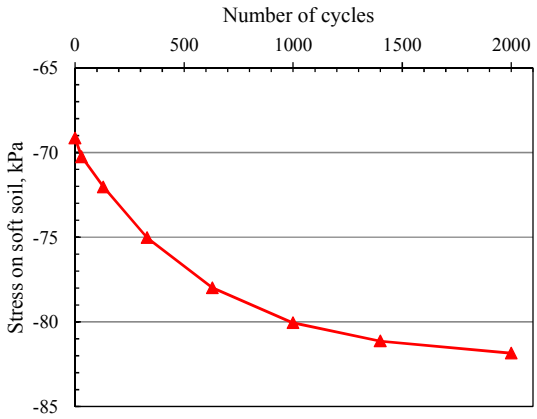

Fig. 5.27. Stress on the soft soil (point D) under the number of load cycles

Embankment and soft soil settlements

Figs. 5.28 and 5.29 show the development of the vertical settlement induced by the cyclic loading. The results indicate an increase of the cumulative settlement with the number of load cycles. As seen in Fig. 5.28, the cumulation of settlements is found not only inside the embankment fill but also within the soft soil, which starts to increase faster before 300 cycles, then increases gradually till 1000 cycles. In the following 1000 load cycles, the soft soil settlement remains stable while the embankment displacement continues to increase significantly. This is due to the fact that the pressure on the soft soil remains constant after 1000 cycles (refer to Fig. 27). On the other hand, the displacement of the pile head slightly changes during all the loading cycles. It is due to the fact that the behavior of the pile is linearly elastic and also due to the fact that the pile is very stiff. The reduction of the vertical displacements inside the system (embankment fill and soft soil) with the depth is presented in Fig. 5.29. The settlements can be ignored for a depth higher than 6 m. This is explained by the stress decrease with the depth. In addition, a significant settlement cumulation is found in the granular soil (z= -1.5 to 0.0 m) with the load cycles. It accounts for more than a half of the total settlement.

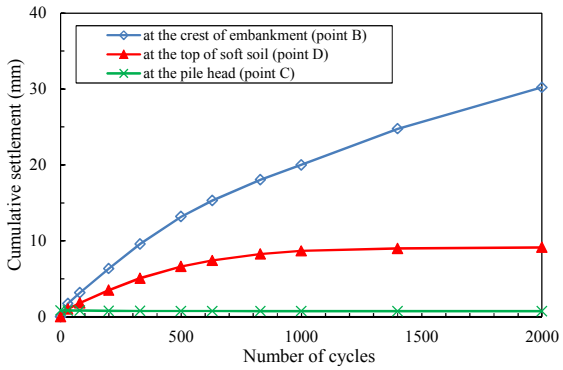

Fig. 5.28. Cumulative settlement under load cycles

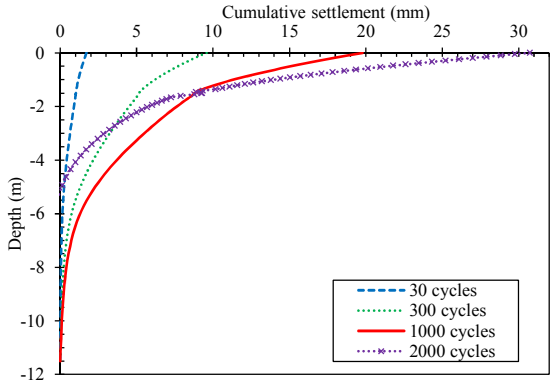

Fig. 5.29. Cumulative settlement with the depth under load cycles (along the line BE)

5.4.6.4. Influence of the vehicle speed

The vehicle speed leads to a change of the amplitude and of the frequency of the cyclic loading (Table 5.7). In this study, the speeds of traffic vehicle are considered in the range of 60 to 130 km/h.

Load transfer mechanism

Fig. 5.30 presents the influence of the traffic speed on the stress concentration ratio (*SCR*). It can be seen that the *SCR* is significantly reduced with the traffic velocity. For the reference case, the ratio starts at 6.2 for the static loading, then considerably decreases to only a half under 330 cycles. It then gradually decreases for 1000 cycles and reaches the level of 0.75 (a decrease of 88%) at 2000 cycles. In comparison, the *SCRs* induced by the speeds of 80, 100 and 130 km/h reach the lowest points after 500, 300 and 250 cycles, respectively, which are followed by a slight increase phase. It can then be concluded that the higher the speed applied on the embankment crest, the quicker the arching effect reduction.

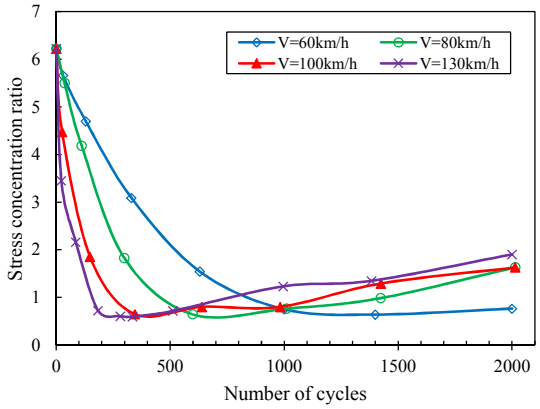

Fig. 5.30. Stress concentration ratio under load cycles with different vehicle speeds

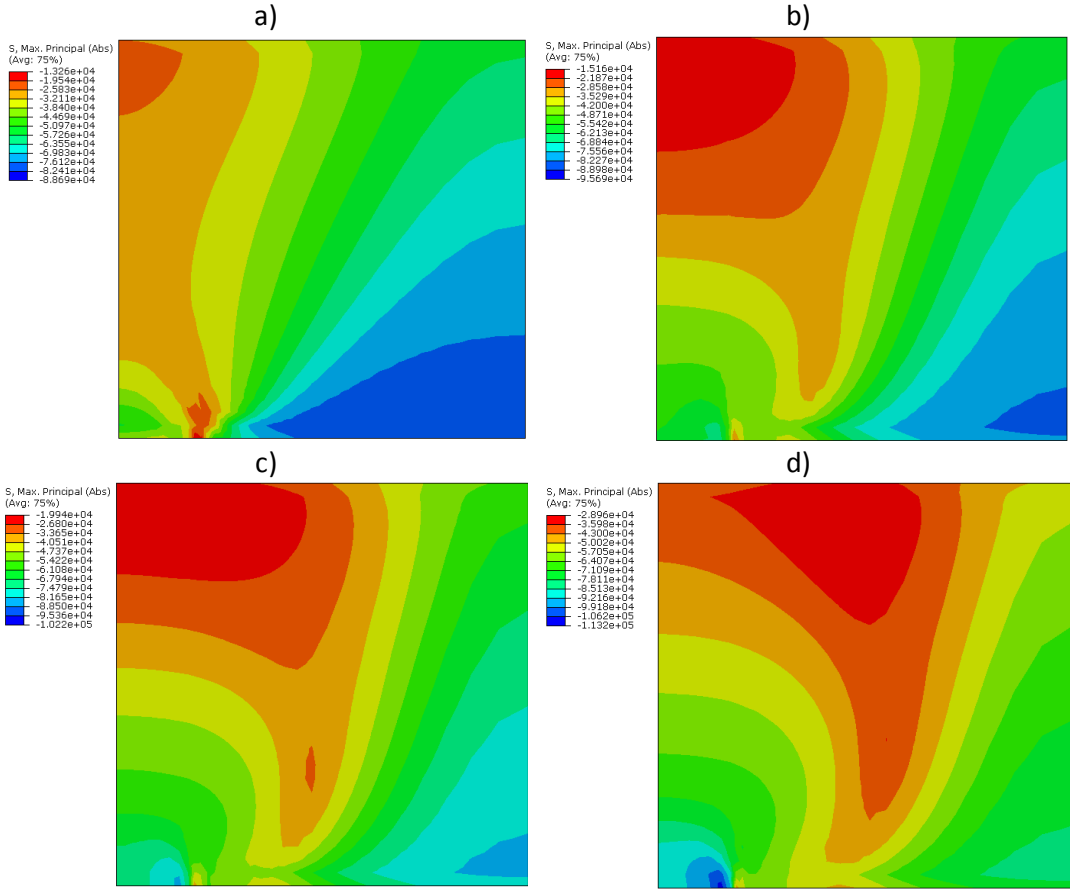

Fig. 5.31. The evolution of arching effect within embankment fill after 300 load cycles with V = 100 km/h: a) after 300 cycles; b) after 1000 cycles; c) after 1400 cycles; d) after 2000 cycles

Speeds with a higher amplitude and frequency can lead to an earlier destruction of the arching which is in agreement with the tendency of the experimental works conducted by Heitz et al. (2001) and Han et al. (2015). The other finding is that a slight increase of the arching ratio is visualized after 1000 cycles with V = 100 km/h, as shown in Fig. 5.31. The stress on pile slightly increases while the pressure applied on soft soil

reduces for a number of cycling loadings higher than 1000. The results are in good accordance with the experimental results of Heitz et al. (2001), in which the soil arching ratio slightly increased after 700 cycles.

Embankment and soft soil settlements

The effect of the traffic speed on the permanent settlements at the crest of the embankment fill is shown in Fig. 5.32. It is shown that the vehicle speed has a significant influence on the permanent settlements at the embankment crest. The cumulative settlements induced by the speeds of 80, 100 and 130 km/h are respectively equal to 1.5, 2 and 2.2 times those induced by the speed of 60 km/h. At the speed of 60 km/h, the permanent settlements first highly increase under 300 load cycles and then increases gradually. A slight increase after 1000 cycles can be observed. In the case of 100 km/h, the displacement cumulation is over 20 mm for 300 load cycles, it then doubles and triples for respectively 1000 and 2000 cycles, respectively.

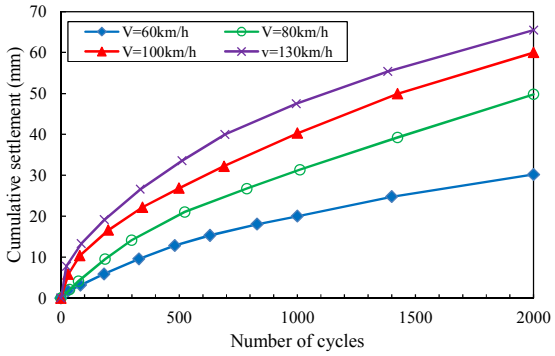

Fig. 5.32. Cumulative settlements of the embankment crest (point B) for different vehicle speeds

Fig. 5.33 describes the dependency of the soft soil settlements with the vehicle speed. The vertical settlement considerably increases with a limited number of cycles, it then remains stable. While the permanent settlements reach 9 mm after 1000 cycles at a speed of 60 km/h, this stability is obtained after only 300 cycles for 100 km/h. It may be due to the fact that the soil arching is reduced under cyclic loading, which may result in a considerable increase of the stress on the soft soil and of the surface settlement (Zhuang and Li, 2015). Furthermore, a higher traffic speed with the higher frequency and the larger amplitude leads to a quicker arching degradation. This may explain why the permanent settlement in the case of 130 km/h increases faster than in the cases of 60, 80 and 100 km/h. The load transfer on the pile and on the soft soil is constant due to no arching effect after load cycles, which leads to not more settlement cumulation on the soft soil.

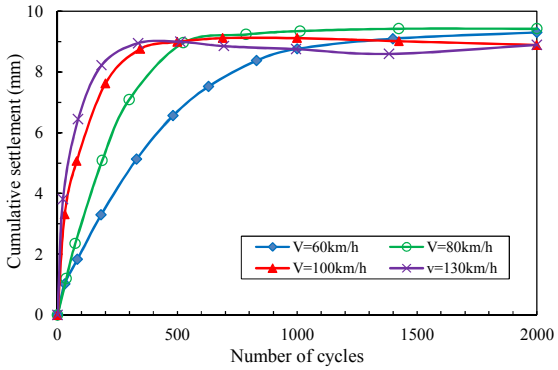

Fig. 5.33. Cumulative settlement of the soft soil (point D) for different vehicle speeds

5.4.6.5. Influence of the embankment height

In this part, all the case studies are performed with a traffic speed of 60 km/h, but different heights of the embankment are considered.

Load transfer mechanism

Fig. 5.34 represents the influence of the embankment height on the stress concentration ratio with the load cycles. In general, the *SCR* increases when the embankment height increases. This tendency is in good agreement with the results obtained by Han and Gabr (2002). In addition, the stress concentration ratio significantly decreases with a repeated number of cycles. With a height of 2 m, the *SCR* decreases by 3 times when the cycle increases from 300 to 1000. In comparison, the value only reduces by 2 times for a height of 4 m. Furthermore, the arching effect collapse is seen after 1000 cycles as the value of *H/s* is below 1.1 (*H* = 2.5 m, *s* = 2.28 m) where the *SCR* is less than 1.0. Meanwhile, it is stable for all loading cycles number for an *H/s* of 1.7 (*H* = 4 m). These results are in good agreement with the numerical results obtained by Han et al. (2015).

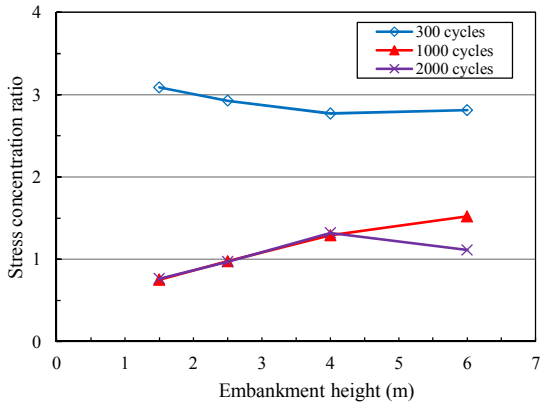

Fig. 5.34. Stress concentration ratio for different embankment heights

Embankment and soft soil settlements

Fig. 5.35 shows the cumulative settlement at the embankment crest for different embankment heights. It can be clearly seen that the permanent displacements significantly increase when the height increases to 4 m, it then slightly increases at the height of 6 m. It may be due to the fact that the higher the embankment fill is the more the settlements are. In other words, the cumulated settlements at the crest increase with the number of load cycles.

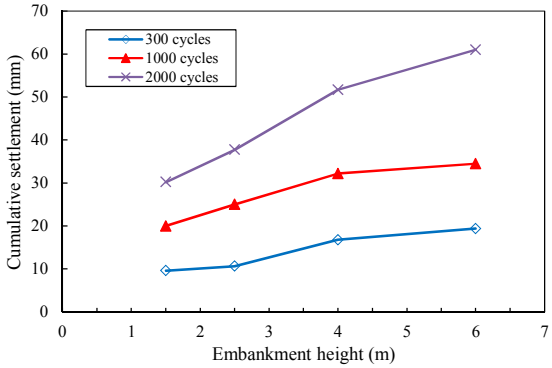

Fig. 5.35. Cumulative settlement at the crest (point B) with different embankment heights

Fig. 5.36 presents the cumulative settlement of the soft soil with different embankment heights. In general, the soft soil vertical movement dramatically decreases as the height increases. In the case of 1000 cycles, the settlement cumulation is about 9 mm for the reference case, it then decreases to a half for a height of 4 m. Then, a significant drop to a quarter for a 6-m embankment height can be seen. These findings suggest that a higher embankment height results in the development of soil arching, which leads to less pressure on the soft soil. Furthermore, the rate of cumulation slows down as the repeated number of load cycles increases and its behavior do not change after 1000 cycles. The soft soil stress does not increase when the cycles number overpass the value of 1000 (Table 5.9).

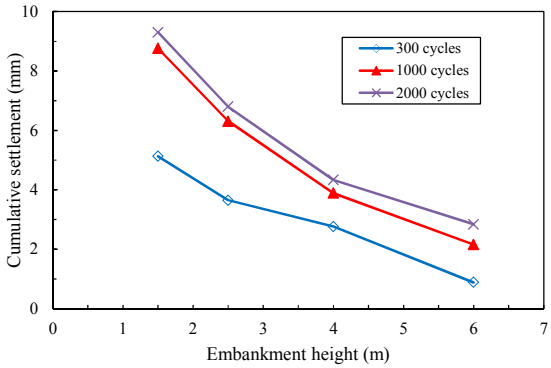

Fig. 5.36. Cumulative settlements of the soft soil (point D) for different embankment heights

5.4.7. Conclusions

In this part, the behavior of a piled embankment subjected to different traffic loadings was investigated. 3D numerical models using a finite element method (FEM) are conducted. The presence of the soft soil was taken into account, and an advanced constitutive model for the embankment behavior was also considered.

Based on these calculations, several conclusions can be figured out.

Concerning the constitutive models for the embankment, for the static analysis, due to the consideration of the density evolution with the stress level of the HYP model, the stress on the pile by HYP model is only a half of that using MC one, which results in a twice larger settlement in the HYP than in the MC. In terms of cyclic aspect, while the settlements using the MC model are not accumulated, those by the HYP one are incremental in a cyclic loading. In addition, the gradual decrease in the pile head stress and the slight increase in soft soil stress under a number of load cycles are found as the HYP model is employed for the embankment fill. The HYP model permits to simulate well the cyclic response of a piled embankment.

Furthermore, a significant effect of a number of cyclic loading on the piled embankment in terms of load transfer mechanisms was found. An increase in the cyclic number results in a significant decrease of the stress on pile head, and a moderate rise of the soft soil stress. It means that the arching effect declines with the number of load cycles. There is no soil arching monitored after 1000 load cycles. The accumulation of embankment and soft soil settlements under cyclic loading is also figured out. The cumulative settlements increase faster during the first 300 cycles, then rise gradually until 1000 cycles, after that, be slightly greater till 2000 cycles.

Larger values of frequencies and load amplitudes induced by the vehicle speed can result in a quicker decrease of the arching mechanism. At the speed of 100 km/h, the arching can be reduced after 300 cycles while for 60 km/h, this phenomenon occurs after 1000 cycles. Moreover, the traffic loading influences significantly the cumulation of the embankment and soft soil settlements. After 2000 cycles, the cumulative embankment settlement induced by the traffic speed of 100 km/h doubles the one induced by the traffic speed of 60 km/h. A higher speed of traffic induces quicker permanent settlements of soft soil.

The increase of the arching ratio was also found for a significant number of load cycles (after 1000 cycles), but this process happens gradually. The arching failure happens when the height of embankment is below 2.5 m (*H/s~1.1)*, this point is in good accordance with a 2D numerical analysis performed by Han et al. (2015). In addition,

the cumulative embankment settlements increase significantly as the embankment height increases to 4 m, then it rises slightly as the height reaches at 6 m. By contrast, the accumulative settlement of the soft soil reduces gradually with the embankment height.

5.5. 3D numerical modeling of geosynthetic-reinforced pile-supported embankment under cyclic loading

5.5.1. Introduction

In this part, 3D simulations are set up to better understand the behavior of GRPS embankments under a cyclic loading. Appropriate constitutive models are employed for the embankment fill and for the soft soil to consider its complex behavior. Numerical results taking into account the load transfer mechanisms, soft soil and embankment settlements as well as the behavior of the geosynthetic under a high number of load cycles are presented. The role of the geosynthetic is highlighted by comparing the behavior of the piled embankment with and without the geosynthetic reinforcement. The influences of different types of traffic cyclic loadings, of the embankment height, and of the number of geosynthetic layers are also presented.

5.5.2. Geometry

The column model is also suggested as similarity to the case of non-reinforced piled embankment. However, a layer of geosynthetic reinforcement was integrated into the embankment. It was placed on a 0.1-m-thick fill above the pile, which was the typical thickness used in practice (Han and Gabr 2002; Nunez et al. 2013).

5.5.3. Numerical modeling

In 3D numerical simulations, the geosynthetic layer was modeled by 4-node quadrilateral membrane (M3D4) elements. The 3D mesh is illustrated in Fig. 5.37. The geosynthetic was considered to behave in a linearly elastic way. Interfaces were placed between the granular and the geosynthetic.

5.5.4. Geosynthetics properties

In the studies of Han and Gabr (2002), Liu et al. (2007), and Lee et al. (2017), the geosynthetic was modeled by an isotropic linear elastic material with a tensile stiffness (J) around 1000 kN/m and a Poisson's ratio (ν) equal to 0.3. In the following study, a tensile stiffness of 1000 kN/m and a Poisson's ratio of 0.3 were also considered. The material parameters are presented in Table 5.10. The soil-geogrid interface was simulated by the Coulomb friction model (Hussein and Meguid 2013; Liu et al. 2007). In this study, the soil-geosynthetic and soil-pile interfaces are modeled using the basic Coulomb friction model. The coefficient of friction, μ, was assumed to be equal to 0.67 (HKS, 2014).

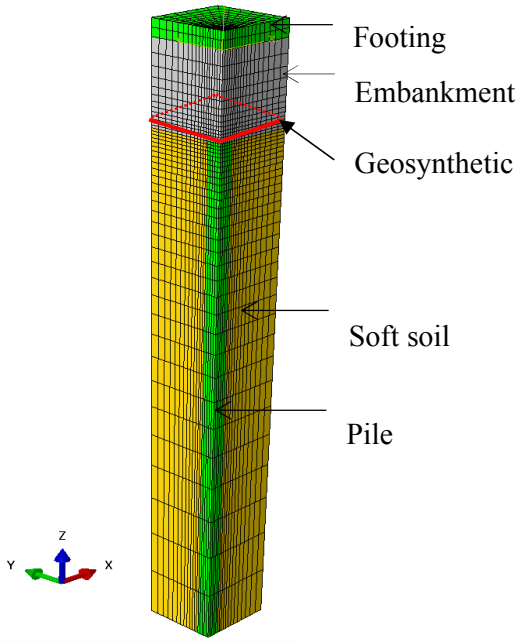

Fig. 5.37. Finite element mesh of the GRPS embankment

Table 5.10. Material parameters for the geosynthetic reinforcement

Materials	Parameters
Geosynthetic	$J = E \times t$ = 1,000 (kN/m) and $\nu = 0.3$

5.5.5. Loading and analysis steps

In this study, the cyclic loading considered as simple sinusoidal curves were similar to the above part with the speed of 100 km/h. Just like the case of the piled embankment, the analysis steps for the GRPS embankment also include the initial step, the geostatic, the static wheel loading and the cyclic one.

5.5.6. Numerical results

5.5.6.1. Parametric studies

To study the behavior of the GRPS embankment under cyclic loading, a reference case was initially established. It comprises a 1.5-m embankment on a 10 m pile-supported soft soil layer. A vehicle speed of 100 km/h resulted in a loading cycle, which was then applied at the footing top. The following factors are taken into consideration for parametric analysis, which includes the presence of geosynthetic in the piled embankment, the number of loading cycles, and the number of geosynthetic layers.

The influence of these parameters on the behavior of the studied system is presented in terms of soil arching, settlements and geosynthetic behavior under cyclic loading.

5.5.6.2. Presence of the geosynthetic in the piled embankment

The case of GRPS embankment is firstly compared to that of the piled embankment without geosynthetic to better understand the geosynthetic role in the system.

Fig. 5.38 and Table 5.11 show that the presence of the geosynthetic reinforcement increases the stress applied to the pile head and decreases the stress in the soft soil. In other words, the piled embankment reinforced by geosynthetic can enhance the stress transfer from the embankment fill to the piles. In addition to that, a stress concentration ratio for the reinforced case, which is higher than the one of the unreinforced case, is confirmed. As can be seen in Fig 5.38, thanks to the presence of GR, the vertical stress on piles increases by 25% (from 600 kPa to 750 kPa), which is similar to the numerical results obtained by Han and Gabr (2002). An increase of 25% of the vertical stress on pile results in a decrease of 3.4% in the average stress on soft soil (from 61.12 kPa to 59.08 kPa), as given in Table 5.11.

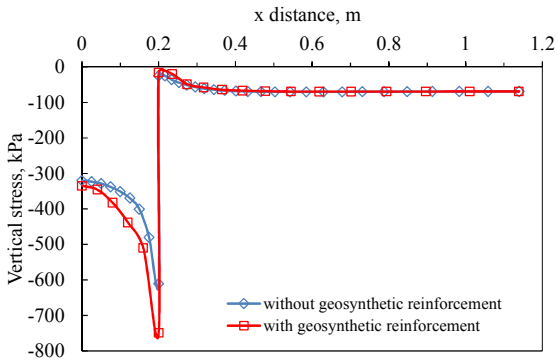

Fig. 5.38. Stress distribution at the pile head plan (along the CD line)

Table 5.11. Vertical stress on the soft soil

Vertical stresses (kPa)	Non reinforced	Reinforced
Average stress on the soft soil	-61.12	-59.08

Figs. 5.39 and 5.40 compare the embankment and soft soil settlements induced by the static loading between the improved and unimproved cases. As seen from these figures, the efficiency of geosynthetic reinforcement can reduce the settlements by about 5%. The decrease of the soft soil and the embankment settlements could be caused by a decrease in the average pressure on soft soil.

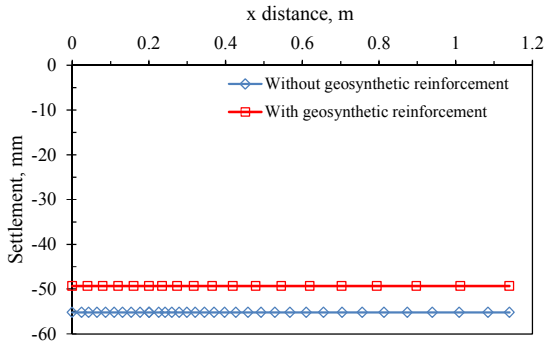

Fig. 5.39. Settlement of the embankment (along the AB line)

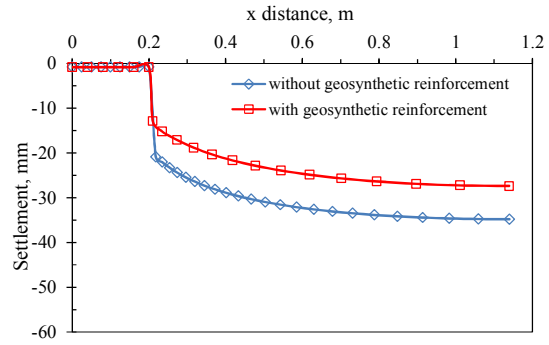

Fig. 5.40. Settlement of the soft soil (along the CD line)

The distribution of the geosynthetic tensile force with the distance from the pile center is illustrated in Fig. 5.41. The non-uniformity of the tension along the geosynthetic is shown, and the maximum value is positioned at the pile boundary. This tendency is similar to the obtained curves from the numerical results reported by Han and Gabr (2002) and the computed values by Liu et al. (2007).

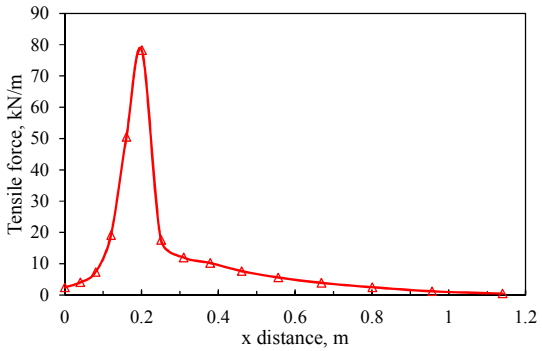

Fig. 5.41. Tensile force distribution in the geosynthetic (along the CD line)

5.5.6.3. Number of load cycles

In this part, the piled embankment and the GRPS one were subjected to 2000 load cycles at a traffic speed of 100 km/h. As shown in Fig. 5.42, the stress concentration ratio of the unreinforced and reinforced cases decreases with the number of load

cycles. A significant reduction of the soil arching is observed. The soil arching collapses after 300 load cycles for the case without geosynthetic reinforcement, that is in close agreement with the experimental results obtained by Yu et al. (2009) who discovered that the vertical stress inside the embankment fill did not change with the depth during 300 loading cycles. It means that there is no existence of soil arching. Similarly, the statement of Heitz et al. (2001) was that the soil arching is only formed by a limited number of load cycles. The reduction of soil arching might be caused by the punching mechanism of the pile heads through the embankment. The inclusion of the geosynthetic permits a significant improvement for a number of cycles lower than 300. It can be seen because of a greater SCR for the reinforced case which is lower than that for the unreinforced case. In addition to that, the geosynthetic reinforcement leads to a slowdown in the reduction of the arching effect. Evidently, the degradation of the soil arching occurs within the first 600 cycles of the reinforced case. The soil arching is, then, slightly improved with the following loading cycles. A small pile stress increase and a small stress decrease on the soft soil can be observed in Fig. 5.43. The soil zone over the pile head shows the post-peak softening (damage of the soil) at 600 cycles, then it is followed by a slight increase in residual strength (Soltani and Maekawa 2015). A similar behavior was seen in soil near the soil-geosynthetic interface in Anubhav and Wu (2015). In addition, after 600 cycles, the effect of the post-peak softening speed (damage of the soil) starts dominating. It can be seen from Fig. 5.44 that softening speed in the points between piles is slower than in the points in the pile head soil region. A slight volumetric hardening in the soil between piles continues. Therefore, slight soil arching improvement can be observed.

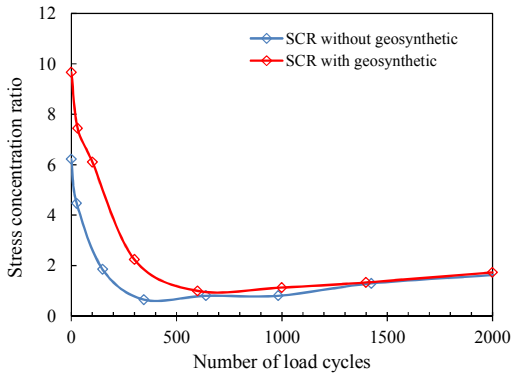

Fig. 5.42. Stress concentration ratio under cyclic loading (V = 100 km/h)

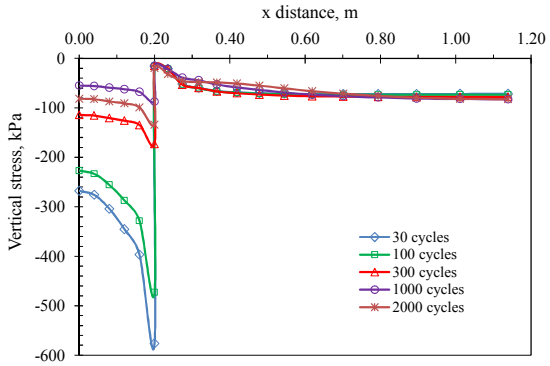

Fig. 5.43. Vertical stress at pile head plan (along the CD line) under cyclic loading (V = 100 km/h)

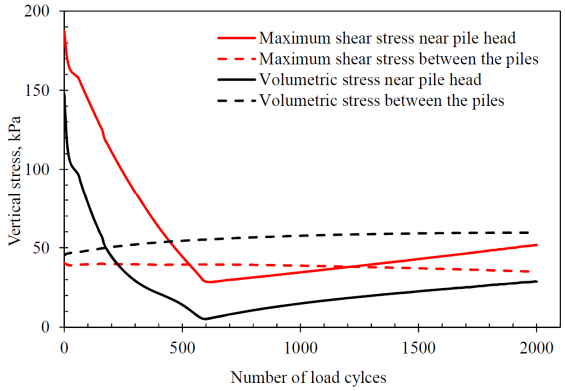

Fig. 5.44. Variation of shear and volumetric stresses under cyclic loading in the pile head zone and between piles

In the study, piles carry about 23% of the total load in the static loading case. The efficacy then shows a decrease of 20% after 600 cycles, as given in Table 5.12. The small improvement area ratio (2.4%) considered in the study results in a low efficacy value. These results are in reasonable accordance with the experimental results by Heitz et al. (2001), in which the load carried by the piles decreases by 20% from 79% to 59%.

Table 5.12. Influence of cyclic loading on the efficacy of the GRPS embankments

Compared cases	Improvement area ratio (%)	Efficacy after a certain number of cycles (%)				
		0	600	1000	2000	10000
Our case with f = 2.8 Hz	2.4	23.37	2.41	2.72	4.18	-
Heitz's case with f = 1 Hz	10.24	78.73	58.86	59.56	59.45	62.50

In addition to that, the inclusion of geosynthetic reinforcement (GR) has the advantages such as reducing the stress on the soil foundation and cumulative settlements, as demonstrated in Figs. 5.45 and 5.46. Under a number of 1000 loading

cycles, the stress on the soft soil increases significantly, as shown in Fig. 5.45. The cumulative settlements of soft soil and embankment are shown in Fig. 5.46. However, the rate of the cumulative settlements decreases with the number of load cycles. The accumulated settlement of the embankment after 2000 cycles is a half of the one after the first 1000 cycles. For the soft soil settlement, after the soil arching, there is a stable stage (600 cycles) during which the pressure on soil remains constant, which results in constant settlements.

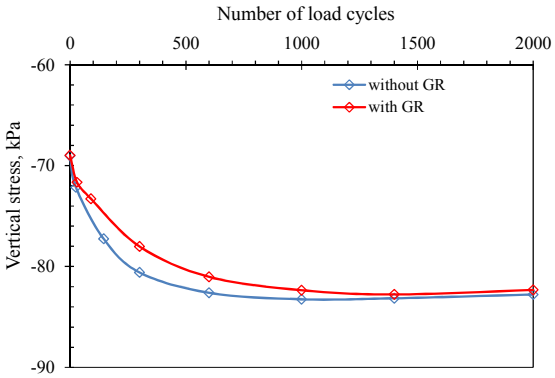

Fig. 5.45. Vertical stress on the soft soil (point D) under cyclic loading (V = 100 km/h)

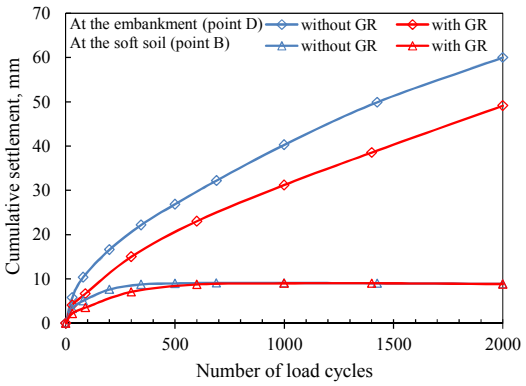

Fig. 5.46. Cumulative settlements under cyclic loading (V = 100 km/h)

The tensile stress of geosynthetic reinforcement (GR) during the cyclic loading is presented in Fig. 5.47. It is shown that the tensile stress of GR on pile cap significantly decreases while it slightly increases with the loading cycles on the soft soil. The decrease of the GR tensile stress is related to the decrease of the vertical stress on the pile that is observed in Fig. 5.43. It is due to the fact that the cyclic loading induces a punching mechanism at the pile head and induces soil plasticity surrounding. A slight increase in the GR tensile stress on soft soil was also found in the work done by Han and Bhandari (2009).

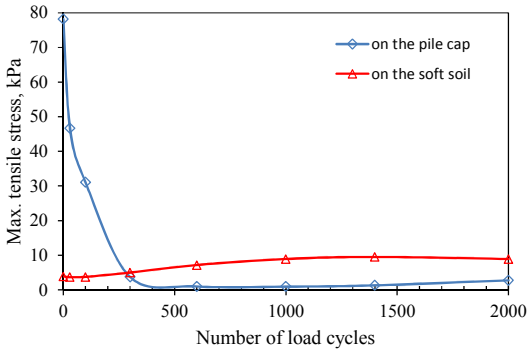

Fig. 5.47. Tensile stress in geosynthetic under cyclic loading (V = 100 km/h)

5.5.6.4. Influence of the number of geosynthetic layers

To consider the influence of geosynthetic layers on the GRPS embankment, the three cases are set up including a single layer case (located at 0.1 m from pile head); two layers (positioned at 0.1 and 0.3 from pile head); and three layers (located at 0.1, 0.3 and 0.5 m from pile head). The influence of the number of geosynthetic layers on the soil arching and the embankment settlement is presented in Table 5.13. It can be seen that under the static loading, the soil arching slightly increases and the settlement reduces marginally with the number of geosynthetic layers. An insignificant influence of the number of geosynthetic reinforcements on the soil arching mechanism was also stated by van Eekelen et al. (2012a, 2012b). Under the cyclic loading, an insignificant change in the soil arching and in the accumulative settlement with the number of geosynthetics is seen. The results are in a reasonable accordance with the numerical results of Moormann et al. (2016). According to their work, there is no significant influence of the number of layers of reinforcement on soil arching.

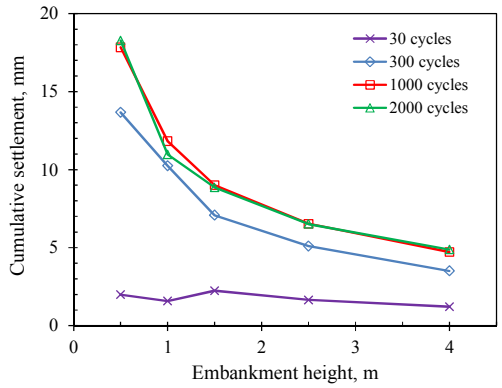

Fig. 5.48. Cumulative settlements of the soft soil (point D) for different embankment heights

Table 5.13. Influence of the number of geosynthetic layers on the GRPS embankment under the static and cyclic loadings

Influence on	Number of geosynthetic layers		
	1 layer	2 layers	3 layers
Stress concentration ratio under static loading, *SCR*	9.67	9.84	9.94
Crest settlement under static loading, mm	49.32	48.40	44.57
Stress concentration ratio after 2000 cycles, *SCR*	1.73	1.53	1.52
Accumulative settlement of embankment crest after 2000 cycles, mm	49.10	49.92	47.11

5.5.7. Conclusions

3D numerical simulations are performed to investigate the behavior of a GRPS under traffic cyclic loadings. By comparing a piled and GRPS embankment and considering the influence of cyclic loading number and of GR layers number. The numerical results point out the following conclusions.

With regard to the static loading aspect, the presence of GR in the piled embankment increases a moderate amount of pile head stress and decreases a minor portion of soft soil stress. Additionally, as compared to the piled embankment, the GRPS system can reduce by 5% in the embankment and soft soil settlements. The tensile force distribution in geosynthetic in the study is found to be in a good agreement with that in the previous ones obtained by Han and Gabr (2002), Liu et al. (2007).

For the case of cyclic loading, the application of the HYP model for the embankment demonstrates that it can simulate well the cyclic response of the GRPS embankment since it can address the arching decrease and the cumulative settlements under the number of cyclic loading.

Moreover, a decrease of the stress concentration ratio is related to the arching effect degradation with the number of cycles. The performance of the geosynthetic reinforcement slows down the reduction of the soil arching. The degradation of the soil arching occurs at the cycle numbers of 300 and 600 for the unreinforced and reinforced piled embankments, respectively.

The existence of GR in the piled embankment results in a decrease of 20% in the accumulation of embankment settlement. A reduction in the cumulation rate of soft soil and embankment settlements with the number of cyclic loading is also indicated.

The geosynthetic layers number seems not to be influent on the soil arching and the cumulative settlements.

In this study, a simplified assumption for traffic loading is employed as a type of cyclic

loading, which does not cover either the whole dynamic effects or the moving loads. This limitation may lead to results far from reality. In future works, the complexity of the traffic loading should be taken into consideration. Small or full-scale model tests will also be required to validate the numerical analysis.

5.6. Conclusions

Based on a validation of the proposed numerical study against laboratory tests and the other numerical one of Houda (2016) for the monotonic and cyclic responses of a rigid inclusion-improved soil, the following major points are concluded.

Both the numerical studies underestimate the efficacy of the system under cyclic loading as compared to the experimental one. While the measured efficacy is nearly constant with a number of load cycles, the numerical ones reduce gradually. Concerning the settlement, the experimental work and both the numerical studies show that an increase in cyclic number results in the cumulative settlement, and the cumulation per cycle decreases gradually with the following cycles. Less the accumulated settlement for the over-consolidated soft soil than for normally consolidated one is found as well. Moreover, the cumulative settlements in the case without slab are only two-thirds of those in the slab case.

In addition, using the hypoplastic constitutive model for granular soils can address the monotonic and cyclic behaviors of the rigid inclusion-improved soil. In comparison with the numerical study by Houda (2016), more accuracy in the results in terms of efficacy and the cumulative settlement of the HYP model than of the CYsoil one is found.

The studies on the cyclic responses of piled and GRPS embankments under different traffic loadings indicate several main conclusions that are presented below.

While the MC model used for the embankment cannot produce the accumulated settlements and the soil arching decrease, the HYP model for the LTP simulates well the cumulative settlements and the soil arching degradation under cyclic loading.

Furthermore, as the number of cyclic loading increases the arching effect decreases, it is showed by the significant decrease of the pile head stress, and the moderate rise of the soft soil stress. No arching with the specific number of load cycles is also found. As regards of the settlement, the cumulative settlements develop quickly during the first 300 cycles, followed by a gradual rise till 1000 cycles, they are then slightly greater until 2000 cycles.

As taking into account the difference in traffic loading, the higher the vehicle speed, the quicker the decrease of soil arching and the more the cumulative embankment settlement. Moreover, an increase in the traffic speed results in the faster permanent settlement of soft soil.

In addition, the soil arching and the cumulative embankment settlement increase as the embankment height increases. By contrast, the accumulative settlement of soft

soil reduces gradually with the embankment height.

The addition of GR in the piled embankment is consequent in the moderate increase of pile head stress and the minor decrease of soft soil stress in the static loading case. Concerning the cyclic aspect, the presence of the GR can slow down the soil arching decrease as compared to the unreinforced piled embankment. In terms of the settlement, the GR in a piled embankment can reduce by 20% in the accumulative embankment settlement.

Furthermore, the numerical results figure out that the soil arching and the cumulative settlements seem not to be significantly influenced by the number of geosynthetic layers.

Conclusions and recommendations

Conclusions

A study on the literature review on piled and GRPS embankments indicates that the research on piled and GRPS embankments under static loading case is well-understood. Several analytical methods were proposed to investigate the load transfer mechanisms of such systems. Several design standards provide guidelines for the practicing engineers. Furthermore, the complexity of the piled and GRPS embankments systems induce a difficulty in the determination of total and differential settlements for analytical models. Besides, the presence of soft soil is often disregarded in analytical models as well.

Numerical simulations have been demonstrated that they can provide some advantages for analyzing piled embankments, which include an economic efficiency, a reduced calculation time, the problem-solving complexity, a detailed visualization and reliable results. The numerical studies allow showing clearly the load transfer mechanism as well as the settlements.

In this work, the implementation steps are presented for simulating a piled and GRPS embankments. The detail of simulation steps enables to define the tasks and procedures including model idealization, discretized mesh, constitutive models and material parameters, soil/structure interaction, boundary conditions and loads, analysis procedure, and result visualization. Moreover, a brief review of the available constitutive models in FLAC and ABAQUS is introduced. It is beneficial for users to select the appreciate ones.

With regard to the footing over a rigid inclusion-reinforced soil without a mattress under complex loadings, the main results obtained are the following:

In terms of load transfer aspects, the results derived from the centered vertical loading tests indicate that the efficiency increases since the stress onto inclusion is higher than the soft soil one. The pressure on inclusion seems to be linear with the vertical loading on the footing for the considered applied stresses.

The eccentrically vertical loading induces a difference in the inclusion head pressure. The larger the eccentricity, the higher the pressure on the weighted side and the smaller the one on the lifted side. In addition, the horizontal loading on the footing results in an increase of the stresses on rigid inclusion. A few numbers of load cycles on the footing cause the decrease of the inclusion head

pressure as well.

With regard to the footing displacements, the footing settlement in the case of reinforced footing is only an half of the unreinforced one. In addition, the vertical load has a significant influence on the footing displacement. As the vertical load is not large enough, the footing displacement is small and the settlements are accumulated insignificantly under several load cycles. On the other hand, the vertical loading is large enough (over 700 kN) and, induces a large footing displacement and significant cumulative settlements.

For the horizontal loading tests, as similar to the vertical loading, a significant lateral footing displacement only occurs as the horizontal loading is large enough. Moreover, a lower lateral displacement of the inclusion head than the one of the footing is found under the horizontal loading tests. It might be due to the non-connection between the inclusion and footing.

A study on the foundation solutions for wind turbines subjected to real loading cases, in which the footing over a rigid inclusion-reinforced soft soil is considered as a foundation solution. The numerical results have verified that the rigid inclusion-improved soil method overcomes some disadvantages of the other classical ones, which include:

The total and differential surface settlements of the RI-reinforced foundation and the piled raft solutions have decreased significantly compared to the shallow foundation cases.

As regards of the RI-improved raft, an increase in the area improvement ratio results in the decrease of soil settlements, foundation rotation, and axial forces and bending moments on the reinforcements.

The applied overturning moment on a foundation not only causes an increase in the total and differential soil settlements but also leads to a redistribution of the axial forces and bending moments on inclusions/piles.

A comparison between the piled raft and the RI reinforced foundation figured out that the RI inclusion method provides an efficient method for WT foundations in terms of axial forces and moments on reinforcements. Additionally, the ground improvement by rigid inclusions also brings an appropriate and reliable choice owing to its efficiency and applicability.

The occurrence of cyclic loading action on the structures and soils is important in nature. Due to the cyclic action, the increase of the total and differential settlements

are caused by the cumulated strain. It needs to be considered in geotechnical problems. The cumulative strain depends significantly on the cyclic loading number, the stress/strain amplitude, the initial relative density, and the grain-size distribution. Meanwhile, it is less influenced by the cyclic frequency and average mean stress.

As reviewing the several constitutive models of soils under cyclic loading, it is found that the classical models (MC and MCC) underestimate the cyclic response of soils in terms of stiffness degradation and accumulative strain while the advanced ones like HYP and kinematic hardening have better abilities to model these complex phenomena.

The hypoplastic model is suggested to be used due to the fact that it can consider the variation in density, dilatancy and stress level in the numerical model. It can then permits to model the soil behavior in a realistic manner. The degradation of stiffness is also taken into account by three additional constants. The addition of the *intergranular* strain concept allows the HYP model to capture well the stiffness increase with the stress rotation.

The numerical simulations of the behaviors of a rigid inclusion reinforced soft soil under cyclic loading have permitted to draw several conclusions.

The literature review on piled and GRPS embankments under cyclic loading points out that a limited attention was paid to the cyclic response of these systems. The simple soil constitutive models used for LTP could not capture the cyclic response, which leads to under- or overestimations on designs. The load transfer mechanism and cumulated settlements need to be well modeled under a high number of cyclic loading.

The application of the hypoplastic model for the LTP (embankment) can exhibit the monotonic and cyclic behavior of the rigid inclusion-improved soil. In comparison, more accuracy in the results in terms of efficacy and cumulative settlement of the HYP model than of the simple ones (MC and CYsoil) is found.

The numerical modeling of the small-scale laboratory tests of Houda (2016) on the rigid inclusion-reinforced soil systems under monotonic and cyclic loadings has pointed out some main results. As the HYP model is employed for the LTP, the numerical studies are in good agreement with the experimental tests done by Houda (2016).

Besides that, the experimental work and both the numerical studies point out that the cumulative settlement increases as the cyclic loading number increases,

and the cumulation over cycle declines gradually with the following cycles. The cumulated settlements for the case of over-consolidation soft soil are less than that the normally consolidated ones. The accumulated settlements in the slab case are a third greater than those in the non-slab case.

The numerical studies on the cyclic response of a piled and GRPS embankments indicate several valuable points. The arching effect decreases as the number of cyclic loading increases. No arching effect with the specific number of load cycles is also found. As regards of the settlements, the settlements accumulated under cyclic loading, the rate of accumulative settlements slows down as the cyclic loading number increases.

The numerical results also indicate that the higher the traffic speed, the quicker the degradation of arching effect and the larger the cumulative settlement of embankment. Meanwhile, as the traffic speed increases, the permanent settlement of soft soil reaches faster. Moreover, the soil arching and the cumulative embankment settlement rise with the increase of embankment height, while the accumulative settlement of soft soil decreases moderately.

The presence of the geosynthetic reinforcement (GR) in a piled embankment can slow down the soil arching decrease. In terms of settlements, the accumulative embankment settlement of the GRPS embankment is 20% smaller than that of the piled embankment. The numerical results indicate that the arching effect and the accumulated settlements seem not to be significantly affected by the GR layers number.

Recommendations

In the case of the footings over rigid inclusion-reinforced soil, the numerical outcomes are sometimes under-estimated for the unloading-reloading process. It might be due to the fact that the constitutive models which were adopted for soils were too simple and cannot account for the soil behavior under cycles.

Concerning the work on wind turbine foundation, the presented research only considers a static loading which represents an envelope of the cyclic loading involved in wind turbines (due to the wind and the generator rotation). Monitoring data on a real wind turbine will be necessary to validate the obtained numerical results. This work focused on a simplified way to consider the cyclic loading signal due to wind turbines, an effort will also be done to take into account for the impact of the cyclic loadings using an appropriate constitutive model in the following step.

As regards of a validation of small-scale experimental tests of Houda (2016), a set of parameters for the intergranular strain concept was assumed in the analyses. The parameters to be introduced in the numerical analysis will be more accurate and will permit to better simulate the experimental tests. Moreover, the Cam-clay model did not address well the accumulative settlements after 20 load cycles. For the further studies, a more complex one is a good suggestion for the cyclic behavior of soft soil.

In the cases of a piled and GRPS embankments, a simplified assumption for traffic loading is employed as a type of cyclic loading, which does not cover either the whole dynamic effects or the moving loads. This limitation may lead to results far from reality. In future works, the complexity of the traffic loading should be taken into consideration. Small or full-scale model tests will also be required to validate the numerical analysis.

References

Al-Tabbaa, A. and Muir Wood, D. (1989) 'An experimentally based `bubble' model for clay', in S. Pietruszczak, G. N. P. (ed.) International Symposium on Numerical Models in Geomechanics. Elsevier Applied Science Publishers, pp. 91–99.

Andromeda, J. and Briançon, L. (2008). 'Load transfer mechanisms in pile-supported earth platform under slab foundation'. Proc. BGA International Conference on Foundations, ICOF2008, Dundee, Scotland, 1291-1302.

Anubhav and Wu, H. (2015) 'Modelling of Non-linear Shear Displacement Behaviour of Soil–Geotextile Interface', International Journal of Geosynthetics and Ground Engineering. Springer International Publishing, 1(2), p. 19.

Ariyarathne, P., Liyanapathirana, D. S. and Leo, C. J. (2013) 'Comparison of Different Two-Dimensional Idealizations for a Geosynthetic-Reinforced Pile-Supported Embankment', International Journal of Geomechanics, 13(6), pp. 754–768.

Bauer, E. (1996) 'Calibration of a Comprehensive Hypoplastic Model for Granular Materials.', Soils and foundations, 36(1), pp. 13–26.

Boussetta, S., Bouassida, M. and Zouabi, M. (2016) 'Assessment of observed behavior of soil reinforced by rigid inclusions', Innovative Infrastructure Solutions. Springer International Publishing, 1(1), pp. 1–12.

Brendan, F. P., Richard, G. and Jeromy, M. (2009) 'Design and Construction of Intermediate Foundation Solutions for Wind Turbines', in Contemporary Topics in Deep Foundations. Reston, VA: American Society of Civil Engineers, pp. 504–511.

Briançon, L., Dias, D. and Simon, C. (2015) 'Monitoring and numerical investigation of a rigid inclusions–reinforced industrial building', Canadian Geotechnical Journal, 52(10), pp. 1592–1604.

Briançon, L. and Simon, B. (2009) 'Performance of Pile-Supported Embankment over Soft Soil: Full-Scale Experiment', Journal of Geotechnical and Geoenvironmental Engineering, 138(4), pp. 551–561.

Byrne, B. W. and Houlsby, G. T. (2003) 'Foundations for offshore wind turbines', Philosophical Transactions of the Royal Society A: Mathematical, Physical and Engineering Sciences, 361(1813), pp. 2909–2930.

Byrne, W. B. and Houlsby, G. T. D. (2006) 'Assessing Novel Foundation Options for Offshore Wind Turbines', in World Maritime Technology Conference. London, UK, pp. 1–10.

C.F.M.S (2011) Working group on Wind Turbine Foundations. Recommendations for the design, calculation, installation and inspection of wind-turbine foundations.

Carlsson, B. (1987) 'Reinforced soil, principles for calculation', in Terratema A. B. Linkoping, Sweden.

Catană, G., Savu, A.-A. and Ealangi, I. (2013) 'Modelling methods for soil-structure interaction applied in wind turbine foundation design', Mathematical Modelling in Civil Engineering, 9(4).

Chen, R. P. et al. (2008) 'A theoretical solution for pile-supported embankments on soft soils under one-dimensional compression', Canadian Geotechnical Journal, 45(5), pp. 611–623.

Chevalier, B., Villard, P. and Combe, G. (2011) 'Investigation of Load-Transfer Mechanisms in Geotechnical Earth Structures with Thin Fill Platforms Reinforced by Rigid Inclusions', International Journal of Geomechanics, 11(3), pp. 239–250.

Ciopec, A. et al. (2013) 'Alternative energy resources: foundation solution for Wind turbine', Constanta Maritime University Annals, 13, pp. 150–153.

Clare, R. and May, I. D. (1990) 'Development of vertical axis wind turbine', Proceedings of the Institution of Civil Engineers, 88(4), pp. 705–714.

Collin, J. G. (2004) 'Column supported embankment design considerations', in 52nd Annual Geotechnical Engineering Conference. University of Minnesota.

Combault, J., Morand, P. and Pecker, A. (2000) 'Structural response of the Rion-Antirion Bridge', Proceedings 12th World Conference on Earthquake Engineering, pp. 1–8.

Cook, N. J. (1990) The Designer's Guide to Wind Loading of Building Structures. Butterwort. London.

Croce, A. (2011) Analisi dati di monitoraggio del rivestimento della galleria del passante ferroviario di Bologna (in Italian). Polytechnics of Turin, Italy.

Dafalias, Y. F. and Popov, E. P. (1975) 'A model of nonlinearly hardening materials for complex loading', Acta Mechanica, 21(3), pp. 173–192.

Deb, K. (2010) 'A mathematical model to study the soil arching effect in stone column-supported embankment resting on soft foundation soil', Applied Mathematical Modelling. Elsevier Inc., 34(12), pp. 3871–3883.

Deb, K. and Mohapatra, S. R. (2013) 'Analysis of stone column-supported geosynthetic-reinforced embankments', Applied Mathematical Modelling, 37(5), pp. 2943–2960.

Dias, D. and Simon, B. (2015) 'Spread Foundations on Rigid Inclusions Subjected to Complex Loading: Comparison of 3D Numerical and Simplified Analytical Modelling', American Journal of Applied Sciences, 12(8), pp. 533–541.

Do, N. A. et al. (2013) '3D modelling for mechanized tunnelling in soft ground-influence of the constitutive model', American Journal of Applied Sciences, 10(8), pp. 863–875.

van Eekelen, S. J. M. et al. (2012a) 'Model experiments on piled embankments. Part I', Geotextiles and Geomembranes. Elsevier Ltd, 32, pp. 82–94.

van Eekelen, S. J. M. et al. (2012b) 'Model experiments on piled embankments. Part II', Geotextiles and Geomembranes. Elsevier Ltd, 32, pp. 82–94.

van Eekelen, S. J. M., Bezuijen, A. and van Tol, A. F. (2015) 'Validation of analytical models for the design of basal reinforced piled embankments', Geotextiles and Geomembranes, 43(1).

van Eekelen, S. J. M., Bezuijen, A. and Van Tol, A. F. (2013) 'An analytical model for arching in piled embankments', Geotextiles and Geomembranes. Elsevier Ltd, 39, pp. 78–102.

Eskişar, T., Otani, J. and Hironaka, J. (2012) 'Visualization of soil arching on reinforced embankment with rigid pile foundation using X-ray CT', Geotextiles and Geomembranes, 32, pp. 44–54.

Filz, G. et al. (2012) 'Column-Supported Embankments: Settlement and Load Transfer', in Proceedings of Geo-Congress. Geotechnical Engineering State of the Art and Practice, pp. 54–77.

Gajo, A., Bigoni, D. and Muir Wood, D. (2004) 'Multiple shear band development and related instabilities in granular materials', Journal of the Mechanics and Physics of Solids, 52(12), pp. 2683–2724.

Gajo, A. and Muir Wood, D. (1999) 'A kinematic hardening constitutive model for sands: the multiaxial formulation', International Journal for Numerical and Analytical Methods in Geomechanics, 23(9), pp. 925–965.

Girout, R. et al. (2014) 'Numerical analysis of a geosynthetic-reinforced piled load transfer platform - Validation on centrifuge test', Geotextiles and Geomembranes. Elsevier Ltd, 42(5), pp. 525–539.

Gotschol, A. (2002) Veranderlich elastisches und plastisches Verhalten nichtbindiger Boden und Schotter unter zyklisch-dynamischer Beanspruchung. Universitat Gh Kassel.

Gudehus, G. (1996) 'A Comprehensive Constitutive Equation for Granular Materials.', Soils and foundations, 36(1), pp. 1–12.

Gudehus, G. et al. (2008) 'The soilmodels.info project', International Journal for Numerical and Analytical Methods in Geomechanics, 32(12), pp. 1571–1572.

Guido, V. A., Knueppel, J. D. and Sweeny, M. A. (1987) 'Plate Loading Tests on Geogrid-Reinfoced Earth Slabs', in Geosynthetic '87 Conference New Orleans USA: Proceedings, pp. 216–225.

Habib, S., Dehnavi, Y. and Alavi, A. (2010) 'Numerical modeling of stress-strain behavior of sand under cyclic loading', Engineering Geology. Elsevier B.V., 116(1–2), pp. 53–72.

Han, G., Gong, Q. and Zhou, S. (2011a) 'An Experimental Investigation of Soil Arching under Dynamic Loads', in Proceedings of the 11th International Conference of Chinese

Transportation Professionals. Towards Sustainable Transportation Systems, ASCE, pp. 3030–3037.

Han, G., Gong, Q. and Zhou, S. (2011b) 'Mechanical analysis of soil arching under dynamic loads', in 2011 Pan-Am CGS Geotechnical Conference.

Han, G., Gong, Q. and Zhou, S. (2015) 'Soil Arching in a Piled Embankment under Dynamic Load', International Journal of Geomechanics, 15(6), p. 4014094.

Han, J. and Bhandari, A. (2009) 'Evaluation of Geogrid-Reinforced Pile-Supported Embankments under Cyclic Loading using Discrete Element Method', in 2009 US-China Workshop on Ground Improvement Technologies. Advances in Ground Improvement, pp. 242–251.

Han, J. and Gabr, M. (2002) 'Numerical Analysis of Geosynthetic-Reinforced and Pile-Supported Earth Platforms over Soft Soil', Journal of Geotechnical and Geoenvironmental Engineering, 128(1), pp. 44–53.

Hardin, B. O. and Drnevich, V. P. (1972) 'Shear Modulus and Damping in Soils: Design Equations and Curves', Geotechnical Special Publication, 98(118).

Hassen, G., Dias, D. and de Buhan, P. (2009) 'Multiphase Constitutive Model for the Design of Piled-Embankments: Comparison with Three-Dimensional Numerical Simulations', International Journal of Geomechanics, 9(6), pp. 258–266.

Heitz, C., Luking, J. and Kempfert, H.-G. (2001) 'Geosynthetic Reinforced and Pile Supported Embankments Under Static and Cyclic Loading', EuroGeo4, 1(215), pp. 1–8.

Le Hello, B. and Villard, P. (2009) 'Embankments reinforced by piles and geosynthetics-Numerical and experimental studies dealing with the transfer of load on the soil embankment', Engineering Geology. Elsevier B.V., 106(1–2), pp. 78–91.

Helm, J., Laue, J. and and Triantafyllidis, T. (2010) 'Untersuchungen an der RUB zur Verformungsentwicklung von Boden unter zyklischen Belastungen', in Boden unter fast zyklischer Belastung: Erfahrungen und Forschungsergebnisse, pp. 201–222.

Herle, I. and Gudehus, G. (1999) 'Determination of parameters of a hypoplastic constitutive model from properties of grain assemblies', Mechanics of Cohesive-frictional Materials, 4(5), pp. 461–486.

Hewlett, W. J. and Randolph, M. F. (1988) 'Analysis of piled embankments', Ground Engineering.

HKS (2014) Abaqus 6.14 Documentation.

Hong, P. Y. et al. (2014) 'An elastoplastic model with combined isotropic-kinematic hardening to predict the cyclic behavior of stiff clays', Computers and Geotechnics, 62, pp. 193–202.

Houda, M. (2016) 'Comportement sous chargement cyclique des massifs de sol renforcés par inclusions rigides : expérimentation en laboratoire et modélisation numérique', p. 186.

Houda, M., Jenck, O. and Emeriault, F. (2016) 'Physical evidence of the effect of vertical cyclic loading on soil improvement by rigid piles: a small-scale laboratory experiment using Digital Image Correlation', Acta Geotechnica. Springer Berlin Heidelberg, 11(2), pp. 325–346.

Huang, J. (2003) Coupled Mechanical and Hydraulic Modeling of Geosynthetic-reinforced Column supported Embankment. University of Kansas.

Huang, J., Han, J. and Collin, J. (2005) 'Geogrid-Reinforced Pile-Supported Railway Embankments: A Three-Dimensional Numerical Analysis', Transportation Research Record, 1936(1), pp. 221–229.

Huang, J. and Han, J. (2009) '3D coupled mechanical and hydraulic modeling of a geosynthetic-reinforced deep mixed column-supported embankment', Geotextiles and Geomembranes. Elsevier Ltd, 27(4), pp. 272–280.

Huang, J. and Han, J. (2010) 'Two-dimensional parametric study of geosynthetic-reinforced column-supported embankments by coupled hydraulic and mechanical modeling', Computers and Geotechnics. Elsevier Ltd, 37(5), pp. 638–648.

Hussein, M. G. and Meguid, M. a (2013) 'Three-Dimensional Finite Element Analysis of Soil-Geogrid Interaction under Pull-out Loading Condition', GeoMontreal, (1984), p. 7.

Ishihara, K. (1996) Soil behavior in earthquake geotechnics.

Itasca (2009) Online manual of Flac3D version 4.0. Edited by I. Itasca consulting Group.

Janbu, N. (1963) 'Soil compressibility as determined by oedometer and triaxial tests.', in Proc. of the European Conf. on Soil Mechanics and Foundations Engineering, Wiesbaden. Essen : Deutsche Gesellschaft für Erd-und Grundbau:, pp. 19–25.

Jenck, O., Dias, D. and Kastner, R. (2006) 'Three-dimensional modelling of an embankment over soft soil improved by rigid piles', Numerical Methods in Geotechnical Engineering – Schweiger (ed.) © 2006 Taylor & Francis Group, London., pp. 817–822.

Jenck, O., Dias, D. and Kastner, R. (2007) 'Two-dimensional physical and numerical modeling of a pile-supported earth platform over soft soil', Journal of Geotechnical and Geoenvironmental Engineering, 133(3), pp. 295–305.

Jenck, O., Dias, D. and Kastner, R. (2009a) 'Discrete element modelling of a granular platform supported by piles in soft soil - Validation on a small scale model test and comparison to a numerical analysis in a continuum', Computers and Geotechnics. Elsevier Ltd, 36(6), pp. 917–927.

Jenck, O., Dias, D. and Kastner, R. (2009b) 'Three-dimensional numerical modeling of a piled embankment', International Journal of Geomechanics, (June), pp. 102–112.

Jennings, K. and Naughton, P. J. (2012) 'Similitude Conditions Modeling Geosynthetic-Reinforced Piled Embankments Using FEM and FDM Techniques', ISRN Civil Engineering, 2012, pp. 1–16.

Jiang, Y., Han, J. and Zheng, G. (2014) 'Numerical analysis of a pile-slab-supported railway embankment', Acta Geotechnica, 9(3), pp. 499–511.

Kempfert, H. et al. (2004) 'German recommendations for reinforced embankments on pile-similar elements', EuroGeo3-3th European Geosynthetics Conference, pp. 279–283.

Kempfert, H. G., Gotschol, A. and Stocker, T. (2000) Kombiniert zyklische und dynamische Elementversuche zur Beschreibung des Kurz- und Langzeitverhaltens von Schotter und granularen B˜ oden.

Kim, K. J. (2017) I-64 Widening in Tyrrell County. North Carolina.

Kokusho, T. (1980) 'Cyclic triaxial test of dynamic soir properties fer wide strain range', Soils and Foundations, pp. 305–312.

Kolymbas, D. and Karlsruhe (1991) 'An outline of hypoplasticity', Archive of Applied Mechanics, 61, pp. 143–151.

Kolymbas, D. and Wu, W. (1990) 'Recent results of triaxial tests with granular materials', Powder Technology, 60(2), pp. 99–119.

Kondner R.L (1963) A Hyperbolic Stress-strain Formulation for Sands. Northwestern University.

Kramer, S. L. (1996) Geotechnical Earthquake Engineering. Prentice-Hall International Series in Civil Engineering and Engineering Mechanics.

Lade, P. V. (2005) 'Overview of Constitutive Models for Soils', Soil Constitutive Models, 40771(January 2005), pp. 1–34.

Lang, R. et al. (2015) 'Study on Load-bearing Characteristics of Different Types of Pile Group Foundations for an Offshore Wind Turbine', Journal of Coastal Research, 73, pp. 533–541.

Leclaire, F. et al. (2017) 'Application of Controlled Modulus Columns for Refinery and Petrochemical Tank Farm', 2(1), pp. 13–26.

Lee, S. C., Leung, C. F. and Chow, Y. K. (2005) 'Performance of Oil Tank Foundation', in GSP 132 Advances in Deep Foundations, pp. 1–11.

Lee, S. J. et al. (2017) 'Analysis of Cyclic Loading Transferred Mechanism on Geosynthetic-Reinforced and Pile-Supported Embankment', Journal of the korean geotechnical society, 32(12).

Lehn, J., Moormann, C. and Aschrafi, J. (2016) 'Numerical Investigations on the Load Distribution over the Geogrid of a Basal Reinforced Piled Embankment under Cyclic Loading', Procedia Engineering, 143(Ictg), pp. 435–444.

Lentz, R. W. and Baladi, G. Y. (1980) 'Simplified procedure to characterize permanent strain in sand subjected to cyclic loading', in Soils under cyclic and transient loading, volume 1. Proc. International symposium, pp. 89–95.

Li, Z. et al. (2016) 'A hypoplastic macroelement for single vertical piles in sand subject to three-dimensional loading conditions', Acta Geotechnica.

Liu, H., Charles, W. W. N. and Fei, K. (2007) 'Performance of a Geogrid-Reinforced and Pile-Supported Highway Embankment over Soft Clay: Case Study', Journal of Geotechnical and Geoenvironmental Engineering, 133(12), pp. 1483–1493.

Love, J. and Milligan, G. (2003) 'Design methods for basally reinforced piled-supported embankments over soft ground', Ground Engineering.

Low, B. K., Tang, S. K. and Choa, V. (1994) 'Discussion: Arching in Piled Embankments', Journal of Geotechnical Engineering, 122(4), pp. 318–318.

Magnan, J. P. (1994) 'Methods to reduce the settlement of embankments on soft clay: a review', in Vertical and Horizontal Deformations of Foundations and Embankments. ASCE Geotechnical Special Publication, pp. 77–91.

Marr, W. A. and Christian, J. T. (1981) 'Permanent displacements due to cyclic wave loading', Journal of the Geotechnical Engineering Division, ASCE, 107(GT8), pp. 1129–1149.

Matutano, C. et al. (2014) 'The effect of scour protections in offshore wind farms', Journal of Coastal Research, 70, pp. 12–17.

McKelvey, J. A. (1994) 'The anatomy of soil arching', Geotextiles and Geomembranes, 13(5), pp. 317–329.

Messioud, S. et al. (2016) 'Dynamic Response of Pile Reinforced Soils and Piled Foundations', Geotechnical and Geological Engineering, 34(3), pp. 789–805.

Messioud, S., Sbartai, B. and Dias, D. (2017) 'Estimation of Dynamic Impedance of the Soil–Pile–Slab and Soil–Pile–Mattress–Slab Systems', International Journal of Structural Stability and Dynamics, 17(6), p. 1750057.

Mirza, S. A. and Brant, W. (2009) 'Chapter 5: Footing Design', in ACI Design Handbook. Publication SP- 17(09) (M. Saatcioglu, editor), American Concrete Institute, Farmington Hills, Michigan, pp. 189–204.

Moormann, C., Lehn, J. and Aschrafi, J. (2016) 'Design of reinforced piled earth structures under static and variable loads', in GeoAmericas 2016 3rd Pan-American Conference on Geosynthetics.

Ng, C. W. W. et al. (2015) 'Influence of sand density and retaining wall stiffness on three-dimensional responses of tunnel to basement excavation', Canadian Geotechnical Journal, 52(11), pp. 1811–1829.

Nguyen, D. D. C., Jo, S.-B. and Kim, D.-S. (2013) 'Design method of piled-raft foundations under vertical load considering interaction effects', Computers and Geotechnics, 47, pp. 16–27.

Niemunis, A. and Herle, I. (1997) 'Hypoplastic model for cohesionless soils with elastic strain range', Mechanics of Cohesive-Frictional Materials, 2(4), pp. 279–299.

Nunez, M. A., Briançon, L. and Dias, D. (2013) 'Analyses of a pile-supported embankment over soft clay: Full-scale experiment, analytical and numerical approaches', Engineering Geology, 153(October 2015), pp. 53–67.

Nunez, M. A., Briançon, L. and Dias, D. (2013) 'Analyses of a pile-supported embankment over soft clay: Full-scale experiment, analytical and numerical approaches', Engineering Geology, 153, pp. 53–67.

O'Reilly, M. P. and Brown, S. F. (1991) Cyclic loading of Soils. Edited by V. N. Reinhold. United States of America.

Ochmański, M., Modoni, G. and Bzówka, J. (2015) 'Numerical analysis of tunnelling with jet-grouted canopy', Soils and Foundations.

Okur, D. V. and Ansal, A. (2007) 'Stiffness degradation of natural fine grained soils during cyclic loading', Soil Dynamics and Earthquake Engineering, 27(9), pp. 843–854.

Okyay, U. S. et al. (2012) 'Impedance Functions of Slab Foundations with Rigid Piles', Geotechnical and Geological Engineering, 30(4), pp. 1013–1024.

Okyay, U. S. et al. (2014) 'Centrifuge Modeling of a Pile-Supported Granular Earth-Platform', Journal of Geotechnical and Geoenvironmental Engineering, 140(2), p. 4013015.

Okyay, U. S. and Dias, D. (2010a) 'Use of lime and cement treated soils as pile supported load transfer platform', Engineering Geology. Elsevier B.V., 114(1–2), pp. 34–44.

Okyay, U. S. and Dias, D. (2010b) 'Use of lime and cement treated soils as pile supported load transfer platform', Engineering Geology. Elsevier B.V., 114(1–2), pp. 34–44.

Okyay, U. S., Lyon, I. De and Dias, D. (2008) 'Dynamic analysis of pile supported embankment systems : Model generation and sensitivity study', in International conference on numerical computation in geotechnical engineering. Skikda, Algeria, pp. 3–9.

Poblete, M., Fuentes, W. and Triantafyllidis, T. (2016) 'On the simulation of multidimensional cyclic loading with intergranular strain', Acta Geotechnica. Springer Berlin Heidelberg, 11(6), pp. 1263–1285.

Pramthawee, P., Jongpradist, P. and Sukkarak, R. (2017) 'Integration of creep into a modified hardening soil model for time-dependent analysis of a high rockfill dam', Computers and Geotechnics, 91, pp. 104–116.

Prisco, P. D. and Wood, D. M. (2012) Mechanical behaviour of Soils under environmentally induced cyclic Loads. Springer Wien New York.

Raithel, M., Kirchner, a and Kempfert, H. (2008) 'Pile-supported embankments on soft ground for a high speed railway-Load Transfer, Distribution and Concentration by different construction methods', Advances in Transportation …, pp. 401–407.

Rogbeck, Y. et al. (1998) 'Reinforced Piled Embankments in Sweden - Design Aspects', in International conference on Geosynthetic; Vol 2; Soil reinforcement applications; geotechnical and hydraulic applications, pp. 755–762.

Roscoe, K. H. and Burland, J. B. (1968) 'On the Generalized Stress-Strain Behavior of Wet Clays', in Engineering Plasticity, pp. 535–609.

Russell, D. and Pierpoint, N. (1997) 'An assessment of design methods for piled embankments', Ground Engineering, 30(10), pp. 39–44.

Salciarini, D. and Tamagnini, C. (2009) 'A hypoplastic macroelement model for shallow foundations under monotonic and cyclic loads', Acta Geotechnica, 4(3), pp. 163–176.

Satibi, S. (2009) Numerical analysis and design criteria of embankments on floating piles, Univ. Stuttgart, Inst. f. Geotechnik, Phd Thesis.

Sawicki, A. and Swidzinski, W. (1987) 'Compaction curve as one of basic characteristics of granular soils', in D.Cordary, I. E. F. and (ed.) 4th Colloque Franco-Polonais de Mechanique des Sols Appliquee. Grenoble, pp. 103–115.

Sawicki, A. and Swidzinski, W. (1989) 'Mechanics of a sandy subsoil subjected to cyclic loadings', International Journal for Numerical and Analytical Methods in Geomechanics, 13(5), pp. 511–529.

Seniwongse, M. (2010) 'Slab-on-Grade versus Framed Slab', Journal of Architectural Engineering, 16(4), pp. 164–169.

Shenton, M. J. (1985) 'Ballast deformation and track deterioration', in Track technology, Proceedings of a conference held at University of Nottingham. Pergamon Press, pp. 253–265.

Silver, M. L. and Seed, H. B. (1971) 'Deformation characteristics of sands under cyclic loading', Journal of the Soil Mechanics and Foundations Division, ASCE, 97(SM8), pp. 1081–1098.

Silver, M. L. and Seed, H. B. (1971) 'Volume changes in sands during cyclic loading', Journal of the Soil Mechanics and Foundations Division, ASCE, 97(SM9), pp. 1171–1182.

Simon, B. and Scholsser, F. (2006) 'Soil reinforcement by vertical stiff inclusions in France', Symposium of Rigid iIlusion in Difficult Soft Soil Conditions, pp. 3–23.

Soldo, B., Ivandic, K. and Babic, H. (2005) 'Experimental Study and DesignAnalysis of Piles in Clay', Electronic Journal of Geotechnical Engineering, 10B, pp. 16–20.

Soltani, M. and Maekawa, K. (2015) 'Numerical simulation of progressive shear localization and scale effect in cohesionless soil media', International Journal of Non-Linear Mechanics. Elsevier, 69, pp. 1–13.

Stewart, M. E. and Filz, G. M. (2005) 'Influence of Clay Compressibility on Geosynthetic Loads in Bridging Layers for Column-Supported Embankments', in GSP 131 Contemporary Issues in Foundation Engineering, pp. 1–14.

Suiker, A. S. J. (1999) Static and cyclic loading experiments on non-cohesive granular materials. TU Delft.

Terzaghi, K. (1943) Theoretical Soil Mechanics. Hoboken, NJ, USA: John Wiley and Sons, Inc.

Wichtmann, T., Niemunis, A. and Triantafyllidis, T. (2005) 'Strain accumulation in sand due to drained uniaxial cyclic loading', Soil dynamics and Earthquake Engineering, 25(12), pp. 967–979.

von Wolffersdorff, P.-A. and Schwab, R. (2009) 'The Uelzen I Lock - Hypoplastic finite-element analysis of cyclic loading', Bautechnik, 86, pp. 64–73.

von Wolffersdorff, P. A. (1996) 'A hypoplastic relation for granular materials with a predefined limit state surface', Mechanics of cohesive-frictional materials, 1(March), pp. 251–271.

Wood, M. (1990) Soil behaviour and critical state soil mechanics. Cambridge. Cambridge.

Youd, T. (1973) 'Factors Controlling Maximum and Minimum Densities of Sands', in Evaluation of Relative Density and its Role in Geotechnical Projects Involving Cohesionless Soils. 100 Barr Harbor Drive, PO Box C700, West Conshohocken, PA 19428-2959: ASTM International.

Youd, T. L. (1972) 'Compaction of sands by repeated shear straining', Journal of the Soil Mechanics and Foundations Division, ASCE, 98(SM7), pp. 709–725.

Yu, C. et al. (2009) 'The Behavior of Piled Embankments under Embankment Loads and Traffic Loads', International Conference on Transportation Engineering 2009, 2009(Icte 2009), pp. 1566–1571.

Zhan, Y. X., Yao, H. L. and Jiang, G. L. (2013) 'Design method of pile-slab structure roadbed of ballastless track on soil subgrade', Journal of Central South University, 20(7), pp. 2072–2082. doi: 10.1007/s11771-013-1709-2.

Zhang, J. et al. (2013) 'Coupled mechanical and hydraulic modeling of a geosynthetic-reinforced and pile-supported embankment', Computers and Geotechnics. Elsevier Ltd, 52, pp. 28–37.

Zhang, Y. and Liang, B. (2001) 'Dynamic Response to Subgrade of Highway in Geometric Irregularity Condition', Journal of Lanzhou Railway Uniiversity, 20(4), pp. 66–69.

Zhou, W. H. et al. (2016) 'Three-dimensional Finite Element Modelling of Soil Arching in Pile-supported Geogrid-reinforced Embankments', Procedia Engineering. The Author(s), 143(Ictg), pp. 607–614.

Zhuang, Y. (2009) 'Numerical modelling of arching in piled embankments including the effects of reinforcement and subsoil', (September), pp. 1–278.

Zhuang, Y. and Ellis, E. a. (2016) 'Finite-element analysis of a piled embankment with reinforcement and subsoil', Géotechnique, 66(7), pp. 596–601. doi: 10.1680/jgeot.15.P.139.

Zhuang, Y., Ellis, E. and Yu, H. (2008) 'The effect of subsoil support in plane strain finite element analysis of arching in a piled embankment', Advances in Transportation Geotechnics, pp. 417–423.

Zhuang, Y. and Li, S. (2015) 'Three-dimensional finite element analysis of arching in a piled embankment under traffic loading', Arabian Journal of Geosciences, 8(10), pp. 7751–7762.

Zhuang, Y. and Wang, K. (2018) 'Finite element analysis on the dynamic behavior of soil arching effect in piled embankment', Transportation Geotechnics. Elsevier Ltd, 14, pp. 8–21.

Zhuang, Y., Wang, K. Y. and Liu, H. L. (2014) 'A simplified model to analyze the reinforced piled embankments', Geotextiles and Geomembranes.